True Chemical Abundances of Galaxies in the Nearby Universe: A Comparison of Abundance Methods, Interstellar Processes, and Galaxy Types

A DISSERTATION
SUBMITTED TO THE FACULTY OF THE GRADUATE SCHOOL
OF THE UNIVERSITY OF MINNESOTA
BY

Danielle Amanda Berg

IN PARTIAL FULFILLMENT OF THE REQUIREMENTS
FOR THE DEGREE OF
Doctor of Philosophy

Evan D. Skillman, Advisor

August, 2013

Acknowledgements

This work began with my journey into graduate school in the Fall of 2008. Through the past five years I have grown immensely as both a scientist, and a person. I entered this field hesitantly curious, and am emerging hungry for knowledge through collaboration and my own critical analysis and reasoning. I have become a creative dreamer and found a sense of beauty in the way science can so simply explain aspects of our uniquely complex cosmos. I am truly left in awe and wonderment. And I get to experience this every day as an astrophysicist. That's right, I am a scientist.

Many have asked, *Are you a "rocket scientist"?* Nope. Even though that sounds way more cool. *"Rocket scientist"* most commonly refers to an aerospace engineer. The kind you are thinking of designs or builds rockets, satellites, etc. I do not know how to engineer anything. I am also not a cosmetologist or an astrologer, although cosmetology has more to do with science than astrology. Rather, I am an observer and a physicist. I have had the opportunity to travel to world class observing facilities, using the 5-m Palomar Telescope in California and the 6.5-m MMT and 8.4-m twin mirror Large Binocular Telescopes in Arizona. There I have gazed beyond our galaxy and peered into the cosmos where other galaxies of various sizes live. By examining the trickling of light detected from these far away wonders, I am able to evaluate the physical properties of the regions where stars have recently been born. After collecting this data, I apply the principle of physics, which are well understood in the laboratory, to these foreign environments. It is literally out of this world.

In practice, modern astronomical research involves a substantial amount of physics, and yes that means math, but it also feeds our innate human curiosity. It seeks to answer the larger questions always looming in the back of our minds of who we are, how we got here, and if we are unique. I am so blessed to have the opportunity to do

something that I truly love, and am grateful to the many people in my life who have supported and loved me through this journey.

For my mother, Dawn, and my father, Ben: It seems I came out of the womb screaming for attention and begging for knowledge. For the many years that I relentlessly asked *who?*, *when?*, *where?*, *how?*, and *why?*, I cannot thank you enough for their patience, love, and support. No matter how exaggerated my dreams may have been (somehow I missed my calling to be an Olympic gymnast and didn't reach math prodigy status at MIT like in Good Will Hunting), I owe every opportunity to you, for you gave me the wings I needed to fly.

For my sister, Alyson: I simply would not be who I am today without you. You are my other half, with out whom I would not be whole. No one can ever really understand you quite the way a sister does, and it was during the most difficult periods of this work that you were the light I needed in my life to keep going. I owe many of my happiest memories to you. Thank you for helping me laugh my way through the bumps.

For my brother, Chris: Thank you for the consistent and sarcastic outlook on life that has kept me smiling through the past 4 years of living together.

For my advisor and mentor, Evan: I could not ask for a better person to guide me through graduate school. I was always determined to finish my degree, but I never really believed that I could be successful as a researcher. Because of your continued support and understanding, the uncountable opportunities you have provided me, and your belief in me, you have pushed me to become a better scientist than I ever thought I could be. I am excited to pursue a career in research for the first time in my life, and I am grateful to you for giving me that opportunity.

For my unofficial junior advisor/mentor, collaborator, and friend, Kristy: You have worn many hats through out my time in graduate school and have played many important roles in my development. If nothing else, I want you to know that you profoundly impacted my path by showing me how to be a strong, independent women in a male dominated department and academic field. I cannot thank you enough for countless words of wisdom, encouragement, and support. You have given me the confidence to reach for higher goals, the perspective to learn from new situations, and a friendship that I cherish on both an intellectual and personal level.

For my fellow graduate students and the department: Surviving graduate school is

sort of like rowing a boat that has a hole in it. It has taken everyone of you to keep me afloat; for all of us have kept rowing together through the tides and continue to help bail each other out of murky situations. I am particularly grateful to L.A. Helton for inspiring me to work harder and challenge myself. You were my rock for 3 years, and I will never forget the selfless support and love you gave me. To my many officemates over the years: Dan, Steve, Damon, Kyle, and Jake, you have given me many of my favorite memories over the years. Thank you for answering my countless questions and putting up with my many sides. I am especially grateful to Dan, Steve, and Kyle for being my computer-whisperers and for many thought provoking scientific discussions, and to Terry Thibeault and Corinne Komor for all the magic they do behind the scenes.

For my collaborators: I am grateful to Liese van Zee for enhancing my graduate education through many helpful and stimulating discussions, sharing her expert observing knowledge, and endless support. Additionally, Liese is a dedicated and determined researcher who has been an exemplary role model for me during my graduate career.

I cannot thank Rick Pogge enough for many teaching moments while observing at the Large Binocular Telescope, during MODS data reduction "Boot Camp", and throughout our collaboration on the CHAOS project. You get more done in a day than anyone else I know, and still manage an interesting and outgoing life - an inspiration to me and all that encounter you.

Many other astronomers have had impacts on my career. I must thank Andrew Marble for introducing me to observing and spectral data reduction. You are a great teacher, exhibiting extreme patience and intellect in all of our interactions, and you have been the most important editor of the papers contained in this thesis. I am grateful to Kevin Croxall for so gracefully entering the CHAOS project; for substantially improving the work I had started and accommodating my every need. You have made working on CHAOS a joy and I look forward to our continued work. Finally, I very grateful to Julianne Dalcanton for generously including me in an extension of the PHAT project. It has provided me with many new scientific connections and learning opportunities. You have been as inspiration to me, and taught me much about refining the more subtle aspects of being a successful scientist.

For my friends: I cannot imagine my life with out you. Someone once said to me, *"you scientists are no walk in the park!"* I have no doubt that being around my constant

analytic nature can be taxing, but you have stuck by me through the good and the bad. To Kyleen (Oleson) Johnson, Kelsie (Droogsma) Koppel, Kasey Lyng, Laura Hemmy, Aubrey Austin, Lisa (Mudd) Blacker, Nicole Gergen, Kate Pachan, Katie and Greg Pokorski, Leif Anderson, Peter Spitsnogle, Matt Flores, Erin Illlosi, Lauren Tallarita, Adrienne Richter, and Nina Denio - you are more than my friends, you are my family, and I am so grateful to have you in my life and feel so loved.

To many other who helped me complete this journey, thank you.

Dedication

For LAH who taught me the joy of critical thinking and with out whose support and encouragement this work would not have been possible. And for LJR who taught me to listen to my heart and dream BIG.

Abstract

This work was motivated by recent ISM studies which have raised questions regarding long-standing trends. Peeples et al. (2008) identified low-mass, high oxygen abundance outliers from the well studied mass-metallicity (M-Z) relationship, challenging our understanding of galaxy evolution. We present MMT spectroscopic observations of four of these dwarf galaxy outliers, extending the wavelength coverage from the previous Sloan Digital Sky Survey (SDSS) observations. We re-examined these anomalous spectra and compared to the parameter space of galaxies for which standard strong-line methods are calibrated. We discuss the physical nature of these galaxies that leads to their unusual spectra (and previous classification as outliers), finding their low excitation, elevated N/O, and strong Balmer absorption are consistent with the properties expected from galaxies evolving past the "Wolf-Rayet galaxy" phase. We compare our results to the "main" sample of Peeples et al. (2008) and conclude that they are outliers primarily due to enrichment of nitrogen relative to oxygen, and not due to unusually high oxygen abundances for their masses or luminosities.

The M-Z relationship is well defined using strong-line abundance calibrations, but a comparable relationship derived from direct abundances is lacking. Examining outliers from the M-Z relationship highlights the biases and limits of various strong-line calibrations, and stresses the importance of using direct oxygen abundances to compare and rank galaxies. However, the low-mass dwarf galaxies that occupy the metal-poor end of the M-Z relationship are intrinsically faint, making direct oxygen abundance detections increasingly difficult.

To address the issue of securing the low-luminosity end of the M-Z relationship, we present MMT spectroscopic observations of H II regions in 42 low-luminosity galaxies in the *Spitzer* Local Volume Legacy (LVL) survey. Direct oxygen abundances were determined based on the temperature sensitive [O III] λ4363 line, measured at a strength of 4σ or greater, for 31 of the 42 galaxies in our sample. Combining our results with previous direct abundance studies, we present a further refined sample, requiring reliable distance determinations (based on the tip of the red giant branch or Cepheid variables). Using the resulting sample composed of 38 objects, we compared to B-band

luminosities, 4.5 μm luminosities, and stellar masses in order to characterize the L-Z and M-Z relationships at low-luminosity. We show that the measured dispersions in the direct abundance relationships are significantly smaller than seen in strong-line abundance relationships. This leads us to conclude that if an accurate distance is available, the luminosity of a low-luminosity galaxy is often a better indicator of metallicity than that derived using certain strong-line methods. Additionally, our results provide the first direct estimates of oxygen abundance for 19 local volume dwarf galaxies.

Unlike the uniform physical conditions observed for dwarf galaxies, properties of the ISM of spiral galaxies are known to show radial variations, such as in their dust-to-gas ratio and abundance ratios. However, a large enough database to compare relative trends amongst galaxies does not exist. Motivated by the need to place gradients on the same scale for comparisons amongst galaxies, we present direct abundance gradients of the nearby spiral galaxies NGC 628 and NGC 2403, and the direct observations of M31. In the case of NGC 628, the new metallicity gradient deviates from previous strong-line studies in that the measured slope is significantly shallower. With these new direct metallicities we are also able to revisit the 70/160 μm color metallicity relationship. By using only high signal-to-noise direct oxygen abundance measurements, we set a reliable and consistent basis for comparing to previous direct abundance studies and the derivation of future abundance gradients in spirals.

Additionally, we measure N, S, Ne, and Ar abundances. A bi-modal N/O gradient pattern is measured for NGC 628, and other non-barred spiral galaxies in the literature. Notably, the N/O ratio plateaus beyond R_{25}, demonstrating that primary nitrogen production is the dominant mechanism in the outer disk. The outer disk beyond R_{25} was not sampled in NGC 2403. Similar to previous studies, we measure a negative N/O gradient with radius for the inner disks of spiral galaxies ($R < R_{25}$), indicative of significant contributions from secondary nitrogen production. As expected for α-process elements, we show that S/O, Ne/O, and Ar/O appear to be constant over a range in oxygen abundance in both NGC 628 and NGC 2403 such that the α-elements and O are produced in lock-step.

Through this work we find that significant improvements can be made to abundance relationships using the direct abundance method. We promote the use direct oxygen abundances over strong-line abundance calibrations, when possible, as a more consistent

way to rank and compare galaxies. Furthermore, we have defined more secure L-Z and M-Z relationships for dwarf galaxies and abundance gradients for nearby spiral galaxies, decreasing the extrinsic observational uncertainties. To continue this worthwhile enterprise of ISM studies, future work will expand upon the dwarf and spiral galaxy direct abundances presented in this thesis.

Contents

List of Tables

List of Figures

Chapter 1

Introduction

1.1 Why We Study Chemical Abundances in Galaxies:

The universal question that has preplexed the human race since the beginning of our existence is how did we get here? One of the main goals of astronomy is to understand the evolution of galaxies, and in turn explain how our own galaxy formed, evolved, and became host to life as we know it. A key tracer of how a galaxy has changed over time is to look at how the chemical composition of galaxies, i.e., their elemental abundances, have evolved. After our Universe was created in the Big Bang, the majority of the resulting gas was hydrogen and helium ($\approx$ 75% H and $\approx$ 25% He), from which the first galaxies formed. Within these galaxies, stars began to synthesize heavy elements (elements heavier than hydrogen and helium, known to astronomers as *metals* or Z) via nucleosynthesis (nuclear fusion), which were then dispensed into the surrounding medium when the progenitor stars died. Because these first galaxies had little to no metals present, they are known as *low metallicity* or *metal poor* galaxies. Each successive generation of massive stars forms from the local gas that is enriched by the nucleosynthetic products of the previous episodes of star formation. This cycle causes metallicity to increase monotonically with time as recycled metals in the gas continue to build up. Therefore, due to the nature of its production, the metallicity of a galaxy is a sensitive observational diagnostic of its past star formation history and present day evolutionary state.

Accurate abundance measurements provide valuable insight into the the interplay

between many fundamental processes in galaxy evolution. In an ideal closed box, the metal content of a galaxy is dictated by how much star formation has occurred. In reality, additional forces such as tidal interactions between galaxies, gas accretion, gas outflows, and supernova-driven feedback can all play a role in shaping the metal content of a galaxy. Oxygen abundance is an important tracer of metal content because it is the most abundance element (by number) in the Universe after hydrogen and helium and is convenient to observe since its emission lines are ubiquitous in the rest-frame optical regime. For these reasons, the oxygen abundance relative to hydrogen is often used as a proxy for metallicity, denoted 12+log(O/H). Furthermore, because these lines originate principally in star-forming regions, they trace the physical conditions in the gas from which the current generation of massive stars is forming. In the present epoch, the majority of star formation is taking place in spiral galaxies, where the varying conditions across the face of spirals allow abundances to be sampled over a large range in parameter space. Additionally, dwarf galaxies often allow observations of a single well mixed environment, and tend to be metal poor with little previous star formation, making them ideal laboratories for studying the early stages of chemical evolution.

1.2 How do we learn about the interstellar medium?

1.2.1 How do we know what we are really seeing?

We first need to know how to detect different elements in the interstellar medium (ISM; the gas and dust that fills the space between stars). This can be done by analyzing elemental components of gas in laboratories here on Earth. Each element on the periodic table has a unique structure, and thus a unique set of energy levels that its electrons can be excited to. We can create a mental cartoon of an atom's energy levels as a 1D skee-ball machine (1D in the sense that we assume perfectly straight throws such that we cannot miss our target side to side, only vertically), where it takes more energy to get to each higher target hole. When an element absorbs light (energy), it can respond in one of three ways: (1) If the energy is too small, our skee-ball does not reach any of the higher levels and it falls back down to the bottom. Similarly, nothing happens to an actual bound electron as it falls back down to its ground state. (2) If the energy is equal to or greater than than one of the unique energy levels of the atom, our skee-ball has

enough energy to reach one of the target holes and stays there. In terms of the atom, an electron will be excited up to that energy level. (3) Finally, if the energy exceeds the highest energy level of the atom, our skee-ball has so much speed that it flies off of the board. In this case, the electron can escape and the atom is now ionized, meaning it is missing an electron. Unlike my favorite arcade game, electrons can return from these energy levels. When an electron travels back down the energy ladder, it emits a photon (light) with an energy equal to the difference in energy steps it transitioned. In the laboratory we can excite different elements in gas form and record the light emitted from them. We detect the result using a spectroscope, which splits up light similar to a prism and creates a rainbow, except we record a spectra, or photon detections on a CCD camera at different wavelengths, rather than seeing the color. In the visible, red light has a long wavelength ($\lambda \sim 700$ nm) corresponding to a low energy and blue light has a short wavelength ($\lambda \sim 400$ nm) corresponding to high energy levels. Because each element has a specific set of energy levels or wavelengths that it emits at, we detect a set of peaks unique to that element that can be used as a *spectral fingerprint*. When we then turn our detectors to the skies, the same spectral fingerprints are seen, identifying the elements in these distant laboratories.

1.2.2 Looking in Distant Laboratories:

When new stars form, they emit high-energy photons (light at short wavelengths) that ionize the surround hydrogen gas (the skee-ball escapes). This forms a region of (almost) completely ionized hydrogen that astronomers refer to as an *H II* region. Figure 1.1 shows a schematic of such a region where the newly formed, hot O- and B-type stars ionize the surround ISM of atomic or neutral hydrogen. For hydrogen atoms, they are continuously ionized by the copious amounts of UV radiation produced by the central stars, but eventually they will recombine with previously freed electron and emit a photon. This process produces a set of lines known as the *Balmer series*. There are many lines produced in this series, but there are four lines almost always seen in the visible portion of an H II region spectrum: Hδ λ4101 is the weakest of these lines, and is produced when an electron in the 6th energy level jumps down to the 2nd energy level (or 1st excited state). The next strongest line is Hγ λ4340, which comes from an electron traveling from the 5th to the 2nd energy level. Next, Hβ λ4861 is produced by the 4$\rightarrow$2

energy level transition in hydrogen. Finally, the strongest Balmer line is Hα λ6563, which is produced by the 3→2 transition. These are not the only possible transitions for hydrogen electrons. A captured electron could, for instance, travel from 6→3 and then from 3→2. Many different combinations exist, but arriving at the 3rd energy level has the greatest number of possible avenues, which is what makes the subsequent 3→2 Hα transition the strongest Balmer line.

For less common elements, such as oxygen (O/H$\sim 10^{-4}$) which require higher excitation energies, emission lines are produced by collisional excitations with fast moving atoms (when a high energy UV photon ionizes an atom, the extra energy is stored as kinetic energy), followed by spontaneous decay. Figure 1.2 shows a typical H II region is characterized by a strong emission-line spectrum of ionized hydrogen and trace amounts of ionized oxygen and nitrogen on top of a continuum of diffuse emission. These features provide a wealth of knowledge about the physical parameters of the region, where the ratio of intrinsically faint (auroral) lines to strong-lines provides an estimate of the electron temperature (e.g., [O III] λ4363/(λ4959+λ5007)), and emission lines originating from the same energy level but ending at a fine structure split level (e.g., [S II] λ6731/λ6717) give an estimate of the electron density. Given the temperature and density of the H II region and the strength of ionic emission lines, one can determined the local chemical abundances, i.e., the amount of trace metals relative to hydrogen. This method provides the most *accurate* chemical abundances and is known as the *direct* method. Because the faint auroral lines are difficult to detect, first order correlations with the stronger emission lines can be used to *estimate* abundances - there are the so called *strong-line* calibrations. These correlations are widely used, but are only statistical indications of chemical abundances, with large associate systematic uncertainties.

1.3 Extragalactic Chemical Abundances

Nearby galaxies of all morphologies (i.e., spirals, dwarfs, irregulars, and ellipticals) have been studied in depth to learn more about their chemical abundances. From this work, a fundamental relationship between the mass of the stars in a galaxy and its metallicity evolution (the M-Z relationship) has been observed (e.g., Tremonti et al., 2004). However, the mass of a galaxy is difficult to determine from observations. Fortunately, the

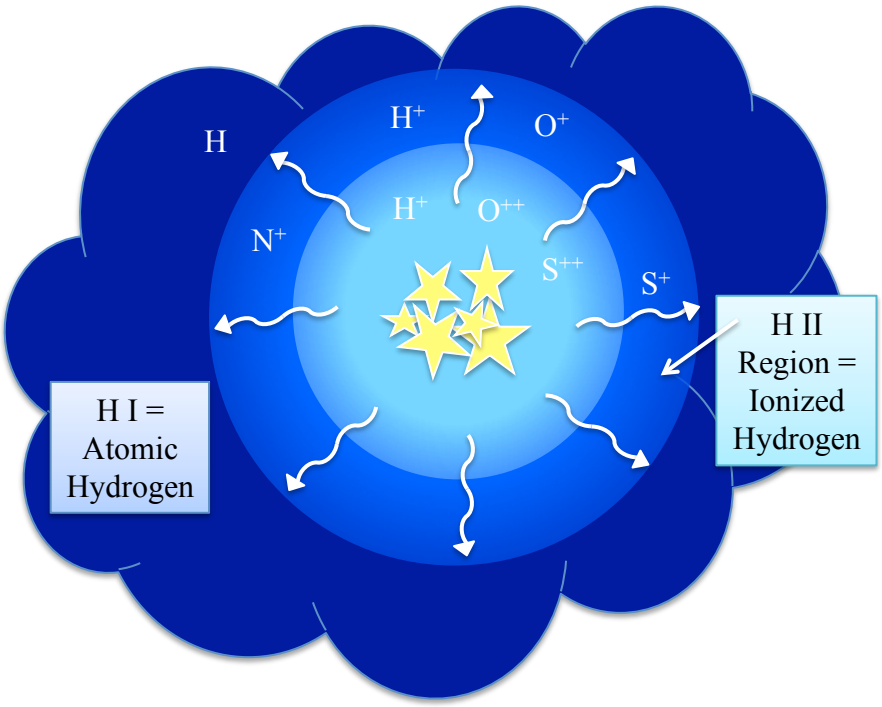

Figure 1.1: A simple schematic of an H II region. Bursts of star formation occur in molecular clouds, represented by the darkest blue structure. At the center, the hottest O- and B-type stars emit copious amounts of high energy photons (UV light), which ionizes the gas around it. The extent to which the stars ionize hydrogen in the cloud defines the edge of the H II region. Within this region, we can imagine a simple 2-zone structure in which elements in the inner sphere of gas (lightest blue) can be doubly ionized (lose two electrons) and is surrounded by an outer sphere (medium blue) in which elements are singly ionized (lose one electron). Thus the energy diminishes as you move farther out in radius from the central stars until eventually no more elements are ionized and the medium is now composed of neutral atomic hydrogen.

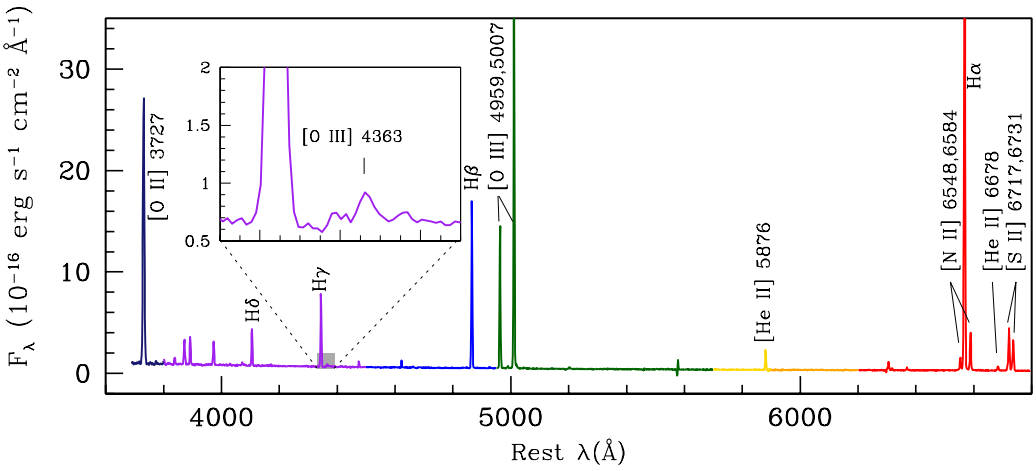

Figure 1.2: A spectrum of a typical H II region in a nearby dwarf galaxy, NGC 4449. Wavelength is plotted on the horizontal axis and flux on the vertical axis, showing the amount of light (photons) detected at each wavelength (energy) in the visible portion of the electromagnetic spectrum. Color has been added to the plot to denote the ranges in wavelength of each hue our eyes are able to detect. Note that the far blue end begins to get very dark as these energies are at the edge of the detection limits of our eyes. The spectrum is made up of a flat continuum, or continuous energy from the recently formed stars, and emission lines emitted by different elements in the gas. A portion of the graph is expanded to show the important, but faint, temperature-sensitive emission line located there.

mass and luminosity of a galaxy are also closely related. A luminosity-metallicity (L-Z) relationship has been observed for low-redshift (nearby) dwarf galaxies (e.g., Skillman et al., 1989; Lee et al., 2006a, and references therein) and spiral galaxies (e.g., McCall et al., 1985; Garnett & Shields, 1987; Zaritsky et al., 1994; Tremonti et al., 2004, and references therein). This relationship is observed over a range of 10 magnitudes in galaxy optical luminosity, where a magnitude is measured in logarithmic scale such that a magnitude difference of 1 represents a difference in brightness scaled by 2.5 times. However, since galaxies are naturally fainter at the low-luminosity end, few accurate abundances observations have been recorded there making the data relatively sparse. Additionally, the physical drive of the M-Z relation remains under debate. As astronomers examine the interrelationship between chemical abundance measurements, star formation, gas accretion, and gas outflow by measuring the evolution of the M-Z relationship, a secure M-Z relationship for the current epoch is needed for comparison.

1.3.1 Dwarf Galaxies

Dwarf galaxies are abundant in our nearby universe and are among the most well-studied galaxies in the universe. As relatively simple, often isolated environments, dwarf galaxies set a basis from which astronomers can build their understanding of galaxy formation and evolution of both individual and groups of galaxies. This has lead to massive campaigns studying the kinematics, metallicities, and stellar contents of dwarf galaxies (see, for example, Blanton & Moustakas, 2009). From these studies, dwarf galaxies have been observed to follow the M-Z relationship. In the sequence of galaxy types, dwarf galaxies have the smallest masses, are the least luminous, and have had the least amount of star formation, making them the most metal-poor. In this sense, dwarf galaxies are the most basic building blocks of galaxy evolution that we can directly study.

1.3.2 Spiral Galaxies

The process of analyzing spiral galaxies presents a larger challenge than dwarf galaxies, as a single abundance measure is not sufficient to characterize the entire galaxy. However, the study of spiral galaxies is a worth while enterprise as they allow observations

of a wide range of environment parameters in a single location. Dominant sites of star formation are also abundant in relatively low density environments in spirals. These characteristics make spiral galaxies ideal laboratories for examining star formation and chemical evolution.

Aller (1942) and Searle (1971) were the first to infer radial gradients in excitation across the disks of spiral galaxies. They found that the inner disk of the galaxy tends to be the most luminous, with ongoing star formation. Here star forming regions are metal-rich and have low gas temperatures. As we move farther out in radius along the disk of the galaxy, less cumulative star formation has occurred such that metallicity is seen to decrease with radius and electron temperature is seen to increase. Since these first observations, numerous studies have shown that, typically, spiral galaxies exhibit these radial abundance gradients. This trend was first measured in our own galaxy by Shaver et al. (1983) and was confirmed by observations of other nearby spiral galaxies (e.g., Pagel & Edmunds, 1981; Shields, 1990). While the first-order description of spiral galaxies is secure, additional accurate abundance studies of spirals are needed to understand the the key processes regulating their chemical evolution.

The properties of the ISM of spiral galaxies are known to show radial variations, such as in their dust-to-gas ratio and abundance ratios, however, a large enough database to compare relative trends amongst galaxies does not exist. In order to place gradients on the same scale for comparison amongst galaxies, reliable and consistent derivations of abundances are needed (see, e.g., Moustakas et al., 2010). Thus, there is motivation to observe spiral galaxies in the nearby universe with low inclinations, meaning the galaxy appears more face-on (or like a pancake) in the sky, rather than edge-on. This vantage point offers the opportunity to measure chemical abundances over the entire surface of the galaxy and subsequently compare these abundances with variations in physical conditions. Since the physical conditions in the ISM are likely important to the star formation process and play a role in the composition, conditions, and size distribution of dust grains, understanding the connection between chemical abundances and the physical conditions in the ISM is fundamental to understanding star formation and galaxy evolution.

1.4 The Chapters

The organization of this thesis follows the chronology in which the projects were undertaken. Many questions concerning extragalactic chemical abundances and galaxy evolution remain, leading to the broad goals established for this work:

- Chapter 2 examines and compares the strong-line abundance calibrations used to define the mass-metallicity relationship.
- Chapter 3 measures reliable oxygen abundances of nearby local dwarf galaxies and extends the mass-metallicity relationship to lower abundances.
- Chapter 4 analyzes the radial abundance gradients in well studied nearby spiral galaxies NGC 628 and NGC 2403.
- Chapter 5 presents the the continuation of our study of radial abundance gradients with observations across M31.

Chapter 2

Re-examining High Abundance SDSS Mass-Metallicity Outliers: High N/O, Evolved Wolf-Rayet Galaxies?

A slightly modified version of this chapter has been published in The Astrophysical Journal with the following bibliographic reference: Berg, D. A., Skillman, E. D., & Marble, A. R. 2011, ApJ, 738, 2

Abstract

We present new MMT spectroscopic observations of four dwarf galaxies representative of a larger sample observed by the Sloan Digital Sky Survey (SDSS) and identified by Peeples et al. (2008) as low-mass, high oxygen abundance outliers from the mass-metallicity relation. Peeples et al. (2008) showed that these four objects (with metallicity estimates of $8.5 \leq 12 + \log(\mathrm{O/H}) \leq 8.8$) have oxygen abundance offsets of 0.4-0.6 dex from the M_B luminosity-metallicity relation. Our new observations extend the wavelength coverage to include the [O II] $\lambda\lambda$3726,3729 doublet, which adds leverage in oxygen abundance estimates and allows measurements of N/O ratios. All four spectra are low excitation, with relatively high N/O ratios

(N/O $\gtrsim$ 0.10), each of which tend to bias estimates based on strong emission lines toward high oxygen abundances. These spectra all fall in a regime where the "standard" strong-line methods for metallicity determinations are not well calibrated either empirically or by photoionization modeling. By comparing our spectra directly to photoionization models, we estimate oxygen abundances in the range of $7.9 \leq 12 + \log(\mathrm{O/H}) \leq 8.4$, consistent with the scatter of the mass-metallicity relation. We discuss the physical nature of these galaxies that leads to their unusual spectra (and previous classification as outliers), finding their low excitation, elevated N/O, and strong Balmer absorption are consistent with the properties expected from galaxies evolving past the "Wolf-Rayet galaxy" phase. We compare our results to the "main" sample of Peeples et al. (2008) and conclude that they are outliers primarily due to enrichment of nitrogen relative to oxygen, and not due to unusually high oxygen abundances for their masses or luminosities.

2.1 Introduction

There is a fundamental relationship between the mass of stars in a galaxy and its metallicity evolution (hereafter, the M-Z relation). Empirically, this has been observed as a luminosity-metallicity relationship for low redshift dwarf galaxies (e.g., Lequeux et al., 1979; Skillman et al., 1989; Lee et al., 2006b, and references therein) and spiral galaxies (e.g., McCall et al., 1985; Garnett & Shields, 1987; Zaritsky et al., 1994; Tremonti et al., 2004, and references therein). This robust relationship is observed over a range of 10 magnitudes in galaxy optical luminosity (e.g., Zaritsky et al., 1994; Tremonti et al., 2004; Lee et al., 2006b). In recent years, galaxies at higher redshifts have also shown a mass-metallicity or luminosity-metallicity relationship, and mounting evidence suggests this relationship evolves with time (e.g., Kobulnicky et al., 2003; Kobulnicky & Kewley, 2004; Shapley et al., 2004; Savaglio et al., 2005; Maiolino et al., 2008, and references therein), but see also Mannucci et al. (2010). Thus, this relationship provides both a very strong constraint on theories of galaxy evolution and a tool to better understand galaxies at higher redshifts.

Tremonti et al. (2004, hereafter T04) derived luminosities, metallicities, and masses for ∼53,000 low redshift galaxies observed in the Sloan Digital Sky Survey (SDSS; York et al., 2000) and convincingly demonstrated that the basis of the empirically observed luminosity-metallicity relationship is an underlying association between stellar mass and metal abundance. The metallicities were estimated by fitting all observable strong emission lines and deriving a metallicity likelihood distribution for each galaxy based on theoretical model fits calculated using a combination of stellar population synthesis and photoionization models. These models were then used with z-band luminosities to form mass estimates.

The physical driver for the M-Z relationship is still debated. Many studies favor supernova driven winds for the inability of a low-mass galaxy to retain its newly synthesized heavy elements, resulting in a lower effective yield with decreasing mass (e.g., Dekel & Silk, 1986). Other observational and theoretical studies are critical of this theory. For example, Dalcanton (2007) emphasizes the additional importance of star formation efficiency as outflows are an insufficient regulator in the absence of depressed star formation. Thus, a better understanding of the mass-metallicity relationship remains important.

Although the M-Z relationship is well defined, it shows measurable scatter. Since observational error accounts for only half of the metallicity spread in the M-Z relation (Cooper et al., 2008), one or more physical processes may be responsible for the remainder. Suggestions for the scatter include variations in the star formation history (e.g., recent starbursts, Contini et al., 2002), variations in stellar surface mass density (Ellison et al., 2008), and variations in local galaxy density (e.g., Cooper et al., 2008, and references therein). Motivated by the fact that outliers often provide key insights into the nature of physical relationships (e.g., Skillman et al., 1996), Peeples et al. (2008, hereafter P08) and Peeples et al. (2009) identified samples of outlier galaxies from the T04 study.

P08 analyzed a sample of 41 high oxygen abundance, low-luminosity galaxy outliers from the M-Z relation of T04. Their "main" sample is comprised of 24 high abundance ($8.95 \leq 12 + \log(\mathrm{O/H}) \leq 9.27$), relatively low-mass ($9.1 \leq \log(\mathrm{M_\star/M_\odot}) \leq 9.9$), low-luminosity (sub-$\mathrm{L_\star}$; $-19 \leq \mathrm{M}_B \leq -17$) dwarf galaxies. A redshift lower limit of $z > 0.024$ was imposed to ensure the inclusion of the [O II] $\lambda\lambda$3726,3729 emission doublet

in the SDSS spectral coverage.[1] The data set was extended to include even lower mass galaxies, creating a second "very low mass" sample, with $7.4 \leq \log(M_\star/M_\odot) \leq 9.0$, $-17 \leq M_B \leq -14$, and $8.68 \leq 12 + \log(O/H) \leq 9.12$. In order to increase the sample to these lower masses, the redshift limit was dropped. All galaxies in the resulting "very low mass" sample have $z < 0.024$, and thus lack an [O II] $\lambda\lambda$3726,3729 spectral measurement. The typical oxygen abundance offset in the O/H - M_B plane for a galaxy in the "main" sample is ≈ 0.4 dex, while the typical offset for the "very low mass" sample is ≈ 0.6 dex (with offsets as large as ≈ 0.9 dex).

P08 favored isolated or undisturbed systems with relatively low gas mass fractions nearing the end of their star formation activity as an explanation for the unexpectedly high oxygen abundances. Other possible causes for the high abundance outliers were considered and ruled out, such as discrepantly low luminosities for their masses or inaccurate metallicity calculations.

Nebular oxygen abundances derived from the observations of strong emission lines and in the absence of direct measurements of the electron temperature are always subject to systematic effects (e.g., Kennicutt et al., 2003a, and references therein). This is particularly true at the higher abundances typically found in spiral galaxies where several calibrations of methods based solely on strong lines result in systematically higher oxygen abundances when compared to oxygen abundances derived from direct measurements of the electron temperature (see, e.g., discussion in Bresolin, 2007, and references therein). Importantly, Yin et al. (2007) and Pérez-Montero & Contini (2009) have pointed out that strong-line calibrators that are based on the strength of the [N II] $\lambda\lambda$6548,6584 emission lines are biased in the sense that large values of N/O lead to overestimates of the oxygen abundance. At lower values of oxygen abundance, in general, the strong-line methods show better agreement with the oxygen abundances derived from direct temperature measurements, but van Zee et al. (2006) have shown that there can be significant discrepancies at low values of excitation (λ5007/λ3727). Given the uncertainties in strong-line oxygen abundance measurements, it is warranted to reinvestigate the conclusions of P08.

The prospect of galaxy outliers from the M-Z relationship, and their consequences

[1] Seven galaxies with $z < 0.024$ passed the subsequent error and visual inspection cuts imposed by Peeples et al. (2008) and so were kept in their "main" sample.

for galaxy evolution models, motivated the re-analysis of these objects. In this paper we discuss the previous SDSS and new MMT observations in § 3.3 and describe the analysis of the latter in § B.1. In § 2.4 we use our new observations of the [O II] $\lambda\lambda$3726,3729 emission lines to compare the properties of the outliers to the SDSS galaxies. Section 5.4 is dedicated to looking at several metallicity determinations and the appropriate applications, including the O3N2 method (§ 2.5.3), the N2 indicator (§ 2.5.3), and the R_{23} index (§ 2.5.3). Our best estimates of the oxygen abundances, the nature of the objects in the "very low mass" sample that gives rise to their discrepant spectra, and an inspection of the nature of the objects in the P08 "main" sample are discussed in § 3.7.

2.2 Data

2.2.1 Sample

Four of the 17 metal-rich galaxies identified by P08 as "very low mass" ($\log(M_\star/M_\odot) < 8.7$) outliers from the M-Z relationship were selected for follow-up observations with the MMT (see Table 2.1). These targets were chosen both for their significant departures from the mass-metallicity relationship and their availability during a single scheduled observing run. They have suggested high metallicities, as measured by T04, of $8.69 \leq 12 + \log(O/H) \leq 8.86$. For SDSS J022628.28+010937.7, SDSS J024121.80+000329.2, SDSS J082639.19+253553.5, and SDSS J082633.77+252959.2 respectively (hereafter abbreviated as SDSS- plus the first six digits of the Right Ascension), these oxygen abundances lie 0.37, 0.40, 0.55, and 0.55 dex above (and well outside the ~ 0.1 dex scatter of) the luminosity-metallicity relationship histogram medians presented by P08. Like all of the objects in the P08 parent sample, these four galaxies are fairly isolated[2] , low-redshift ($0.0051 < z < 0.0227$) dwarfs ($-17 < M_B < -15$), with no obvious companions and somewhat depressed star formation rates (P08).

[2] Note that J082639.19+253553.5 and J082633.77+252959.2 are members of the same group (Peeples, private communication, 2010).

Table 2.1. Sub-Sample of Low-Luminosity Outliers from Peeples et al. (2008)

Object/ SDSS Spectra	R.A. (J2000)	Dec. (J2000)	M_B (mag)	log $M_\star$ ($M_\odot$)	Redshift	g-r (mag)
SDSS J022628.28+010937.7 spSpec-51869-0406-561.fits	36.6179	1.16053	-16.86	7.92	0.0051	0.51
SDSS J024121.80+000329.2 spSpec-52177-0707-355.fits	40.3408	0.05813	-16.56	8.70	0.0227	0.46
SDSS J082639.19+253553.5 spSpec-52945-1586-164.fits	126.6633	25.59821	-15.87	8.59	0.0078	0.71
SDSS J082633.77+252959.2 spSpec-52945-1586-161.fits	126.6407	25.49979	-15.23	8.07	0.0072	0.55

Note. — Publicly available SDSS spectra can be found at SDSS.org. The R.A., Dec., M_B, log M$\star$, and redshift values are taken from P08 (see their Table 1 for more details). The SDSS DR 7 provided g-r colors.

2.2.2 SDSS Spectra

The measurements made by T04 and used by P08 were derived from the publicly available SDSS[3] Data Release 4 (Adelman-McCarthy et al., 2006) data files referenced in Table 2.1. We used the SDSS pipeline reduced spectra (rather than performing our own 1-D extraction and reductions) to minimize differences between analyses. For a thorough description of the data reduction refer to Adelman-McCarthy et al. (2006). While the median signal-to-noise (S/N) values for the SDSS spectra (12–47) meet the S/N (per pixel) > 8 requirement for reliable metallicity estimates (Kobulnicky et al., 1999), the wavelength coverage (3800–9200 Å) excludes the [O II] λ3727 emission line from their spectra. Although the red [O II] $\lambda\lambda$7320,7330 lines are included in the wavelength range, they are only detected in the spectrum of SDSS-022628. In Figures 2.1.1-2.1.4, we have indicated the locations of the [O II] λ3727 and [O II] $\lambda\lambda$7320,7330 emission lines.

In § 2.4 and later in the paper, we compare galaxies from P08 to samples from the SDSS. In these comparisons, we use values of nebular emission line strengths, stellar absorption line strengths, star formation rates, and stellar masses based on SDSS spectra

[3] http://www.sdss.org/dr4/

and photometry from the MPA-JHU data catalogue.[4] Stellar masses were determined based on fits to photometry following the work of Kauffmann et al. (2003), and star formation rates (SFR) were based on Brinchmann et al. (2004) and Salim et al. (2007).[5]

Objects with [O II], [O III], Hβ, [N II], and Hα line strengths less than 5σwere filtered out in order to increase the quality of this data set.

2.2.3 MMT Spectra

Observations

New MMT observations were acquired in order to obtain improved S/N spectra and extended blue wavelength coverage including the [O II] λ3727 line. The MMT data were taken with the Blue Channel spectrograph (Schmidt et al., 1989) on the UT date of 2008 November 1-2. Sky conditions were optimal with no cloud cover and sub-arcsecond seeing. A 500 line grating, 1″ slit, and UV-36 blocking filter were used, yielding an approximate dispersion of 1.2 Å per pixel, a full width at half maximum resolution of $\lesssim$ 3 Å, and a wavelength coverage of 3690–6790 Å. Bias frames, flat-field lamp images, and sky flats were taken each night. The latter were primarily necessary due to significant differences between the chip illumination patterns of the sky and the MMT Top Box that houses the Blue Channel incandescent flat-field lamp. Multiple standard stars from Oke (1990) with spectral energy distributions peaking in the blue and containing minimal absorption were observed throughout the night using a 5″ slit over a range of airmasses.

All four galaxies had strong central brightness peaks which were centered on the 1″ × 180″ slit. Three 900 second exposures (600 seconds for SDSS-086239) were made at a fixed position angle which approximated the parallactic angle at half the total integration time. This, in addition to observing the galaxies at an airmass below 1.5, served to minimize the wavelength-dependent light loss due to differential refraction (Filippenko, 1982). A single slit position for each target was sufficient to characterize the global oxygen abundance, as metallicity gradients are small in low-mass galaxies (e.g., Skillman et al., 1989; Kobulnicky & Skillman, 1996, 1997a; Lee et al., 2006a). Finally, combined helium, argon, and neon arc lamps were observed at each pointing

[4] http://www.mpa-garching.mpg.de/SDSS/

[5] MPA-JHU used a method similar to Salim et al. (2007) to aperture correct their SFRs.

for accurate wavelength calibration.

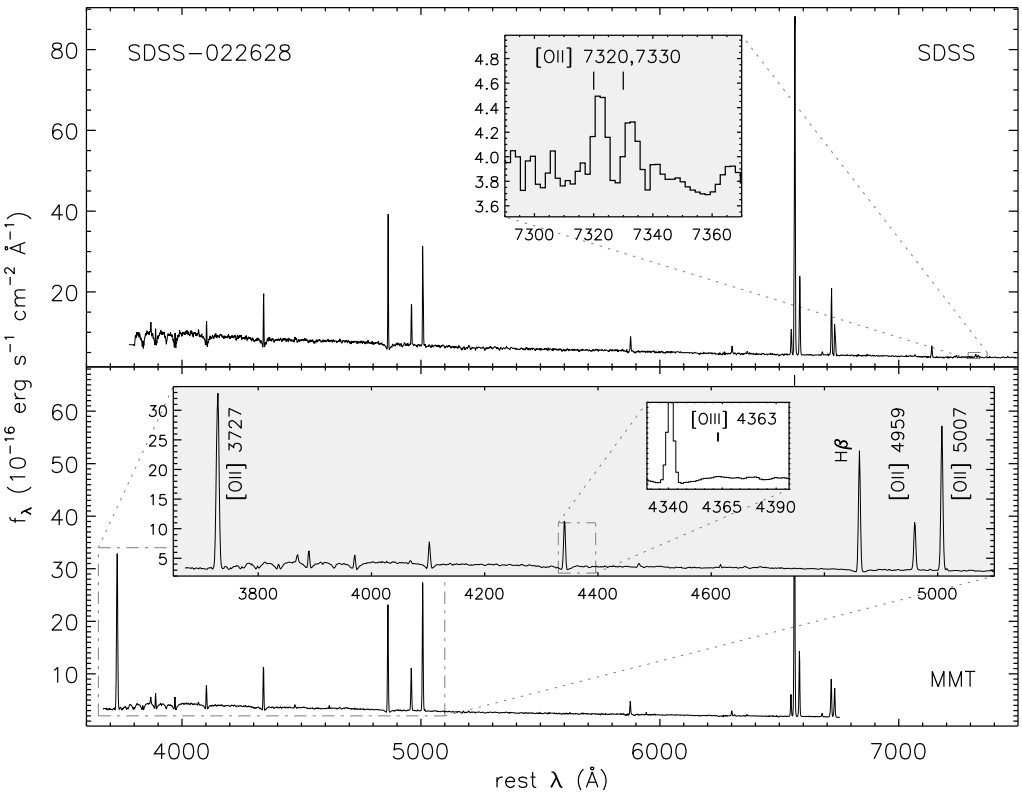

Figure 2.1.1

Data Reduction

Details of the data reduction techniques used in this thesis are described in Appendix A. Figures 2.1-2.4 show the resulting one-dimensional spectra (with median S/N values > 30) in comparison to the SDSS spectra. Inset windows with a narrower spectral range emphasize the blue emission lines and the dominance of [O II] over [O III] in all four galaxies.

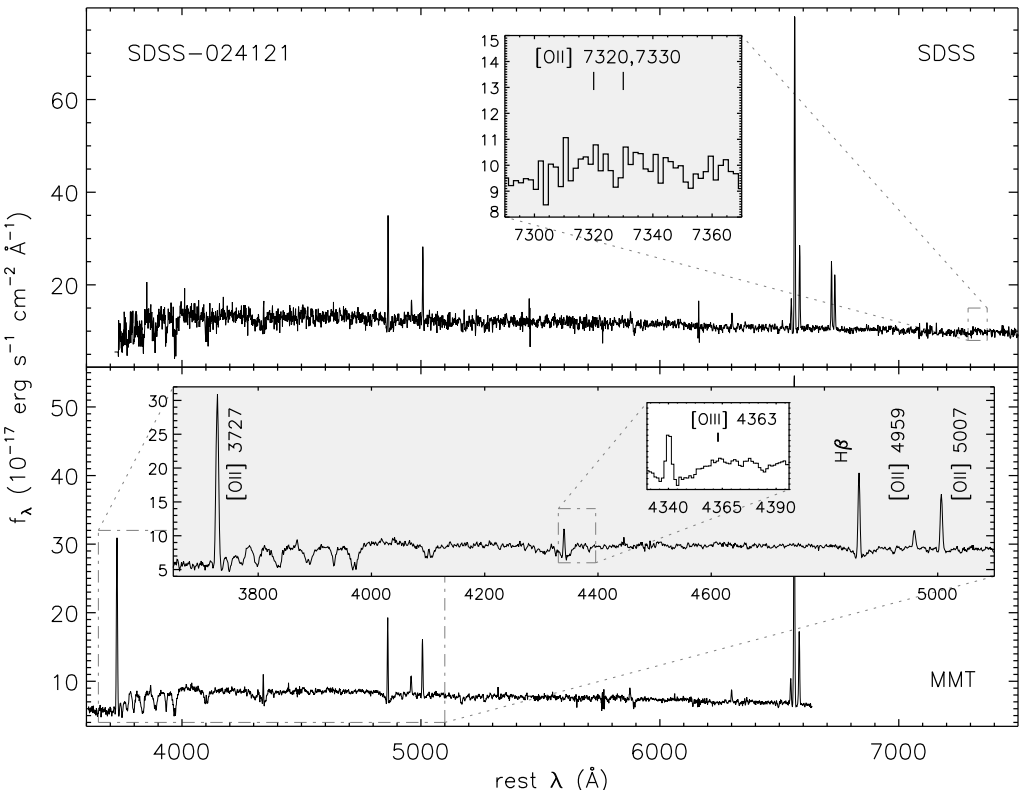
SDSS−024121
SDSS
MMT
[OII] 7320,7330
[OII] 3727
[OIII] 4363
Hβ
[OII] 4959
[OII] 5007
f_λ (10^−17 erg s^−1 cm^−2 Å^−1)
rest λ (Å)

Figure 2.1.2

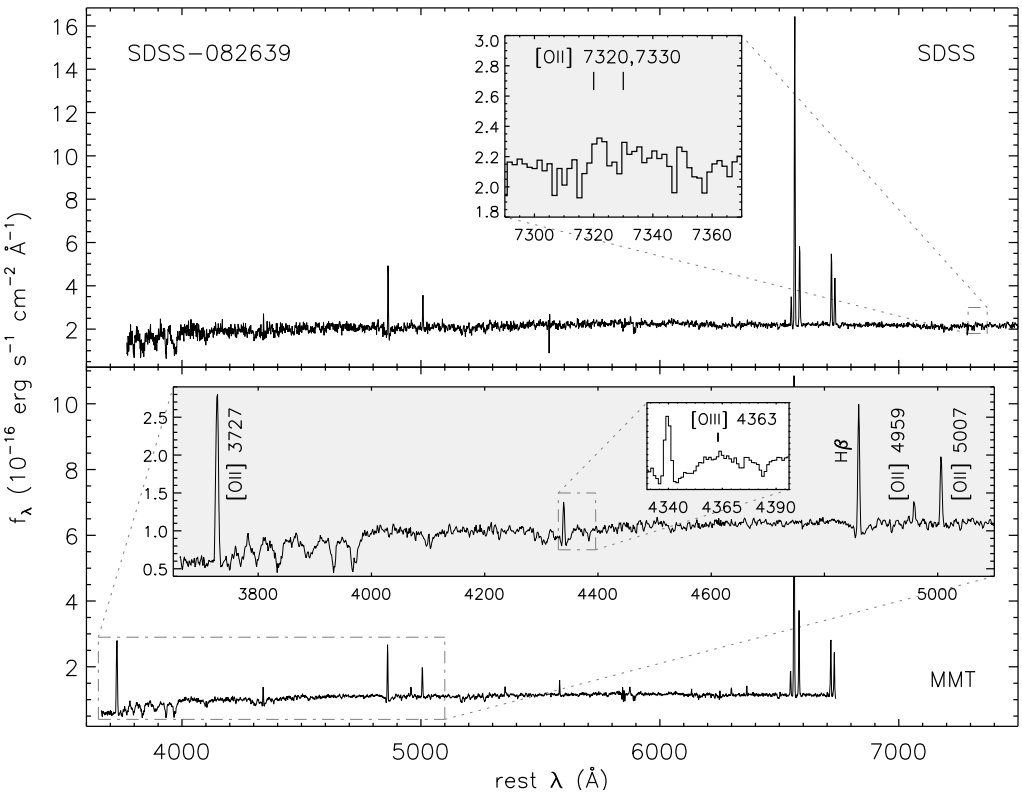
SDSS−082639
SDSS
MMT
[OII] 7320,7330
[OII] 3727
[OIII] 4363
Hβ
[OII] 4959
[OII] 5007
f_λ (10^{-16} erg s^{-1} cm^{-2} Å^{-1})
rest λ (Å)

Figure 2.1.3

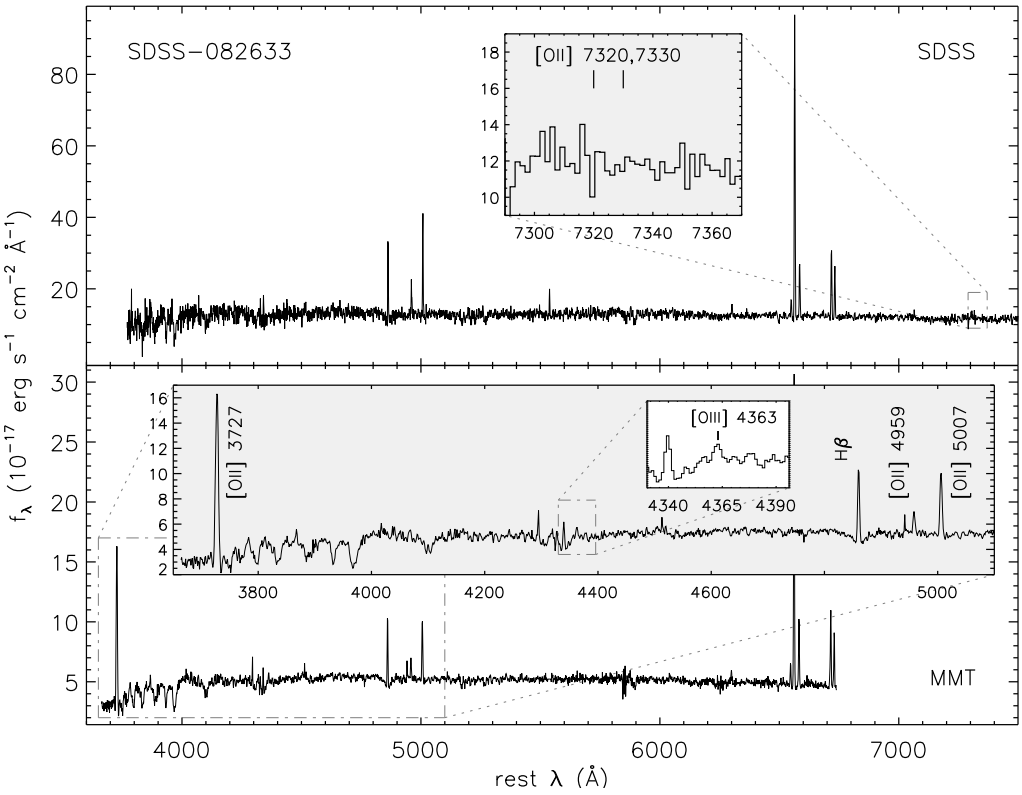

Figure 2.1.4

Figure 2.1: Spectra of targets. The two panels compare the optical H II region spectra from the SDSS and the MMT. Note that the SDSS spectral bandpass does not contain [OII] λ3727, but does encompass measurable [O II] $\lambda\lambda$7320,7330, as shown in the upper inset box. The bottom inset box is an enlarged view of the MMT spectrum to emphasize the dominance of [O II] over [O III]. This scale also reveals the significant [N II] $\lambda\lambda$6548,6584 strength and the lack of a [O III] λ4363 detection.

2.3 ANALYSIS

2.3.1 Emission Line Measurements

A discussion of the emission line measurements can be found in Appendix B. Specific to this work, special attention was paid to the Balmer lines, which are located in troughs of significant underlying stellar absorption. Although the equivalent widths of the Hα emission lines were large enough that the underlying absorption was not a concern, this was not the case for Hβ and the bluer Balmer lines. We experimented with several different methods to correct the measurement of the Hβ emission flux for the effects of underlying absorption. At one extreme, maximizing the Hβ line intensity (by overestimating the underlying absorption) leads to a minimum Hα/Hβ value and a minimum estimate of the reddening. Because the underlying absorption is much broader than the emission and these features are both well resolved and relatively high signal-to-noise, the subtraction of the underlying absorption represents only a small contribution to the uncertainty in the reddening corrections (see Table 2.2).

For our final analysis of the Balmer emission lines, we used the PAN[6] analysis package to simultaneously fit the continuum, the Gaussian emission peak, and a broad, negative Lorentzian absorption feature. PAN uses a least-squares fit to minimize χ^2 and estimates the uncertainty using a "bootstrap" Monte Carlo error analysis, providing a reliable measurement of the flux and associated uncertainty of the Balmer emission line. Figure 2.5 exhibits both the individual component and total fits determined by PAN, with minimal residuals validating the goodness of fit to our spectra. The emission line fluxes are reported relative to Hβ in Table 2.2, and represent the multiple component fits for the Hβ and Hγ emission lines and the single or deblended Gaussian profile fits from SPLOT for the rest of the emission lines.

As we were not able to detect [O III] λ4363 and He II λ4686 at the level of more than 3σin any of the spectra, a flux upper limit was estimated using Equation B.2. We calculated upper limits on the electron temperatures based on these λ4363 fluxes, but none provided significant constraints for abundance calculations. In some cases,

[6] PAN was written by Rob Dimeo as a part of the Data Analysis and Visualization Environment, which is a software package developed at the NIST Center for Neutron Research for the reduction, visualization, and analysis of inelastic neutron scattering data, and was funded by the National Science Foundation.

the Hα/Hβ ratios for the SDSS and MMT spectra are significantly different. Using the MMT data for our reference ratio, the average percentage difference between the SDSS and MMT Hα/Hβ ratio is 15%, whereas the average [O III] λ5007/Hβ percentage difference is 16%. Since the [O III]/Hβ ratio is less sensitive to flux calibrations, these differences between the two data sets are likely due to using long-slit (MMT spectra) versus circular fiber apertures (SDSS spectra).

2.3.2 Reddening Corrections

The detailed steps used for reddening corrections are listed in Appendix B. Assuming standard H II region characteristics ($T_e = 1.25 \times 10^4$ K and $n_e = 10^2$ cm^{-3}), both the MMT and SDSS spectra were de-reddened using a Balmer decrement of 2.82 (Hummer & Storey, 1987) and the Cardelli et al. (1989) reddening law (with $A_V = 3.1\ E(B-V)$). Original and de-reddened flux values for both the MMT and SDSS data are given in Table 2.2, where errors were propagated from those associated with the individual line measurements. All of the Hα/Hβ ratios are larger than 2.82, indicative of significant extinction and reddening due to dust. Since the Galactic latitudes for the four galaxies are all large (ranging from 31° to 54°), little foreground extinction from Galactic dust is expected, and, indeed, the calculated values of $E(B-V)$ (see Table 2.2) are substantially greater than the foreground extinction determined by Schlegel et al. (1998). Our reddening corrections can be checked by comparing the corrected Hγ/Hβ ratios with their theoretical values. As seen in Table 2.2, this ratio is consistent with the theoretical case B recombination ratio of 0.47 (Hummer & Storey, 1987) in all four cases. This result implies accurate reddening corrections were made, which strengthens the argument for significant intrinsic extinction.

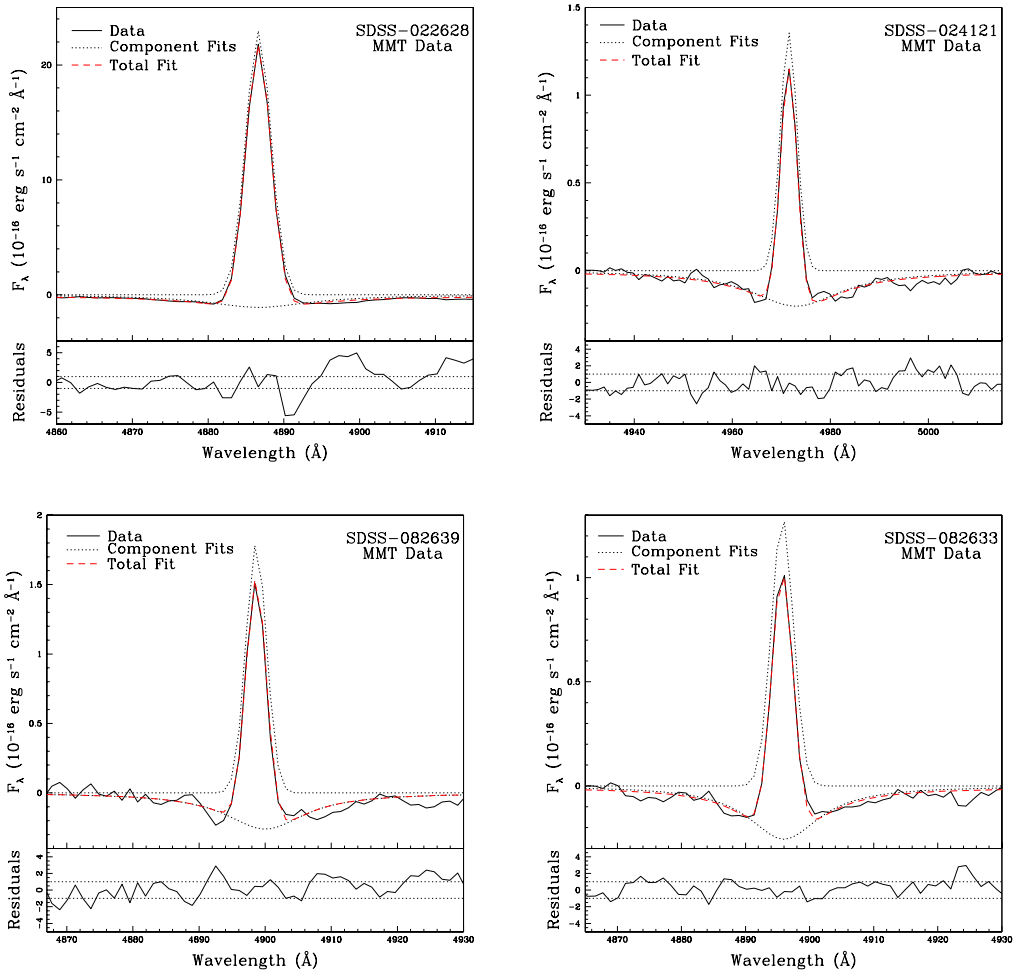

Figure 2.5: Hβ region of the MMT spectra, as measured in PAN. The dotted gray lines correspond to the Lorentzian absorption and Gaussian emission component fits. The red dashed line displays the best overall fit to the original data (solid black line). The residual difference between the fit and data is shown in the bottom panel, with very little divergence near the emission peak, confirming a successful fit. The ensuing Hβ emission flux, accounting for Balmer absorption, can be found in Table 2.2.

Table 2.2. Emission Line Intensity Ratios for the Observed Sample

	SDSS-022628		SDSS-024121		SDSS-082639		SDSS-082633	
MMT Data	F(λ)/F(Hβ)	I(λ)/I(Hβ)	F(λ)/F(Hβ)	I(λ)/I(Hβ)	F(λ)/F(Hβ)	I(λ)/I(Hβ)	F(λ)/F(Hβ)	I(λ)/I(Hβ)
[O II] λ3727	2.12±0.06	2.47±0.09	2.62±0.13	4.13±0.22	1.89±0.12	3.67±0.25	3.50±0.17	3.90±0.22
Hγ λ4340	0.40±0.01	0.43±0.01	0.33±0.04	0.41±0.05	0.37±0.06	0.49±0.08	0.34±0.05	0.38±0.05
[O III] λ4363	< 0.02 (3σ)	< 0.02 (3σ)	< 0.12 (3σ)	< 0.14 (3σ)	< 0.15 (3σ)	< 0.19 (3σ)	< 0.16 (3σ)	< 0.17 (3σ)
He II λ4686	< 0.01 (3σ)	< 0.01 (3σ)	< 0.10 (3σ)	< 0.10 (3σ)	< 0.15 (3σ)	< 0.16 (3σ)	< 0.10 (3σ)	< 0.10 (3σ)
Hβ λ4861	1.00±0.03	1.00±0.03	1.00±0.04	1.00±0.04	1.00±0.03	1.00±0.03	1.00±0.06	1.00±0.06
[O III] λ4959	0.39±0.01	0.39±0.01	0.28±0.04	0.27±0.03	0.18±0.05	0.17±0.05	0.32±0.08	0.31±0.08
[O III] λ5007	1.18±0.03	1.16±0.03	0.70±0.04	0.67±0.04	0.54±0.05	0.50±0.05	0.95±0.09	0.93±0.09
He I λ5876	0.12±0.02	0.11±0.02	0.15±0.02	0.11±0.02	0.23±0.04	0.15±0.03	0.13±0.02	0.13±0.02
[N II] λ6548	0.20±0.01	0.17±0.01	0.35±0.04	0.23±0.02	0.42±0.05	0.23±0.03	0.19±0.05	0.15±0.04
Hα λ6563	3.24±0.10	2.79±0.08	4.30±0.15	2.79±0.10	5.19±0.15	2.79±0.10	3.50±0.16	2.79±0.13
[N II] λ6584	0.63±0.02	0.55±0.02	1.02±0.05	0.67±0.03	1.38±0.06	0.74±0.04	0.71±0.06	0.57±0.04
Hβ Flux[1]	956±19		57.7±1.7		70.3±1.4		55.4±2.3	
Hβ EW[2]	-23.6±0.7		-6.1±0.8		-4.9±0.9		-5.1±0.9	
Hβ Abs EW	5.7±0.2		8.1±0.5		6.9±0.3		7.0±0.4	
Hα EW	-87.2±1.8		-34.5±2.5		-25.7±1.4		-24.9±1.8	
E(B-V)	0.14±0.01		0.42±0.02		0.62±0.03		0.22±0.01	
C(Hβ)	0.20±0.01		0.61±0.02		0.88±0.03		0.31±0.01	

2.4 Comparison of Sample Galaxies to the SDSS

Our new observations allow us to examine these Peeples et al. (2008) galaxies against larger samples drawn from the MPA-JHU SDSS database. Since the "very low mass" sample lacked [O II] measurements, we are particularly interested in how the strengths of these emission lines compare. Figure 2.6 illustrates properties of the four observed galaxies with respect to star-forming galaxies in the SDSS that fall in the "very low mass" sample range of $7 \leq \log(M_\star/M_\odot) \leq 9$. We have further restricted the SDSS comparison sample to those objects with s/n ≥ 5 in the relevant lines.

The top panel in Figure 2.6 shows a comparison of the excitation, measured by the [O II]/[O III] ratio. The two more massive galaxies are clearly discrepantly strong in [O II] emission; these are very low excitation galaxies. With decreasing mass, the SDSS comparison sample becomes relatively sparse, but the two lower mass galaxies have comparatively low excitation.

The second panel shows a comparison of the [N II]/[O II] ratio, primarily a function of the N/O abundance. Again, for the two more massive galaxies, there is a clear offset from the locus defined by the SDSS galaxies. While the [N II]/[O II] ratios are of comparable strength in the two lower mass galaxies, the trend in the SDSS sample is less clear. Extrapolating from the higher mass galaxies, the lower mass galaxies would be clearly discrepant, but they lie in the middle of a very sparse scatter in the diagram. Quantitatively, in a comparison with a least-squares fit to the SDSS compilation, the values of log(N/O) for our four observed galaxies are $0.2 - 0.4$ dex higher than is typical for objects in the same stellar mass range.

The lower two panels compare the equivalent widths of the underlying stellar absorption and the star formation rates derived from Hα. The four objects presented in this paper have Hβ absorption equivalent widths on the high end of the SDSS distribution and star formation rates on the low side of the distribution.

In sum, the four galaxies which we have observed are outliers in a number of properties. Given that oxygen abundances derived from strong emission lines are subject to a number of systematic uncertainties, it is clearly warranted to revisit their status as oxygen abundance outliers.

Table 2.2 (cont'd)

MMT Data	SDSS-022628 F(λ)/F(Hβ)	SDSS-022628 I(λ)/I(Hβ)	SDSS-024121 F(λ)/F(Hβ)	SDSS-024121 I(λ)/I(Hβ)	SDSS-082639 F(λ)/F(Hβ)	SDSS-082639 I(λ)/I(Hβ)	SDSS-082633 F(λ)/F(Hβ)	SDSS-082633 I(λ)/I(Hβ)
	SDSS-022628		SDSS-024121		SDSS-082639		SDSS-082633	
SDSS Data	F(λ)/F(Hβ)	I(λ)/I(Hβ)	F(λ)/F(Hβ)	I(λ)/I(Hβ)	F(λ)/F(Hβ)	I(λ)/I(Hβ)	F(λ)/F(Hβ)	I(λ)/I(Hβ)
Hβ λ4861	1.00±0.03	1.00±0.03	1.00±0.11	1.00±0.11	1.00±0.09	1.00±0.09	1.00±0.09	1.00±0.09
[O III] λ4959	0.39±0.02	0.38±0.02	0.18±0.07	0.17±0.07	···	···	0.37±0.07	0.36±0.07
[O III] λ5007	0.92±0.03	0.88±0.03	0.61±0.09	0.59±0.08	0.42±0.08	0.39±0.07	1.00±0.09	0.96±0.09
[N II] λ6548	0.28±0.01	0.19±0.01	0.30±0.04	0.23±0.03	0.42±0.05	0.22±0.02	0.22±0.05	0.15±0.03
Hα λ6563	4.09±0.13	2.79±0.09	3.71±0.29	2.79±0.22	5.34±0.34	2.79±0.18	4.02±0.28	2.79±0.19
[N II] λ6584	0.87±0.03	0.60±0.02	0.95±0.08	0.72±0.06	1.46±0.10	0.77±0.05	0.74±0.07	0.52±0.05
[O II] λ7320	0.03±0.01	0.02±0.01	···	···	···	···	···	···
[O II] λ7330	0.02±0.01	0.01±0.01	···	···	···	···	···	···
Hβ Flux	979±24		87.2±6.6		114.7±7.2		88.0±5.8	
Hβ EW	-23.5±1.2		-5.4±2.1		-5.5±1.2		-5.9±1.8	
Hβ Abs EW	9.8±0.4		7.5±0.6		9.5±0.4		7.2±0.6	
Hα EW	-89.5±2.9		-30.7±2.3		-27.9±0.9		-28.8±2.1	
E(B-V)	0.37±0.02		0.28±0.01		0.64±0.03		0.36±0.02	
Galactic Lat.	-53.626		-52.102		31.400		31.351	
Galactic E(B-V)	0.031		0.029		0.080		0.070	

Note. — The spectra were de-reddened assuming Hummer & Storey (1987) case B for $T_e = 1.25 \times 10^4$ K and $n_e = 100$ cm^{-3} and the Cardelli et al. (1989) reddening law with $R_V = 3.1$. For each galaxy, the measured flux ratio is given by F(λ)/F(Hβ), and the dereddened flux ratio by I(λ)/I(Hβ). The Galactic $E(B-V)$ is taken from Schlegel et al. (1998). The equivalent widths measure the Hβ and Hα Balmer emission lines using SPLOT, and the broad Hβ absorption features using PAN. EWs are given in units of Å.

[1]The Hβ flux is given for reference, with units of 10^{-17} erg s^{-1} cm^{-2}.

[2]Equivalent width errors calculated from Vollmann & Eversberg (2006).

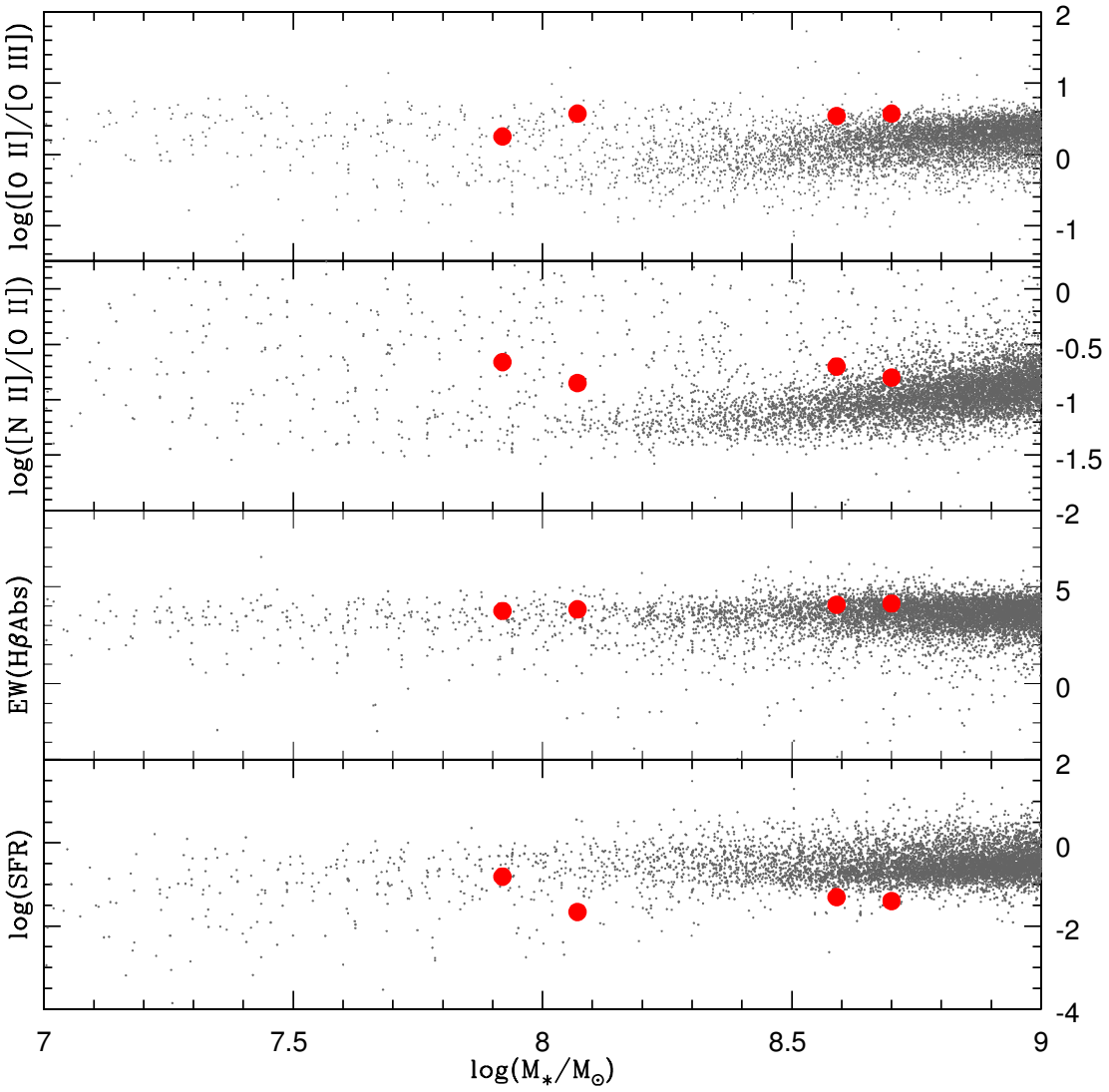

Figure 2.6: Properties of low-mass star-forming galaxies in the SDSS (gray dots) plotted against stellar mass. The four objects presented in this chapter are shown as red dots in comparison. Interestingly, the [N II]/[O II] ratios are well above average for the mass range, and the [O II]/[O III] ratios show that these objects have significantly lower excitation than is typical. Additionally, their SFRs are relatively low and their Hβ absorption EWs are on the high end of the SDSS range.

2.5 Oxygen Abundance Determinations

Relative to the SDSS spectra, our MMT spectra have the advantages of higher signal to noise and the inclusion of the blue [O II] λ3727 line. Kniazev et al. (2003) showed from SDSS spectra that O^+/H^+ ionic abundances can be determined reasonably well by observing the red [O II] $\lambda\lambda$7320,7330 lines (as a substitute for [O II] λ3727); however, because they are auroral lines, their strong sensitivity to temperature can result in relatively high abundance uncertainties. In all four MMT spectra (Figures 2.1-2.4) the preferred [O II] λ3727 emission line strengths are noticeably stronger than the [O III] λ5007 lines, underscoring the importance of accurately accounting for the contribution from the lower ionization state in determining oxygen abundances.

Accurate direct oxygen abundance determinations from H II regions require a measurement of the electron temperature (typically via observation of the temperature sensitive [O III] λ4363 auroral line). However, as metallicity increases, cooling via metal lines becomes more efficient and the electron temperature decreases, making these intrinsically faint lines even more difficult to detect. Since we did not reliably detect [O III] λ4363 in any of our targets, abundances must be estimated empirically or theoretically using relationships dependent upon relative strong-line flux ratios.

Alloin et al. (1979) and Pagel et al. (1979) were the first to provide strong-line calibrations, where oxygen abundance is related to one or more ratios of recombination and collisionally excited lines. Several other methods have since been developed and categorized as semi-empirical, empirical, or theoretical. Semi-empirical calibrations were determined using a combination of electron temperature measurements at low metallicity and photoionization models at high metallicity in correspondence with observational limitations. Empirical calibrations result from observations of H II regions with electron temperature measurements. However, the relatively small number of direct oxygen abundance determinations available are typically biased in the sense that they are based upon high-excitation H II regions only. In contrast, theoretical strong-line calibrations use *ab initio* photoionization models. One advantage to theoretical models is that they allow a wide range in ionization parameter in addition to input metallicity. However, these models rely on simplified assumptions of nebular properties and so do not yet

provide entirely realistic representations of H II regions. Most troubling is that all theoretical strong-line abundance determination methods over-predict abundances in the metal-rich (roughly solar metallicity and above) regime when compared to abundances determined from direct temperature measurements.

Here we review the original oxygen abundances as determined by T04 using Bayesian models, the revised strong-line oxygen abundances calculated by P08, strong-line oxygen abundances from our new MMT spectra (with and without the addition of the blue [O II] emission), and the N/O relative abundance ratios. T04 found this type of comparison is valid for SDSS data by showing that analytic R23-metallicity relations roughly bracket the range of metallicities that they derive, concluding that their M-Z relationship is in line with previous strong-line calibrations. The culmination of these efforts is presented in Figure 2.8, which allows us to compare all of the oxygen abundance estimates with those expected from the M-Z relationship. Note that Figures 2.7 and 2.8 is shown for illustrative purposes only, and not to suggest which calibrator is more fundamentally correct.

2.5.1 The T04 Oxygen Abundances

P08 initially identified outliers from luminosities, gas-phase oxygen abundances, and stellar masses provided by T04. The T04 abundance calculations are based on a Bayesian statistical analysis of the strongest six emission lines using stellar population synthesis models from Bruzual & Charlot (2003) and photoionization models from CLOUDY (Ferland et al., 1998). Note that while the T04 abundances were used to identify the outliers (in a self-consistent manner), P08 derived their own abundances, which are systematically lower than the T04 abundances. Yin et al. (2007, hereafter Y07) compared the oxygen abundances from T04 with oxygen abundances derived from direct temperature measurements (using auroral lines) and found the T04 oxygen abundances to be systematically higher on average. Y07 further showed that the magnitude of this offset correlates well with the N/O abundance ratio, and concluded that the offset is due to the assumption of a single N enrichment trend in the underlying Charlot & Longhetti (2001) modeling.

Kewley & Ellison (2008, hereafter KE08) compared the M-Z relationships derived from ten different strong-line methods and found large systematic discrepancies between

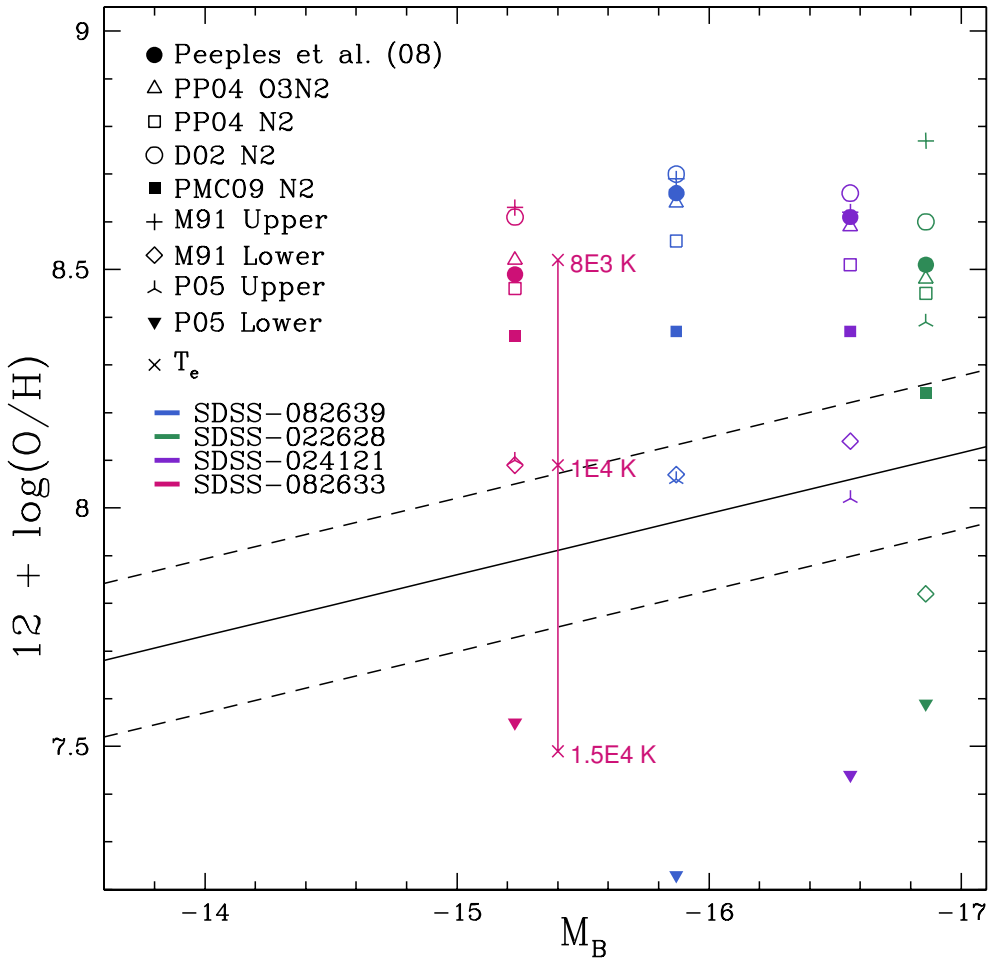

Figure 2.7: $12 + \log(\mathrm{O/H})$ vs. M_B is plotted for our sample. The solid line is the linear fit to dwarf galaxies found by Lee et al. (2006b) for comparison, with the dashed lines representing the 1σuncertainty. This relationship is similar to that of van Zee et al. (2006), but provides an average dispersion for both the L-Z and M-Z relationships. The points plotted display calculated oxygen abundances for our sample. Each method is denoted with a different symbol, where objects are differentiated by color: green for SDSS-022628, purple for SDSS-024121, blue for SDSS-082639, and pink for SDSS-082633. The 'x' symbols denote the oxygen abundances calculated from emissivities assuming various electron temperatures for SDSS-082633.

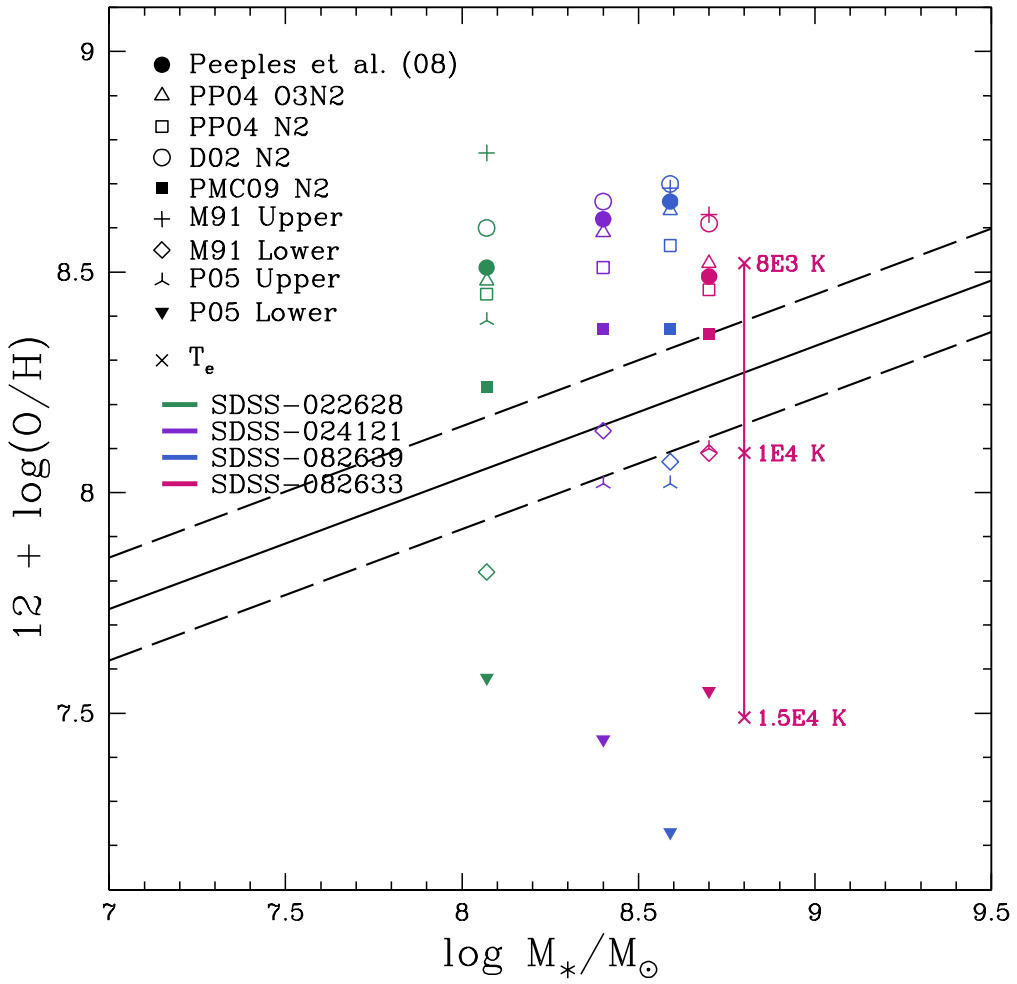

Figure 2.8: $12 + \log(O/H)$ vs. $\log(M_\star/M_\odot)$ is plotted for our sample. Similar to Figure 2.7, the solid line depicts the linear relationship and 1σuncertainty of Lee et al. (2006b) for mass. The points plotted display calculated oxygen abundances for our sample. Each method is denoted with a different symbol, where objects are differentiated by color: green for SDSS-022628, purple for SDSS-024121, blue for SDSS-082639, and pink for SDSS-082633. The 'x' symbols denote the oxygen abundances calculated from emissivities assuming various electron temperatures for SDSS-082633.

empirical and theoretical calibrations. In the KE08 study, T04 metallicities tend to be in the middle of the range when low metallicities are considered (12 + log(O/H) $\approx$ 8.5) and at the high end of the range when the high metallicities are considered (12 + log(O/H) $\approx$ 9.0). KE08 provide relations for converting one metallicity scale to another, but the results of the Y07 analysis imply that a simple conversion is not always sufficient. That is, not only can the absolute abundances provided by the strong-line methods be systematically offset from the true nebular abundances, but, in some cases, the strong-line methods do not even accurately rank the abundances (see Table 2.3 and Figures 2.7 and 2.8 for different rankings among the 4 objects presented here).

2.5.2 The P08 Oxygen Abundances

P08 derived their own oxygen abundances for the outliers identified from the T04 sample. Since there was insufficient information to reproduce the results of the Bayesian statistical analysis of T04, P08 used two of the methods investigated by KE08. They used the [N II]/[O II] ratio as calibrated by KE08 for the "main" sample (where [O II] λ3727 was observed), and the [O III]/[N II] ratio (the "O3N2" method) as calibrated by Pettini & Pagel (2004) for the remaining galaxies in the "very low mass" sample. P08 did not use the R_{23} diagnostic for their "main" sample because of concerns regarding its calibration at high metallicities (the presumed regime for their samples). P08 found that their oxygen abundances derived from the [N II]/[O II] ratio for the "main" sample agreed well with the T04 oxygen abundances. However, the O3N2 abundances were consistently lower than the T04 abundances by roughly 0.3 dex (in concordance with the offsets determined by KE08). The net effect is that the abundances derived by P08 are lower than those derived by T04. P08 concluded that, regardless of the metallicity calibration used, their sample of 41 galaxies are true high-metallicity, low mass outliers from the mass-metallicity relation. Despite any offsets between the T04 and P08 data sets, both use a strong-line calibration based partially on [N II] strength, which make abundance estimates liable to overestimates if the galaxies are nitrogen-enhanced (see § 2.5.3 and § 3.6).

2.5.3 Strong Line Methods Revisited

We have chosen to re-compute the oxygen abundances for this sample using the MMT spectra with several strong-line calibrations: the O3N2 method, the N2 method, the R_{23} index, and determinations using assumed temperatures. This serves to highlight differences amongst methods, outline the resulting range of possible abundances, and demonstrate that strong-line calibrations are not appropriate for the present sample. These measurements are discussed below and compared in Figures 2.7 and 2.8.

"O3N2" Method

The O3N2 method is one of two empirical calibrations used by P08 for the "main" sample, and the only calibration used for the "very low mass" sample since these objects lacked the necessary [O II] measurements. It was introduced by Pettini & Pagel (2004, hereafter PP04) using empirical fits to strong-line ratios from H II regions with direct oxygen abundances. Derived for the purpose of measuring metallicities in galaxies at high redshift, lines close in wavelength are used to mitigate the need for flux calibrations and reddening corrections. Direct metallicities were compared to the ratio of ([O III] λ5007/Hβ)/([N II] λ6584/Hα) for a sample of 137 H II regions. See the resulting O3N2 relationship of Equation 3 in PP04, where O3N2 = log(([O III] λ5007/Hβ)/([N II] λ6584/Hα)).

P08 favored the O3N2 method with its high sensitivity to oxygen abundance. Indeed, O3N2 is a good calibration in the high-metallicity regime, where [N II] tends to saturate, but the strength of [O III] continues to decrease with increasing metallicity. Note that the choice by PP04 to use only objects with direct metallicities, in an effort to provide a more secure calibration, introduces a bias because low excitation spectra (i.e., relatively low values of λ5007/λ3727) are excluded from the calibration. Thus, the unintended consequence of the choice to limit the sample to objects which were perceived to have more accurate abundances has resulted in a biased sample. This biased sample gives the impression of a smaller scatter in the relationship than occurs in nature (cf., Yin et al., 2007).

To confirm consistency with P08, we duplicated the O3N2 measurements for the SDSS spectra and calculated O3N2 from our MMT spectra. The results are listed in

Table 2.3 and closely match the measurements by P08 using the same O3N2 methodology; they are lower than the values found by T04 by 0.2 - 0.3 dex.

Y07 showed a large scatter in the comparison of abundances derived from the O3N2 calibration with oxygen abundances derived from the direct method. They suggest that the scatter could be due to excluding the ionization parameter in the O3N2 calibration. The importance of the ionization parameter strengthens in the low-metallicity regime where O3N2 is much less dependent on metallicity. Additionally, at low Z, N is thought to be a primary element, implying that the N/O ratio is independent of O/H.

Since the calibration of the O3N2 method does not account for possible variations in N/O for a given O/H, inherent biases are possible. Pérez-Montero & Contini (2009, hereafter PMC09) found that a strong correlation exists between metallicity derived from the O3N2 parameter and the N/O ratio, such that when the N/O is enhanced, the O3N2 strong-line calibration tends to overestimate the O/H abundances. PMC09 corrected for this dependence by using 12 + log(O/H) versus O3N2 residuals to modify the O3N2 calibration (see Equation 8 in PMC09). Using the N/O calculations from § 3.6 and given in Table 2.4, we calculated the revised O3N2 abundances and list them in Table 2.3. This calibration lowers the O3N2 abundances only slightly (by an average of ~ 0.1 dex) relative to PP04 O3N2 estimates. In § 2.5.5 we look at the higher abundances from the O3N2 method relative to relationships predicted by direct and photoionization model abundances.

"N2" Indicator

Denicoló et al. (2002, hereafter D02) proposed the use of the [N II] λ6584/Hα ratio as a sensitive metallicity indicator. This is a promising estimator: like O3N2 it eliminates uncertainties due to reddening and flux calibrations, and functions well for metallicity values below the [N II] saturation level. The original N2 calibration developed by D02 (see Equation 2 in D02), where N2 = log([N II] λ6584/Hα), was based on $\sim$155 H II regions and used a least squares fit with an estimated uncertainty of $\sim$0.2 dex. For our objects, this method produces oxygen abundances ($8.61 \leq 12 + \log(\mathrm{O/H}) \leq 8.70$) in agreement with the P08 values.

PP04 re-calibrated this parameter, primarily with electron temperature-based metallicities, characterizing the fit both linearly and with a third-order polynomial. The

polynomial fit is given in Equation 2 of PP04, yielding oxygen abundances of $8.45 \leq 12 + \log(\mathrm{O/H}) \leq 8.56$. The results for both calibrations are listed in Table 2.3.

Note, again, as with the PP04 calibration of the O3N2 method, the exclusive use of calibrators determined with measured electron temperatures underestimates the scatter in the relationship, and biases against low-ionization H II regions. Yin et al. (2007) found similar results in their analysis of the N2 method as found for the O3N2 method. The uncertain roles of the ionization parameter and the relationship between N/O and O/H as a function of metallicity result in appreciable uncertainty and scatter in the N2 method. Expanding on this idea, PMC09 found an expectedly strong dependence of metallicities predicted by N2 on the N/O ratio. PMC09 derived a calibration correcting for this effect (see their Equation 13). Using N/O ratios from § 3.6 and tabulated in Table 2.4, we present the results of this calibration in Table 2.3. This method predicts oxygen abundances which are $\sim$ 0.1 and $\sim$ 0.2 dex smaller on average than those predicted by the PP04 and D02 N2 methods respectively. Shifts to smaller oxygen abundances of this size can account for roughly half of the offset from the L-Z and M-Z relationships.

$\mathbf{R_{23}}$ Index

Pagel et al. (1979) promoted the use of the R_{23} index, $R_{23} = ([\mathrm{O\ II}]\ \lambda 3727 + [\mathrm{O\ III}]\ \lambda\lambda 4959, 5007)/(\mathrm{H}\beta)$, as a good estimate of oxygen abundance in the absence of an electron temperature measurement. Because the optical [O II] and [O III] emission lines decrease at both high abundances (due to an increasing role of fine structure line cooling) and low abundances (due to the decrease in the relative number of oxygen atoms), the relationship is bi-valued and, therefore, potentially ambiguous. The turn-around in the relationship occurs at oxygen abundances near $12 + \log(\mathrm{O/H}) \approx 8.4$ where R_{23} reaches a maximum of $\approx$10. However, the degeneracy between the two branches of solutions can, in most situations, be broken with an additional determinant. Also, since R_{23} is based on emission lines with significant separation in wavelength, accurate reddening corrections and uncertainties are important. Below, we discuss two R_{23} calibrations, one constructed from photoionization models, and another empirically based. Since P08 believed the sample to be high-metallicity, they did not consider the R_{23} diagnostic due to the potential of [O II] + [O III] to saturate and the lack of [O II] measurements

in their "very low mass" sample.

McGaugh (1991) created a calibration based on theoretical photoionization models using R_{23} and the additional O_{32} index: O_{32} = ([O III] $\lambda\lambda$4959,5007)/([O II] λ3727). McGaugh developed this model using the photoionization code CLOUDY (Ferland et al., 1998) and zero-age H II region models, accounting for photoionization parameter variations. To discriminate between the two branches, van Zee et al. (1998), followed by others, advised using the ratio of ([N II] λ6584)/([O II] λ3727). McGaugh (1994) suggested that [N II]/[O II] is approximately < 0.1 for low abundances and > 0.1 for high abundances, giving a rough distinction between lower and upper branches. Note, however, that McGaugh (1994) also points out (his Figure 3) that there is a dependence on the N/O ratio on the behavior of this discriminant. For the four galaxies in our sample, [N II]/[O II] ranges from 0.15 to 0.22 with an average uncertainty of $\sim$0.02, naively suggesting that they are upper branch objects near the turn-around region. We determined oxygen abundances using the analytic equations of the semi-empirical calibration from Kobulnicky et al. (1999), which have an estimated accuracy of $\sim$0.15 dex (Kobulnicky & Kewley, 2004). The results for both upper and lower branch calculations are listed in Table 2.3. The upper branch values define an upper limit to the metallicity estimates and are roughly equal to the P08 values, while the lower branch values are approximately 0.3 to 0.5 dex lower and would be consistent with the scatter in the luminosity-metallicity relation.

Pilyugin et al. (2001a) and Pilyugin et al. (2001b) empirically calibrated the R_{23} index with electron temperature based H II region oxygen abundances. This relation was later refined by Pilyugin & Thuan (2005, hereafter PT05), where the resulting fit incorporates the excitation parameter (which accounts for the effect of the ionization parameter) P = ([O III] $\lambda\lambda$4959,5007/Hβ)/R_{23}. The upper and lower branches correspond to electron temperature based metallicities with 12 + log(O/H) > 8.25 and 12+ log(O/H) < 8.0 respectively (see Equations 22 and 24 in PT05). The PT05 model upper and lower branch values, both of which are several tenths of dex below the P08 values and have an estimated accuracy of $\sim$0.1 dex, are given in Table 2.3. However, note that all four of our objects lie outside of the calibrated region for the PT05 method (see PT05, Figure 12).

The [O III]/[O II] ratio is sensitive to the ionization parameter, and important for

characterizing the physical conditions in the H II region. Since the age of an H II region is linked to the evolution of the ionization parameter and shape of the ionizing spectrum, photoionization models which assume a zero-age main sequence can lead to systematic errors. van Zee & Haynes (2006) and van Zee et al. (2006) discuss these effects and suggest they may be significant for H II regions with $\log(O_{32}) < -0.4$, such as for three of the four objects in our sample (see Table 2.3 and § 3.7). The small $\lambda5007/\lambda3727$ ratios in these spectra are indicative of a low ionization parameter, and correspond to very small P values (see Table 2.3) that are inconsistent with our high values of $\log(R_{23})$ for the PT05 upper branch calibration. Similarly, our low P values fall outside the range of calibration for their lower branch. If we naively extrapolate their calibrations, these objects fall close to or within the turn-around region which has an abundance range of $8.0 < 12 + \log(O/H) < 8.4$.

[N II]/Hα is often used as a second indicator of branch division. However, as it is less sensitive to metallicities and more responsive to ionization than [N II]/[O II], the division is less clearly defined. The latter ratio loses the ability to clearly break the degeneracy near the turn-around point of [N II]/[O II] ~ 0.1 (or $12 + \log(O/H) \sim 8.4$). With its dependence on both oxygen abundance and excitation, R_{23} seems like a superior metallicity indicator, but the ambiguity between branches requiring a secondary measurement like [N II]/Hα or [N II]/[O II] clearly render it less than ideal. The enhanced [N II]/[O II] values for the four objects investigated in this paper result in highly uncertain R_{23} metallicity estimates. Note, however, that the turn-around between the two branches happens at relatively low oxygen abundances, for all values of excitation, already indicating that the higher oxygen abundances reported by T04 and P08 are less likely.

Finally, we note the possible utility of the red [O II] emission lines in low redshift SDSS spectra. Kniazev et al. (2003) showed that SDSS abundances estimated using the red [O II] $\lambda\lambda$7320,7330 lines as a substitute for [O II] λ3727 yield comparable results for spectra with direct electron temperature measurements. Since the red [O II] emission lines were detected in the SDSS-022628 spectrum (Figure 2.1) we were able to derive alternative R_{23} abundance estimates for that galaxy. By using the relative emissivities to estimate the relative strengths of the blue [O II] emission lines from the red [O II]

emission lines, we found that the $\lambda5007/\lambda3727$ ratio is less than unity (suggesting relatively low ionization) over the range 1×10^4 K $\leq$ T$_e$ $\leq 1.25 \times 10^4$ K (for n$_e$ = 100 cm^{-3}). The corresponding R$_{23}$ calibrated O/H values are consistent with our MMT spectra findings, but, of course, the branch choice ambiguity remains.

2.5.4 N/O Relative Abundances

Since many of the methods of abundance determination discussed here rely on N abundance values either to calibrate O/H values or to discriminate between bi-valued solutions, a confident measurement of the N abundance is important. Due to the relative insensitivity of the derived N/O ratio to electron temperature, it is possible to get a reliable estimate of this ratio in the absence of an electron temperature determination. We calculated the N/O values for our four galaxies (see Table 2.4), assuming that N^+/O^+ is approximately equivalent to that of N/O (based on their similar ratio of ionization potentials, Vila-Costas & Edmunds, 1993) and an electron temperature of 12,500 $\pm$2,500 K.

The N/O versus O/H trend is well studied in galaxies of varying types. Vila-Costas & Edmunds (1993) presented a thorough overview of theoretical expectations and observations available at the time. A salient point is that N can be produced as both a primary and a secondary element and that the secondary component is expected to be delayed relative to oxygen and to dominate at high abundances. Garnett (1990) convincingly demonstrated that there can be significant scatter in N/O at a given O/H, and Izotov & Thuan (1999) confirmed that this scatter is significant for oxygen abundances above 12 + log(O/H) = 7.7. Garnett (1990) proposed that much of the scatter could be explained by the time delay between producing oxygen and secondary nitrogen. However, Henry et al. (2006) conclude that the scatter in N/O could be produced by a variety of causes.

As already indicated in § 2.4, the four objects in our sample have unusually high values of N/O. PMC09 and, later, Amorín et al. (2010) (in their study of the abundances of the "green pea" galaxies) present a modern view of N/O versus O/H assembled from a sample of 475 H II objects and the SDSS DR7 catalog of observations respectively. A clear trend is obvious, but with scatter in log(N/O) on the order of 0.5 dex or more for a given O/H. An inspection of Figure 2 from Amorín et al. (2010) shows

Table 2.3. Metallicity Estimates for H II Regions Using Empirical Methods

	MMT Data			
	SDSS-022628	SDSS-024121	SDSS-082639	SDSS-082633
O3N2	0.77±0.05	0.45±0.08	0.28±0.11	0.66±0.13
N2	-0.71±0.04	-0.63±0.06	-0.58±0.06	-0.69±0.09
log R_{23}	0.60±0.02	0.71±0.04	0.64±0.06	0.71±0.05
log O_{32}	-0.20±0.04	-0.64±0.08	-0.74±0.12	-0.50±0.11
[N II]/[O II]	0.22±0.01	0.16±0.01	0.20±0.02	0.15±0.01
[N II]/Hα	0.20±0.01	0.24±0.01	0.26±0.02	0.20±0.02
P	0.39±0.01	0.19±0.01	0.15±0.02	0.24±0.03
N/O	0.16±.01	0.12±0.01	0.15±0.02	0.11±0.01
Pettini and Pagel (O3N2)	8.48	8.59	8.64	8.52
Pérez-Montero and Contini (O3N2)	8.37	8.52	8.54	8.47
Pettini and Pagel (N2)	8.45	8.51	8.56	8.46
Denicolo (N2)	8.60	8.66	8.70	8.61
Pérez-Montero and Contini (N2)	8.30	8.44	8.42	8.41
Kewley and Dopita (N II/O II)	8.83	8.74	8.80	8.71
McGaugh Upper (R_{23})	8.77	8.63	8.70	8.64
McGaugh Lower (R_{23})	7.81	8.13	8.06	8.08
Pilyugin Upper	8.40	8.03	8.07	8.11
Pilyugin Low	7.58	7.43	7.22	7.55
van Zee expected from M_B1	8.22	8.17	8.07	7.97

	SDSS Data			
	SDSS-022628	SDSS-024121	SDSS-082639	SDSS-082633
Pettini and Pagel (O3N2)	8.53	8.61	8.68	8.50
Pettini and Pagel (N2)	8.48	8.54	8.59	8.43
Denicolo (N2)	8.63	8.69	8.73	8.58
Tremonti (T04)	8.82	8.90	8.86	8.69
Peeples 08	8.51	8.61	8.66	8.49

Note. — Values for various methods of determining metallicity estimates from the strong lines of the MMT spectra are listed, with the O3N2 and N2 estimates for the SDSS spectra given below for comparison. Interestingly, the N2 method produces similar values for all 4 galaxies, and the O3N2 method reproduces similar values to those found by P08.

[1]Metallicity estimates calculated using Equation 2.1 of this paper, as determined by van Zee et al. (2006).

Table 2.4. N/O Ratio Estimates for a Range in Temperature

Temperature	log(N/O) - MMT Data			
	SDSS-022628	SDSS-024121	SDSS-082639	SDSS-082633
1.00×10^4 K	-0.94	-1.08	-0.98	-1.12
1.25×10^4 K	-0.80	-0.94	-0.84	-0.98
1.50×10^4 K	-0.70	-0.84	-0.74	-0.88
Adopted	-0.80 ±0.12	-0.94 ±0.12	-0.84 ±0.12	-0.98 ±0.12

Note. — N/O values for our four galaxy sample, calculated for a range of reasonable electron temperatures (12,500 ±2,500 K).

that our four galaxies, which range between $-0.8 \leq \log(\mathrm{N/O}) \leq -1.0$, correspond to values of $12 + \log(\mathrm{O/H}) \approx 8.6$ (derived from following the ridgeline of the data). Thus, empirically calibrated strong-line methods, such as O3N2 and N2, would predict oxygen abundances close to this value. However, the galaxies in this range of log(N/O) also extend to abundances as low as $12 + \log(\mathrm{O/H}) \approx 7.9$. From a plot of log(N/O) versus stellar mass for the SDSS compilation given by Amorín et al. (2010) (their Figure 3), our values of log(N/O) are roughly 0.6 dex higher than is typical for objects in the same stellar mass range.

2.5.5 Expected Oxygen Abundances

All strong-line calibrations correspond to an assumed electron temperature, so it is informative to explore the affects of varying this parameter. Since our MMT spectra include emission lines from both O^+ and O^{++}, we can calculate an expected range in O/H values based on an assumed reasonable possible range in electron temperature. As an example, oxygen abundances were calculated for SDSS-082633 assuming electron temperatures of $T_e = 8 \times 10^3$ K, 1×10^4 K, and 1.5×10^4 K. The resulting values of oxygen abundance cover the range of $12 + \log(\mathrm{O/H}) = 7.5 - 9$, and are indicated by 'x' symbols in Figures 2.7 and 2.8; similar results are found for the other 3 galaxies. Thus, we cannot rule out any of the various strong-line calibration estimates based on this consideration.

Finally, we can estimate the expected oxygen abundances from the luminosity-metallicity relationship and compare these to the strong-line estimates in Figure 2.7. Each calibration is represented by a different symbol, and each of our four galaxies is designated with a different color. Using the M-Z relationship of van Zee et al. (2006),[7]

$$12 + \log(\mathrm{O/H}) = 5.67 - 0.151\ \mathrm{M}_B, \tag{2.1}$$

we calculate expected oxygen abundances of 8.22, 8.17, 8.07, and 7.97 for the four objects in our sample. The M-Z relationship found by Lee et al. (2006b), based on oxygen abundances obtained via the direct method and corroborated by Marble et al. (2010), covers the relevant range in luminosity for our sample and is plotted in Figure 2.8. (Note that the range of the T04 relation does not extend down to encompass our low-luminosity sample). For each galaxy, a large spread is seen amongst the various indicators, highlighting the large uncertainties inherent in metallicity determinations.

2.6 Discussion

2.6.1 Oxygen Abundances and Photoionization Models

The MMT spectra show that three of the objects observed have discrepantly low excitation (i.e., low $\lambda5007/\lambda3727$ ratio; $\log(\mathrm{O}_{32}) < -0.4$). This implies that the observed nebulae may have relatively low ionization parameters and/or be excited by an aging stellar population, which explains why we do not see other ions with high ionization potentials (such as He II $\lambda4686$) in our spectra. Since most strong-line methods are calibrated for zero-aged main sequence starbursts, and many do not incorporate the effects of excitation, one must exercise care in applying these methods to determine oxygen abundances (see discussion in van Zee et al., 2006). In general, the strong-line methods tend to over-estimate the oxygen abundance for low excitation nebulae, and this offset can be as severe as $\sim$0.6 dex (van Zee et al., 2006). Note that it may be possible to mitigate some error by combining empirical and theoretical determinations using an average as Moustakas et al. (2010) suggest.

[7] van Zee et al. (2006) used both direct and empirical oxygen abundances from the literature for 50 objects in determining their M-Z relationship.

Additionally, all four of the objects observed have relatively high values of N/O compared to systems of similar stellar mass. As discussed by Yin et al. (2007), PMC09, and Amorín et al. (2010), the assumption of a single relationship between N/O and O/H in photoionization model calibrations of the strong-line methods can lead to discrepant results when the N abundance does not fit this assumed trend. At higher than average values of N/O, the strong-line methods tend to over-estimate the oxygen abundance.

The combination of relatively low excitation and relatively high N/O values leads to a large bias in the results from the strong-line calibrations. In Figure 2.9 we have plotted a comparison of the [O II] and [O III] line strengths for our four objects to photoionization models from Stasińska & Leitherer (1996). Each set of different colored points represents the evolution of a starburst assuming a Salpeter initial mass function (M_{up} = 100 $M_{\odot}$), a stellar mass between 10^6–10^9 $M_{\odot}$, and a metallicity between 12 + log(O/H) = 7.33 and 8.93. Increasing symbol size denotes a progression from 1–10 Myr. These models are particularly valuable because they demonstrate the additional scatter that can be introduced as the exciting stars of an H II region age, and both the ionization parameter and shape of the ionizing spectrum evolve. Figure 2.9 shows that H II region models with oxygen abundances in the range of $7.9 \leq 12 + \log(O/H) \leq 8.3$ tend to have maximum values of R_{23} (thus defining the turn-around regime in R_{23}; recall $\log(R_{23})$ has an upper limit near 1.0). Our four spectra fall among the points for maximum R_{23} at lower excitation. Figure 2.9 demonstrates that the four objects are inconsistent with relatively high (or relatively low) values of O/H, and, actually, are consistent with the values of O/H predicted from either the luminosity-metallicity relationship or the M-Z relationship.

Note that in constructing Figure 2.9, some of the Stasińska & Leitherer (1996) high-metallicity models showed more scatter in this diagram. These models included contributions by Wolf-Rayet (W-R) stars to the ionizing spectra, resulting in very hard radiation fields. We have not plotted these model points in Figure 2.9 because our non-detections of He II λ4686 indicate very little contribution from W-R stars at present.

MPA-JHU data for SDSS galaxies in the mass range of $7 \leq \log(M_{\star}/M_{\odot}) \leq 9$ are plotted in Figure 2.10 (gray points). Three of the four objects in the present sample, SDSS-024121, SDSS-082639, and SDSS-082633, are discrepantly low excitation nebulae relative to the SDSS sample, which tend to have higher excitation. However, most of

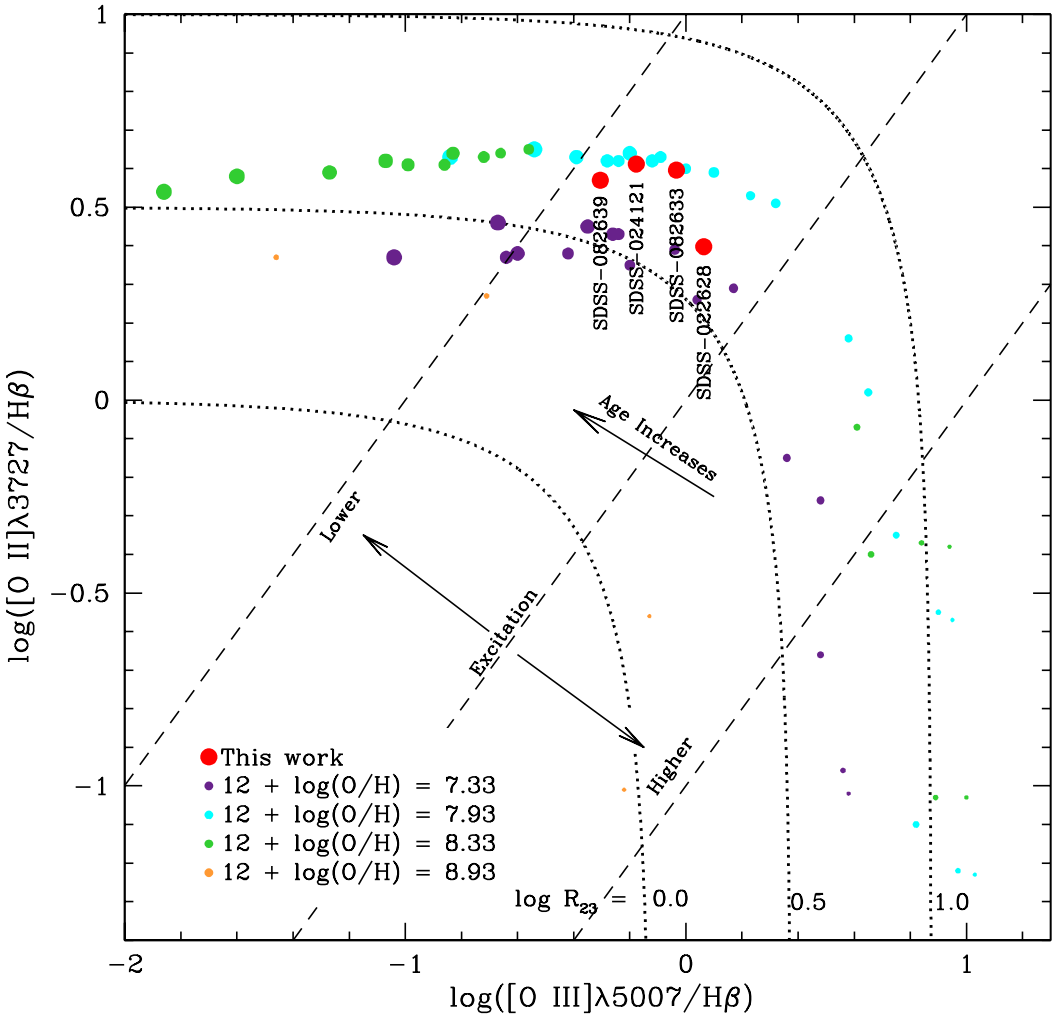

Figure 2.9: A comparison of the results from our MMT spectra with results from a large range of photoionization models evolved over 10 Myr as determined by Stasińska & Leitherer (1996) (symbol size corresponds to aging sequence). The overlaid dotted contours represent lines of constant R_{23}; from left to right $\log(R_{23}) = 0.0$, 0.5, and 1.0. The turn-around region encompasses $\log(R_{23})$ values of approximately 0.5 to 1.0. Dashed lines display excitation, where constant excitation of [O III]/[O II]= 1 coincides with the central line, [O III]/[O II]=0.1 is the low excitation line, and [O III]/[O II]=10 is the high excitation line. Our four spectra are all found near the maximum values of R_{23} for relatively low excitation nebulae, indicating probable 12 + log(O/H) values in the range of 7.9 to 8.3.

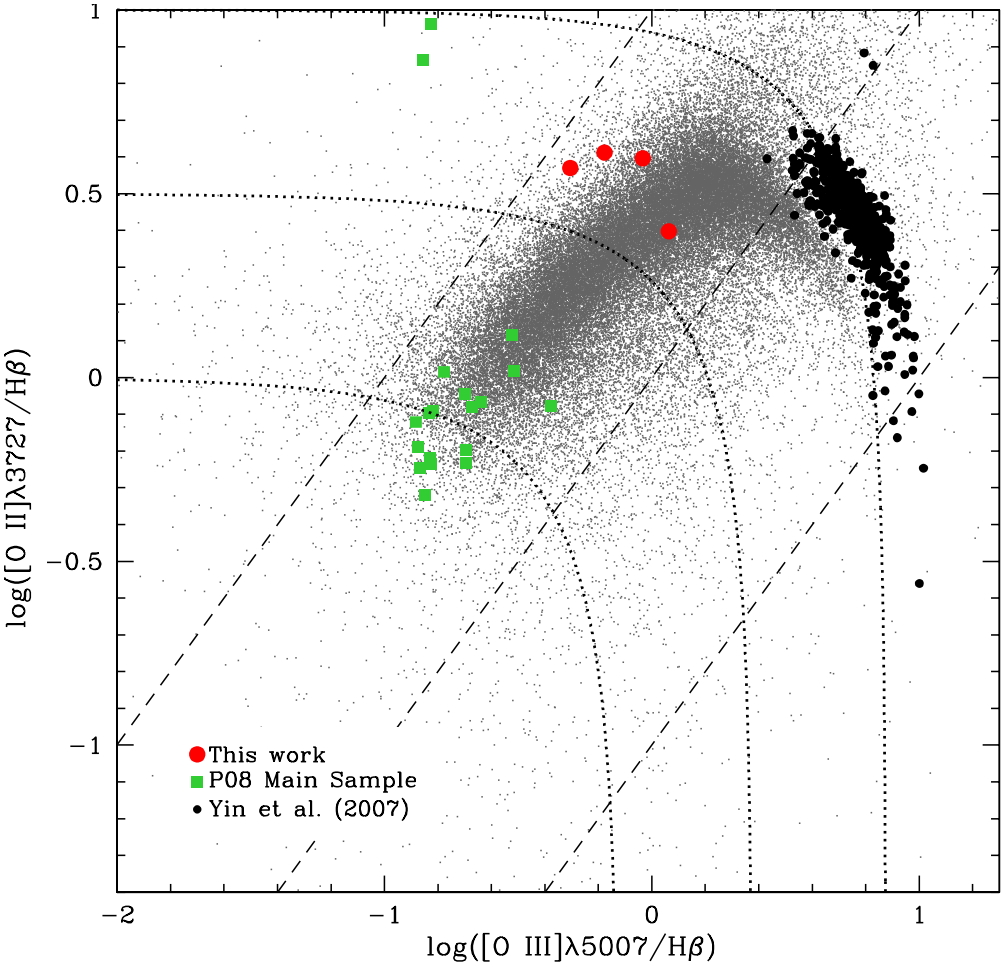

Figure 2.10: The excitation is plotted in terms of [O III] versus [O II], which is another form of looking at the information given in Figure 2.9. The overlaid dotted contours represent lines of constant R_{23}; from left to right $\log(R_{23}) = 0.0$, 0.5, and 1.0. The turn-around region encompasses $\log(R_{23})$ values of approximately 0.5 to 1.0. Dashed lines display excitation, where constant excitation of [O III]/[O II]= 1 coincides with the central line, [O III]/[O II]=0.1 is the low excitation line, and [O III]/[O II]=10 is the high excitation line. The numerous gray dots are the MPA-JHU data for SDSS galaxies in the range of $7.0 \leq \log(M_\star/M_\odot) \leq 9.0$, which have higher excitation than SDSS-024121, SDSS-082639, and SDSS-082633. Values presented by Yin et al. (2007) for a sample of SDSS galaxies containing direct method abundances are also included for comparison. Notice that three of our objects from the "very low mass" sample are discrepantly low excitation relative to the SDSS and Yin et al. (2007) samples, whereas the "main" sample has ordinary excitation values for the most part.

the P08 "main" sample objects have ordinary excitation values. Note that seven of the 24 "main" sample objects did not have z > 0.024 (consequently, they didn't have [O II] λ3727 in their spectra), and so could not be plotted here.

A complementary analysis is seen in Figure 2.11 where excitation (P) is plotted against log(R_{23}) for this same set of low mass SDSS galaxies (also see Moustakas et al. (2010) Figure 12 for a similar comparison). As discussed in § 2.5.3, three of our four objects lie well below the mean excitation for a given R_{23} value. Figure 2.11 also shows an upper limit of log(R_{23}) naturally falls near 1.0, where the present sample lies within the turn-around region defined by $0.5 \lesssim \log(R_{23}) \lesssim 1.0$, corresponding to $7.9 \leq 12 + \log(O/H) \leq 8.3$. A similar conclusion is drawn from the N2 calibration of PMC09 (§ 2.5.3) which suggests an oxygen abundance range of $8.30 \leq 12 + \log(O/H) \leq 8.44$ for the present objects based on the abnormal N/O variations present ($\sim 0.1 - 0.2$ dex less than other strong-line N2 calibrations). While we can't constrain the oxygen abundance more precisely for this sample (based on the arguments here in § 2.6.1) than to put them in the range of $7.9 \leq 12 + \log(O/H) \leq 8.4$, this is sufficient to disqualify them as high-metallicity M-Z outliers.

Note that the recalibration of the O3N2 and N2 abundance indicators by PMC09 reduced the inferred oxygen abundances, but only by about half of what was needed to bring the objects in line with their expected abundances that we are proposing here. Even after recalibration, there is still a significant amount of scatter in these relationships. We speculate that taking into consideration the additional concern of low excitation would move these points further in the direction of concordance with expectations.

2.6.2 The True Nature of the High Oxygen Abundance Outliers

Although it appears that the "very low mass", high oxygen abundance galaxies from P08 may not be true outliers from the M-Z relation, understanding how these galaxies produced spectra that lie far from the median relationships defined by the SDSS galaxies in various diagnostic diagrams remains an interesting question. Our MMT observations reveal that these spectra are characterized by (1) low excitation (low λ5007/λ3727 ratios; $\log(O_{32}) < -0.4$, see Figures 2.9, 2.10, and 2.11), (2) relatively high N/O abundance ratios for their stellar masses (see Figure 2.6), and (3) relatively deep underlying stellar

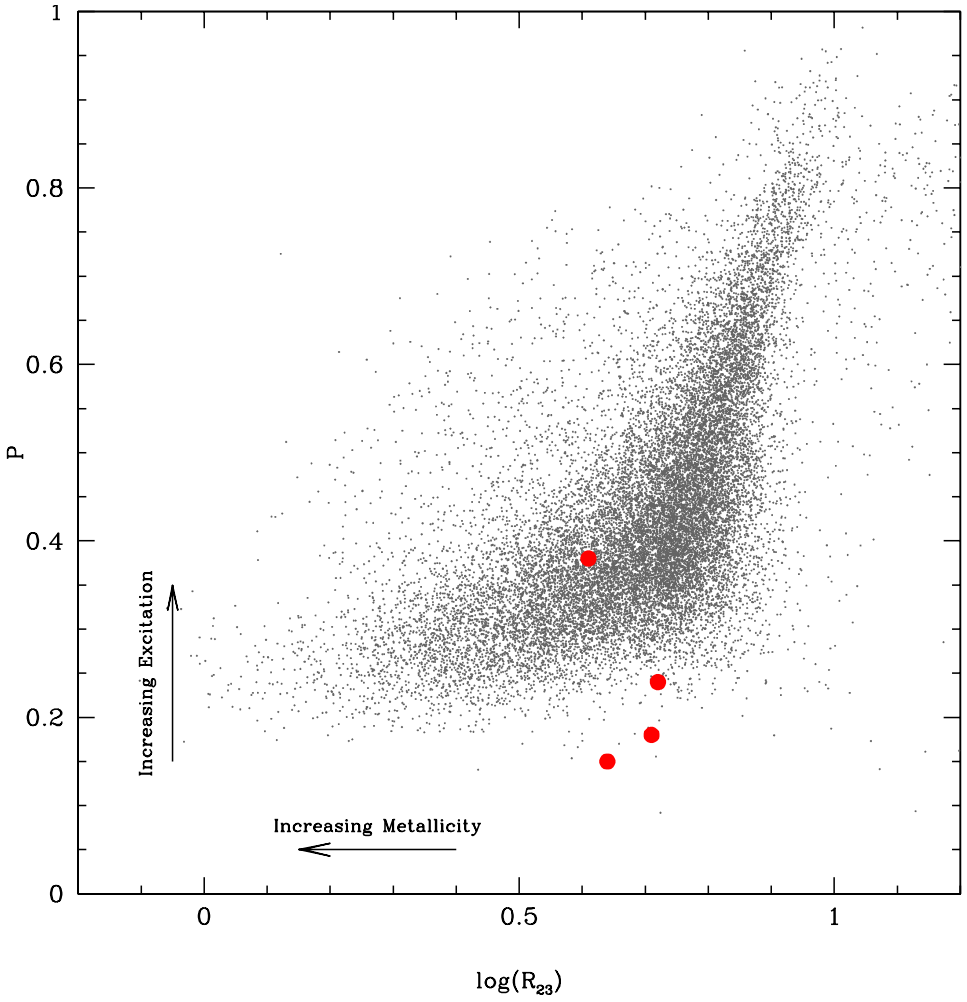

Figure 2.11: Exitation parameter P versus the metallicity sensitive R_{23} index for the four objects in this paper (red dots) and the low-mass star-forming galaxies in the SDSS (gray dots). Arrows indicate direction of increasing excitation and increasing metallicity for the R_{23} upper branch. For three of these objects, the excitation is rather low for their R_{23} values.

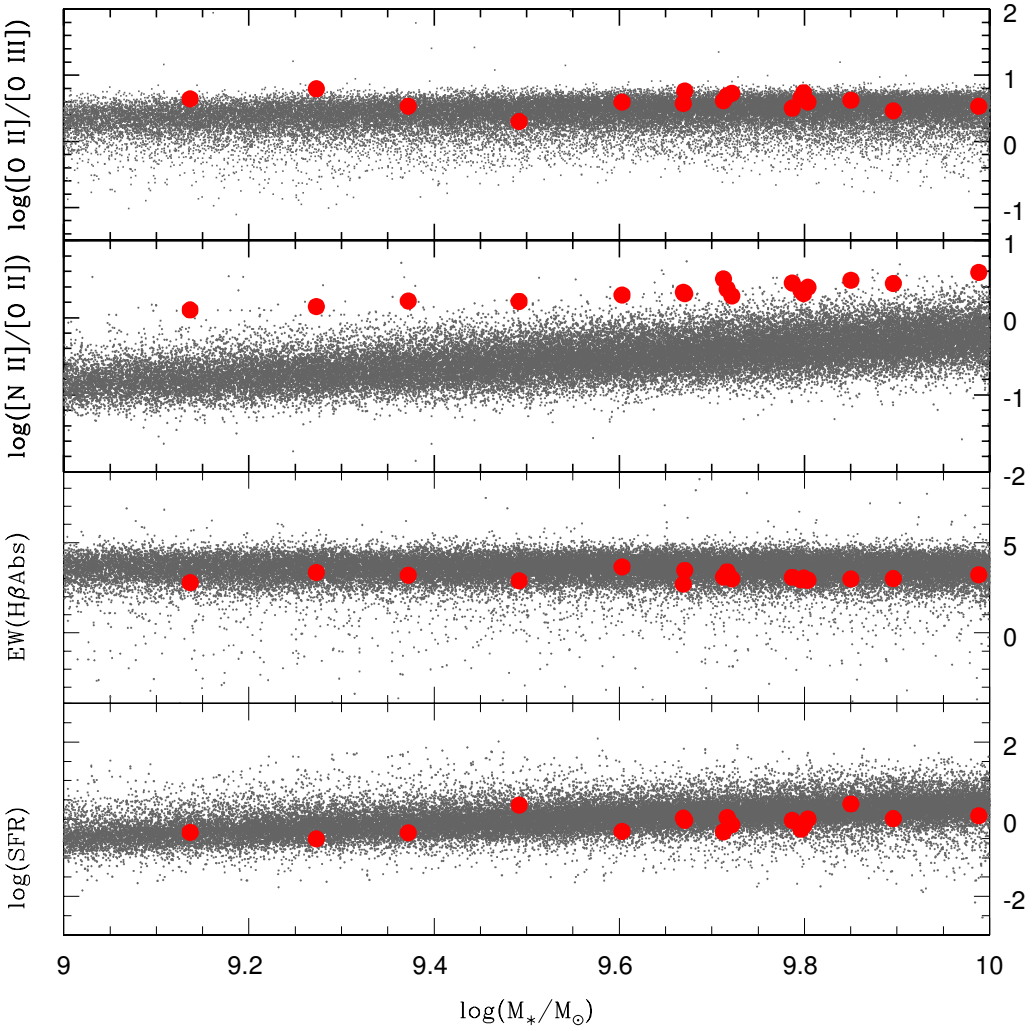

Figure 2.12: Properties of SDSS star-forming galaxies (gray dots) plotted against stellar mass ($9 \leq \log(M_\star/M_\odot) \leq 10$). In comparison, the P08 "main" sample (the 17 objects with measurable [O II]) are plotted in red. The top panel shows that in contrast to the "very low mass" sample, the "main" sample has normal ionization levels. Extremely high N values for the "main" sample relative to the SDSS average are shown in the second panel. The bottom two panels show that these objects have Hβ absorption equivalent widths and SFRs congruent with the SDSS sample. As all objects in the P08 samples exhibit elevated N/O ratios, we suggest N enrichment is the prominent factor influencing these objects.

Balmer absorption (ranging from 4 to 8 Å). All three characteristics can be explained by a previous, but recent burst of star formation. Essentially, these properties are all expected $\sim$ 5 Myr or longer after a starburst characterized as a "Wolf-Rayet galaxy."

Kunth & Sargent (1981) demonstrated that the presence of strong W-R features in the spectrum of a star forming region are indicative of an intense episode of star formation lasting a relatively short (on the order of 10^6 years) duration. For an instantaneous starburst, these W-R stars appear and disappear during the interval of 3 to 6 Myr (Leitherer & Heckman, 1995). Afterward, the most massive O stars have all evolved, and the less massive O and B stars produce a significantly softer spectrum resulting in lower excitation nebulae. The starburst models of González Delgado et al. (1999) show that the equivalent width of underlying stellar Hβ absorption increases from roughly 2.7 to 4.5 Å as an instantaneous starburst of solar metallicity ages from 0 to 10 Myr, and continues on to nearly 9 Å at an age of 100 Myr. On this basis, the MPA-JHU estimates of the Balmer absorption are consistent with H II region ages greater than 4 Myr (3.4 Å), while our estimates (larger due to aperture differences), suggest a lower limit of 7 Myr (5.8 Å). Finally, during the W-R stage, it is possible for stars to release a large amount of N back into the local ISM (see, e.g., Esteban & Vilchez, 1992; Kobulnicky et al., 1997b; López-Sánchez & Esteban, 2010, and references therein), producing inflated N/O ratios such as is seen in the four MMT spectra.

2.6.3 P08 "Main" Sample

Since all four of our objects, which were picked at random, have roughly identical spectral characteristics, we assume that the majority of the "very low mass" sample of P08 are probably similar. The "main" sample of P08 was defined by different restrictions, including a redshift cut to ensure the coverage of both [O II] and [O III] in the sample spectra (for 17 of the 24 "main" sample objects). We obtained the SDSS emission line strengths for the "main" sample from emission line analysis by the MPA-JHU collaboration. From these data we found the "main" sample galaxies (those with measured [O II] λ3727) have normal $\lambda3727/\lambda5007$ ratios for their masses. In Figure 2.12 we show some the properties of the "main" sample relative to the SDSS parent sample, highlighting the normal ionization strengths in the top panel, followed by average Hβ absorption equivalent widths and SFRs in the bottom two panels. The "main" and 'very low mass"

samples are different in that the "main" sample galaxies appear to have normal excitations. However, more importantly, in Figure 2.12 we have also plotted N/O ratio versus stellar mass for the P08 "main" sample, showing these galaxies all have very high N/O values. Similar to the four galaxies in our sample, the P08 "main" sample data suggest that they have also experienced recent N enrichment. Since high N/O values tend to bias strong-line methods towards high abundances, and the metallicity offsets for the "main" sample are smaller than for the "very low mass" sample, this bias could easily account for most of this deviation.

All objects of the P08 parent sample display the characteristic nitrogen enhancement expected for a galaxy after passing through the "Wolf-Rayet galaxy" phase. P08 suggest that these objects are "transitional objects running out of fuel": i.e., the high metallicity results because there is only a small amount of ISM to enrich. Our overall conclusion is that the high-metallicity outliers are special, not due to unusually high oxygen abundances for their mass or rate of star formation, but, rather, due to an enrichment of nitrogen relative to oxygen. This nitrogen enrichment may be due to being observed during a rare and short lived evolutionary phase.

2.7 Conclusions

In this chapter we have investigated four of the 41 luminosity-metallicity outliers from the low-mass, high oxygen abundance galaxy sample reported by Peeples et al. (2008). New spectral observations were obtained from the MMT, providing extended wavelength coverage, higher resolution, and improved signal-to-noise. As an improvement over the SDSS spectra, these data allowed all ionic species of oxygen to be evaluated simultaneously, while also considering the implications of additional spectral features. With this analysis we found:

(1) Three of four galaxies have relatively low excitation (low $\lambda5007/\lambda3727$ ratios; $\log(O_{32}) < -0.4$). Since most strong-line abundance methods are calibrated against high excitation H II regions, large uncertainties are introduced when applied to objects outside these conditions.

(2) All four galaxies exhibited high N/O values. Nitrogen is a delayed product of stellar nucleosynthesis (at least in part) and has been observed to increase over time

post-starburst. This characteristic can lead to overestimates of the oxygen abundance if standard strong-line calibrations are used. Furthermore, when combined with large variations in excitation, significant metallicity deviations can be produced, as seen for the P08 sample.

(3) By comparing our four spectra to the photoionization models of Stasińska & Leitherer (1996) (which include the effects of aging of the exciting stars), and the empirical calibrations of PMC09 (which correct for variations in the N/O ratio), we found that significantly lower oxygen abundances are favored. The Stasińska & Leitherer (1996) oxygen abundances are in line with those expected from the luminosities and stellar masses of the galaxies, while the PMC09 estimates shift oxygen abundances in the right direction. While the "very low mass" sample displays low star formation rates, the normal star formation within the "main" sample rules out exhaustive star formation as the variable responsible for the unusual sample spectra.

With these conclusions, we propose that these low-mass, high oxygen abundance SDSS galaxies are best described as nitrogen enriched, which may result from having recently passed through the "Wolf-Rayet galaxy" phase.

2.8 Acknowledgements

We acknowledge Liese van Zee for several helpful discussions and the anonymous referee for constructive comments and suggestions that greatly improved the analysis and clarified the text. D.A.B. is grateful for support from a Penrose Fellowship and a NASA Space Grant Fellowship from the University of Minnesota. E.D.S. is grateful for partial support from the University of Minnesota.

Observations reported here were obtained at the MMT Observatory, a joint facility of the Smithsonian Institution and the University of Arizona. MMT observations were obtained as part of the University of Minnesotas guaranteed time on Steward Observatory facilities through membership in the Research Corporation and its support for the Large Binocular Telescope. Funding for the Sloan Digital Sky Survey (SDSS) has been provided by the Alfred P. Sloan Foundation, the Participating Institutions, the National Aeronautics and Space Administration, the National Science Foundation, the U.S. Department of Energy, the Japanese Monbukagakusho, and the Max Planck

Society. The SDSS Web site is http://www.sdss.org/. This research has made use of NASAs Astrophysics Data System Bibliographic Services and the NASA/IPAC Extragalactic Database (NED), which is operated by the Jet Propulsion Laboratory, California Institute of Technology, under contract with the National Aeronautics and Space Administration.

Chapter 3

Direct Oxygen Abundances for Low Luminosity LVL Galaxies†

†Observations reported here were obtained at the MMT Observatory, a joint facility of the University of Arizona and the Smithsonian Institution.

A slightly modified version of this chapter has been published in The Astrophysical Journal with the following bibliographic reference: Berg, D. A., Skillman, E. D., Marble, A. R. 2011, et al., ApJ, 754, 98

Abstract

We present MMT spectroscopic observations of H II regions in 42 low-luminosity galaxies in the *Spitzer* Local Volume Legacy (LVL) survey. For 31 of the 42 galaxies in our sample, we were able to measure the temperature sensitive [O III] λ4363 line at a strength of 4σ or greater, and thus determine oxygen abundances using the direct method. Our results provide the first direct estimates of oxygen abundance for 19 of these galaxies. Direct oxygen abundances were compared to B-band luminosities, 4.5 μm luminosities, and stellar masses in order to characterize the luminosity-metallicity and mass-metallicity relationships at low-luminosity.

We present and analyze a "Combined Select" sample composed of 38 objects (drawn from a sub-set of our parent sample and the literature) with direct

oxygen abundances and reliable distance determinations (based on the tip of the red giant branch or Cepheid variables). Consistent with previous studies, the B-band and 4.5 μm luminosity-metallicity relationships for the 38 objects were found to be 12 + log(O/H) = (6.27±0.21) + (−0.11 ± 0.01)M_B and 12 + log(O/H) = (6.10±0.21) + (−0.10 ± 0.01)$M_{[4.5]}$ with dispersions of σ = 0.15 and 0.14 respectively. The slopes of the optical and near-IR L-Z relationships have been reported to be different for galaxies with luminosities greater than that of the LMC. However, the similarity of the slopes of the optical and near-IR L-Z relationships for our sample probably reflects little influence by dust extinction in the low-luminosity galaxies. For this sample, we derive a mass-metallicity relationship of 12 + log(O/H) = (5.61±0.24)+(0.29±0.03) log($M_\star$), which agrees with previous studies; however, the dispersion ($\sigma = 0.15$) is not significantly lower than that of the L-Z relationships. Because of the low dispersions in these relationships, if an accurate distance is available, the luminosity of a low-luminosity galaxy is often a better indicator of metallicity than that derived using certain strong-line methods, so significant departures from the L-Z relationships may indicate that caution is prudent in such cases. With these new direct metallicities we also revisit the 70/160 μm color metallicity relationship.

Additionally, we examine N/O abundance trends with respect to oxygen abundance and B-V color. We find a positive correlation between N/O ratio and B-V color for $0.05 \lesssim B - V \lesssim 0.75$: log(N/O) = (1.18±0.9)×(B-V) + (−1.92±0.08), with a dispersion of σ = 0.14, that is in agreement with previous studies.

3.1 Introduction

There is a fundamental relationship between the mass of stars in a galaxy and its metallicity evolution (e.g., Tremonti et al., 2004, hereafter, the M-Z relation). Empirically, this has been observed as a luminosity-metallicity relationship (hereafter, the L-Z relation) for low redshift dwarf galaxies (e.g., Lequeux et al., 1979; Skillman et al., 1989; Lee et al., 2006a, and references therein) and spiral galaxies (e.g., McCall et al., 1985;

Garnett & Shields, 1987; Zaritsky et al., 1994; Tremonti et al., 2004, and references therein). This relationship is observed over a range of 10 magnitudes in galaxy optical luminosity (e.g., Zaritsky et al., 1994; Tremonti et al., 2004; Lee et al., 2006a), but the data are relatively sparse at the low luminosity end where the intrinsic faintness of these galaxies makes metallicity determinations more difficult.

The physical driver of the M-Z relation remains under debate. One possibility is that low-mass galaxies are younger, in that they only recently started forming stars (Noeske et al., 2000; Leitner & Kravtsov, 2011). Another is that they have been less efficient at producing metals (Brooks et al., 2007). Many studies favor a different interpretation, where supernova driven winds preferentially expel metals from low-mass galaxies, resulting in a lower effective yield with decreasing mass (e.g., Dekel & Silk, 1986). However, Dalcanton (2007) emphasizes the importance of star formation efficiency as outflows are an insufficient regulator in the absence of depressed star formation. In addition, Dalcanton's calculations show that low effective yields cannot be due to gas infall. Alternatively, Köppen et al. (2007) showed that the M-Z relationship may be observed naturally if a SFR-dependent, and therefore mass-dependent, stellar initial mass function (IMF) is assumed. Clearly a better understanding of the mass-metallicity relationship at low-luminosity remains important to determine how galaxies evolve (e.g., see discussion in Moustakas et al., 2012, and references therein). In addition, a well defined low-luminosity M-Z relationship will provide clues to the source of its measurable scatter. While observational errors play a role, one or more physical processes may be responsible for the remainder. Suggestions for the scatter include variations in the star formation history (e.g., recent starbursts, Contini et al., 2002), variations in stellar surface mass density (Ellison et al., 2008), inflow of metal poor gas, perhaps triggered by interactions (Lee et al., 2004), and variations in local galaxy density (e.g., Cooper et al., 2008, and references therein). As astronomers examine the interrelationship between chemical abundance measurements, star formation, gas accretion, and gas outflow by measuring the evolution of the M-Z relationship, a secure M-Z relationship for the current epoch is needed for comparison.

Empirical and theoretical oxygen abundance calibrations often introduce bias, further limiting the M-Z relationship (e.g., Yin et al., 2007; Pérez-Montero & Contini, 2009; Moustakas et al., 2010; Berg et al., 2011). Notably, for 53,000 SDSS galaxies,

which span 10 orders in B-band magnitude, Tremonti et al. (2004) found a dispersion of 0.16 for their L-Z relationship and 0.10 for their M-Z relationship. Lee et al. (2006a, hereafter L06) were able to extend the mass-metallicity relation lower by 2.5 decades in stellar mass using 4.5 μm luminosities for 27 nearby dwarf irregular galaxies. Interestingly, L06 found the dispersion in the near-infrared L-Z relationship to be smaller than the corresponding dispersion in the B-band L-Z relationship and nearly identical to that of the M-Z relationship. The smaller dispersion in the near-infrared is not totally unexpected, as NIR luminosities are less sensitive to extinction from dust and variations in star formation rate. However, the significant but uncertain stochastic effects of asymptotic giant branch (AGB) stars on the total NIR luminosities of low-luminosity galaxies must also be considered (see, e.g., Fouesneau & Lançon, 2010; Meidt et al., 2012; Melbourne et al., 2012).

To thoroughly examine the L-Z and M-Z relations, we need a robust sample of galaxies. The *Spitzer* Local Volume Legacy survey[1] (LVL; Dale et al., 2009) covers a volume-complete sample of 258 galaxies in the local universe with multiwavelength observations spanning the ultraviolet to the radio. The LVL is leveraged by ancillary data including Hα (Kennicutt et al., 2008) and UV (Lee et al., 2011) imaging from the 11 Mpc Hα and Ultraviolet Galaxy Survey (11HUGS; Lee et al., 2011) and the Nearby Galaxy Survey (NGS; Gil de Paz et al., 2007). A subsample of the LVL also contains stellar population mapping from the ACS Nearby Galaxy Survey Treasury (ANGST; Dalcanton et al., 2009), HI mapping from the VLA and GMRT, and optical broad-band imaging (Cook et al., 2012; van Zee et al., 2013) and spectroscopy. However, many of the faintest objects are missing the high-quality optical spectroscopy needed to determine direct oxygen-abundance metallicity estimates.

As the L-Z relationship provides both a very strong constraint on theories of galaxy evolution and a tool to better understand galaxies at higher redshifts (Kobulnicky et al., 2003), we are motivated to better characterize the low-luminosity end of the L-Z relationship. Thus, we obtained high-resolution MMT spectroscopy of 42 low-luminosity star-forming galaxies in the Local Volume with the goal of detecting the [O III] λ4363 line in order to constrain electron temperature measurements.

We present our low-luminosity sample in § 3.2.2, with spectral observations obtained

[1] http://www.ast.cam.ac.uk/research/lvls

from the MMT in § 5.2.1 and IRAC photometry in § 3.2.4. Section 3.3 describes the data reduction, followed by the description of the method used to determine direct oxygen abundances in § 5.4. Our "Select" sample, compiled from objects with direct oxygen abundances and secure distance estimates, is defined in § 3.5.1. Using this sample, metallicity is compared to expected trends with B-band luminosity, 4.5 μm luminosity, and stellar mass in § 3.5.2, § 3.5.3, and § 3.5.4 respectively. N/O relative abundances are discussed in § 3.6. In § 3.7 we discuss the results of the relationships found in § 3.5.2-§ 3.5.4, the "young galaxy" hypothesis, and the quality of abundance estimators. Finally, we summarize our conclusions in § 5.5. Section 2.9: Appendix A presents the strong-line abundances for the low-luminosity LVL galaxies for which we were unable to determine direct abundances. and Section 2.10: Appendix B presents our new direct abundances in comparison to the color-temperature metallicity relationship of Engelbracht et al. (2008).

3.2 Sample Selection

3.2.1 *Spitzer* LVL Survey

LVL is a *Spitzer Space Telescope* legacy program that combines IRAC (Infrared Array Camera) and MIPS (Multiband Imaging Photometer) infrared imaging for a complete sample of 258 galaxies for the nearest 11 Mpc of our local universe. These data build upon recent Local Volume galaxy surveys: narrowband Hα (Kennicutt et al., 2008), *GALEX* ultraviolet (Lee et al., 2011), and *Hubble Space Telescope* resolved stellar population imaging (Dalcanton et al., 2009). While previous surveys comprehensively cover high surface brightness systems in flux-limited samples, the LVL survey, although also biased toward high surface brightness galaxies, provides a multi-wavelength inventory of a statistically robust, approximately volume-limited sample, which is well-suited for studies of dwarf galaxies. By studying the nearby, low-luminosity galaxies, we can increase the dynamic range covered by the luminosity-metallicity and mass-metallicity relationships, which will help to better constrain the slopes.

3.2.2 Low-Luminosity LVL Sample

We selected a sample of 42 low-luminosity galaxies in the LVL survey in order to obtain new MMT high-resolution spectra. These low-luminosity spirals and dwarf irregulars span a range in distance of $2.5 \leq \mathrm{D} \leq 14.0$ Mpc.[2] The luminosities for this sample range in the near-IR (determined from IRAC (Fazio et al., 2004) photometry) from $M_{[4.5]} = -13.1$ to -21.7, with B-band magnitudes of $-10.8 \geq M_B \geq -18.8$. Most of the objects were chosen because they lack direct oxygen abundances in the literature, their abundance estimates are dated, or were studied with instruments which were known to have problems.

Although not LVL objects, two additional galaxies were added to the sample (increasing the sample total to 44 objects) because they played a role in motivating this project. Both UGC 4393 and UGC 10818 were identified by Engelbracht et al. (2008) as low metallicity outliers from the global trend of 70/160 μm color temperature as a function of metallicity. These two galaxies affect the interpretation of the trend for aromatic emission to weaken below $12 + \log(\mathrm{O/H}) = 7.9$ in the mid-IR (see e.g., Engelbracht et al., 2008) and the far-IR (see e.g., Draine et al., 2007; Engelbracht et al., 2008). Because of the possibility that these objects' oxygen abundances were underestimated using the lower branch of the $\mathrm{R_{23}}$ calibration (Pilyugin & Thuan, 2005), they were included in this sample to be re-examined (see discussion in Section 2.10: Appendix B). See Table 5.1 for sample characteristics.

[2] Since the inception of the LVL Spitzer program, four galaxies included in the sample have updated distances which place them outside of 11 Mpc (see Dale et al., 2009; Lee et al., 2011).

Low-Luminosity LVL Sample

Galaxy	RA (J2000)	DEC (J2000)	$F_{[4.5]}$ (mJy)	F_{K_S} (mJy)	D (Mpc)	Reference Method	M_B (mag)	$M_{[4.5]}$ (mag)	M_{K_S} (mag)	$(B-V)_0$ (mag)	log $L_{[4.5]}$ ($L_\odot$)	log $M_\star$ ($M_\odot$)
UGC 521	00:51:12.1	12:01:26	2.24	5.43±2.88	10.9	13, v(flow)	-15.16±0.50	-17.93±0.61	-17.46±0.52	0.34±0.05	8.50±0.61	7.96±0.61
UGC 695	01:07:46.4	01:03:52	3.02	< 8.45	10.2	6, v(flow)	-15.13±0.50	-18.11±0.61	-17.80±0.52	0.45±0.06	8.57±0.61	8.08±0.61
NGC 404	01:09:27.0	35:43:05	239	676±340	3.05±0.04	4, trgb	-16.39±0.07	-20.23±0.35	-19.94±0.14	0.83[4]	9.42±0.35	9.20±0.35
UGC 1056	01:28:47.6	16:41:21	4.14	29.1±4.0	10.32	6, v(flow)	-15.09±0.52	-18.47±0.61	-19.17±0.50	0.57±0.07	8.72±0.61	8.62±0.61
UGC 1176	01:40:09.9	15:54:20	6.22	< 26.6	9.04±1.66	9, bs	-15.48±0.93	-18.63±0.98	-18.78±0.92	0.31±0.10	8.78±0.98	8.48±0.98
NGC 784	02:01:16.9	28:50:09	35.0	72.2±9.9	5.19±0.12	12, trgb	-16.50±0.12	-19.30±0.36	-18.66±0.20	0.40±0.04	9.05±0.36	8.48±0.36
UGC 2716	03:24:08.1	17:45:15	7.58	22.2±4.7	6.2	6, v(flow)	-15.31±0.50	-18.04±0.61	-17.78±0.51	0.31±0.06	8.55±0.61	8.13±0.61
KKH 37	06:47:45.4	80:07:26	1.58	6.43±2.81	3.39±0.12	4, trgb	-11.98±0.20	-15.01±0.39	-15.11±0.20	0.54±0.06	7.34±0.39	7.01±0.39
NGC 2537	08:13:14.6	45.59:30	51.4	160±10	6.88	10, bs	-17.14±0.50	-20.34±0.61	-20.36±0.51	0.72[4]	9.47±0.61	9.10±0.61
UGC 4278	08:13:58.9	45:44:37	15.5	35.8±5.1	7.6	6, v(flow)	-16.36±0.50	-19.24±0.60	-18.73±0.52	0.35[4]	9.03±0.60	8.50±0.60
NGC 2552	08:19:19.2	50:00:37	22.7	54.9±8.1	7.7	6, v(flow)	-16.72±0.50	-19.67±0.61	-19.21±0.52	0.43±0.04	9.20±0.61	8.69±0.61
UGC 4393	08:26:04.4	45:58:04	7.24	···	16.8±2.9	15, TF	-17.67±0.85	-21.65±0.86[2]	···	0.60[3]	9.99±0.86	9.43±0.86
CGCG 35-007	09:34:44.9	06:25:32	2.88	13.5±3.4	5.2	6, v(flow)	-13.38±0.51	-16.58±0.61	-16.83±0.51	0.54±0.10	7.97±0.61	7.69±0.61
UGC 5139	09:40:30.0	71:11:05	5.98	16.0±7.3	3.90±0.05	4, trgb	-14.42±0.12	-16.76±0.51	-16.41±0.20	0.36±0.07	8.04±0.51	7.39±0.51
IC 559	09:44:43.8	09:36:54	5.55	23.7±4.1	4.9	6, v(flow)	-14.12±0.50	-17.19±0.61	-17.34±0.51	0.48[3]	8.21±0.61	7.86±0.61
UGC 5272	09:50:22.4	31:29:16	5.12	15.8±4.2	7.11±0.77	8, bs	-14.98±0.55	-17.90±0.64	-17.70±0.55	0.37[4]	8.49±0.64	8.00±0.64
UGC 5340	09:56:45.8	28:49:32	1.94	< 9.36	12.1±0.7	16, trgb	-15.83±0.55	-17.99±0.44	-18.28±0.29	0.13±0.08	8.53±0.44	7.97±0.45
UGC 5423	10:05:30.6	70:21:52	3.63	13.6±2.7	5.27±0.40	10, bs	-13.77±0.38	-16.88±0.85	-16.89±0.53	0.48±0.04	8.09±0.85	7.77±0.85
UGC 5672	10:28:20.8	22:34:16	7.71	25.3±5.3	6.25	10, bs	-14.73±0.52	-18.06±0.61	-17.93±0.51	0.64±0.05	8.56±0.61	8.38±0.61
UGC 5692	10:30:36.6	70:37:03	17.7	66.4±8.4	3.80±0.05	4, trgb	-14.68±0.08	-17.88±0.35	-17.89±0.11	0.68±0.04	8.48±0.35	8.16±0.35
UGC 5797	10:39:25.2	01:43:05	4.09	11.7±4.2	6.8	6, v(flow)	-14.56±0.51	-17.57±0.61	-17.29±0.51	0.46±0.08	8.36±0.61	7.75±0.61
UGC 5923	10:49:07.6	06:55:03	6.41	21.8±2.5	7.2	6, v(flow)	-14.70±0.50	-18.16±0.61	-18.06±0.51	0.66±0.02	8.59±0.61	8.29±0.61
NGC 3738	11:35:48.6	54:31:29	39.9	104±8	4.9±0.6	3, trgb	-16.51±0.61	-19.32±0.70	-18.93±0.63	0.39[4]	9.06±0.70	8.50±0.70
NGC 3741	11:36:05.8	45:17:11	3.24	11.2±4.5	3.24±0.13	4, trgb	-13.18±0.22	-15.69±0.40	-15.62±0.22	0.31±0.07	7.61±0.40	7.05±0.40
UGC 6782	11:48:57.0	23:50:17	2.30	< 8.88	13.7	7, bs	-15.54±0.51	-18.45±0.61	-18.49±0.51	0.53[4]	8.71±0.61	8.29±0.61
UGC 6817	11:50:54.1	38:52:51	4.99	21.5±6.0	2.59±0.17	4, trgb	-13.70±0.34	-15.68±0.48	-15.84±0.34	0.30[4]	7.60±0.48	6.97±0.48
UGC 6900	11:55:39.4	31:31:10	5.41	18.1±5.2	7.5	6, v(flow)	-14.62±0.53[1]	-18.06±0.61	-17.95±0.51	0.64[4]	8.56±0.61	8.19±0.61
NGC 4163	12:12:09.2	36:10:10	11.5	32.6±5.8	2.88±0.04	4, trgb	-13.65±0.12[1]	-16.81±0.35	-16.52±0.14	0.44[4]	8.06±0.35	7.61±0.35
CGCG 269-049	12:15:47.2	52:23:17	1.24	3.31±1.99	1.60±0.04	4, trgb	-10.83±0.14	-13.12±0.36	-12.76±0.18	0.28±0.06	6.58±0.36	5.90±0.36
UGC 7577	12:27:40.9	43:29:44	14.2	41.9±6.9	2.58±0.07	4, trgb	-14.12±0.14	-16.80±0.36	-16.55±0.18	0.48[4]	8.05±0.36	7.50±0.36
NGC 4449	12:28:10.1	44:05:31	315	893±46	3.82±0.26	14, trgb	-18.02±0.34	-21.02±0.48	-20.73±0.36	0.37±0.04	9.74±0.48	9.25±0.48
UGC 7599	12:28:28.5	37:14:01	1.43	4.01±2.06	6.9	7, bs	-14.35±0.51[1]	-16.45±0.61	-16.14±0.52	0.40[4]	7.91±0.61	7.19±0.61
UGC 7605	12:28:38.5	35:42.58	2.41	6.09±2.45	4.43±0.57	3, trgb	-13.49±0.66[1]	-16.05±0.73	-15.63±0.66	0.29±0.04	7.75±0.73	7.12±0.73
UGC 7639	12:29:53.4	47:31:52	7.68	26.4±5.5	7.1±0.5	11, sbf	-15.55±0.37[1]	-18.33±0.49	-18.25±0.37	···	8.67±0.49	8.25±0.49
NGC 4656	12:43:57.7	32:10:05	70.5	135±14	8.6	6, v(flow)	-18.75±0.51[1]	-21.15±0.61	-20.44±0.53	0.42[4]	9.79±0.61	9.04±0.61
UGC 8201	13:06:24.5	67:42:28	9.09	37.3±6.3	4.57±0.40	3, trgb	-15.17±0.44	-17.56±0.60	-17.67±0.45	0.24±0.04	8.36±0.60	7.82±0.60

TABLE 1—*Continued*

Galaxy	RA (J2000)	DEC (J2000)	$F_{[4.5]}$ (mJy)	F_{K_S} (mJy)	D (Mpc)	Reference Method	M_B (mag)	$M_{[4.5]}$ (mag)	M_{K_S} (mag)	$(B-V)_0$ (mag)	log $L_{[4.5]}$ ($L_\odot$)	log $M_\star$ ($M_\odot$)
UGC 8245	13:08:35.2	78:56:14	5.98	20.0±4.3	3.64	6, v(flow)	-13.67±0.50	-16.61±0.61	-16.50±0.51	0.47±0.04	7.98±0.61	7.53±0.61
UGC 8508	13:30:44.1	54:54:40	4.87	13.9±4.2	2.58±0.03	4, trgb	-13.03±0.07	-15.64±0.35	-15.36±0.13	0.37±0.03	7.59±0.35	7.00±0.35
UGC 8638	13:39:19.2	24:46:36	5.01	15.2±4.6	4.27±0.34	5, trgb	-13.77±0.40	-16.77±0.53	-16.55±0.41	0.47±0.04	8.04±0.53	7.57±0.53
UGC 8837	13:54:45.7	53:54:03	10.1	26.5±7.1	8.3	2, bs	-15.92±0.51[1]	-18.97±0.61	-18.59±0.52	0.42[4]	8.92±0.61	8.41±0.61
NGC 5477	14:05:33.1	54:27:39	5.17	22.0±4.5	7.7	2, bs	-15.22±0.51[1]	-18.08±0.61	-18.23±0.51	0.34[4]	8.56±0.61	8.15±0.61
UGC 9405	14:35:24.4	57:15:19	3.97	12.9±5.0	8.02±0.74	8, bs	-14.97±0.47[1]	-17.88±0.58	-17.74±0.47	0.68[3]	8.48±0.58	7.97±0.58
UGC 10818	17:19:42	61:18:47	4.65	···	56	1, h(flow)	-18.59±0.50	-20.96±0.51[2]	···	···	9.72±0.51	9.45±0.51
KKH 98	23:45:34.3	38:43:00	1.56	7.56±3.09	2.45±0.04	4, trgb	-11.10±0.16	-14.29±0.36	-14.58±0.11	0.20±0.13	7.05±0.36	6.72±0.36

NOTE.—The low-luminosity LVL sample listed by right ascension. Col(1): Galaxy name. Col(2) and Col(3): Right ascension and declination of the galaxy. Col(4): Flux density at 4.5 μm corrected for fore-ground extinction from Dale et al. (2009). Col(5): Flux density in the 2MASS K_S band corrected for fore-ground extinction from Dale et al. (2009). Col(6) and (7): Distance and source reference. Direct measurements from the literature are used when possible. The methods used to calculate the distances are abbreviated by: trgb (tip of the red giant branch), bs (brightest blue stars), sbf (surface brightness fluctuations), v(flow) (Virgocentric flow model), h(flow) (redshift and Hubble flow model), and TF (Tully-Fisher relation). Col(8): M_Bs are aperture matched to the LVL photometry and are taken from van Zee et al. (2012), unless otherwise noted. The photometry is corrected for fore-ground extinction. Col(9): $M_{[4.5]}$ is calculated from the 4.5 μm IRAC photometry presented in Dale et al. (2009) and distance; from Col(4) and Col(6). Col(10): M_{K_S} is calculated from the 2MASS K_S photometry presented in Dale et al. (2009) and distance; from Col(5) and Col(6). Note that 179.7 and 666.7 are the zero point fluxes in Janskys for the 4.5 μm IRAC and K_S 2MASS bands respectively. Col(11): $(B-V)_0$ color taken from van Zee et al. (2012); see $B-V$ superscripts for source of exceptions. Col(12): Luminosity at 4.5 μm, assuming $M_{[4.5]} \simeq 3.3$ for the Sun following L06. Col(13): log $M_\star$ calculated following method presented in L06; see § 3.5.4. Note that UGC 10818 and UGC 4393 are not a part of the LVL survey, but have been included here for completeness (See § 3.2.2).

[1]Kennicutt et al. (2008); photometry is extinction corrected.
[2]Engelbracht et al. (2008), photometry is extinction corrected.
[3]Calculated from $g-r$ colors, available on SDSS.org, with foreground extinction correction and 1st order k_{filter} extinction correction.
[4]de Vaucouleurs et al. (1991); photometry is extinction corrected and k-corrected.

References. — (1) Engelbracht et al. (2008); (2) Karachentsev et al. (1994); (3) Karachentsev et al. (2003); (4) Dalcanton et al. (2009) (5) Karachentsev et al. (2006); (6) Kennicutt et al. (2008); (7) Makarova et al. (1998); (8) Makarova & Karachentsev (1998); (9) Sharina et al. (1996); (10) Sharina et al. (1999); (11) Rekola et al. (2005) (12) Tully et al. (2006); (13) van Zee et al. (2006); (14) Annibali et al. (2008); (15) Springob et al. (2009); (16) A. Aloisi, private communication 2011

Table 3.2. Observing Log for LVL Sample

Slit Position	RA (2000)	Dec (2000)	PA (deg)	Run	T_{int} (sec)
UGC 521-A	00:51:11.9	12:01:34	-55.71	Nov08	3 × 900
UGC 521-B	00:51:12.1	12:01:31	-55.71	Nov08	2 × 900
UGC 695-E	01:07:46.5	01:03:53	29.44	Jan10	4 × 900
NGC 0404-A	01:09:26.0	35:43:00	-76.70	Jan10	3 × 600
UGC 1056-A	01:28:47.3	16:41:16	45.19	Jan10	3 × 900
UGC 1056-B	01:28:47.5	16:41:21	45.19	Jan10	4 × 900
UGC 1176-A	01:40:11.9	15:54:46	42.14	Jan10	4 × 900
UGC 784-B	02:01:16.5	28:50:06	52.76	Jan10	4 × 900
UGC 784-A	02:01:17.5	28:50:16	52.76	Jan10	4 × 1200
UGC 2716-A	03:24:07.2	17:45:11	63.24	Jan10	3 × 900
KKH 037-A	06:47:43.1	80:07:27	-176.05	Jan10	1 × 1800
NGC 2537-A	08:13:13.0	45:59:39	-94.27	Jan10	3 × 900
NGC 2537-B	08:13:13.3	45:59:39	-94.27	Jan10	3 × 900
UGC 4278-B	08:14:00.2	45:42:58	-128.00	Oct08	3 × 1800
UGC 4278-A	08:14:00.0	45:42.57	-128.00	Oct08	3 × 1800
NGC 2552-A	08:19:17.1	50:00:14	-120.00	Oct08	3 × 1200
UGC 4393-B	08:26:05.3	45:58:10	-124.65	Jan10	3 × 900
UGC 4393-C	08:26:01.5	45:47:43	-124.65	Jan10	3 × 900
CGCG 035-007-A	09:34:44.4	06:25:31	42.78	Jan10	3 × 900
UGC 5139-A	09:40:16.0	71:10:06	-140.00	Nov08	4 × 1200
IC 559-A	09:44:42.9	09:36:54	-64.15	Jan10	4 × 900
UGC 5272-A	09:50:22.3	31:29:15	-80.51	Oct08	3 × 600
UGC 5340-A	09:56:46.8	28:50:10	-75.61	Jan10	4 × 900
UGC 5423-A	10:05:28.7	70:22:05	127.00	Jan10	3 × 900
UGC 5423-B	10:05:32.1	70:21:52	127.00	Jan10	3 × 900
UGC 5672-A	10:28:21.1	22:34:05	-57.80	Jan10	4 × 900
UGC 5692-A	10:30:34.8	70:37:11	-147.53	Jan10	4 × 900
UGC 5797-A	10:39:25.0	01:43:00	-4.17	Jan10	3 × 900
UGC 5923-A	10:49:07.5	06:55:08	20.00	Jan10	5 × 600
NGC 3738-A	11:35:46.8	54:31:32	93.73	Jun09	4 × 900
NGC 3738-B	11:35:48.2	54:31:31	93.73	Jun09	4 × 900

3.2.3 MMT Spectra

Observations

New spectroscopy was acquired at the MMT in order to achieve high signal-to-noise (S/N) spectra with the goal of detecting the faint [O III] λ4363 auroral line at a strength of 4σ or higher. The observations were obtained with the Blue Channel spectrograph (Schmidt et al., 1989) on the UT dates of 2008 October 30-November 1, 2009 June 15-22, and 2010 January 11-12. Sky conditions varied, but contained minimal cloud coverage and approximately arcsecond seeing. A 500 line grating, $1''$ slit, and UV-36 blocking filter were used, yielding an approximate dispersion of 1.2 Å per pixel, a full width at half maximum resolution of $\lesssim 3$ Å, and a wavelength coverage of 3690–6790 Å. The sensitivity, resolution, and wavelength coverage of the MMT and Blue Channel spectrograph combination allowed for the measurement of all emission lines relevant to oxygen abundance determinations. Bias frames, flat-field lamp images, and sky flats were taken each night. The latter were primarily necessary due to significant differences between the chip illumination patterns of the sky and the MMT Top Box that houses the "BC" incandescent flat-field lamp. On average, four standard stars from Oke (1990) with spectral energy distributions (SEDs) peaking in the blue and containing minimal absorption were observed throughout the night using a $5''$ slit over a range of airmasses. This allows the flux calibration to be determined as a function of airmass. The large slit width mitigates the effects of atmospheric differential refraction and allows accurate measurements of relative fluxes across a large range in wavelength. Note that since we only care about relative abundances, an absolute flux calibration is not critical.

All 44 galaxies had at least one strong Hα brightness peak that was aligned with the $1'' \times 180''$ slit. Typically, three 900 second exposures[3] were made with the slit at a fixed position angle which approximated the parallactic angle at the midpoint of the observation and laid across several Hα bright regions when possible. This, in addition to observing the galaxies at airmasses less than 1.5, served to minimize the wavelength-dependent light loss due to differential refraction (Filippenko, 1982). A single slit position for each target was deemed sufficient to characterize the global oxygen

[3] Some galaxy observations were adjusted to shorter or longer exposures depending on the brightness of the [O III] λ4363 line strength, or included additional exposures when the observing program allowed for it; see Table 5.2.

Table 3.2 (cont'd)

Slit Position	RA (2000)	Dec (2000)	PA (deg)	Run	T_{int} (sec)
NGC 3741-A	11:36:05.9	45:17:00	101.03	Jun09	3 × 1200
UGC 6782-A	11:48:57.2	23:50:32	64.55	Jun09	3 × 1200
UGC 6817-A	11:50:52.9	38:52:52	93.87	Jun09	3 × 1200
UGC 6900-A	11:55:36.2	31:31:19	81.43	Jun09	3 × 1200
UGC 4163-A	12:12:09.4	36:09:59	87.48	Jun09	3 × 1200
CGCG 269-049-A	12:15:46.6	52:23:14	-187.93	Jan10	4 × 900
UGC 7577-A	12:27:42.8	43:29:06	100.00	Jun09	3 × 1200
NGC 4449- C	12:28:14.5	44:07:13	75.00	Jun09	3 × 600
NGC 4449- B	12:28:14.1	44:07:12	75.00	Jun09	3 × 600
NGC 4449-A	12:28:13.9	44:07:10	75.00	Jun09	3 × 600
UGC 7599-A	12:28:27.2	37:14:16	86.11	Jun09	3 × 1500
UGC 7605-A	12:28:38.4	35:43:15	89.00	Jun09	5 × 1200
UGC 7639-A	12:29:54.6	47:31:40	95.77	Jun09	2 × 1200, 1 × 600
NGC 4656-A	12:43:56.6	32:10:12	-79.80	Jan10	3 × 900
UGC 8201-A	13:06:17.4	67:42:08	120.00	Jun09	3 × 1200
UGC 8245-A	13:08:41.0	78:56:22	150.00	Jun09	3 × 1200
UGC 8508-A	13:30:44.5	54:54:24	90.09	Jun09	2 × 1200, 1× 900
UGC 8638-A	13:39:19.3	24:46:28	69.76	Jun09	3 × 1200
UGC 8638-B	13:39:20.5	24:46:33	69.76	Jun09	3 × 1200
UGC 8837-A	13:54:40.5	53:53:09	123.33	Jun09	3 × 900
NGC 5477-C	14:05:32.9	54:27:41	99.00	Jun09	3 × 900
NGC 5477-A	14:05:33.4	54:27:41	99.00	Jun09	3 × 900
UGC 9405-A	14:35:25.9	57:15:29	125.00	Jun09	4 × 1200
UGC 10818-A	17:19:41.1	61:18:31	-180.00	Jun09	3 × 900
KKH 098-A	23:45:33.5	38:43:15	-110.00	Jan10	3 × 1800

Note. — The low-luminosity LVL sample observing log. Galaxy name and H II region label are listed in Column 1. The right ascension and declination of the individual H II regions are given in units of hours, minutes, and seconds, and decrees, arcminutes, and arcseconds respectively. The position angle (PA) gives the rotation of the slit counter clockwise from North. Note that the RA and Dec positions for "A" regions are accurate and denote the center slit placement. However, "B" and "C" regions only have estimated RA and Dec positions, as these are just extra extractions along the same slit that is aligned through "A".

abundance, as metallicity gradients are observed to be small or non-existent in low-mass galaxies (e.g., Skillman et al., 1989; Kobulnicky & Skillman, 1996, 1997a; Lee et al., 2006b; Croxall et al., 2009). Finally, combined helium, argon, and neon arc lamps were observed at each pointing for accurate wavelength calibration. A log of the observations is provided in Table 5.2. Figure 5.1 shows the R-band continuum and Hα continuum-subtracted images for each galaxy, motivating our slit location choices. The brightest Hα regions observed are ordered alphabetically by decreasing flux, and the slit positions on the galaxies are shown. The images scale as 60x60 arcseconds with North oriented up and East to the left.

Spectra Reduction

Details of the data reduction techniques used in this thesis are described in Appendix A. Figure 5.2 shows a sample of four of the resulting one-dimensional spectra extracted for galaxies that had significant [O III] λ4363 detections. The inset windows display a narrower spectral range to emphasize the [O III] λ4363 strength. This sample does not feature the best spectra from our sample, but rather galaxies are ordered by ionizing radiation field strength from highest to lowest as given by the [O III] λ5007/[O II] λ3727 ratio, highlighting the variation within the sample.

3.2.4 Photometry

To better characterize our low-luminosity sample, absolute magnitudes in several different bands were obtained. Here we describe their origin and reference their subsequent use. M_B values were determined by van Zee et al. (2013) using photometry from apertures matched to the infrared LVL photometry (unless otherwise noted). Optical photometry for the entire LVL sample is given in Cook et al. (2012), whereas van Zee et al. (2013) focuses on the analysis of colors and EW gradients of dwarf galaxies. The data are used to examine the optical luminosity-metallicity relationship (see Section 3.5.2).

$M_{[4.5]}$ values from the 4.5 μm IRAC photometry presented in Dale et al. (2009) were calculated using

$$M_{[4.5]} = -2.5 \log \frac{F_{[4.5]}(d/10)^2}{179.7}, \tag{3.1}$$

where $F_{[4.5]}$ is the 4.5 μm flux in Janskys, d is the distance in parsecs, and 179.7 is the

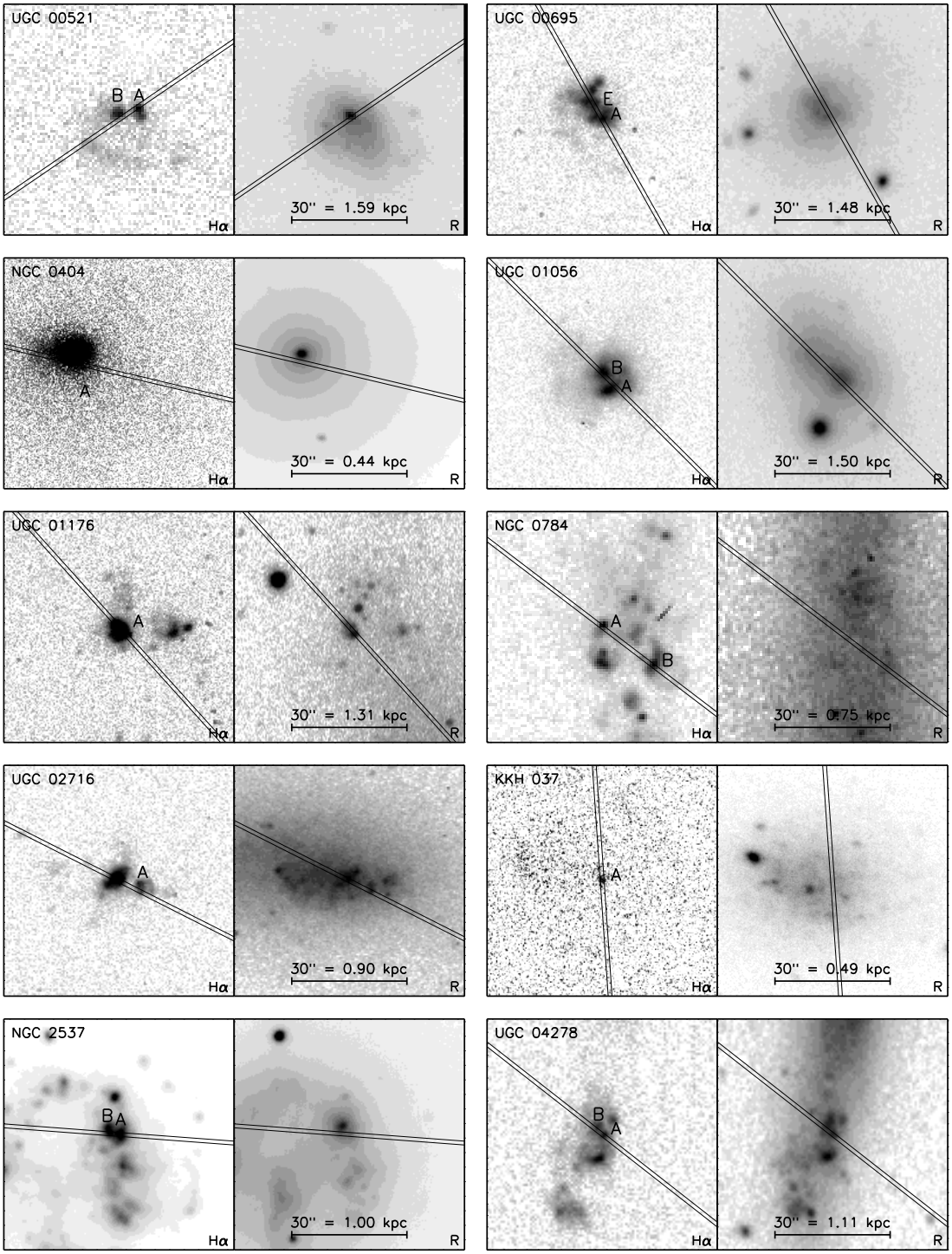
UGC 00521
B A
30'' = 1.59 kpc
Hα
R
UGC 00695
E
A
30'' = 1.48 kpc
Hα
R
NGC 0404
A
30'' = 0.44 kpc
Hα
R
UGC 01056
B
A
30'' = 1.50 kpc
Hα
R
UGC 01176
A
30'' = 1.31 kpc
Hα
R
NGC 0784
A
B
30'' = 0.75 kpc
Hα
R
UGC 02716
A
30'' = 0.90 kpc
Hα
R
KKH 037
A
30'' = 0.49 kpc
Hα
R
NGC 2537
B A
30'' = 1.00 kpc
Hα
R
UGC 04278
B
A
30'' = 1.11 kpc
Hα
R

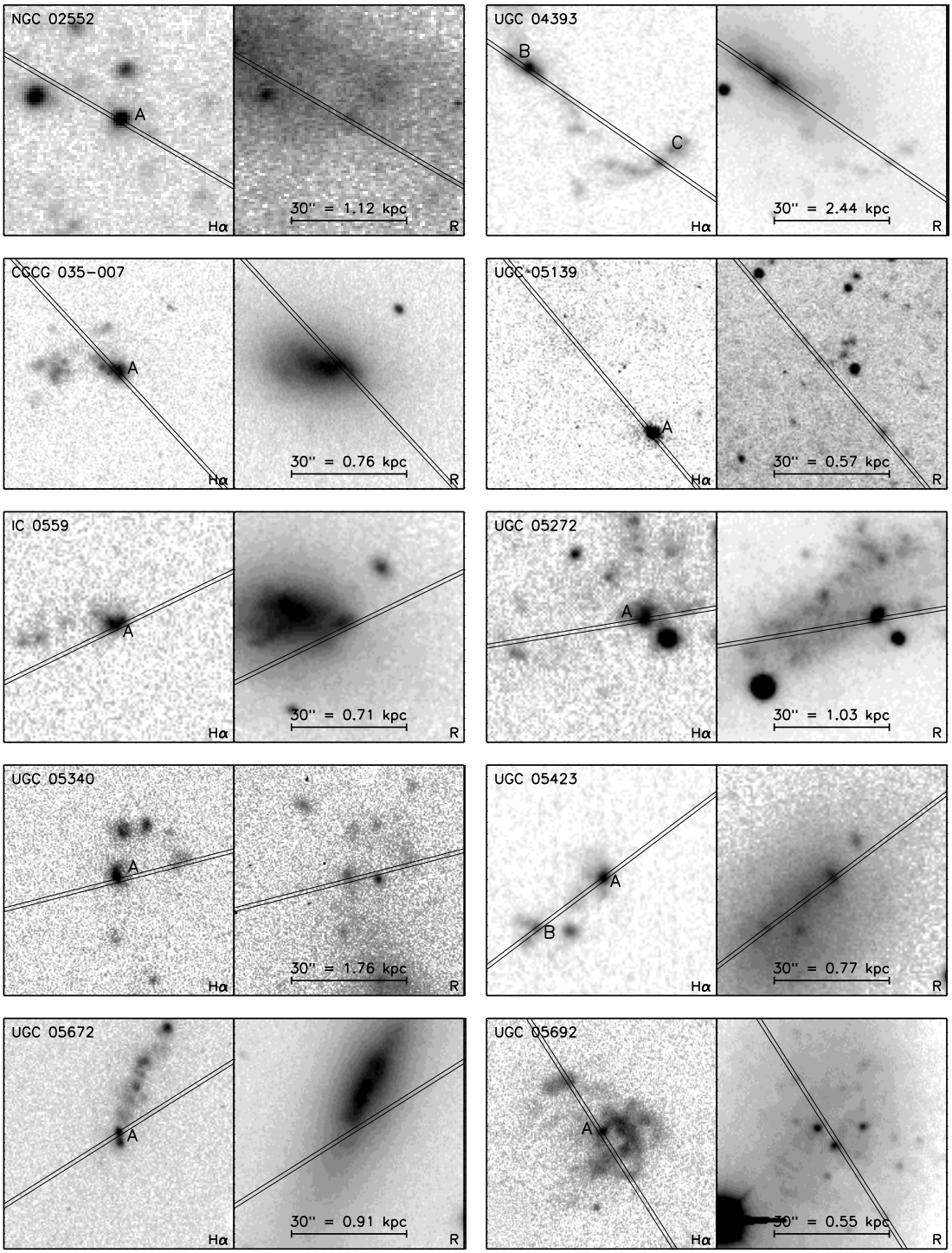
NGC 02552
A
30'' = 1.12 kpc
Hα
R
UGC 04393
B
C
30'' = 2.44 kpc
Hα
R
CGCG 035−007
A
30'' = 0.76 kpc
Hα
R
UGC 05139
A
30'' = 0.57 kpc
Hα
R
IC 0559
A
30'' = 0.71 kpc
Hα
R
UGC 05272
A
30'' = 1.03 kpc
Hα
R
UGC 05340
A
30'' = 1.76 kpc
Hα
R
UGC 05423
A
B
30'' = 0.77 kpc
Hα
R
UGC 05672
A
30'' = 0.91 kpc
Hα
R
UGC 05692
A
30'' = 0.55 kpc
Hα
R

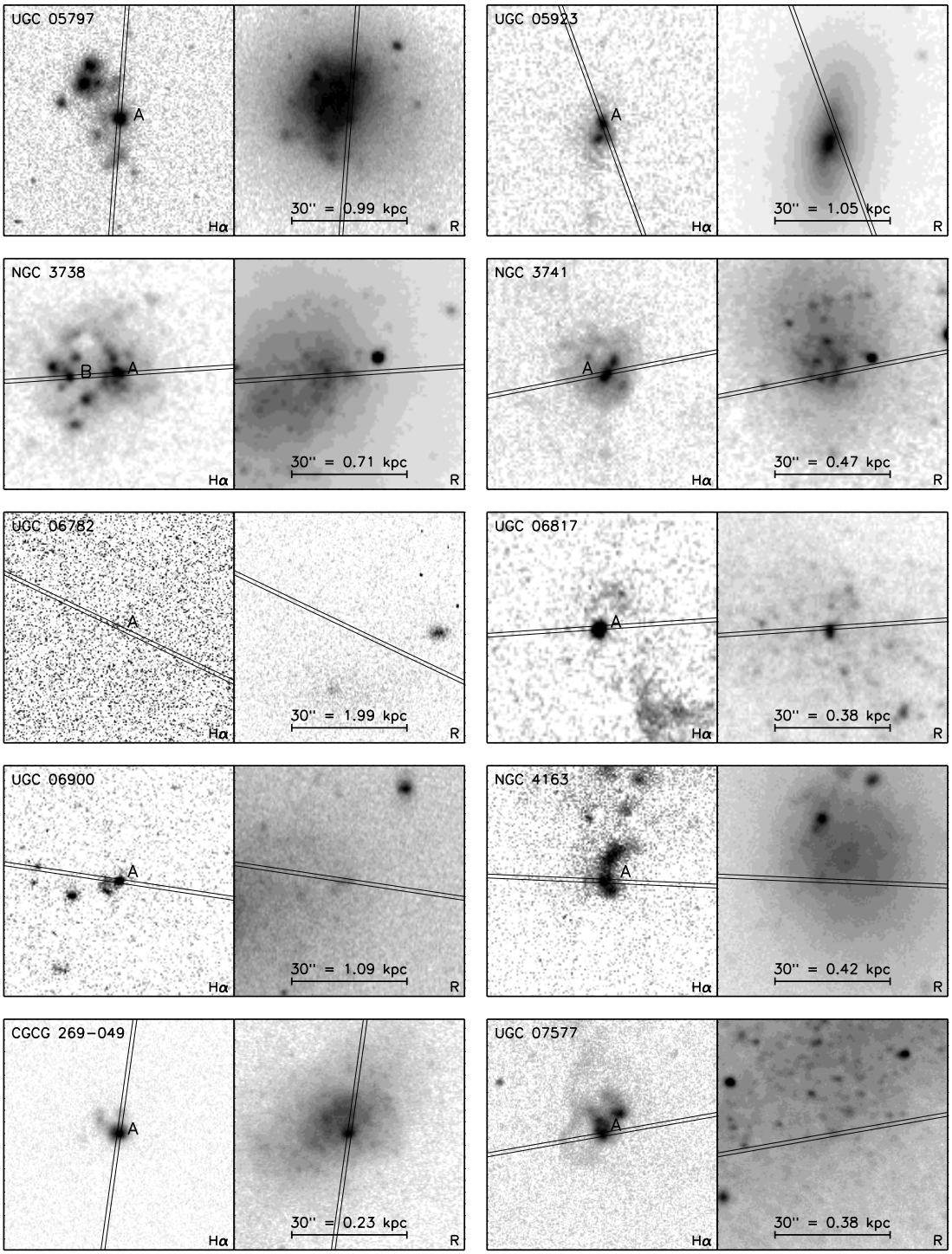
UGC 05797
A
Hα
30'' = 0.99 kpc
R
UGC 05923
A
Hα
30'' = 1.05 kpc
R
NGC 3738
B
A
Hα
30'' = 0.71 kpc
R
NGC 3741
A
Hα
30'' = 0.47 kpc
R
UGC 06782
A
Hα
30'' = 1.99 kpc
R
UGC 06817
A
Hα
30'' = 0.38 kpc
R
UGC 06900
A
Hα
30'' = 1.09 kpc
R
NGC 4163
A
Hα
30'' = 0.42 kpc
R
CGCG 269-049
A
Hα
30'' = 0.23 kpc
R
UGC 07577
A
Hα
30'' = 0.38 kpc
R

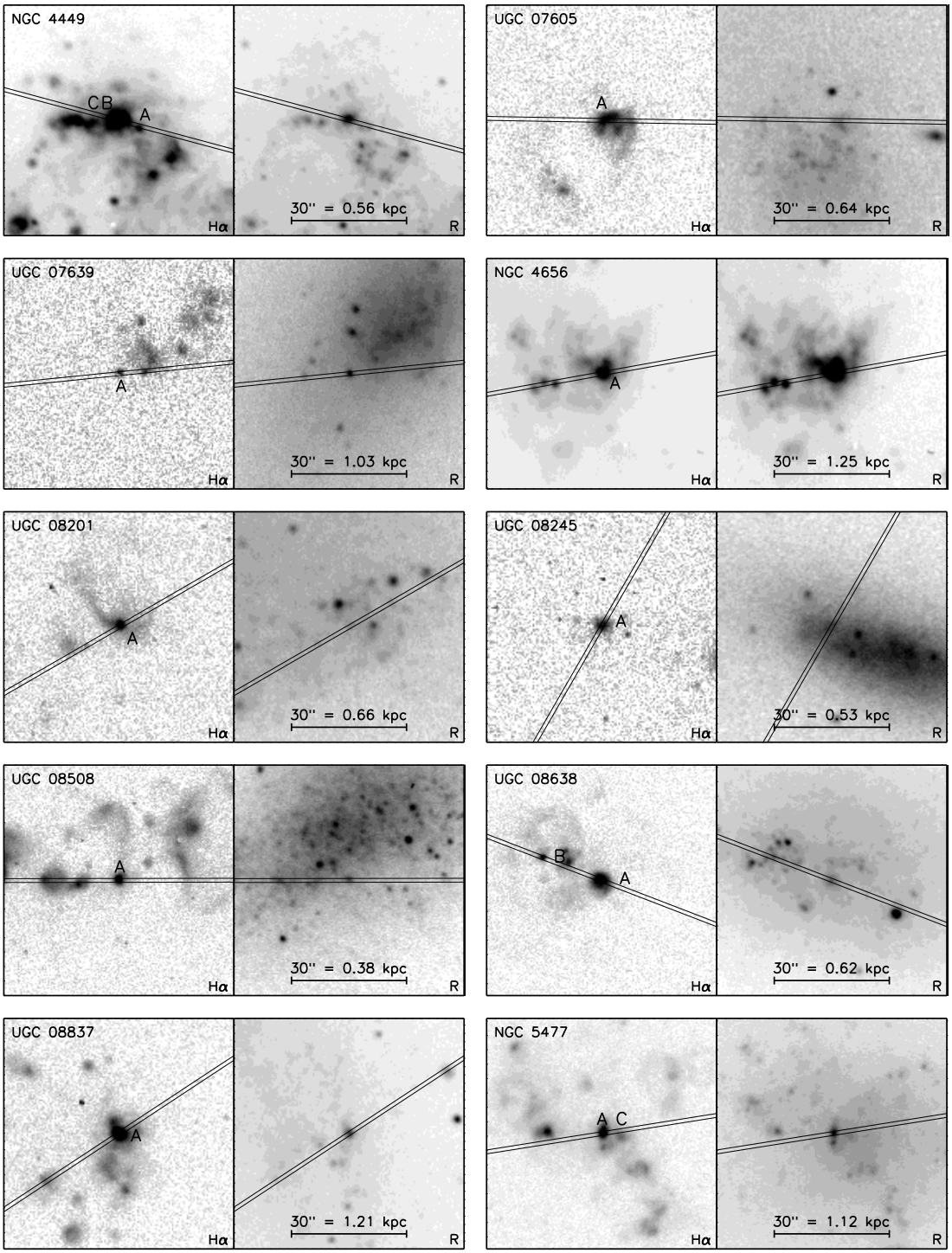
NGC 4449
C B
A
Hα
30'' = 0.56 kpc
R
UGC 07605
A
Hα
30'' = 0.64 kpc
R
UGC 07639
A
Hα
30'' = 1.03 kpc
R
NGC 4656
A
Hα
30'' = 1.25 kpc
R
UGC 08201
A
Hα
30'' = 0.66 kpc
R
UGC 08245
A
Hα
30'' = 0.53 kpc
R
UGC 08508
A
Hα
30'' = 0.38 kpc
R
UGC 08638
B
A
Hα
30'' = 0.62 kpc
R
UGC 08837
A
Hα
30'' = 1.21 kpc
R
NGC 5477
A C
Hα
30'' = 1.12 kpc
R

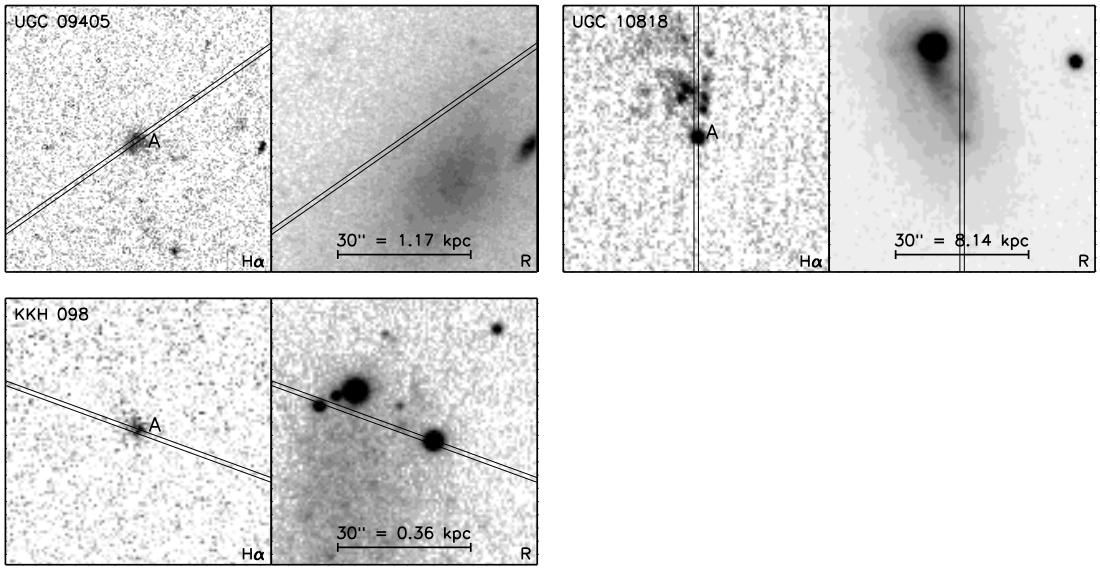

Figure 3.1: Hα and R-band images of the objects in the present low-luminosity LVL sample. The angular scale of the images is $60'' \times 60''$with North directly up and East to the left. The line across the images represents the slit position during observation. The brightest H II regions are labeled with letters. See Table 1 for more details.

zero point flux in Janksys for the 4.5 μm IRAC band (Reach et al., 2005). Distances are taken from the literature, as described in Table 5.1, and assumed to have 10% uncertainty where none were provided. IRAC calibration uncertainties are $5 - 10\%$ for the 4.5 μm data. Later, in Section 3.5.4, we use these $M_{[4.5]}$ magnitudes to analyze the NIR luminosity-metallicity relationship. Similarly, M_{K_S} values were determined by Dale et al. (2009) from 2MASS imaging, where 666.7 is the zero point flux in Janksys for the 2MASS K_S band. Although 2MASS F_{K_S} values are available for those objects which Dale et al. (2009) don't provide K_S magnitudes, we choose not to use them. The small apertures used in the 2MASS extraction produce unexpectedly faint magnitudes for smaller galaxies when compared to similar extractions from IRAC 3.6 and 4.5 μm data (see, e.g., Figures 4 and 5 in Dale et al., 2009), and so may not be terribly accurate for our sample. The K_S magnitudes were used to determine stellar masses in Section 3.5.4.

Finally, V-band magnitudes were needed to calculate $B - V$ colors (see Table 5.1). When available, M_V values were provided by van Zee et al. (2013), using the LVL elliptical aperture. In other cases, values are taken from de Vaucouleurs et al. (1991) or

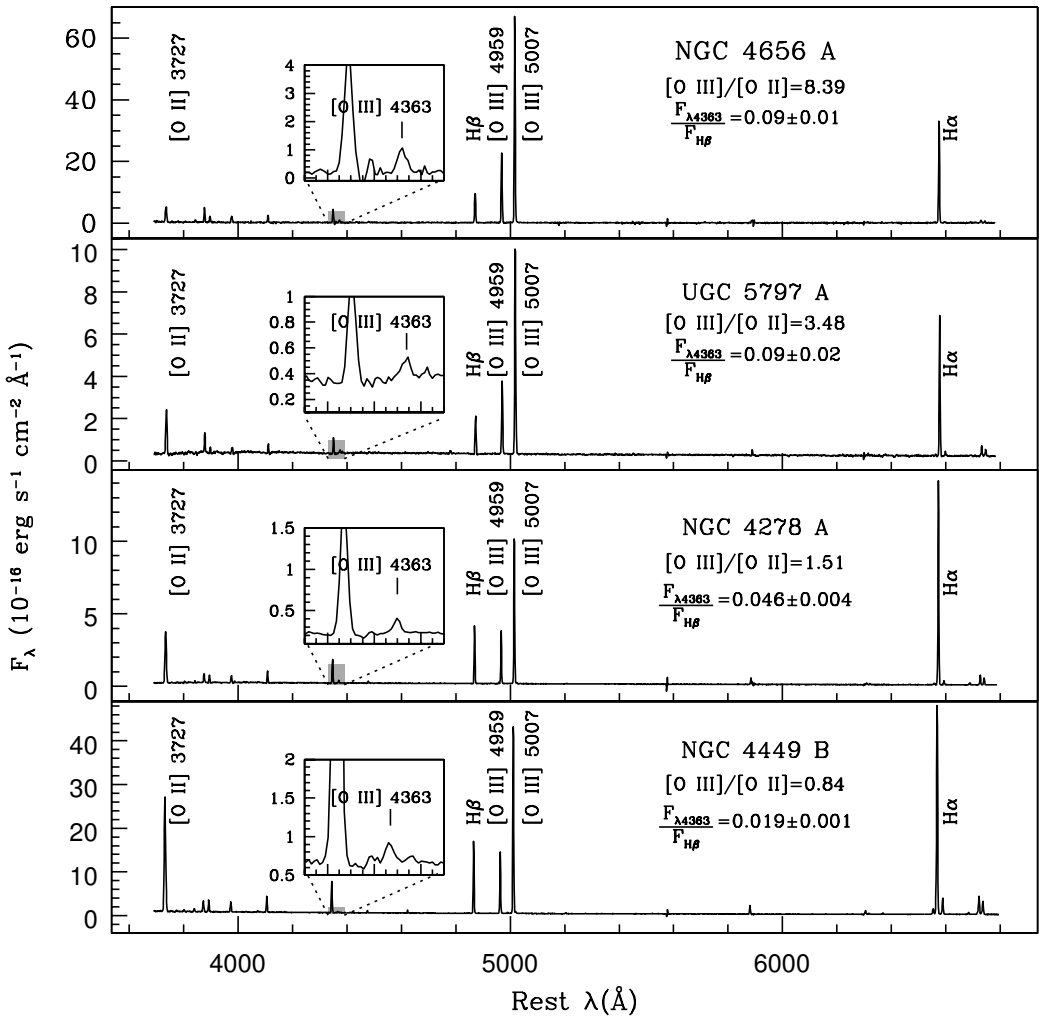

Figure 3.2: Four sample spectra representative of the low-luminosity LVL sample presented in this paper. The full spectral range of these high-quality, high signal-to-noise observations is shown. The inset windows expand the region around the intrinsically faint [O III] λ4363 line used to determine T_e. Note that the much stronger line blueward of [O III] λ4363 is Hγ λ4340. These spectra demonstrate the range in ionization field strength seen for this sample, ranging from low ionization in the bottom panel (NGC 5477) to high ionization in the top panel (UGC 4656).

are determined using g- and r-band photometry available from the Sloan Digital Sky Survey (SDSS; York et al., 2000). The SDSS values are then used to estimate the $B-V$ color following Jester et al. (2005):

$$B - V = \frac{(g - r) + 0.22}{1.02}. \tag{3.2}$$

The available M_B, $M_{[4.5]}$, and $B - V$ colors and references for this sample are listed in Table 5.1. Note that the main source of uncertainty in these magnitudes lies in the distance determinations. Eight of the objects in our sample have distance errors of approximately 10%. Furthermore, 20 of the 44 objects in our sample do not have uncertainties associated with their distance determinations. For these objects we used an uncertainty of 10%, which may be an underestimate for some of them. The distance uncertainties tend to dominate over the photometric uncertainties.

3.3 Nebular Abundance Analysis

3.3.1 Emission Line Measurements

A discussion of the emission line measurements can be found in Appendix B. Special attention was paid to the Balmer lines for this study, are they are located in troughs of significant underlying stellar absorption for some of our objects. The Hα emission lines typically had equivalent widths of $\sim$ 350 Å, large enough that the underlying absorption was not a concern. Even for those Hα emission lines with lower EWs, the underlying absorption was negligible. This was often not the case for Hβ and the lower equivalent width Balmer lines. The Hβ absorption EWs for our sample range from 1-8 Å. These values are typical of local low-luminosity galaxies, with the majority having Hβ absorption EWs between 0 Å and 5 Å (see, e.g., Figure 6 in Chapter 2). For the bluer Balmer lines, a multiple component fit was used in which the absorption was fit by a broad, negative Lorentzian profile and the emission was fit by a narrow, positive Gaussian profile. To ensure a proper fit of the [O III] λ4363 line, Hγ was first fit by a Gaussian profile, then [O III] λ4363 was forced to be fit to the same line profile with the assumption that the profile widths of these two neighboring lines should be the same.

Note that we chose to fit the underlying Balmer absorption with Lorentzian profiles, as opposed to using stellar population synthesis continuum fitting common in many studies (e.g., Tremonti et al., 2004). Given the large equivalent widths of the Balmer emission lines, the differences between the two methods are negligible, and the Lorentzian profiles have the advantage of require no additional assumptions. Most importantly, for spectra dominated by young stars, at S/N values typical of our spectra, population synthesis models may not provide a unique solution. There are also very large variations in the population synthesis models for young ages, with large uncertainties in how the Wolfe-Rayet phase, stellar winds, rotation, and other parameters are treated. Since mass loss and mixing processes in stellar evolution are still poorly understood, stellar phases, like Wolf-Rayet stars or Red Super Giants, are particularly affected by such uncertainties (Leitherer & Ekstrom, 2011). Later phases, like AGB stars, are covered only crudely in models or not at all, pushing parameters into regimes that are not properly calibrated. When discrepancies between models are found, they can usually be attributed to different intrinsic input parameters and/or treatment of these aberrant stellar evolutionary phases (Vázquez & Leitherer, 2005; Conroy & Gunn, 2010). By not using the models to fit our continuum, we avoid the uncertainties associated with these implicit assumptions.

31 of the 44 galaxies in our sample were measured to have [O III] λ4363 line strengths $> 4\sigma$. The measured [O III] λ4959/λ5007 ratios match theoretical expectations within the errors, supporting our error estimates and the assumption that the continuum subtraction dominates the uncertainties for the weak lines. For all the objects in the present sample, flux line strengths and corresponding errors are listed in Table 5.3. We concentrate the rest of our analysis on the objects for which direct electron temperature and chemical abundance determinations can be made. An analysis of the remaining spectra using strong-line methods is reported in Section 2.9: Appendix A.

3.3.2 Reddening Corrections

The detailed steps used for reddening corrections are listed in Appendix B. The resulting Balmer ratios are within errors of the Hummer & Storey (1987) Case B values for all objects meeting the selection criteria of our "Select" sample (see § 3.5.1), with an average of $\chi^2 = 0.03$. Our reddening corrections are tabulated in Table 5.3.

Table 3.3: Emission-Lines for the Low-Luminosity LVL Galaxies ($I(\lambda)/I(H\beta)$)

	$I(\lambda)/I(\mathrm{H}\beta)$									
Ion	UGC 521 A	UGC 695 E	UGC 1056 A	UGC 1056 B	UGC 1176 A	NGC 784 A	NGC 784 B	UGC 2716 A	KKH 037 A	NGC 2537 A
[O II] λ3727	1.59±0.03	3.25±0.07	3.32±0.13	2.80±0.06	2.27±0.05	2.19±0.06	2.61±0.07	2.08±0.04	6.51±0.08	3.42±0.07
He I λ3820	···	···	···	···	···	···	···	···	···	···
H9 λ3835	0.07±0.02	0.11±0.01	···	···	0.07±0.01	0.04±0.01	0.07±0.01	0.08±0.02	···	···
[Ne III] λ3868	0.33±0.02	0.19±0.01	0.27±0.04	0.30±0.02	0.28±0.01	0.33±0.01	0.29±0.01	0.38±0.02	···	0.15±0.01
He I+H8 λ3889	0.17±0.02	0.25±0.01	0.17±0.03	0.24±0.02	0.19±0.01	0.18±0.01	0.23± 0.01	0.26±0.01	···	0.17±0.01
[Ne III]+H7 λ3968	0.34±0.02	0.36±0.01	0.37± 0.02	0.54±0.02	0.59±0.01	0.20±0.01	0.51± 0.01	0.32±0.01	···	0.30±0.01
He I λ4026	···	···	···	···	···	···	···	···	···	0.025±0.003
[S II] λ4068	···	0.03±0.02	···	···	···	···	···	···	···	···
Hδ λ4101	0.26±0.02	0.29±0.02	0.27±0.02	0.26±0.01	0.26±0.01	0.264±0.006	0.59±0.01	0.27±0.01	···	0.27±0.01
Hγ λ4340	0.48±0.01	0.53±0.01	0.49±0.01	0.50±0.01	0.46±0.01	0.460±0.009	0.48±0.01	0.51±0.01	0.47±0.20	0.47±0.01
[O III] λ4363	0.09±0.01	0.04±0.01	0.04±0.01	0.04±0.01	0.05±0.01	0.051±0.005	0.05±0.01	0.06±0.01	···	0.012±0.002
He I λ4471	···	···	···	···	···	0.036±0.005	0.03±0.01	0.038±0.005	···	0.042±0.002
[Fe III] λ4658	···	···	···	···	···	···	···	···	···	···
He II λ4686	···	···	···	···	···	···	···	···	···	···
Hβ λ4861	1.00±0.01	1.00±0.02	1.00±0.01	1.00±0.02	1.00±0.02	1.00±0.02	1.00±0.04	1.00±0.02	1.00±0.17	1.00±0.02
[O III] λ4959	1.21±0.02	0.54±0.01	0.78±0.01	1.09±0.02	1.20±0.02	1.37±0.03	1.12±0.02	1.43±0.03	···	0.71±0.01
[O III] λ5007	3.64±0.07	1.62±0.03	2.35±0.05	3.27±0.07	3.61±0.07	4.13±0.08	3.32±0.07	4.26±0.09	0.53±0.15	2.14±0.04
[N I] λ5199	···	···	···	···	···	···	0.013±0.003	···	···	···
He I λ5876	0.08±0.01	0.10±0.01	0.13±0.01	0.11±0.01	0.097±0.004	0.111±0.003	0.095±0.005	0.113±0.004	···	0.12±0.03
[O I] λ6300	0.02±0.01	0.07±0.01	0.07±0.01	0.04±0.01	0.012±0.005	0.051±0.002	0.031±0.003	0.034±0.003	···	0.045±0.002
[S III] λ6312	0.03±0.01	···	···	0.02±0.01	0.019±0.005	0.020±0.002	0.015±0.003	0.022±0.003	···	0.016±0.002
[O I] λ6363	0.01±0.01	0.03±0.01	0.02±0.01	0.13±0.01	···	0.022±0.002	0.016±0.003	0.011±0.003	···	0.013±0.002
[N II] λ6548	···	0.034±0.009	0.05±0.01	0.04±0.01	0.032±0.003	0.036±0.002	0.020±0.003	0.031±0.003	···	0.15±0.01
Hα λ6563	2.77±0.06	2.86±0.06	2.80±0.11	2.82±0.06	2.82±0.06	2.89±0.07	2.81±0.07	2.86±0.06	2.80±0.14	2.87±0.07
[N II] λ6584	0.05±0.01	0.125±0.009	0.14±0.01	0.12±0.01	0.122±0.003	0.109±0.003	0.080±0.003	0.092±0.003	0.14±0.12	0.48±0.01
He I λ6678	0.02±0.01	···	0.04±0.01	0.029±0.004	0.028±0.004	0.027±0.002	0.025±0.003	0.034±0.003	···	0.030±0.002
[S II] λ6717	0.11±0.01	0.434±0.009	0.40±0.02	0.26±0.01	0.17±0.01	0.203±0.004	0.144±0.004	0.196±0.004	0.38±0.10	0.36±0.01
[S II] λ6731	0.07±0.01	0.274±0.009	0.31±0.02	0.17±0.01	0.12±0.01	0.150±0.003	0.103±0.003	0.137±0.003	0.27±0.10	0.27±0.01
C(Hβ)	0.00±0.01	0.17±0.01	0.23±0.05	0.28±0.01	0.22±0.01	0.43±0.02	0.41±0.02	0.29±0.02	0.63±0.04	0.43±0.02
F(Hβ)	8.69±0.07	13.5±0.3	9.75±0.11	20.8±0.42	19.3±0.4	22.6±0.5	29.1±1.2	24.2±0.5	0.51±0.09	117±2
EW(Hβ)	30.7	21.4	19.9	25.4	129	70.1	63.7	46.6	5.9	70.1
EW(Hα)	130.	112	96.0	134	622	467	386	269	33.3	339

TABLE 3—*Continued*

	$I(\lambda)/I(\mathrm{H}\beta)$								
Ion	NGC 2537 B	UGC 4278 B	UGC 4278 A	NGC 2552 A	UGC 4393 B	UGC 4393 C	CGCG 035-007 A	UGC 5139 A	IC 559 A
[O II] λ3727	2.79±0.06	2.03±0.04	1.68±0.04	2.39±0.05	2.60±0.06	4.06±0.09	4.00±0.09	1.88±0.04	3.12±0.06
He I λ3820	···	···	···	···	···	···	···	···	···
H9 λ3835	···	0.12±0.01	0.07±0.01	···	0.08±0.01	0.05±0.01	···	0.05±0.01	···
[Ne III] λ3868	0.11±0.01	0.17±0.01	0.20±0.01	0.25±0.01	0.27±0.01	0.26±0.01	···	0.30±0.01	0.25±0.02
He I+H8 λ3889	0.20±0.01	0.27±0.01	0.19±0.01	0.24±0.01	0.15±0.01	0.21±0.01	···	0.19±0.01	0.16±0.01
[Ne III]+H7 λ3968	0.15±0.01	0.43±0.01	0.23±0.01	0.50±0.01	0.39±0.01	0.24±0.01	···	0.24±0.01	0.16±0.01
He I λ4026	0.024±0.007	···	···	···	···	0.016±0.006	···	0.03±0.01	···
[S II] λ4068	0.018±0.007	0.06±0.01	0.022±0.005	0.02±0.01	···	0.040±0.005	···	···	···
Hδ λ4101	0.27±0.01	0.25±0.01	0.24±0.01	0.25±0.01	0.26±0.01	0.27±0.01	0.24±0.02	0.25±0.01	0.270±0.008
Hγ λ4340	0.44±0.01	0.46±0.01	0.44±0.01	0.47±0.01	0.47±0.01	0.48±0.01	0.46±0.02	0.48±0.01	0.451±0.008
[O III] λ4363	0.016±0.004	0.033±0.005	0.046±0.004	0.021±0.003	0.034±0.008	0.036±0.005	0.06±0.02	0.051±0.008	0.028±0.008
He I λ4471	0.040±0.004	0.026±0.005	0.032±0.004	0.028±0.003	0.05±0.01	0.039±0.005	···	···	0.025±0.007
[Fe III] λ4658	···	···	···	···	···	···	···	···	···
He II λ4686	···	···	···	···	···	···	···	···	···
Hβ λ4861	1.00±0.02	1.00±0.02	1.00±0.02	1.00±0.02	1.00±0.02	1.00±0.02	1.00±0.02	1.00±0.02	1.00±0.02
[O III] λ4959	0.60±0.01	0.63±0.01	0.83±0.02	0.97±0.02	1.10±0.02	0.86±0.04	0.68±0.01	1.24±0.03	0.93±0.02
[O III] λ5007	1.78±0.04	1.91±0.04	2.53±0.05	2.91±0.06	3.28±0.07	2.59±0.05	2.03±0.04	3.66±0.07	2.80±0.06
[N I] λ5199	···	···	0.007±0.002	0.013±0.002	···	···	···	···	···
He I λ5876	0.112±0.002	0.08±0.01	0.096±0.004	0.10±0.01	0.12±0.01	0.11±0.01	0.079±0.013	···	0.09±0.01
[O I] λ6300	0.021±0.002	0.03±0.01	0.026±0.004	0.037±0.002	0.055±0.005	0.084±0.005	···	0.04±0.01	···
[S III] λ6312	0.013±0.002	0.013±0.006	0.013±0.004	0.015±0.002	0.011±0.005	0.017±0.005	···	0.02±0.01	···
[O I] λ6363	0.005±0.002	0.008±0.006	0.005±0.004	0.012±0.002	0.016±0.004	0.024±0.004	···	0.06±0.01	···
[N II] λ6548	0.128±0.003	0.017±0.004	0.017±0.003	0.08±0.01	0.092±0.004	0.096±0.003	0.06±0.01	0.02±0.01	0.034±0.014
Hα λ6563	2.79±0.06	2.80±0.06	2.86±0.06	2.86±0.06	2.86±0.06	2.87±0.07	2.84±0.06	2.83±0.06	2.86±0.06
[N II] λ6584	0.41±0.01	0.060±0.004	0.054±0.003	0.25±0.01	0.30±0.01	0.31±0.01	0.21±0.01	0.07±0.01	0.15±0.01
He I λ6678	0.030±0.002	0.027±0.004	0.027±0.002	0.025±0.002	0.029±0.003	0.025±0.002	···	0.029±0.006	···
[S II] λ6717	0.26±0.01	0.18±0.01	0.140±0.003	0.34±0.01	0.28±0.01	0.39±0.01	0.49±0.01	0.136±0.006	0.35±0.02
[S II] λ6731	0.184±0.004	0.13±0.01	0.103±0.002	0.25±0.01	0.19±0.01	0.28±0.01	0.33±0.01	0.092±0.006	0.23±0.02
C(Hβ)	0.28±0.01	0.10±0.01	0.31±0.02	0.14±0.01	0.27±0.02	0.34±0.02	0.16±0.01	0.085±0.010	0.30±0.02
F(Hβ)	80.0±1.6	8.93±0.17	15.9±0.32	37.0±0.7	24.2±0.5	19.3±0.4	11.3±0.2	6.40±0.13	21.3±0.4
EW(Hβ)	47.8	64.2	82.7	55.3	22.0	160	16.5	197	49.7
EW(Hα)	188	321	478	312	113	922	72.3	939	273

TABLE 3—*Continued*

	$I(\lambda)/I(\mathrm{H}\beta)$								
Ion	UGC 5272 A	UGC 5340 A	UGC 5423 A	UGC 5423 B	UGC 5672 A	UGC 5692 A	UGC 5797 A	UGC 5923 A	NGC 3741 A
[O II] λ3727	1.06±0.02	0.58±0.02	2.08±0.04	1.78±0.04	3.28±0.04	2.47±0.06	1.59±0.03	4.06±0.11	1.60±0.03
He I λ3820	0.014±0.002	···	···	···	···	···	···	···	···
H9 λ3835	0.084±0.002	0.05±0.01	0.12±0.01	···	···	···	0.27±0.04	0.18±0.03	···
[Ne III] λ3868	0.375±0.007	0.16±0.01	0.33±0.01	0.28±0.02	0.20±0.04	0.21±0.05	0.52±0.04	0.24±0.03	0.24±0.01
He I+H8 λ3889	0.197±0.004	0.17±0.01	0.24±0.01	0.32±0.02	0.16±0.04	0.24±0.05	0.36±0.03	0.33±0.03	0.21±0.01
[Ne III]+H7 λ3968	0.194±0.004	0.47± 0.01	0.28±0.01	0.50±0.02	0.19±0.04	···	0.32±0.03	0.20±0.03	0.49±0.01
He I λ4026	0.015±0.003	···	···	···	···	···	···	···	···
[S II] λ4068	···	···	0.03±0.01	···	···	···	···	···	···
Hδ λ4101	0.26±0.01	0.25±0.01	0.26±0.01	0.26±0.02	0.25±0.03	0.22±0.04	0.28±0.02	0.24±0.02	0.25±0.01
Hγ λ4340	0.46±0.01	0.47±0.01	0.46±0.01	0.46±0.01	0.42±0.03	0.54±0.03	0.47±0.02	0.51±0.02	0.46±0.01
[O III] λ4363	0.083±0.002	0.06±0.01	0.070±0.004	0.07±0.01	0.04±0.02	0.06±0.03	0.09±0.02	0.06±0.01	0.06±0.01
He I λ4471	0.036±0.002	0.04±0.01	0.033±0.004	···	···	···	···	···	0.026±0.003
[Fe III] λ4658	···	···	···	···	···	···	···	···	···
He II λ4686	···	0.024±0.002	0.019±0.002	···	···	···	0.036±0.006	···	···
Hβ λ4861	1.00±0.02	1.00±0.02	1.00±0.02	1.00±0.02	1.00±0.02	1.00±0.02	1.00±0.02	1.00±0.02	1.00±0.02
[O III] λ4959	1.66±0.03	0.64±0.01	1.16±0.02	1.24±0.02	0.85±0.02	0.57±0.02	1.85±0.04	0.84±0.02	0.94±0.02
[O III] λ5007	4.94±0.10	1.89±0.04	3.49±0.01	3.71±0.07	2.51±0.05	1.70±0.03	5.53±0.11	2.48±0.05	2.84±0.06
[N I] λ5199	···	···	0.012±0.004	···	···	···	···	···	···
He I λ5876	0.101±0.001	0.09±0.01	0.10±0.01	0.11±0.01	0.11±0.01	0.14±0.03	0.09±0.01	···	0.097±0.003
[O I] λ6300	0.013±0.001	···	0.080±0.004	0.02±0.01	0.04±0.01	···	0.05±0.02	0.06±0.01	0.022±0.002
[S III] λ6312	0.020±0.001	···	0.021±0.004	0.02±0.01	···	···	0.02±0.02	0.02±0.01	0.018±0.002
[O I] λ6363	0.004±0.001	···	0.020±0.004	0.01±0.01	···	···	0.05±0.02	0.02±0.01	0.004±0.002
[N II] λ6548	0.010±0.001	···	0.035±0.004	0.026±0.009	0.12±0.02	0.10±0.02	0.03±0.01	0.07±0.01	0.017±0.003
Hα λ6563	2.83±0.06	2.81±0.06	2.86±0.06	2.86±0.06	2.87±0.07	2.79±0.06	2.84±0.06	2.78±0.07	2.83±0.06
[N II] λ6584	0.035±0.001	0.016±0.003	0.120±0.004	0.082±0.009	0.23±0.02	0.38±0.02	0.09±0.01	0.24±0.01	0.051±0.003
He I λ6678	0.029±0.002	0.023±0.007	0.027±0.003	0.029±0.007	···	···	···	0.03±0.01	0.026±0.002
[S II] λ6717	0.079±0.002	0.05±0.007	0.31±0.006	0.153±0.007	0.31±0.01	0.61±0.02	0.22±0.01	0.31±0.01	0.122±0.002
[S II] λ6731	0.055±0.002	0.05±0.007	0.22±0.006	0.110±0.007	0.22±0.01	0.40±0.02	0.15±0.01	0.22±0.01	0.088±0.002
C(Hβ)	0.08±0.01	0.00±0.01	0.24±0.01	0.29±0.02	0.40±0.02	0.25±0.01	0.15±0.01	0.51±0.02	0.10±0.01
$F(\mathrm{H}\beta)$	101±2	13.6±0.27	22.8±0.46	9.38±0.19	5.80±0.12	4.71±0.10	8.40±0.17	20.2±0.40	45.0±0.9
EW(Hβ)	201	99.2	94.8	51.4	14.6	24.3	23.8	16.0	59.9
EW(Hα)	943	549	438	247	67.4	120	111	75.3	330

TABLE 3—*Continued*

	$I(\lambda)/I(\mathrm{H}\beta)$								
Ion	NGC 3738 A	NGC 3738 B	UGC 6817 A	UGC 6900 A	NGC 4163 A	CGCG 269-049 C	CGCG 269-049 A	UGC 7577 A	NGC 4449 C
[O II] λ3727	2.91±0.06	3.45±0.07	0.94±0.02	4.13±0.27	3.72±0.07	1.76±0.04	1.02±0.02	1.65±0.03	3.26±0.07
He I λ3820	···	···	···	···	···	···	···	···	···
H9 λ3835	···	···	0.08±0.01	···	···	···	0.09±0.02	0.06±0.02	0.04±0.01
[Ne III] λ3868	0.28±0.01	0.31±0.04	0.25±0.01	···	···	···	0.20±0.02	0.47±0.02	0.19±0.01
He I+H8 λ3889	0.11±0.01	0.32±0.04	0.19±0.01	···	···	···	0.16±0.02	0.20±0.02	0.17± 0.01
[Ne III]+H7 λ3968	0.39±0.01	0.24±0.04	0.53±0.01	···	···	···	0.44±0.01	0.34±0.02	0.19± 0.01
He I λ4026	···	···	···	···	···	···	···	···	···
[S II] λ4068	···	···	···	···	···	···	···	···	···
Hδ λ4101	0.23±0.01	0.24±0.02	0.26±0.01	0.31±0.09	0.17±0.03	0.20±0.06	0.26±0.01	0.25±0.02	0.26±0.01
Hγ λ4340	0.47±0.01	0.45±0.01	0.46±0.01	0.55±0.06	0.31±0.04	0.29±0.06	0.46±0.01	0.47±0.01	0.45±0.01
[O III] λ4363	0.031±0.006	0.04±0.01	0.068±0.002	···	0.014±0.003	0.05±0.01	0.062±0.003	0.08±0.01	0.018±0.004
He I λ4471	0.03±0.01	···	0.033±0.002	···	···	···	0.030±0.003	0.04±0.01	···
[Fe III] λ4658	···	···	···	···	···	···	···	···	···
He II λ4686	···	···	···	···	···	···	···	···	···
Hβ λ4861	1.00±0.02	1.00±0.02	1.00±0.02	1.00±0.11	1.00±0.02	1.00±0.05	1.00±0.02	1.00±0.02	1.00±0.02
[O III] λ4959	0.98±0.02	1.03±0.02	0.97±0.02	0.23±0.10	0.18±0.02	0.52±0.04	0.84±0.02	1.86±0.04	0.77±0.02
[O III] λ5007	2.96±0.06	3.11±0.06	2.89±0.06	0.60±0.10	0.49±0.02	1.53±0.04	2.51±0.05	5.25±0.11	2.33±0.05
[N I] λ5199	0.011±0.005	···	···	···	···	···	···	···	0.017±0.003
He I λ5876	0.12±0.01	0.15±0.02	0.100±0.002	···	0.10±0.02	···	0.097±0.003	0.11±0.02	0.12±0.01
[O I] λ6300	0.05±0.01	0.06±0.01	0.015±0.002	···	0.07±0.02	···	0.008±0.003	···	0.071±0.004
[S III] λ6312	0.02±0.01	···	0.015±0.002	···	···	···	0.012±0.003	···	0.014±0.004
[O I] λ6363	0.02±0.01	0.02±0.01	0.004±0.002	0.29±0.11	···	···	0.003±0.001	···	0.024±0.004
[N II] λ6548	0.06±0.01	0.06±0.01	0.008±0.001	0.16±0.10	0.04±0.02	0.02±0.04	0.010±0.001	0.03±0.01	0.074±0.003
Hα λ6563	2.83±0.06	2.82±0.06	2.83±0.06	2.83±0.10	2.75±0.06	2.79±0.06	2.83±0.06	2.79±0.06	2.84±0.06
[N II] λ6584	0.19±0.01	0.20±0.01	0.03±0.01	0.52±0.10	0.13±0.02	···	0.033±0.003	0.09±0.01	0.23±0.01
He I λ6678	0.03±0.01	···	0.026±0.002	···	···	···	0.024±0.002	0.03±0.01	0.020±0.003
[S II] λ6717	0.3 2±0.01	0.29±0.01	0.068±0.002	1.11±0.09	0.35±0.02	···	0.064±0.002	0.20±0.01	0.35±0.01
[S II] λ6731	0.23±0.01	0.21±0.01	0.049±0.002	0.64±0.09	0.23±0.02	···	0.046±0.002	0.15±0.01	0.25±0.01
C(Hβ)	0.04±0.01	0.19±0.01	0.06±0.01	0.09± 0.01	0.10±0.01	0.16±0.01	0.08±0.01	0.05±0.01	0.14±0.01
F(Hβ)	58.7±1.2	24.8±0.5	42.3±0.8	1.49±0.17	5.24±0.12	1.71±0.08	29.1±0.6	12.5±0.3	54.8±1.1
EW(Hβ)	35.2	23.4	146	20.0	9.21	6.8	81.3	216	119
EW(Hα)	183	121	834	75.5	40.9	37.2	434	854	437

TABLE 3—*Continued*

	$I(\lambda)/I(\mathrm{H}\beta)$								
Ion	NGC 4449 B	NGC 4449 A	UGC 7605 A	UGC 7639 A	NGC 4656 A	UGC 8201 A	UGC 8245 A	UGC 8508 A	UGC 8638 A
[O II] λ3727	3.04±0.07	2.39±0.05	1.91±0.04	3.98±0.12	0.80±0.03	1.62±0.03	2.81±0.06	1.47±0.03	1.77±0.04
He I λ3820	···	0.008±0.004	···	···	···	···	···	···	···
H9 λ3835	0.05±0.01	0.062±0.004	···	···	0.08±0.02	···	···	···	···
[Ne III] λ3868	0.19±0.01	0.23±0.01	0.18±0.02	···	0.50±0.02	0.25±0.01	···	0.29±0.02	0.32±0.01
He I+H8 λ3889	0.19±0.01	0.167±0.004	0.15±0.02	···	0.19±0.02	0.23±0.01	···	0.26±0.02	0.22±0.01
[Ne III]+H7 λ3968	0.19±0.01	0.187±0.004	0.18±0.02	···	0.29±0.02	0.19±0.01	···	0.49± 0.02	0.59±0.01
He I λ4026	···	0.016±0.001	···	···	···	···	···	···	···
[S II] λ4068	···	0.014±0.001	···	···	···	···	···	···	···
Hδ λ4101	0.25±0.01	0.26±0.01	0.25±0.02	0.28±0.05	0.25±0.02	0.26±0.01	0.24±0.02	0.24±0.02	0.26±0.01
Hγ λ4340	0.48±0.01	0.47±0.01	0.46±0.01	0.44±0.07	0.45±0.01	0.47±0.01	0.41±0.02	0.45±0.01	0.45±0.01
[O III] λ4363	0.018±0.003	0.019±0.001	0.04±0.01	0.05±0.05	0.09±0.01	0.05±0.01	0.03±0.02	0.06±0.01	0.055±0.003
He I λ4471	0.032±0.003	0.039±0.001	0.02±0.01	···	···	0.05±0.01	···	0.03±0.01	0.039±0.002
[Fe III] λ4658	···	···	···	···	···	···	···	···	···
He II λ4686	···	···	···	···	···	···	0.05±0.01	···	···
Hβ λ4861	1.00±0.02	1.00±0.02	1.00±0.02	1.00±0.05	1.00±0.02	1.00±0.02	1.00±0.02	1.00±0.02	1.00±0.02
[O III] λ4959	0.84±0.02	1.15±0.02	0.76±0.01	0.48±0.06	2.29±0.05	0.99±0.06	0.43±0.01	1.08±0.02	1.39±0.03
[O III] λ5007	2.54±0.05	3.46±0.07	2.33±0.05	1.33±0.06	6.71±0.13	2.94±0.06	1.25±0.03	3.25±0.06	4.17±0.08
[N I] λ5199	0.013±0.002	0.006±0.001	···	···	···	···	···	···	···
He I λ5876	0.106±0.002	0.115±0.002	0.07±0.02	···	···	0.11±0.01	0.10±0.02	0.10±0.01	0.112±0.002
[O I] λ6300	0.050±0.002	0.028±0.001	0.05±0.02	0.09±0.06	0.02±0.01	0.06±0.01	0.15±0.02	0.04±0.01	0.016±0.001
[S III] λ6312	0.012±0.002	0.014±0.001	0.01±0.02	···	0.03±0.01	0.02±0.01	···	0.02±0.01	0.021±0.001
[O I] λ6363	0.015±0.002	0.009±0.001	···	···	0.01±0.01	0.04±0.01	0.08±0.02	0.02±0.01	0.008±0.001
[N II] λ6548	0.074±0.002	0.048±0.001	0.015±0.018	0.07±0.06	0.009±0.009	···	0.04±0.02	···	0.02±0.01
Hα λ6563	2.86±0.06	2.83±0.06	2.83±0.06	2.83±0.06	2.86±0.06	2.81±0.06	2.83±0.06	2.83±0.06	2.82±0.06
[N II] λ6584	0.205±0.004	0.163±0.003	0.066±0.018	0.21±0.06	0.023±0.009	0.04±0.01	0.12±0.01	0.05±0.01	0.07±0.01
He I λ6678	0.025±0.002	0.029±0.001	0.05±0.01	···	···	0.03±0.01	0.02±0.01	0.029±0.001	0.028±0.002
[S II] λ6717	0.28±0.01	0.18±0.01	0.15±0.01	0.45±0.04	0.07±0.01	0.10±0.01	0.27±0.01	0.12±0.01	0.14±0.01
[S II] λ6731	0.20±0.01	0.13±0.01	0.09±0.01	0.28±0.04	0.04±0.01	0.07±0.01	0.18±0.01	0.08±0.01	0.10±0.01
C(Hβ)	0.21±0.01	0.09±0.01	0.06±0.01	0.08±0.01	0.24±0.01	0.15±0.01	0.11±0.01	0.09±0.01	0.002±0.001
F(Hβ)	64.4±1.3	567±11	6.37±0.13	1.70±0.09	43.4±0.9	8.87±0.18	6.43±0.13	9.79±0.20	41.4±0.8
EW(Hβ)	119	239	75.8	8.25	171	120	20.8	74.0	129
EW(Hα)	587	851	611	37.8	1141	547	91.1	314	601

TABLE 3—*Continued*

	$I(\lambda)/I(\mathrm{H}\beta)$					
Ion	UGC 8638 B	UGC 8837 A	NGC 5477 A	UGC 9405 A	UGC 10818 A	KKH 098 A
[O II] λ3727	1.75±0.04	3.46±0.01	1.31±0.05	3.66±0.37	2.73±0.06	1.85±0.05
H9 λ3835	0.10±0.01	0.054±0.005	0.06±0.01	···	0.16±0.02	···
[Ne III] λ3868	0.32±0.01	0.071±0.005	0.33±0.01	···	0.20±0.02	0.21±0.04
He I+H8 λ3889	0.24±0.01	0.21±0.01	0.23±0.01	···	0.19±0.02	0.17±0.04
[Ne III]+H7 λ3968	0.02±0.01	0.16±0.01	0.33±0.01	···	0.28±0.01	0.09±0.04
[S II] λ4068	0.02±0.01	0.02±0.01	···	···	···	···
Hδ λ4101	0.27±0.01	0.24±0.01	0.28±0.02	···	0.23±0.01	0.36±0.03
Hγ λ4340	0.47±0.01	0.47±0.01	0.47±0.02	0.35±0.22	0.45±0.01	0.58±0.02
[O III] λ4363	0.06±0.01	0.019±0.003	0.06±0.01	···	0.02±0.01	···
He I λ4471	0.03±0.01	0.030±0.003	···	···	0.03±0.01	···
[Fe III] λ4658	···	0.009±0.003	···	···	···	···
Hβ λ4861	1.00±0.02	1.00±0.02	1.00±0.02	1.00±0.13	1.00±0.02	1.00±0.02
[O III] λ4959	1.39±0.03	0.42±0.01	1.55±0.03	0.46±0.14	0.74±0.02	0.63±0.01
[O III] λ5007	4.15±0.08	1.26±0.03	4.64±0.10	1.44±0.14	2.22±0.04	1.91±0.01
[N I] λ5199	···	0.012±0.002	···	···	0.02±0.01	···
He I λ5876	0.107±0.004	0.091±0.002	0.11±0.01	···	0.10±0.01	0.08±0.02
[O I] λ6300	0.013±0.003	0.051±0.002	0.01±0.01	···	0.06±0.01	···
[S III] λ6312	0.018±0.003	0.018±0.002	0.02±0.01	···	0.01±0.01	···
[O I] λ6363	0.004±0.003	0.013±0.002	0.05±0.01	···	0.02±0.01	···
[N II] λ6548	0.02±0.01	0.067±0.002	0.015±0.004	···	0.08±0.01	0.04±0.02
Hα λ6563	2.81±0.06	2.83±0.06	2.84±0.11	2.79±0.17	2.79±0.06	2.79±0.06
[N II] λ6584	0.06±0.01	0.202±0.004	0.047±0.001	0.40±0.16	0.25±0.01	0.08±0.02
He I λ6678	0.026±0.003	0.021±0.002	0.028±0.001	···	···	···
[S II] λ6717	0.11±0.01	0.35±0.01	0.079±0.002	0.76±0.15	···	0.15±0.02
[S II] λ6731	0.09±0.01	0.25±0.01	0.059±0.001	0.55±0.14	···	0.10±0.02
C(Hβ)	0.24±0.01	0.06±0.01	0.09±0.01	0.10±0.01	0.19±0.01	0.24±0.01
F(Hβ)	16.7±0.3	35.4±0.71	78.0±1.6	0.48±0.06	11.3±0.2	3.07±0.06
EW(Hβ)	57.1	114	177	43.6	46.3	50.6
EW(Hα)	301	723	879	216	216	224

NOTE.—Optical line fluxes for H II regions measured from the MMT spectra using deblended Gaussian fits and multiple component fits when necessary. Fluxes are relative to Hβ = 1.00 and are corrected for reddening. The Hβ flux is given for reference, with units of 10^{-17} erg s^{-1} cm^{-2}. EWs are given in units of Å. Multiple extractions are listed for those objects which had more than one bright Hα region aligned in the slit; letter attached to the object name specifies the Hα region label for that extraction (see Figure 1). Note that uncertainties listed in this table reflect the statistical uncertainties in the flux through the slit only, and do not account for slit loses.

3.4 Direct Oxygen Abundance Determinations

In our sample, 31 low-luminosity objects had [O III] λ4363 strengths measured to be $> 4\sigma$, and thus can be used to determine direct electron temperatures and abundances. The low and high ionization region temperatures are tabulated in Table 4.5. Typically H II regions are assumed to have electron temperatures within the range of 1 to 2 $\times 10^4$ K. Temperatures for the present sample agree with this approximation, spanning 10,800 K - 15,200 K for the low ionization region, and 9,600 K - 19,400 K in the high ionization region.

For the 9 objects with multiple H II regions containing strong [O III] λ4363, an error weighted average was used to determine a best estimate of relative abundances and oxygen abundances. The results from individual H II regions are tabulated in Table 4.5 and the mean values, using a weight of $1/\sigma_i^2$ for each component, are listed in Table 4.6. The uncertainties for these mean values are represented by the standard deviation of the weighted mean or the weighted dispersion, which ever is greater. Calculated errors in this paper provide a statistical estimate only. Additional errors may be important, such as systematic errors due to temperature fluctuations or other imperfect assumptions. However, the purpose of this paper is to improve the L-Z and M-Z relationships with abundances from high quality spectra. The statistical errors allow such an assessment of the relative quality of the spectra used, which in turn are weighted higher in the regression fits.

For 7 of the 9 dwarf galaxies with direct abundances from multiple H II regions, the derived oxygen abundances agree within the uncertainties. These support the interpretation that the ISM in typical dwarf galaxies is chemically well mixed, in agreement with past studies (e.g., Skillman et al., 1989; Kobulnicky & Skillman, 1996, 1997a; Lee et al., 2006b; Kehrig et al., 2008; Croxall et al., 2009; Pérez-Montero et al., 2011). Various theoretical studies support this result (e.g., Roy & Kunth, 1995). However, there are two galaxies for which the oxygen abundances don't agree. For NGC 4449 the highest signal to noise spectrum is offset to higher log(O/H) values by 0.16 and 0.18 dex compared to the other two. This discrepancy may be due to the possible contamination of an embedded supernova remnant (e.g., Skillman, 1985), or it may be truly offset. Additional spectra are needed to clarify this. NGC 2537 has two high quality optical

spectra, but the derived values disagree by 0.26 dex. This factor of nearly two difference is intriguing, warranting further investigation of this object. We increased the error of the weighted mean to indicate the dispersion between the two values. Note that the lower value would be in better agreement with the L-Z relationships, but that the mean is not offset very far. Overall, the oxygen abundances determined in this paper are all relatively low ($12 + \log(O/H) < 8.3$; average $12 + \log(O/H) = 7.84$) as we would expect for low-mass, low-luminosity galaxies. The abundances for the two additional objects outside of the LVL sample, UGC 4393 and UGC 10818, are discussed in Section 2.10: Appendix B.

Table 3.4. Ionic and Total Abundances

Galaxy	Hα Region	t_2 (K)	t_3 (K)	O^+/H^+ ($\times10^5$)	O^{++}/H^+ ($\times10^5$)	O/H ($\times10^5$)	12 + log(O/H) (dex)	N^+/H^+ ($\times10^6$)	log(N/O) (dex)	N/H ($\times10^6$)
UGC 521	A	14200±900	16500±1100	1.59±0.32	3.05±0.42	4.64±0.53	7.67±0.05	0.29±0.06	-1.61±0.07	1.15±0.25
UGC 695	E	14000±1900	15800±2200	3.45±1.48	1.50±0.45	4.95±1.55	7.69±0.12	1.07±0.29	-1.49±0.04	1.61±0.53
UGC 1056	A	13000±2500	13500±2600	4.50±2.89	3.26±1.56	7.75±3.29	7.89±0.15	1.48±0.59	-1.48±0.05	2.57±1.14
UGC 1056	B	12600±900	12700±900	4.23±1.06	5.43±1.04	9.66±1.49	7.98±0.06	1.34±0.21	-1.49±0.03	3.16±0.52
UGC 1176	A	12600±500	12800±500	3.40±0.47	5.91±0.59	9.31±0.75	7.97±0.03	1.29±0.11	-1.40±0.02	3.73±0.34
NGC 784	B	12900±600	13400±700	3.57±0.59	4.70±0.58	8.27±0.83	7.92±0.04	0.78±0.08	-1.63±0.02	1.94±0.22
NGC 784	A	12500±500	12400±500	3.41±0.48	7.20±0.78	10.61±0.91	8.03±0.04	1.24±0.11	-1.44±0.02	3.87±0.36
UGC 2716	A	12800±500	13100±500	2.96±0.42	6.41±0.70	9.37±0.82	7.97±0.04	0.99±0.09	-1.47±0.02	3.14±0.31
NGC 2537	A	10900±600	9700±500	8.85±1.94	8.56±1.60	17.4±2.5	8.24±0.06	7.40±0.99	-1.07±0.02	14.8±2.25
NGC 2537	B	11800±900	11200±900	5.26±1.48	4.23±0.96	9.49±1.76	7.98±0.07	5.13±0.88	-1.00±0.02	9.41±1.82
UGC 4278	B	13300±1000	14200±1000	2.53±0.61	2.32±0.41	4.85±0.73	7.69±0.06	0.57±0.09	-1.63±0.03	1.11±0.20
UGC 4278	A	13500±600	14600±600	2.01±0.27	2.86±0.28	4.87±0.38	7.69±0.03	0.52±0.05	-1.58±0.03	1.27±0.13
NGC 2552	A	11400±500	10400±500	5.27±0.88	8.93±1.23	14.19±1.52	8.15±0.04	3.57±0.37	-1.16±0.02	9.68±1.10
UGC 4393	B	12100±1000	11700±1000	4.55±1.36	6.92±1.64	11.5±0.2	8.06±0.07	3.63±0.66	-1.09±0.02	9.39±1.82
UGC 4393	C	12800±800	13100±800	5.80±1.22	3.92±0.63	9.72±1.37	7.99±0.06	3.25±0.42	-1.24±0.02	5.55±0.82
UGC 5139	A	12800±800	13000±800	2.70±0.60	5.65±0.95	8.35±1.13	7.92±0.05	0.72±0.12	-1.56±0.05	2.30±0.41
IC 559	A	12000±1400	11500±1300	5.63±2.31	6.18±2.02	11.81±3.07	8.07±0.10	1.74±0.46	-1.47±0.05	3.97±1.13
UGC 5272	A	13300±500	14100±200	1.34±0.17	6.12±0.22	7.46±0.27	7.87±0.02	0.34±0.03	-1.59±0.02	1.92±0.12
UGC 5340	A	15200±1200	19400±1500	0.47±0.11	1.12±0.16	1.59±0.19	7.20±0.05	0.09±0.02	-1.60±0.08	0.40±0.09
UGC 5423	A	13700±500	15300±500	2.33±0.27	3.55±0.24	5.88±0.36	7.77±0.03	1.08±0.08	-1.32±0.02	2.82±0.21
UGC 5423	B	13400±1100	14400±1200	2.17±0.59	4.37±0.87	6.54±1.05	7.82±0.06	0.79±0.16	-1.43±0.05	2.43±0.48
UGC 5797	A	13200±1000	14000±1000	2.04±0.51	7.06±1.29	9.11±1.39	7.96±0.06	0.95±0.19	-1.35±0.06	4.11±0.84
UGC 5923	A	14300±2500	16600±3000	4.04±2.22	2.08±0.78	6.12±2.35	7.79±0.14	1.97±0.67	-1.30±0.04	3.10±1.23
NGC 3738	A	12100±900	11800±800	4.98±1.27	6.00±1.21	10.98±1.76	8.04±0.06	2.31±0.36	-1.33±0.02	5.14±0.86
NGC 3738	B	12500±1400	12500±1400	5.36±2.15	5.39±1.67	10.75±2.72	8.03±0.10	2.23±0.55	-1.37±0.03	4.57±1.21
NGC 3741	A	13700±500	15200±400	1.81±0.21	2.93±0.20	4.74±0.29	7.68±0.03	0.42±0.04	-1.61±0.03	1.15±0.10

3.5 The L-Z and M-Z Relationships

The new direct oxygen abundances determined in this paper provide an opportunity to expand relationships previously limited by the reliability of empirical calibrations. In particular, these measurements allow us to re-examine the L-Z and M-Z relationships derived by L06, which are limited by small number statistics at the low-luminosity end.

3.5.1 The Total and "Select" Samples

In the following, we analyze various samples based on both abundance measurement and distance measurement quality criteria. Specifically, we label the samples of galaxies with both direct oxygen abundance measurements and accurate distances as "Select." We observed 31 objects with [O III] λ4363 detected at a strength greater than 4σ; this comprises our total sample. Our direct oxygen abundance measurements have relatively small errors, but comparisons to luminosity and stellar mass calculations require accurate distance determinations. This motivated further cuts from our sample to keep only objects with reliable distance determinations using the tip of the red giant branch (TRGB) or Cepheid variables (ceph), giving rise to our 13 object "Select" sample. In addition, the L06 data were updated with 4.5 μm photometry from Dale et al. (2009) (to minimize the effects of aperture differences between the previous photometry and our own), distances from Dalcanton et al. (2009), and direct oxygen abundances from Croxall et al. (2009) when available. Those objects that passed the selection criteria were assembled into a similar "Select L06" sample of 14 objects. Other Local Volume objects presented in van Zee & Haynes (2006) and Marble et al. (2010) were considered for an additional "Select" sample. Using the same criteria mentioned above, this provided 11 additional objects with direct abundances at a strength of 4σ or greater and accurate TRGB distances. The 13 "Select" objects from this paper are noted in Table 4.6 and the properties of the additional objects taken from the literature are listed in Table 4.7. Together these data sets made the final "Combined Select" sample comprised of 38 objects with both secure distance (TRGB or ceph) and oxygen abundance determinations ([O III] $\lambda4363 > 4\sigma$). Note that we have 18 objects with accurate oxygen abundances that require accurate distances from TRGB observations in order to be elevated to the "Select" caliber. Of these, 13 have distances less than 8 Mpc, so their TRGB distances

Table 3.4 (cont'd)

Galaxy	Hα Region	t_2 (K)	t_3 (K)	O^+/H^+ ($\times10^5$)	O^{++}/H^+ ($\times10^5$)	O/H ($\times10^5$)	12 + log(O/H) (dex)	N^+/H^+ ($\times10^6$)	log(N/O) (dex)	N/H ($\times10^6$)
UGC 6817	A	14200±500	16500±300	0.94±0.10	2.47±0.11	3.41±0.15	7.53±0.02	0.26±0.02	-1.53±0.03	1.01±0.07
NGC 4163	A	14800±2000	18200±2500	3.28±1.34	0.34±0.09	3.62±1.34	7.56±0.14	1.00±0.30	-1.49±0.06	1.17±0.47
CGCG 269-049	A	14400±500	17100±500	1.00±0.11	1.95±0.11	2.96±0.16	7.47±0.02	0.20±0.02	-1.57±0.03	0.80±0.08
UGC 7577	A	13100±900	13700±900	2.17±0.49	7.10±1.18	9.27±1.28	7.97±0.06	0.91±0.15	-1.37±0.04	3.96±0.67
NGC 4449	C	11500±900	10600±800	6.92±1.99	6.69±1.59	13.62±2.54	8.13±0.07	3.16±0.55	-1.33±0.02	6.30±1.22
NGC 4449	B	11300±600	10400±600	6.73±1.44	7.79±1.39	14.52±2.00	8.16±0.06	2.96±0.39	-1.36±0.02	6.30±0.91
NGC 4449	A	10800±500	9600±200	6.36±1.16	14.50±1.08	20.87±1.59	8.32±0.03	2.50±0.28	-1.39±0.02	8.50±0.73
UGC 7605	A	13400±2000	15100±2200	2.18±1.01	2.44±0.80	4.61±1.29	7.66±0.11	0.57±0.23	-1.54±0.11	1.32±0.53
NGC 4656	A	12600±700	12700±700	1.20±0.22	11.03±1.53	12.23±1.55	8.09±0.05	0.27±0.11	-1.66±0.14	2.66±1.10
UGC 8201	A	12900±900	13600±900	2.18±0.50	4.07±0.69	6.25±0.85	7.80±0.06	0.28±0.06	-1.77±0.07	1.06±0.30
UGC 8508	A	13300±1100	14300±1200	1.82±0.50	3.90±0.78	5.72±0.92	7.76±0.07	0.34±0.08	-1.60±0.07	1.44±0.36
UGC 8638	A	12600±500	12800±300	2.63±0.36	6.73±0.40	9.36±0.54	7.97±0.02	0.79±0.07	-1.51±0.02	2.88±0.20
UGC 8638	B	13000±500	13500±500	2.38±0.33	5.82±0.60	8.20±0.69	7.91±0.03	0.61±0.07	-1.58±0.04	2.17±0.26
UGC 8837	A	12900±900	13400±900	4.76±1.13	1.80±0.32	6.56±1.18	7.82±0.07	2.12±0.31	-1.35±0.02	2.94±0.55
NGC 5477	A	12800±500	13000±200	1.89±0.25	7.10±0.30	8.99±0.39	7.95±0.02	0.50±0.04	-1.56±0.02	2.45±0.14

Note. — Electron temperatures and ionic and total abundances for objects with an [O III] $\lambda4363$ line signal to noise ratio of 4σ or greater. Electron temperatures were calculated using the [O III] $(\lambda4959 + \lambda5007)/\lambda4363$ diagnostic line ratio.

Table 3.5. Error Weighted Average Abundances

Galaxy	"Select" Sample?	12 + log(O/H) (dex)	[O III]/[O II]	log(N/O) (dex)	Previous Literature Abundances?
UGC 521		7.67±0.05	2.29±0.06	-1.61±0.07	D: 12, 13
UGC 695		7.69±0.12	0.50±0.01	-1.49±0.04	
UGC 1056		7.97±0.06	0.91±0.02	-1.49±0.02	
UGC 1176		7.97±0.05	1.59±0.05	-1.40±0.02	
NGC 784	√	7.97±0.06	1.47±0.04	-1.54±0.10	S: 2,6
UGC 2716		7.97±0.05	2.05±0.06	-1.47±0.02	
NGC 2537		8.14±0.13	0.63±0.02	-1.04±0.04	S: 2, 21-23
UGC 4278		7.69±0.05	1.08±0.02	-1.60±0.03	D: 16, 17
NGC 2552		8.15±0.05	1.28±0.04	-1.16±0.02	S: 2, 17, 18
UGC 4393		8.02±0.05	0.59±0.01	-1.15±0.08	D: 16
UGC 5139	√	7.92±0.05	1.95±0.06	-1.56±0.05	D: 5, 8
IC 559		8.07±0.10	0.90±0.03	-1.47±0.05	
UGC 5272		7.87±0.05	4.66±0.13	-1.59±0.02	D: 6, 10, 11
UGC 5340		7.20±0.05	3.26±0.13	-1.60±0.08	D: 6, 7
UGC 5423		7.78±0.05	1.77±0.03	-1.33±0.04	D: 2, 5
UGC 5797		7.96±0.06	3.48±0.10	-1.35±0.06	
UGC 5923		7.79±0.14	0.61±0.02	-1.30±0.04	S: 9
NGC 3738	√	8.04±0.05	1.02±0.03	-1.34±0.02	D: 2, 18-20
NGC 3741	√	7.68±0.05	1.78±0.05	-1.61±0.03	S: 2, 3
UGC 6817	√	7.53±0.05	3.07±0.10	-1.53±0.03	
NGC 4163	√	7.56±0.14	0.15±0.01	-1.49±0.06	S: 2
CGCG 269-049	√	7.47±0.05	1.13±0.03	-1.57±0.03	D: 1
UGC 7577	√	7.97±0.06	3.18±0.09	-1.37±0.04	
NGC 4449	√	8.26±0.09	0.86±0.02	-1.36±0.02	D: 17, 19, 20, 24-26
UGC 7605	√	7.66±0.11	1.22±0.04	-1.54±0.10	
NGC 4656		8.09±0.05	8.39±0.35	-1.66±0.14	S: 2, 27
UGC 8201	√	7.80±0.06	1.82±0.05	-1.77±0.07	S: 8
UGC 8508	√	7.76±0.07	2.21±0.06	-1.60±0.07	S: 2, 4
UGC 8638	√	7.95±0.05	2.36±0.05	-1.53±0.03	
UGC 8837		7.87±0.07	0.36±0.01	-1.43±0.03	D:15
NGC 5477		7.95±0.02	0.54±0.01	-1.56±0.02	D: 14

Note. — For the 10 objects with multiple H II regions containing strong [O III] λ4363, error weighted averages were used to determine best estimates of relative abundances and oxygen abundances. Column (2) highlights our "Select" sample. Columns (3) - (5) lists the the new direct oxygen abundances, ionization strengths, and nitrogen abundances relative to oxygen determined by this work. Average values were determined using a weight of $1/\sigma_i^2$ for each component, where uncertainties represent the standard deviation of the weighted mean or the weighted dispersion, which ever is greater. Column (6) shows which objects have previous oxygen abundance determinations in the literature, where 'D' is noted for objects with direct oxygen abundances, while 'S' indicates objects with strong-line abundances. Note that we are providing direct oxygen abundances for the first time for 19 of these objects.

References. — (1) Kniazev et al. (2003); (2) Moustakas & Kennicutt (2006); (3) Gallagher & Hunter (1989); (4) vaduvescu et al. (2007); (5) Miller & Hodge (1996); (6) Hunter & Gallagher (1985); (7) Pustilnik et al. (2005); (8) Croxall et al. (2009); (9) Kewley et al. (2005); (10) Kinman & Hintzen (1981); (11) Hopp & Schulte-Ladbeck (1991); (12) van Zee et al. (1997a); (13) van Zee et al. (1997b); (14) Izotov et al. (2007b); (15) Liang et al. (2007); (16) Kniazev et al. (2004); (17) Izotov et al. (2006); (18) Hunter, D. A., & Hoffman, L. (1999); (19) Hunter et al. (1982); (20) Martin, C. L. (1997); (21) Engelbracht et al. (2008); (22) Gil de Paz, A. et al. (2000b); (23) Gil de Paz et al. (2000a); (24) McCall et al. (1985); (25) Kobulnicky et al. (1999); (26) Sabbadin et al. (1984); (27) Matteucci, F., & Tosi, M. (1985)

could be obtained with a relatively small investment of *Hubble Space Telescope* time.

Due to the wealth of B-band photometry available from previous studies, the majority of the sample has B-band absolute magnitude estimates. With the addition of *Spitzer* IRAC photometry, all members of the "Select" sample also have 4.5 μm absolute magnitudes as determined by Dale et al. (2009). In the following sections we discuss the low-luminosity portion of both the optical and NIR L-Z relationships and the subsequently determined $M_\star$-Z relationship, for our whole sample of direct oxygen abundances and a comparison to the filtered "Combined Select" sample.

Table 3.6. Additional "Select" Galaxies from the Literature

Galaxy	RA (J2000)	DEC (J2000)	$F_{[4.5]}$ (mJy)	F_{K_S} mJy	D (Mpc)	Ref	M_B (mag)	$M_{[4.5]}$ (mag)	M_{K_S} (mag)	$(B-V)_0$ mag	log $L_{[4.5]}$ ($L_\odot$)	log $M_\star$ ($M_\odot$)
L06 "Select" Objects												
WLM	00:01:58.6	-15:27:12	62.9	117	0.97±0.02	1	-13.50±0.05	-16.29±0.34	-15.54±0.34	0.46±0.03	7.85±0.34	7.19±0.34
NGC 55	00:14:53.6	-39:11:48	1390	2630	2.11±0.04	2	-18.20±0.11	-21.34±0.36	-20.61±0.16	0.55±0.08[A]	9.87±0.35	9.30±0.35
UGC 00668	01:04:49.1	02:07:31	90.1	232	0.75±0.02	1	-13.61±0.14	-16.13±0.37	-15.73±0.27	0.40±0.04	7.78±0.37	7.14±0.37
NGC 1705	04:54:13.7	-53:21:41	19.3	44.4	5.11±0.17	3	-15.77±0.52	-18.62±0.60	-18.10±0.57	0.38±0.18[A]	8.78±0.60	8.19±0.60
NGC 2366	07:28:49.6	69:12:32	4.99	110	3.21±0.05	2	-15.95±0.11	-18.64±0.35	-18.08±0.33	0.32±0.05	8.79±0.35	8.15±0.35
UGC 4305	08:19:09.0	70:43:28	64.6	216	3.38±0.05	2	-16.11±0.12	-19.03±0.31	-18.92±0.23	0.19±0.06	8.95±0.31	8.48±0.31
UGC 4459	08:34:07.6	66:10:39	3.10	7.93	3.61±0.05	2	-12.93±0.12	-15.88±0.81	-15.48±1.17	0.46±0.08	7.68±0.81	7.15±0.81
Leo A	09:59:24.8	30:44:49	13.6	34.8	0.81±0.04	4	-10.91±0.26	-14.24±0.43	-13.82	0.24±0.06	7.03±0.43	6.58±0.43
Sex B	10:00:00.0	05:19:56	36.1	136	1.39±0.04	2	-13.54±0.16	-16.47±0.38	-16.49±0.25	0.40±0.05	7.92±0.37	7.49±0.38
Sex A	10:11:00.7	-04:41:37	24.9	62.2	1.38±0.05	2	-13.62±0.19	-16.05±0.39	-15.62±0.49	0.24±0.06	7.75±0.39	7.08±0.39
UGC 5666	10:28:35.3	68:25:53	111	165	3.79±0.05	2	-16.81±0.13	-19.87±0.30	-18.88±0.33	0.34±0.06	9.28±0.30	8.62±0.30
NGC 4214	12:15:39.0	36:19:35	224	488	3.03±0.05	2	-17.15±0.10	-20.15±0.36	-19.58±0.17	0.40±0.03	9.39±0.36	8.83±0.36
UGC 8091	12:58:39.8	14:13:06	2.29	8.40	2.08±0.02	2	-11.76±0.07	-14.35±0.35	-14.34±0.97	0.27±0.04	7.07±0.35	6.55±0.36
IC 5152	22:02:41.6	-51:17:40	103	306	1.97±0.07	5	-15.47±0.03	-18.37±0.34	-18.13±0.15	0.41±0.02	8.68±0.34	8.17±0.34

3.5.2 *B*-band L-Z Relationship

In the top panel of Figure 3.3 we compare direct metallicities to corresponding B-band luminosities. Taking into consideration the errors on both quantities (c.f., Press et al., 1992), we determine the most likely linear fit to the data using the MPFITEXY routine (Williams et al., 2010), which depends, in turn, on the MPFIT package (Markwardt, 2009). In this section, and those following, we provide the total scatter (intrinsic + observational) output from the MPFITEXY routine, which is essentially a weighted mean of the scatter of the data about the linear fit. In each case, we compare our results to that of L06, who also use a weighted dispersion routine.

The best fit to the 31 objects in the current sample with direct oxygen abundance measurements results in:

$$12 + \log(\mathrm{O/H}) = (6.59 \pm 0.32) + (-0.08 \pm 0.03) M_B, \tag{3.3}$$

with a dispersion in log(O/H) of $\sigma = 0.19$. Updated data for the L06 sample (see § 3.5.1) is also plotted, and compared to the original least-squares best fit of L06.

The low-metallicity outlier at 12 + log(O/H) = 7.20 is the blue compact dwarf UGC 5340, supporting its classification by previous work as one of the most metal-deficient star-forming galaxies (e.g., Izotov & Thuan, 2007a; Pustilnik et al., 2008b). However, Pustilnik et al. (2008b) note that its present distance could be significantly *underestimated* due to the large negative peculiar velocity in that region, which, if true, would result in an even larger discrepancy. Ekta et al. (2008) and Pustilnik et al. (2008a) have discussed the HI observations of UGC 5340 and concluded that it is likely undergoing a merger, which could explain, at least in part, its discrepant position from the L-Z relationship. From HI observations of a sample of extremely metal poor galaxies, Ekta & Chengalur (2010) find that roughly half of these galaxies show evidence of interactions, and conclude that the very low metallicities in these galaxies are due to recent infall of metal poor gas (see also Lee et al., 2004)). Thus, these galaxies do not lie on the L-Z relationship defined by the average low-luminosity galaxy, and therefore, UGC 5340 has not been included in the relationships of the "Combined Select" sample.[4]

[4] At this time the H I morphologies have not been analyzed for the LVL sample, so we cannot make

Table 3.6 (cont'd)

Galaxy	RA (J2000)	DEC (J2000)	$F_{[4.5]}$ (mJy)	F_{K_S} mJy	D (Mpc)	Ref	M_B (mag)	$M_{[4.5]}$ (mag)	M_{K_S} (mag)	$(B-V)_0$ mag	log $L_{[4.5]}$ ($L_\odot$)	log $M_\star$ ($M_\odot$)
Additional "Select" Objects												
SMC	00:52:44.0	-72:49:42	20.7	···	0.056±0.002	6	-16.04±0.20	-8.89±0.34	···	0.45±0.10[A]	4.89±0.46	···
UGC 00685	01:07:22.8	16:41:02	7.48	11.6	4.70±0.06	5	-14.13±0.11	-17.41±0.34	-16.46	0.60±0.09	8.30±0.34	7.71±0.34
NGC 625	01:35:03.9	-41:26:14	88.3	242	3.89±0.13	7	-16.28±0.04	-19.68±0.34	-19.34±0.17	0.59±0.02	9.20±0.34	8.80±0.34
LMC	05:23:34.6	-69:45:22	1.41	···	0.05±0.01	8	-17.68±0.05	-5.83±0.36	···	0.51±0.08[A]	3.66±0.35	···
UGC 4483	08:37:03.3	69:46:34	0.92	4.19	3.41±0.12	2	-12.71±0.19	-14.44±0.40	-14.66±1.21	0.15±0.05	7.11±0.39	6.42±0.40
UGC 6541	11:33:28.8	49:14:23	3.59	12.6	3.89±0.52	9	-13.51±0.06	-16.20±0.34	-16.14±0.64	0.42±0.04	7.81±0.34	7.30±0.34
UGCA 292	12:38:40.7	32:45:41	0.54	6.57	3.60±0.08	2	-11.52±0.23	-13.94±0.40	-15.27	0.07±0.14	6.91±0.40	6.68±0.40
UGC 8651	13:39:53.9	40:44:26	3.90	15.9	3.14±0.05	2	-13.13±0.11	-15.83±0.36	-15.93±0.79	0.36±0.06	7.66±0.36	7.19±0.36
UGC 9128	14:15:56.8	23:03:22	2.43	9.25	2.21±0.07	2	-12.12±0.18	-14.55±0.38	-14.58±0.88	0.31±0.07	7.15±0.38	6.59±0.39
UGC 9240	14:24:43.1	44:31:37	10.7	33.2	2.79±0.04	2	-13.89±0.09	-16.67±0.36	-16.47±0.47	0.43±0.06	8.00±0.36	7.47±0.36
UGCA 442	23:43:46.3	-31.57:25	7.51	13.4	4.27±0.53	9	-14.34±0.62	-17.21±0.71	-16.41±1.14	0.38±0.03	8.21±0.71	7.56±0.71

Note. — On top are galaxies taken from L06 that meet the "Select" specifications listed in Section 3.5.1. The bottom half lists the additional galaxies taken from Marble et al. (2010) and van Zee & Haynes (2006) that meet the "Select" specifications of having oxygen abundances based on [O III] λ4363 measurements of strength 4 σ or greater and secure distance measurements. All distances were determined using the tip of the red giant branch, with the exception of Leo A, which used Cepheid variables. $(B-V)_0$ optical colors are from Liese van Zee et al. (2013), unless otherwise noted.

References. — (1) Rizzi et al. (2007); (2) Dalcanton et al. (2009); (3) Tosi et al. (2001); (4) Dolphin et al. (2003); (5) Tully et al. (2006); (6) Sanna et al. (2008); (7) Cannon et al. (2003); (8) Sakai et al. (2004); (9) Karachentsev et al. (2003)

Table 3.7. Abundances for Additional "Select" Galaxies

Galaxy	12 + log(O/H) (dex)	log(N/O) (dex)	Reference
WLM	7.83±0.06	-1.49±0.01	1
NGC 55	8.05±0.10	-1.26±0.05	2
UGC 00668	7.62±0.05	-1.51±0.10	3
NGC 1705	8.21±0.05	-1.75±0.06	4
NGC 2366	7.91±0.05	-1.17±0.26	5
UGC 4305	7.92±0.10	-1.52±0.11	6
UGC 4459	7.82±0.09	-1.32±0.17	7
Leo A	7.30±0.05	-1.53±0.09	8
Sex B	7.53±0.05	-1.49±0.06	9
Sex A	7.54±0.06	-1.54±0.13	10
UGC 5666	7.93±0.05	-1.45±0.08	7
NGC 4214	8.22±0.05	-1.32±0.03	11
UGC 8091	7.65±0.06	-1.51±0.07	8
IC 5152	7.92±0.07	-1.05±0.12	6
SMC	7.96±0.15	-1.55±0.15	12
UGC 00685	8.00±0.03	-1.45±0.08	13
NGC 625	8.08±0.12	-1.25±0.03	14
LMC	8.26±0.15	-1.30±0.20	12
UGC 4483	7.56±0.03	-1.57±0.07	13
UGC 6541	7.82±0.06	-1.45±0.13	15
UGCA 292	7.30±0.03	-1.45±0.07	9
UGC 8651	7.85±0.04	-1.60±0.09	13
UGC 9128	7.75±0.05	-1.80±0.12	16
UGC 9240	7.95±0.03	-1.60±0.06	13
UGCA 442	7.72±0.03	-1.41±0.02	14

Note. — The top portion of the table lists the objects and their abundances which were included in the L06 sample. The bottom half lists additional objects found in the literature. All objects meet the "Select" sample criteria.

References. — (1) Lee et al. (2005); (2) Tüllmann et al. (2003); (3) Lee et al. (2003a); (4) Lee & Skillman (2004); (5) Saviane et al. (2008); (6) Lee et al. (2003b); (7) Croxall et al. (2009); (8) van Zee et al. (2006); (9) van Zee, L. (2000); (10) Kniazev et al. (2005); (11) Kobulnicky & Skillman (1996); (12) Russell, S. C. & Dopita, M. A. (1990); (13) van Zee & Haynes (2006); (14) Skillman et al. (2003) (15) Thuan, T. X., & Izotov, Y. I. (2005); (16) van Zee et al. (1997b)

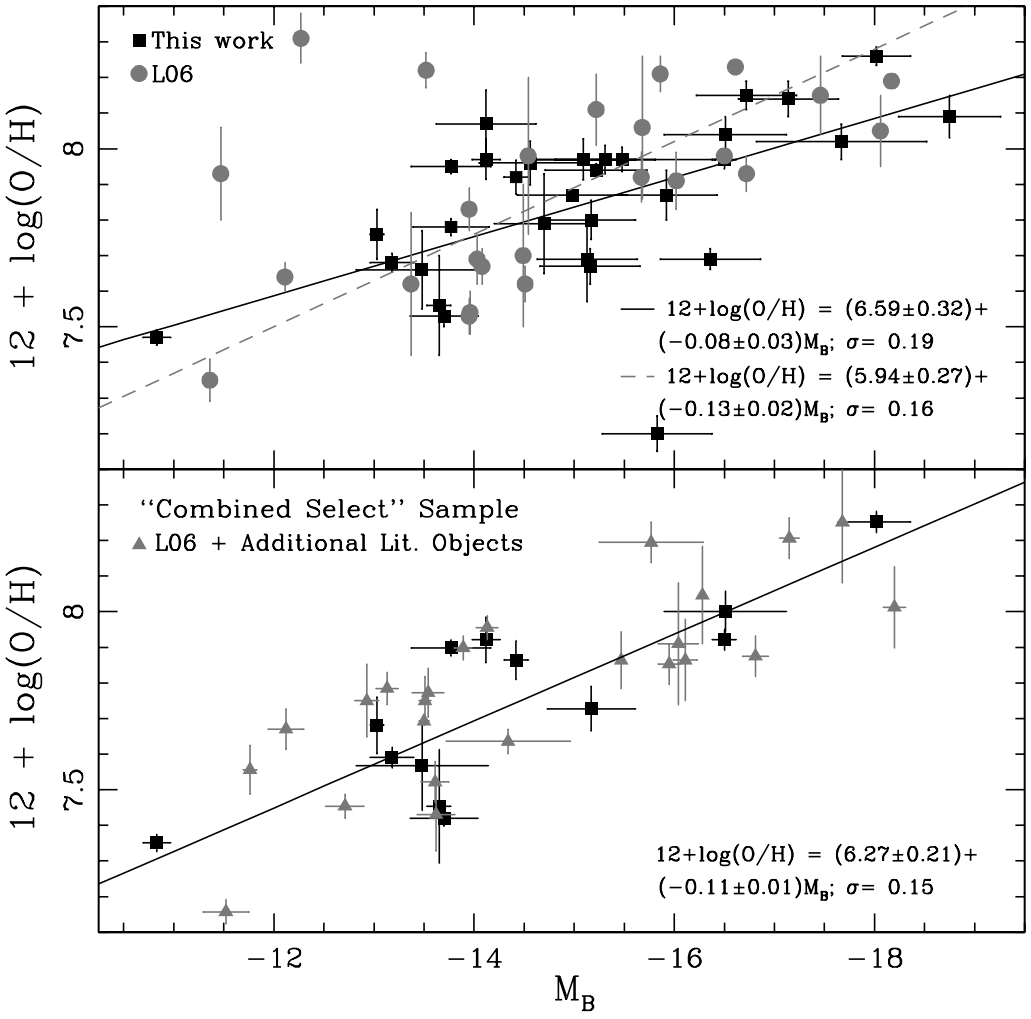

Figure 3.3: On the top, the optical luminosity-metallicity relationship is plotted for the 31 objects in the present sample with direct oxygen abundance measurements (squares). The solid black line represents the least-squares fit to this data. In comparison the original L06 dashed least-squares fit lies close to our line; in fact the slopes agree within the uncertainties. The updated L06 data are plotted (which are slightly offset from the original fit - see §6.3 for discussion of L06 data). On the bottom, the optical luminosity-metallicity relationship is improved by restricting our data to a "Combined Select" sample with direct oxygen abundances and reliable distance estimates (TRGB or ceph). The triangles represent the set of additional "Select" objects comprised from L06, vZ06, and Marble et al. (2010), and the solid line is the least squares fit to the total "Combined Select" sample.

In the lower panel of Figure 3.3 we plot the 38 objects in the "Combined Select" sample. The best fit is given by:

$$12 + \log(\mathrm{O/H}) = (6.27 \pm 0.21) + (-0.11 \pm 0.01) M_B. \tag{3.4}$$

with a resultant dispersion in log(O/H) of $\sigma = 0.15$[5] . Note that the luminosity error bars represent the error propagated from the uncertainty in the photometry and distances. This relationship agrees with that of L06 within errors. Additionally, the MPFITEXY routine allows us to estimate the intrinsic scatter by ensuring that χ^2/(degrees or freedom) ≈ 1. Using this tool, the intrinsic scatter in log(O/H) for the B-band L-Z relationship for the "Combined Select" sample is 0.13 dex, i.e., most of the scatter in this relationship is intrinsic.

3.5.3 4.5 μm L-Z Relationship

L06 found their L-Z slope to be smaller in the NIR than in the optical and to contain less scatter. This result might be expected since luminosities in redder bands are less sensitive to dust extinction and star formation rates than optical luminosities. However, these NIR luminosities are also vulnerable to stochastic effects from the high NIR luminosities of AGB stars. Following the motivation given in L06, we analyze the 4.5 μm L-Z relationship.

In the top panel of Figure 3.4, we plot the 4.5 μm L-Z relationship for our low-luminosity LVL sample. Our results are well matched to the luminosity-metallicity relationship for dwarf galaxies found by L06 (and corroborated by Marble et al., 2010). Using the MPFITEXY least-squares fit to our data, the resulting expression is:

$$12 + \log(\mathrm{O/H}) = (6.37 \pm 0.33) + (-0.08 \pm 0.02) M_{[4.5]}, \tag{3.5}$$

with a standard deviation in log(O/H) of $\sigma = 0.18$. The original L06 least-squares fit and the updated L06 data are also plotted in Figure 3.4, displaying an equivalent slope, but with a notably smaller dispersion in log(O/H) of only 0.12. Note that while the

predictions about the infall of unenriched gas for these galaxies.

[5] Dispersion in log(O/H) of the "Combined Select" sample increases to $\sigma = 0.18$ if UGC 5340 is included.

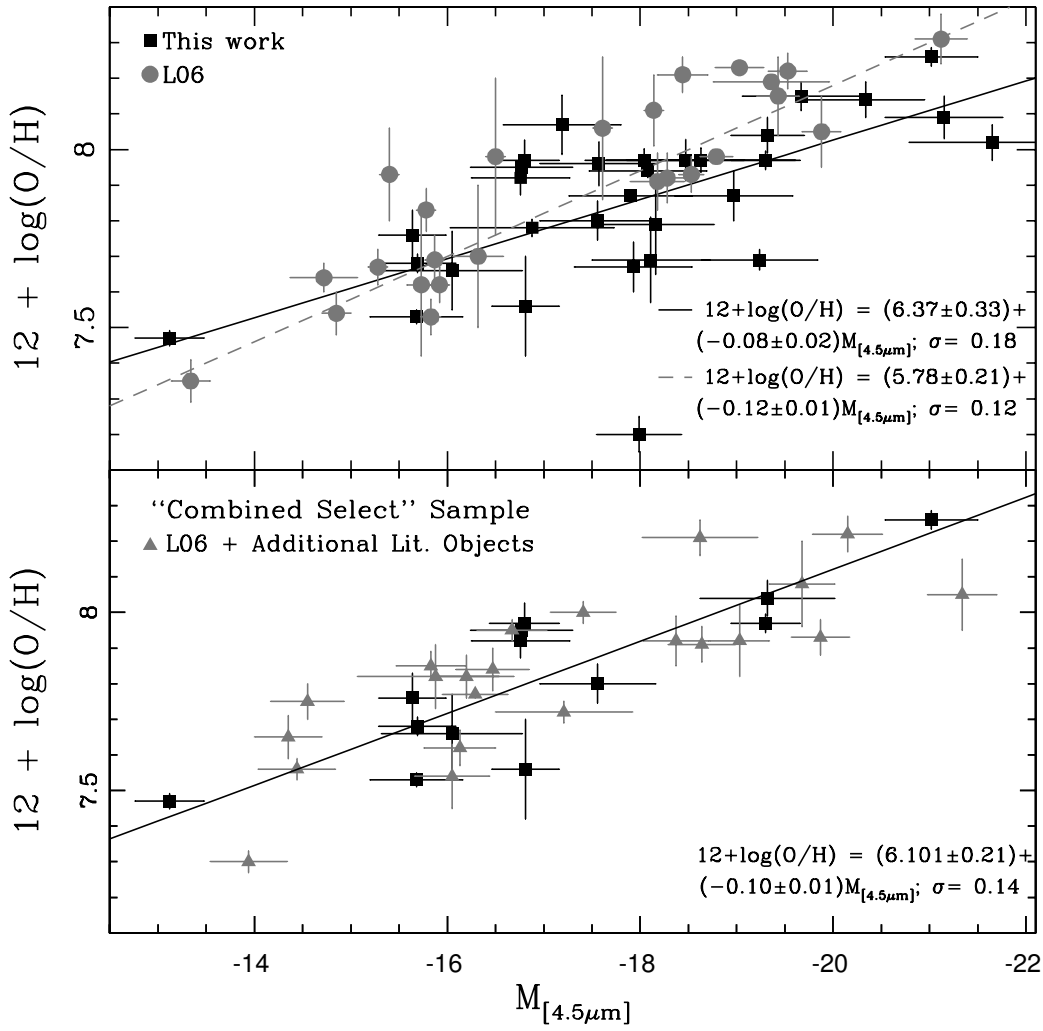

Figure 3.4: In the top panel, the NIR luminosity-metallicity relationship is plotted for the 31 objects in the present sample with direct oxygen abundance measurements (squares). The solid black line represents the least-squares fit to this data. In comparison, updated L06 data are plotted (circles), with the dashed original least-squares fit of L06 lying just above our line. Note that the updated data are slightly offset from the original fit (see §6.3 for discussion of L06 data). In the bottom panel is the NIR luminosity-metallicity relationship for the "Combined Select" sample, with direct oxygen abundances and reliable distance estimates (TRGB or ceph). By filtering our data in this way, the L-Z relationship is strengthened.

two fits have the same slope, they are offset from one another by roughly 0.1 dex in log(O/H); this difference is within the error and can be attributed to the difference in samples and small sample size.

In the bottom panel of Figure 3.4 we have plotted the NIR L-Z relationship for the "Combined Select" sample. A least-squares fit results in:

$$12 + \log(\mathrm{O/H}) = (6.10 \pm 0.21) + (-0.10 \pm 0.01) M_{[4.5]} \tag{3.6}$$

and produces a standard deviation of $\sigma = 0.14$.[6] This is nearly identical to the standard deviation of $\sigma = 0.15$ found for the "Combined Select" sample for the optical L-Z relationship, and the slopes are the same within the uncertainties.

The intrinsic scatter in log(O/H) for the 4.5 μm L-Z relationship for the "Combined Select" sample is 0.11 dex. Since AGB stars can have significant impact on the NIR luminosities, we must consider the effect of stochastic sampling on the overall scatter of our relationship. However, since we find such a small scatter in the NIR L-Z relationship it is unlikely to be due to AGB stars, which would normally drive the data to a larger dispersion. L06 determined dispersions in the optical and NIR L-Z relationships of 0.161 and 0.122 respectively. In comparison, the present work does not find a significant difference between the dispersions of the NIR and optical L-Z relationships. However, the NIR intrinsic scatter in log(O/H) is slightly smaller than the intrinsic scatter for the B-band L-Z relationship for the "Combined Select" sample (0.11 versus 0.15 dex).

3.5.4 $M_\star$-Z Relationship

The underlying relationship between mass and luminosity and the relative ease of measuring luminosities has allowed a widespread use of the L-Z relationship. However, mass is thought to be more fundamentally related to metallicity (see, e.g. Tremonti et al., 2004), and so, when possible, metallicity is also investigated as a function of stellar mass. In order to examine the $M_\star$-Z relationship, we need to estimate stellar masses in a self consistent way. Although SED fitting is commonly used to determine individual masses, the necessary spectral and/or photometric components were not available to us for our

[6] Dispersion in log(O/H) of the "Combined Select" sample increases to $\sigma = 0.22$ if UGC 5340 is included.

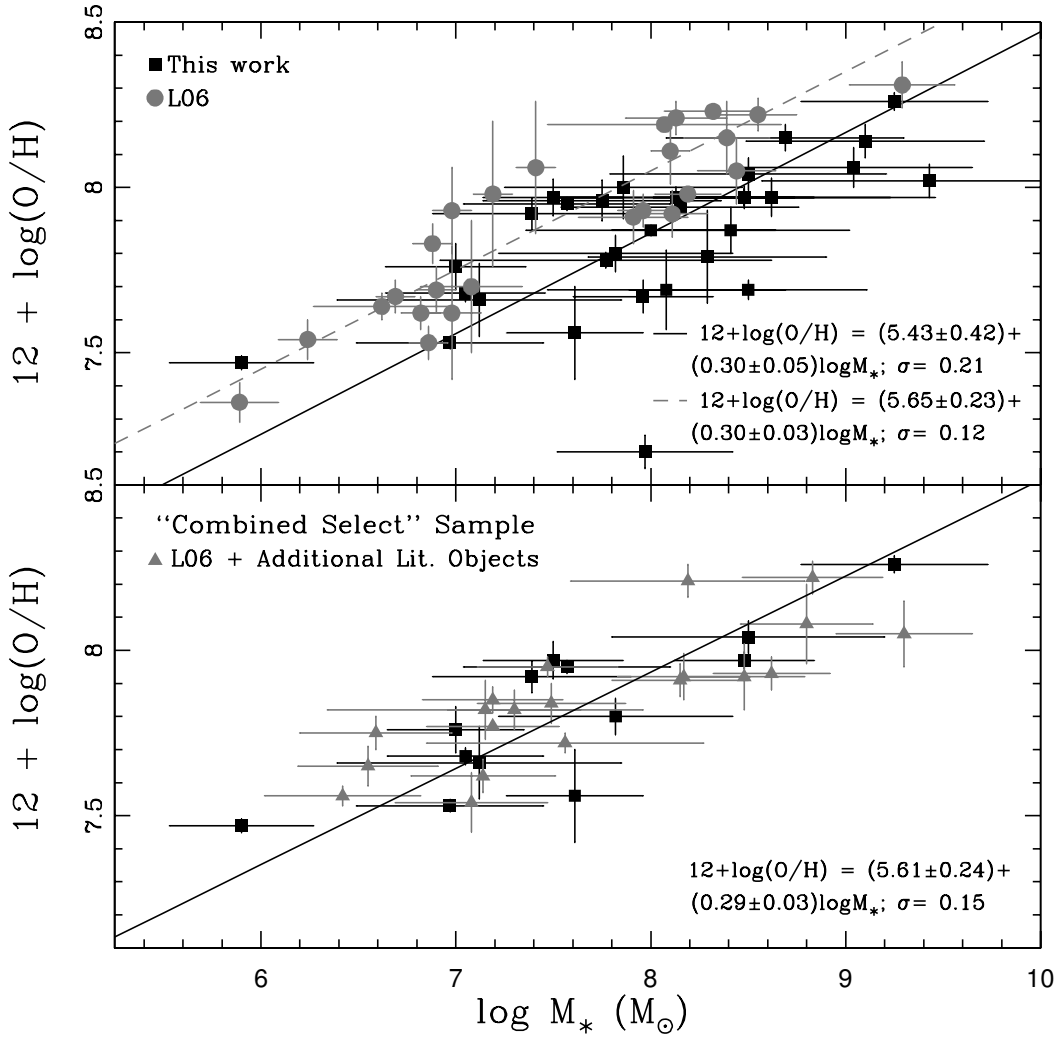

Figure 3.5: In the top panel the mass-metallicity relationship derived from NIR luminosities is plotted for the 31 objects in the present sample with direct oxygen abundance measurements (squares). The solid black line represents the least-squares fit to this data. In comparison, updated L06 data is plotted (circles). We have also plotted the original least-squares fit to the sample of objects from L06 (which is not significantly offset from the updated data; see §6.3 for discussion of L06 data). This dashed gray line is offset from our estimate of the best fit. In the lower panel is the mass-metallicity relationship for the "Combined Select" sample, with direct oxygen abundances and reliable distance estimates (TRGB or ceph).

entire "Combined Select" sample. Stellar mass can also be inferred from luminosity, where optical colors have been widely used to estimate M/L ratios (e.g., Brinchmann & Ellis, 2000; Bell & de Jong, 2001). It is important to note the uncertainties in M/L ratios that occur due to variations in the current star formation rate, which are most significant if galaxies have formed a substantial fraction (>10%) of their stars in a recent episode. Near IR magnitudes are often a better choice to characterize the galaxy luminosity because they are less sensitive than bluer bands to extinction and the age of the stellar population. The dominant emission in NIR wavelengths arises from the stellar populations (as opposed to dust) and is only marginally sensitive to recent star formation, but even so, NIR stellar M/L ratios can vary by up to a factor of ∼2 due to the star formation rate and stellar metallicity (Bell & de Jong, 2001). Furthermore, Lee et al. (2006a) found that although individual stellar masses can vary by as much as ∼0.5 dex with M/L model, the subsequent M-Z relationship spanning four decades in stellar mass is nearly independent of the model chosen.

We chose to estimate stellar mass in a uniform manner from 4.5 μm luminosity and $K-[4.5]$ and $B-K$ color following the method presented by L06:

$$\log \mathrm{M}_\star = \log(\mathrm{M}_\star/L_K) + [\log L_{[4.5]} - 0.4\ (K-[4.5])]. \tag{3.7}$$

L06 derived a mass-to-light ratio ($\mathrm{M}_\star/L_K$) as a linear function of $B-K$ color based on the Bruzual & Charlot model with a Salpeter IMF. Note that there is a systematic uncertainty in NIR M/L ratios of ∼0.2 dex due to uncertainties in AGB evolution (e.g., Conroy & Gunn, 2010; Melbourne et al., 2012). Since K_s photometry is available for the LVL sample (Dale et al., 2009), unlike the procedure of L06, the $B-K$ color was calculated directly (we assume $\mathrm{M}_K \equiv \mathrm{M}_{K_s}$). Based on the direct relationship between the ratio of luminosities and ratio of absolute magnitudes for two objects, we calculated monochromatic luminosities, $L_{[4.5]}$, assuming $M_{[4.5]} \simeq 3.3$ for the Sun (following the logic of L06). The $\mathrm{M}_\star$ results are tabulated in Table 5.1.

In principle, mass estimates can be improved using SED fitting to broad-band photometry which span from the UV to the IR. Johnson et al. (2013) have determined masses for the LVL galaxies using this method. Unfortunately, the broad wavelength coverage and associated analysis is not available for the entire LVL survey, including

objects in our sample. There are 41 LVL galaxies for which we have obtained new spectra or which have spectra in the literature with masses computed by Johnson et al. to which we can compare our stellar masses determined from 4.5μm luminosities. We find an average difference of 0.23 dex in mass, or an offset of a factor of $\sim$2, in the sense that the SED derived masses are smaller and independent of luminosity or optical color. This difference can be accounted for by the use of different IMFs in the modeling (Salpeter IMF in Bell & de Jong (2001) and Chabrier IMF in Johnson et al. (2013)). Note that this average difference, as well as the dispersion of σ=0.24, is smaller than the typical uncertainty in our derived masses. Therefore, adopting these masses would not affect the slope of our derived M-Z relationship. Because we do not have SED derived masses for our entire "Combined Select" sample, we report the present relationship using the masses calculated here.

$M_\star$-Z data are plotted in the top panel of Figure 3.5 in comparison to the updated L06 data and original $M_\star$-Z relationship of L06. The best fit to our data,

$$12 + \log(\mathrm{O/H}) = (5.43 \pm 0.42) + (0.30 \pm 0.05)\log(\mathrm{M}_\star), \tag{3.8}$$

with a dispersion of $\sigma = 0.21$, agrees, within errors, with the fit to the L06 data set. This dispersion is notably larger than the 0.12 dispersion in log(O/H) found by L06. The mass error bars used here are the propagated errors from the 4.5 μm luminosity, K-[4.5] color, and mass-to-light ratio (where we substituted the uncertainty in B-K color). Note that the contrast in dispersion of the two data sets is largely due to the different errors. L06 assumed the same errors for their mass determinations as their 4.5 μm luminosities, whereas we incorporated the additional propagated error from the color terms. This difference accounts for the disparity in uncertainty.

On the bottom of Figure 3.5 we have plotted the "Combined Select" M-Z data. Fitting the combined data set produces the least-squares linear fit,

$$12 + \log(\mathrm{O/H}) = (5.61 \pm 0.24) + (0.29 \pm 0.03)\log(\mathrm{M}_\star), \tag{3.9}$$

with a standard deviation of $\sigma = 0.15$,[7] which is essentially equivalent to the dispersions of the "Combined Select" L-Z data sets. The intrinsic scatter in log(O/H) for the $M_\star$-Z relationship for the "Combined Select" sample is 0.08 dex. This appears to be significantly smaller than the intrinsic scatter in log(O/H) for the 4.5 μm L-Z relationship for the "Combined Select" sample of 0.11 dex.

The dual effects of increasing the number of objects observed and selecting only objects with both reliable oxygen abundances and distances has resulted in a better characterization of the L-Z and M-Z relationships. In this work, we assume that a galaxy with an H II region of sufficiently high surface brightness to allow a λ4363 measurement is a local property of the star forming region, and not related to a characteristic property of the host galaxy. Thus, we don't believe our sample to be biased in terms of mass or galaxy type. Additionally, the observation that strong-line abundances of low-mass galaxies are consistent with the relationships derived here, albeit with increased scatter, supports this assumption. Therefore, the L-Z and M-Z relationships presented here should accurately represent low-mass galaxies in general. In high mass galaxies, Tremonti et al. (2004) found a decrease in the dispersion in the L-Z relationships as one went from $\sigma = 0.16$ for the optical B-band to $\sigma = 0.13$ for the longer wavelength z-band, and then an even smaller dispersion of $\sigma = 0.10$ for the M-Z relationship. The "Combined Select" data show a negligibly smaller dispersion for the NIR L-Z relationship compared to the B-band, and no similar decrease in dispersion for the M-Z relationship.

3.6 N/O Relative Abundances

The N/O versus O/H trend is well studied in galaxies of varying types. Vila-Costas & Edmunds (1993) presented a thorough overview of theoretical expectations and observations available at the time. A salient point is that N can be produced as both a primary and a secondary element and that the secondary component is expected to be delayed relative to oxygen and to dominate at high abundances. A typical scenario might be described by oxygen production in Type II supernovae being released 10 Myr after star formation, whereas nitrogen forming in intermediate mass stars isn't released

[7] Dispersion in log(O/H) of the "Combined Select" sample increases to $\sigma = 0.21$ if UGC 5340 is included.

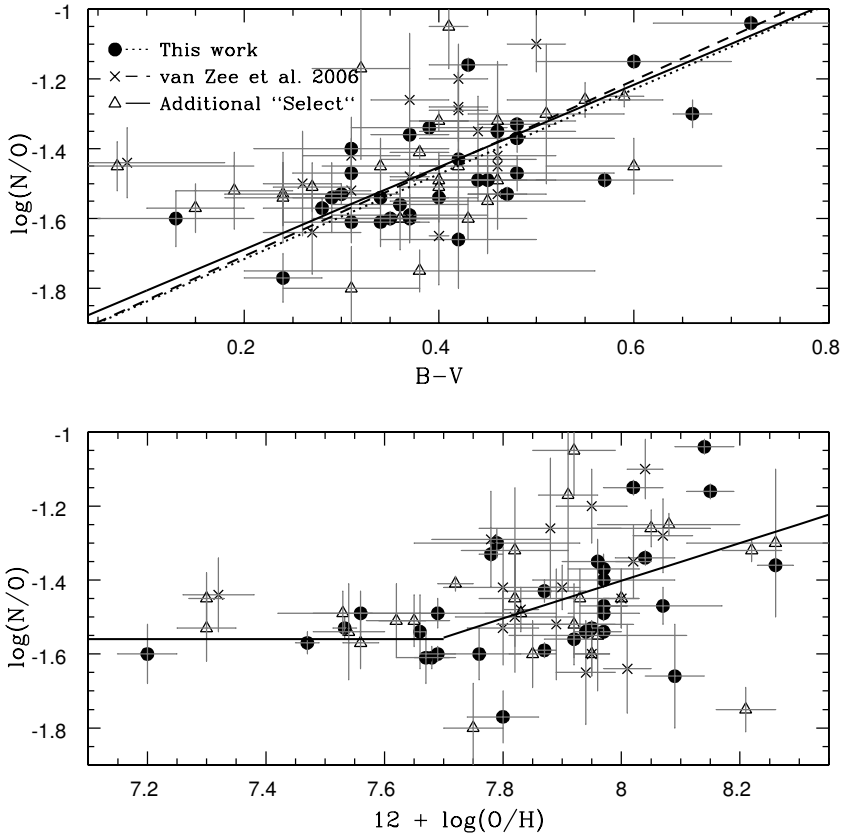

Figure 3.6: Relative N/O abundance is depicted. The top panel compares log(N/O) to $B-V$ color for objects of the present sample with [N II] observations (filled circles), the sample of vZ06 (crosses), and for the additional "Select" galaxies (triangles). The least squares fit for this work is represented by the dotted line. The dashed line is the least squares fit from vZ06. A solid line is shown for the literature combination of all three data sets: the present work, vZ06, and the additional values from the literature; our best estimate of the true relationship for the color range of $0.05 \lesssim B-V \lesssim 0.75$. Below $B-V = 0.20$ the data diverges from the fit, suggesting this fit is most appropriate for the range of $0.20 \lesssim B-V \lesssim 0.75$. The bottom panel displays log(N/O) versus log(O/H) for objects from this work, vZ06, and additional literature values. At values of 12 + log(O/H) $\leq$ 7.7, the N/O values are relatively constant, consistent with the plateau associated with primary nitrogen return. Above this value of O/H, the scatter increases and the trend is to larger values of N/O with the addition of secondary nitrogen.

until much later times ($> 10^8$ Myr; Kobulnicky & Skillman, 1996). Initially, N/O is expected to rapidly decrease as oxygen is returned to the interstellar medium, but will gradually increase with time as nitrogen begins to be returned to the gas reservoir. Thus, in principle, the relative N/O abundance can be used as a clock (e.g., Henry et al., 2000) to indicate the time since the most recent burst of star formation. Note that this effect is not expected if the star formation rate does not show significant variations (Mollá et al., 2006).

Table 4.6 lists the error weighted average N/O values for our sample. The N/O errors were determined by first adding in quadrature the error in flux of both [O II] λ3727 and [N II] λ6584, then adding this value in quadrature with the error in temperature of the low ionization zone. The most extreme values extend from $\log(\mathrm{N/O}) = -1.77$ to -1.00, with an average of $\log(\mathrm{N/O}) = -1.47$; this is comparable to the isolated dwarf irregular sample examined by van Zee et al. (2006, hereafter vZ06), with an average $\log(\mathrm{N/O}) = -1.41$. We tested for a correlation of N/O with reddening and found none, indicating an absence of bias in this regard.

The 9 objects with multiple direct oxygen abundances provides the opportunity to study N/O variations in individual dwarf galaxies. The average N/O ratio dispersion of different H II regions in a given galaxy is only 0.08 dex, indicating that dwarf galaxies, despite appearing to be solid body rotators (Skillman et al., 1988), are well mixed (see also e.g., Roy & Kunth, 1995). Other studies, such as the *green pea* galaxies analyzed by Amorín et al. (2010) and the nitrogen enriched dwarf galaxies analyzed by Pérez-Montero et al. (2011), find N/O abundance dispersions or small gradients hypothesized to be a combination of outflows of enriched gas and inflows of metal-poor gas. Note that errors in N/O account for the dispersion within four of the objects that have multiple N/O measurements (UGC 1056, UGC 4278, NGC 3738, and NGC 4449), but not for 5 others (NGC 784, NGC 2537, UGC 4393, UGC 5423, and UGC 8638). For two of these objects (NGC 784 and UGC 4393) the differences in N/O are significant (0.19 and 0.15). In these last two cases in could be that significant nitrogen enhancement has been detected, although not at the level of the well studied galaxy NGC 5253 (e.g., Kobulnicky et al., 1997b; López-Sánchez et al., 2012) or the more recently discovered N/O anomaly in MRK 996 (James et al., 2009).

vZ06 looked at several variables for their possible influence on N/O abundance. In

particular, they found a correlation between N/O and color, in the sense that redder galaxies have higher N/O as one might expect from time delayed N release. In the top panel of Figure 3.6, log(N/O) is plotted vs. $B-V$ color for objects of our sample with direct abundances and measurable [N II]/[O II] abundances. Similar to vZ06, we find a fairly steep increase in N/O with redder color (demonstrated by the dotted least squares fit):

$$\log(\mathrm{N/O}) = (-1.96 \pm 0.12) + (1.22 \pm 0.26) \times (B-V). \tag{3.10}$$

with a dispersion of $\sigma = 0.13$. In fact, the two groupings of points are visually consistent with one another. When the additional objects from the literature are added to the plot, the least squares fit over $0.05 \lesssim B-V \lesssim 0.75$ to all of the data is

$$\log(\mathrm{N/O}) = (-1.92 \pm 0.08) + (1.18 \pm 0.19) \times (B-V), \tag{3.11}$$

which agrees well with the relationship found by vZ06. Below $B-V = 0.10$ there are two objects with discrepantly large N/O values. Therefore, we suggest this fit is most appropriate for the range of $0.20 \lesssim B-V \lesssim 0.75$. Note the appearance of significant scatter in this figure. We calculate a dispersion in log(N/O) of $\sigma = 0.14$ dex, with an estimated intrinsic scatter of 0.10 dex.

Additionally, the bottom panel of Figure 3.6 shows log(N/O) plotted vs. 12 + log(O/H) for the same sample. Above 12 + log(O/H) $\approx$ 7.7 a trend of N/O increasing with O/H is evident, despite the large scatter. For 12 + log(O/H) $\geq$ 7.7, the best fit to our data yields:

$$\log(\mathrm{N/O}) = (-5.49 \pm 1.36) + (0.51 \pm 0.17) \times [12 + \log(\mathrm{O/H})], \tag{3.12}$$

with a dispersion of $\sigma = 0.16$, where the estimated intrinsic scatter is 0.14 dex. With an increasing slope, this would be indicative of secondary N production in this region. Garnett (1990) proposed that much of the scatter in the 12 + log(O/H) vs log(N/O) relationship could be explained by the time delay between producing oxygen and secondary nitrogen.

For the systems with 12 + log(O/H) $\leq$ 7.7, in agreement with previous studies, there is little trend in N/O with O/H. We have calculated a weighted mean in N/O using the

IDL routine MPFITEXY with the added constraint of setting the slope to zero for the points below 12 + log(O/H) = 7.7. For our eight new observations, the weighted mean is log(N/O) = −1.56 with a standard deviation of 0.05. For the nine observations from the literature, the weighted mean is log(N/O) = −1.51 with a standard deviation of 0.04. For the two sets together we obtain log(N/O) = −1.56 with a standard deviation of 0.05. Of this dispersion, the intrinsic scatter is predicted to be 0.02, so observational scatter may play a large role in determining the observed scatter in this relationship. In most previous studies, no correlation is noted between 12 + log(O/H) and the relative N/O abundance at low oxygen abundances, where nitrogen is expected to behave like a primary nucleosynthesis element. Together the new observations are consistent with the trends in N/O with O/H observed by Vila-Costas & Edmunds (1993), Lee et al. (2004), van Zee & Haynes (2006), Mollá et al. (2006), and Liang et al. (2006).

3.7 Discussion

3.7.1 The L-Z and M-Z Relations for Low Luminosity Galaxies

The dual effects of increasing the sample size and selecting only objects with both reliable oxygen abundances and distances has resulted in an improved characterization of the L-Z and M-Z relationships. In high mass galaxies, Tremonti et al. (2004) found a decrease in the dispersion in the L-Z relationship as one went from the optical B-band ($\sigma = 0.16$) to the longer wavelength z-band ($\sigma = 0.13$), and an even smaller dispersion for the M-Z relationship ($\sigma = 0.10$). The present data show only a slightly smaller dispersion for the NIR L-Z relationship ($\sigma = 0.14$) compared to the B-band ($\sigma = 0.15$), but no similar decrease in dispersion for the M-Z relationship ($\sigma = 0.15$). However, our estimates of the *intrinsic* scatter in the three relationships do show a decreasing trend in the sense that the *intrinsic* scatter of the B-band L-Z relationship is largest ($\sigma = 0.13$), followed by the NIR L-Z relationship ($\sigma = 0.12$), then the M-Z relationship ($\sigma = 0.08$). While this trend could be an artifact of how the errors are estimated for the three different parameters, it is interesting that it follows the same pattern observed in the larger spiral galaxies. Perhaps what is most remarkable is the small *intrinsic* scatter in all three relationships. When averaging the light over an entire galaxy, as done in Tremonti et al. (2004) one might expect relatively low dispersions. However,

oxygen abundances derived from spectroscopic apertures only covering a fraction of the galaxy will be biased if radial gradients exist (e.g., Moustakas et al., 2012). Therefore, one might expect much larger dispersions when observing individual H II regions, yet this is not the case observed in most dwarf galaxies, as they have been shown to be relatively chemically homogeneous (e.g., Croxall et al., 2009).

The L-Z and M-Z relationship slopes determined for the "Combined Select" sample are similar to those found in previous studies (e.g., Tremonti et al., 2004; Lee et al., 2006a). For large galaxies, a different slope may apply as galaxies higher in mass and luminosity contain more metals and dust (e.g., Rosenberg et al., 2006) causing them to appear under-luminous. For smaller, less luminous galaxies, even with the present sample included, the number of galaxies meeting our "Select" criteria is still relatively small. This limitation could affect our measurements of the scatter, but it appears that these relationships have intrinsically smaller dispersions. The evolutionary paths of dwarfs are still poorly understood, making the source of this inherent variation unclear. Some studies argue for the importance of gas infall and outflows (e.g., Garnett, 2002), whereas others point to star formation efficiencies (e.g., Lequeux et al., 1979; Brooks et al., 2007), and variations in initial mass functions (e.g., Köppen et al., 2007). Still other studies have also seen significant scatter at low stellar masses (see for example Tremonti et al., 2004; Amorín et al., 2010).

Amorín et al. (2010) suggest that inherent variation in the L-Z and M-Z relations could result from these objects being relatively young and thus may still be converting large amounts of cold gas into stars. If these young galaxies have not had enough time for several generations of star formation to produce massive AGB stars, then we would expect very little absorption due to dust. The relative uniformity between the dispersions of the L-Z and M-Z relationships and between the slopes of the optical and near-IR L-Z relationships is consistent with this idea, suggesting no more absorption in the optical than in the near-IR, and thus very little dust is present in these low-luminosity galaxies. The fact that the scatter in the L-Z and M-Z relationships is small suggests that AGB stars do not play as significant of a role in determining the scatter in the NIR L-Z relationship for low-mass galaxies. In fact, in our sample it seems that AGB stars are balanced out by the effects of star formation histories. Whatever the actual source of the scatter may be, since we used the most reliable oxygen abundances and

distance estimates possible in constructing the L-Z and M-Z relationships, it appears that the dispersion for this sample is real as it is larger than observational errors. However, the "young galaxy" hypothesis faces other observational challenges.

3.7.2 N/O and the Young Galaxy Hypothesis

Garnett (1990) first showed that the N/O ratio in low metallicity star forming galaxies is relatively constant as a function of O/H (with a mean value of $\log(\mathrm{N/O}) = -1.46^{+0.10}_{-0.13}$) for these "plateau" objects. Later, Izotov & Thuan (1999) drew attention to the plateau with small dispersion in log (N/O) (-1.60 ± 0.02) in extremely metal-poor ($12 + \log(\mathrm{O/H}) \leq 7.6$) blue compact dwarf galaxies. They proposed that the absence of time-delayed production of N (and C) is consistent with the scenario that extremely metal-poor galaxies are now undergoing their first burst of star formation, and that they are therefore young, with ages not exceeding 40 Myr. They further argued that if this were true, then this would argue against the commonly held belief that C and N are produced by intermediate-mass stars at very low metallicities (as these stars would not have yet completed their evolution in these lowest metallicity galaxies). Nava et al. (2006) revisited the observed N/O plateau with a large set of objects and determined a mean value for the N/O plateau of -1.43 with a standard deviation of $^{+0.071}_{-0.084}$. They further concluded from a χ^2 analysis that only a small fraction of the observed scatter in N/O is intrinsic.

From the bottom panel of Figure 3.6, we see that the sample assembled here also shows a plateau in N/O of $\log(\mathrm{N/O}) = -1.56 \pm 0.05$. The level of the plateau in our data is slightly lover than found by Nava et al. (2006), but agrees fairly well with that found by Izotov & Thuan (1999). While the observed dispersion is larger than that found for the blue compact dwarfs by Izotov & Thuan (1999), the *intrinsic* dispersion agrees well for the two samples. Clearly the relatively constant N/O value is a common characteristic of dwarf star forming galaxies, and not just those undergoing a current burst of star formation. van Zee et al. (2006) demonstrated that Leo A, with $12 + \log(\mathrm{O/H}) = 7.38 \pm 0.10$ and $\log(\mathrm{N/O}) = -1.53 \pm 0.09$, and GR 8, with $12 + \log(\mathrm{O/H}) = 7.65 \pm 0.06$ and $\log(\mathrm{N/O}) = -1.51 \pm 0.07$, which are *not* blue compact dwarf galaxies, are consistent with this plateau in $\log(\mathrm{N/O})$ at low values of O/H. However, both Leo A and GR 8 have detailed star formation histories derived from *Hubble Space Telescope* observations

of their resolved stars which clearly show that the bulk of their star formation occurred well before the last 40 Myr (Tolstoy et al., 1998; Cole et al., 2007; Dohm-Palmer et al., 1998; Weisz et al., 2011). In fact, Weisz et al. (2011) show, from a nearly volume limited sample, that the majority of dwarf galaxies formed the bulk of their stellar mass prior to z $\sim$ 1, regardless of current morphological type. Since the low mass, metal-poor galaxies in the present sample and works cited appear to have nearly the same value of N/O, regardless of whether they have a current burst of star formation, it would seem that the young galaxy hypothesis is not a valid explanation for the plateau in N/O at low metallicity.

If the plateau in N/O is not due to young galaxy ages, what is its cause? Clearly nitrogen is behaving as a primary element at low metallicities. Henry et al. (2006) considered various scenarios and concluded that a wide range were consistent with the observations. At this point, a definitive explanation for the N/O plateau appears elusive.

3.7.3 Best Estimate of Abundances

Determining an accurate and reliable oxygen abundance for an individual H II region depends on measuring the combination of bright nebular and faint auroral emission lines (the direct method). Many studies have emphasized that a direct abundance is not without systematic uncertainties. Specifically, due to the high temperature sensitivity of the direct method, inhomogeneous temperature distributions will lead to abundance underestimates. The uncertainty in the absolute oxygen abundance determination by this method is $\sim$ 0.1 dex, but the error in relative metallicities is likely to be $<<$ 0.1 dex (Kewley & Ellison, 2008). However, Bresolin (2007) warns that T_e-based determinations only provide a lower limit if the temperature fluctuations are substantial.

In the absence of a temperature-sensitive auroral line detection, a mix of strong emission lines are used as a proxy for metallicity (strong-line methods: empirical, semi-empirical, and theoretical calibrations). Strong-line calibrations are limited by sample selection effects, potentially making them appropriate for ranking objects on a single scale, but not useful for determining an absolute metallicity as the various methods do not converge (see e.g., Yin et al., 2007; Kewley & Ellison, 2008; Bresolin et al., 2009a; Berg et al., 2011). If a strong-line method must be used, Stasińska (2010) recommends only using a strong-line method for nebulae having *the same properties as those of the*

calibration sample.

Oey & Shields (2000); van Zee & Haynes (2006); van Zee et al. (2006); Yin et al. (2007); Kewley & Ellison (2008); Pérez-Montero & Contini (2009); Amorín et al. (2010); Moustakas et al. (2010), and others have investigated several strong-line calibrations including the O3N2 method, the N2 method, and the R_{23} index, finding inconsistencies between methods that were largely related to variations in the hardness of the ionizing radiation field, nitrogen abundance, and/or age of the stellar cluster. There are several strong-line methods to chose from, but when compared they all have similar uncertainties of 0.1-0.2 dex and discrepancies between them as large as 0.6 dex (e.g., Liang et al., 2006; Bresolin, 2007; Yin et al., 2007; Kewley & Ellison, 2008). Improvements have been made in strong-line calibrations by the introduction of photoionization models to simultaneously fit the most prominent emission lines (e.g., Tremonti et al., 2004; Brinchmann et al., 2004). However, Yin et al. (2007) found the MPA/JHU simultaneous line fitting SDSS abundances determined from the Charlot et al. (2006) photoionization models overestimate oxygen abundances by $\sim$0.34 dex compared to direct abundances. They postulate the difference to be due to the models treatment of the onset of secondary nitrogen production, and thus could be eliminated with improved modeling. One possible exception is the ONS calibration of Pilyugin et al. (2010), for which they find deviations from T_e-based oxygen abundances of just $\sim$0.075 dex.

Here we investigate a subset of strong-line abundances for our objects with direct abundances. Following the methodology of Berg et al. (2011), we calculated oxygen abundances from their strong lines for the 31 objects with direct abundances listed in Table 4.6. We determined abundances using the R_{23} calibration of McGaugh (1991), the ONS calibration of Pilyugin et al. (2010), and the N2 and O3N2 calibrations updated by Pérez-Montero & Contini (2009, hereafter PMC09). The R_{23} calibration of McGaugh (1991) produces a bi-valued solution, so to discriminate between the two branches McGaugh (1994), van Zee et al. (1998), and others advised using the ratio of I([N II] λ6584)/I([O II] λ3727). McGaugh (1994) suggested that [N II]/[O II] is approximately < 0.1 for low abundances and > 0.1 for high abundances, giving a rough distinction between lower and upper branches. Using this distinction, we selected the appropriate branch calibration for each object. Note that for metal poor objects with enhanced nitrogen, [N II]/[O II] becomes a biased discriminator (e.g., Yin et al., 2007;

Berg et al., 2011; Pérez-Montero et al., 2011). In a similar fashion, the ONS method of Pilyugin et al. (2010) requires two discriminators, [N II] and [N II]/[S II], to distinguish between three classes of H II regions.

We followed Berg et al. (2011) and assumed $T_e = 1.25 \times 10^4$ K to examine N/O ratios and calculate abundances with the N2 and O3N2 calibrations of PMC09. This correction may be important for NGC 2537 and UGC 4393, which appear to have somewhat discrepant nitrogen abundances (nitrogen enrichment for log(N/O) > -1.0). The other objects in this sample have average N/O ratios for their masses (see e.g., Berg et al., 2011). The results are tabulated in Table 4.9.

The mean offsets and dispersions relative to the direct abundances are calculated and given at the bottom of Table 4.9. Table 4.9 shows that all four methods have significant dispersions, with the ONS method showing the smallest dispersion (although larger than anticipated) and the O3N2 method having the largest. The ONS method also has the smallest mean offset. Figure 7 presents a plot of differences between the R_{23} and ONS method abundances and the direct abundances as a function of abundance. This illustrates the results of Table 4.9, that the ONS method has a smaller dispersion and a smaller mean offset from the direct method. Thus, our data favor the ONS method, but do not support the claim of the very small error as found by Pilyugin et al. (2010). In Figure 7 we find no clear trend exists between the direct method and the strong-line methods, implying that simple calibrations between methods are not possible.

With the relatively precise M-Z and L-Z relationships in place, and their correspondingly low dispersions, oxygen abundances for normal (non-starburst) low-luminosity galaxies can be inferred with relatively high confidence without a spectrum. In fact, given reliable distance and photometry measurements, the resulting luminosity and mass estimates can be used as more reliable predictors of oxygen abundance than some strong-line calibrations. As counter-intuitive as this idea may seem, it is a natural consequence of the inability of some strong-line methods to accurately predict the metallicity of individual H II regions. Studies of abundances in dwarfs which do not reproduce the L-Z and M-Z relationships, therefore, should raise suspicions concerning methodology.

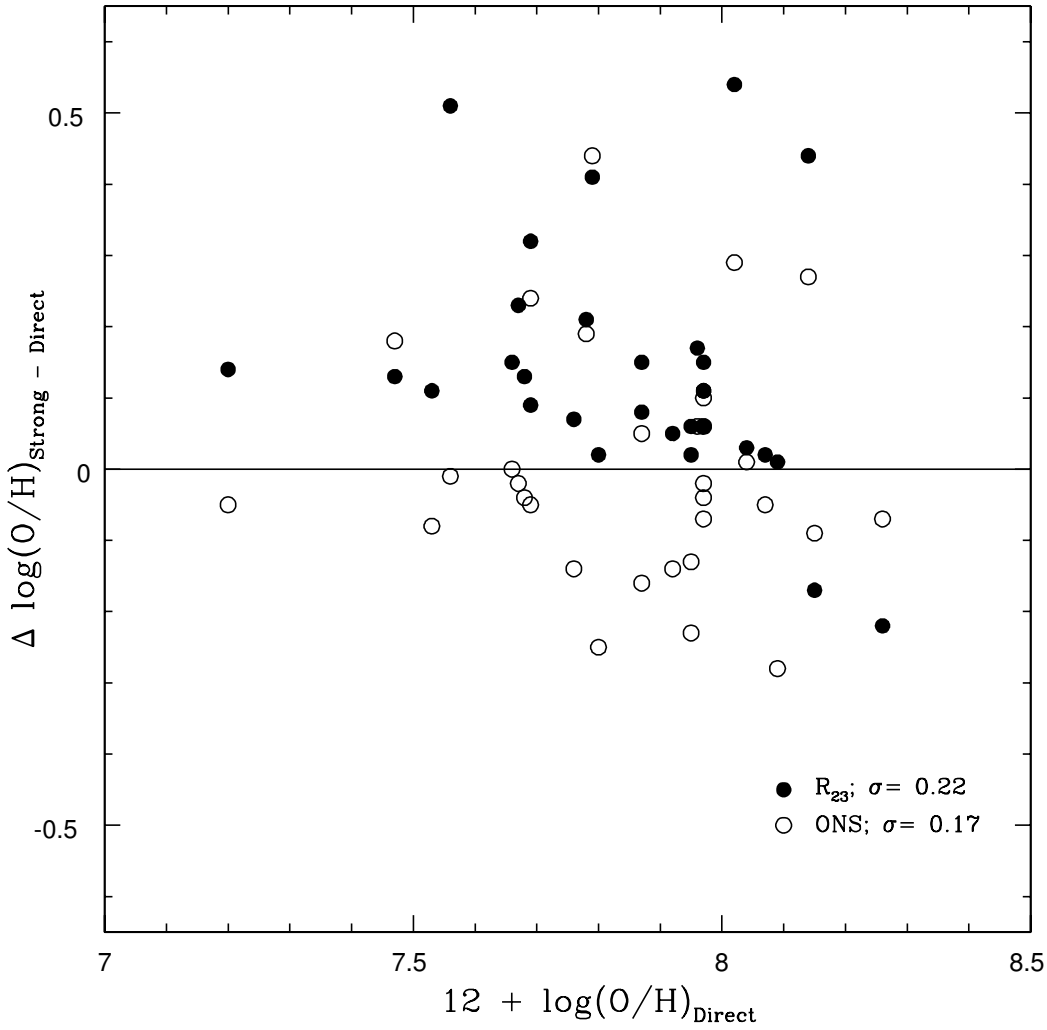

Figure 3.7: We plot the difference in oxygen abundances determined via the direct method and strong-line methods versus the direct method oxygen abundances for the objects listed in Table 4.6. The open circles display the comparison for strong-line abundances determined via the R_{23} method of McGaugh (1991) and the closed circles the ONS calibration of (Pilyugin et al., 2010). The absence of clear trends imply that simple calibrations between methods are not possible.

Table 3.8. Strong-Line Oxygen Abundances for Our Direct Detection Galaxies

		12 + log(O/H)			
Galaxy	[N II]/[O II]	R_{23}	ONS	N2	O3N2
UGC 521 A	0.03	7.90 (L)	7.65 (3)	7.87	8.14
UGC 695 E	0.04	8.01 (L)	7.93 (3)	8.13	8.34
UGC 1056 A	0.04	8.08 (L)	8.03 (3)	8.15	8.29
UGC 1176 A	0.05	8.03 (L)	7.90 (3)	8.04	8.18
NGC 784 A	0.05	8.08 (L)	7.95 (3)	8.02	8.15
UGC 2716 A	0.04	8.08 (L)	7.93 (3)	7.99	8.15
NGC 2537 A	0.14	8.58 (U)	8.41 (2)	8.27	8.29
UGC 4278 A	0.03	7.78 (L)	7.64 (3)	7.88	8.19
NGC 2552 A	0.10	7.98 (L)	8.06 (3)	8.12	8.20
UGC 4393 B	0.12	8.56 (U)	8.31 (2)	8.16	8.19
UGC 5139 A	0.04	7.97 (L)	7.78 (3)	7.94	8.16
IC 559 A	0.05	8.09 (L)	8.02 (3)	8.14	8.26
UGC 5272 A	0.03	7.95 (L)	7.71 (3)	7.73	8.04
UGC 5340 A	0.03	7.34 (L)	7.15 (3)	7.51	8.09
UGC 5423 A	0.06	7.99 (L)	7.97 (3)	8.02	8.17
UGC 5797 A	0.06	8.13 (L)	8.02 (3)	7.92	8.07
UGC 5923 A	0.06	8.20 (L)	8.23 (2)	8.26	8.31
NGC 3738 A	0.07	8.07 (L)	8.05 (3)	8.15	8.24
NGC 3741 A	0.03	7.81 (L)	7.64 (3)	7.87	8.17
UGC 6817 A	0.03	7.64 (L)	7.45 (3)	7.69	8.10
NGC 4163 A	0.03	8.07 (L)	7.55 (3)	8.18	8.52
CGCG 269-049 A	0.03	7.60 (L)	7.65 (3)	7.72	8.05
UGC 7577 A	0.05	8.12 (L)	8.07 (3)	7.94	7.97
NGC 4449 A	0.07	8.04 (L)	8.19 (2)	8.08	8.19
UGC 7605 A	0.03	7.81 (L)	7.66 (3)	7.94	8.22
NGC 4656 A	0.03	8.10 (L)	7.81 (3)	7.62	7.96
UGC 8201 A	0.02	7.82 (L)	7.55 (3)	7.85	8.17
UGC 8508 A	0.03	7.83 (L)	7.62 (3)	7.85	8.14
UGC 8638 A	0.04	8.01 (L)	7.82 (3)	7.93	8.13
UGC 8837 A	0.06	8.02 (L)	7.92 (3)	8.20	8.38
NGC 5477 A	0.04	7.97 (L)	7.72 (3)	7.81	8.08
Offset	···	0.14	-0.001	0.12	0.32
Dispersion	···	0.22	0.17	0.24	0.42

Note. — Strong-line abundances are calculated for the 31 objects with spectra containing an [O III] λ4363 signal-to-noise of 4 or greater. Four strong-line calibrations are given: 1) The R_{23} method of McGaugh (1991) is listed in column (3), where the appropriate branch was selected based on the [N II]/[O II] ratio given in column (2), with [N II]/[O II]$\approx$ 0.1 drawing the division. Branch selection is denoted by (L) for lower branch and (U) for upper branch. 2) The ONS calibration of Pilyugin et al. (2010) is given in column (4). Pilyugin et al. (2010) divides their calibration into 3 classes of H II regions, where we have used (1) for regions with $\log(N_2) > -0.1$, (2) for $\log(N_2) < -0.1$ and $\log(N_2/S_2) > -0.25$, and (3) for $\log(N_2) < -0.1$ and $\log(N_2/S_2) < -0.25$. 3) The N2 calibration, corrected for N/O ratio variations by PMC09, is given in column (5). 4) The O3N2 calibration, also corrected for N/O ratio variations by PMC09, is given in column (6). The last two rows give the average offset and dispersion of the strong-line abundances from their Direct abundance counterparts.

3.8 Conclusions

We have determined uniform oxygen abundance metallicities for 31 low-luminosity galaxies in the *Spitzer* LVL survey. With high-resolution spectral observations taken at the MMT, we were able to measure the intrinsically faint [O III] λ4363 fluxes at strengths of 4σ or greater and explicitly determine electron temperatures. Metallicity measurements are important for characterizing many other properties, especially when the more reliable direct method is used. However, metallicity relationships tend to suffer from small number statistics in the low-luminosity regime. In particular, these measurements allowed us to better characterize the luminosity-metallicity and mass-metallicity relationships by doubling the number of reliable low-luminosity measurements. We created a "Combined Select" sample of objects that have both reliable direct oxygen abundance determinations and distances estimated from the tip of the red giant branch or Cepheid variables. With this sample, we find:

(1) Both the luminosity-metallicity and the mass-metallicity relationships agree well with previous relationships defined for low luminosities.

(2) From the 38 objects making up the "Combined Select" sample, we found an optical L-Z relationship of $12 + \log(\mathrm{O/H}) = (6.27 \pm 0.21) + (-0.11 \pm 0.01)M_B$, with a dispersion of $\sigma = 0.15$. In comparison, the near-IR L-Z relationship for this data is $12 + \log(\mathrm{O/H}) = (6.10 \pm 0.21) + (-0.10 \pm 0.01)M_{[4.5]}$, with a dispersion of $\sigma = 0.14$. While the slopes of the two L-Z relationships agree, our findings confirm the work of L06 in that the near-IR relationship has lower scatter.

(3) By converting NIR luminosity to a stellar mass estimate, we determined the M-Z relationship for our data to be $12 + \log(\mathrm{O/H}) = (5.61 \pm 0.24) + (0.29 \pm 0.03)M_\star$, with a dispersion of $\sigma = 0.15$. In agreement with the idea that mass is more fundamentally related to metallicity than luminosity, we find that the intrinsic scatter of the optical L-Z, NIR L-Z, and M-Z relationships decreases from 0.13 to 0.12 to 0.08.

(4) However, the total dispersion of the M-Z relationship was measured to be no smaller than the L-Z relationships. This suggests, given a reliable distance measurement and appropriate photometry, luminosity is just as strong of a metallicity indicator as stellar mass.

(5) Furthermore, with the dispersions in luminosity and mass roughly equal, either may be used in combination with a reliable distance determination to estimate metallicity of a low-luminosity dwarf with more confidence than when using strong-line calibrations.

(6) Our observations of N/O abundances are in agreement with previous studies. We find a positive correlation between N/O ratio and B-V color for $0.05 \lesssim B-V \lesssim 0.75$; $\log(\mathrm{N/O}) = (-1.92 \pm 0.08) + (1.18 \pm 0.19) \times (B-V)$, with a dispersion of $\sigma = 0.14$.

(7) In agreement with observations of blue compact galaxies, there are no objects with high N/O ratio ($\log(\mathrm{N/O}) > -1.4$) below $12+\log(\mathrm{O/H})=7.7$. Since the typical low-luminosity galaxy in the Local Volume displays roughly constant star formation over the age of the universe, the small dispersion in N/O at low values of O/H cannot be due to the very recent birth of the galaxy.

3.9 Acknowledgements

Special thanks to John Moustakas and L. Andrew Helton for many scientifically stimulating and helpful discussions. DAB is grateful for support from a Penrose Fellowship and a NASA Space Grant Fellowship from the University of Minnesota. EDS is grateful for partial support from the University of Minnesota. Observations reported here were obtained at the MMT Observatory, a joint facility of the Smithsonian Institution and the University of Arizona. MMT observations were obtained as part of the University of Minnesota's guaranteed time on Steward Observatory facilities through membership in the Research Corporation and its support for the Large Binocular Telescope, and granted by NOAO, through the Telescope System Instrumentation Program (TSIP). TSIP is funded by the National Science Foundation.

This research has made use of NASA's Astrophysics Data System Bibliographic Services and the NASA/IPAC Extragalactic Database (NED), which is operated by the Jet Propulsion Laboratory, California Institute of Technology, under contract with the National Aeronautics and Space Administration. This work was initiated as part of the Spitzer Space Telescope Legacy Science Program and was supported by National Aeronautics and Space Administration (NASA) through contract 1336000 issued by the

Jet Propulsion Laboratory (JPL), California Institute of Technology (Caltech) under NASA contract 1407.

3.10 Appendix A: Strong-Line Abundances

In Table 4.10 we present strong-line abundances for the 12 objects in our sample without [O III] λ4363 detections. While these may not be as accurate as the direct abundances for the rest of our sample, they may be useful for studies of these individual galaxies. The O/H values derived using the ONS method for both these 12 objects (Table 4.10) and the objects with direct abundances (Table 4.9) are plotted in Figure 3.8 where they are compared to our direct abundances. The two methods display coincident trends in metallicity with mass, yet the O/H abundances derived via the ONS calibration have a larger dispersion. We have not conducted a statistical comparison, as not all galaxies have accurate distances, and the subset with accurate distance is quite small.

3.11 Appendix B: 70/160 μm Color Temperature-Metallicity Outliers

As noted in § 3.2.2, two objects were of particular interest to this study (UGC 10818 and UGC 4393) because they appear to be outliers from the global trend of 70/160 μm color temperature as a function of metallicity as determined by Engelbracht et al. (2008). Specifically, based on *Spitzer* observations of 66 starburst galaxies, they showed that the far-infrared color temperature of large dust grains increases toward lower metallicity down to 12 + log(O/H) $\sim$ 8. However, the oxygen abundances found by Engelbracht et al. (2008) for these two objects were based on the R_{23} strong-line estimator. Our new spectroscopic results indicate that both UGC 4393 and UGC 10818 (SHOC 567) are near the transition region between the upper and lower branches based on their [N II]/[O II] ratios, and thus the R_{23} method may not yield an accurate abundance for these systems.

While our observations of UGC 10818 are still ambiguous due to the degeneracy in the strong-line metallicity calibrations, we derive an oxygen abundance of 12 + log(O/H)

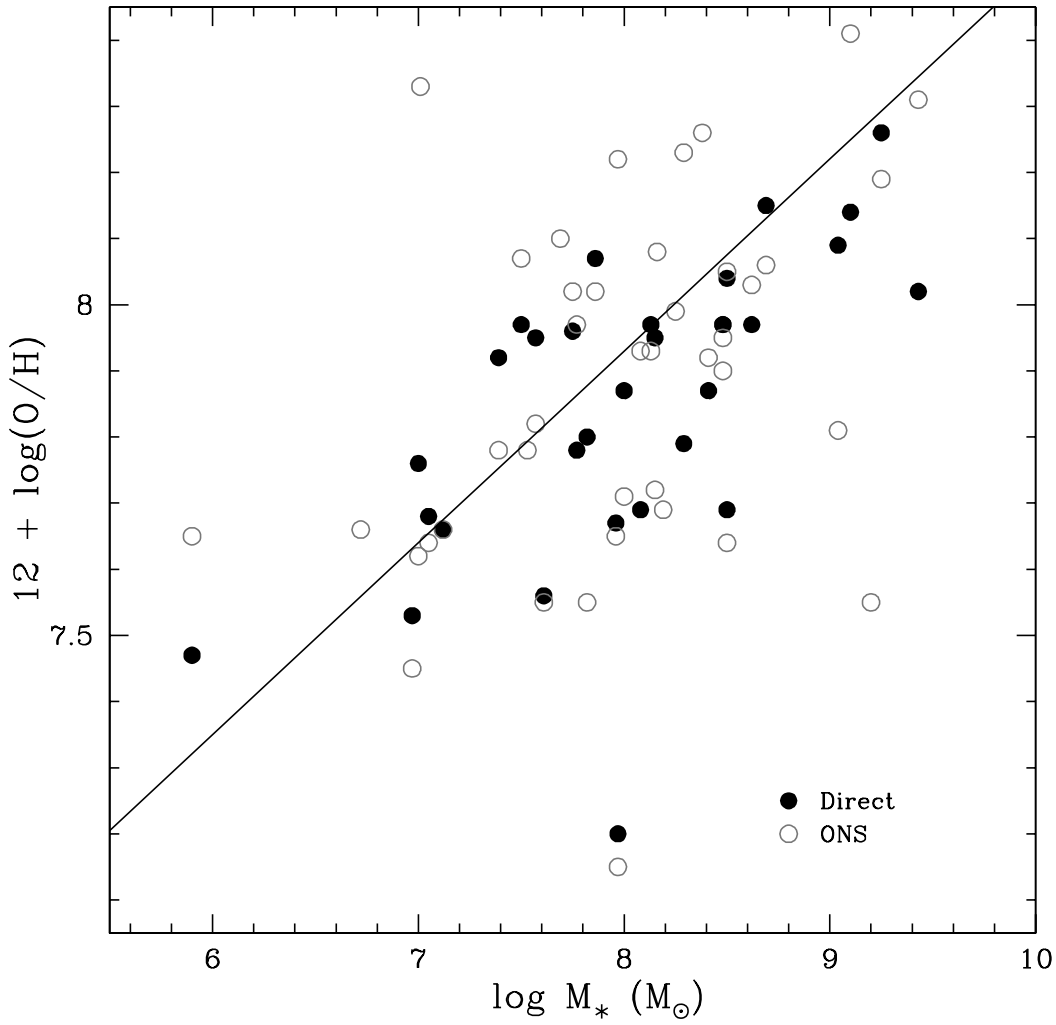

Figure 3.8: The strong-line ONS mass-metallicity relationship is depicted for all the objects for which we calculated strong-line abundances (see Section 2.9: Appendix A). The objects are plotted in comparison to direct abundances determined for the "Combined Select" sample. As a reference, we have plotted Equation 3.9, our M-Z relationship for the "Combined Select" sample, as a solid line. While scatter is apparent, the overall trend is well defined and the two sample coincide. Note that in terms of scatter thedirect method is an improvement over the ONS strong-line calibration.

= 7.82 based on the McGaugh (1991) R_{23} calibration. This increases the oxygen abundance of UGC 10818 by 0.51 dex compared to previous measurements and moves UGC 10818 (SHOC 567) closer to the original trend illustrated in Engelbracht et al. (2008). Conversely, the direct oxygen abundance of UGC 4393 was determined in this paper to be 12 + log(O/H) = 8.02 +/- 0.05, in agreement with the strong-line estimate presented in Engelbracht et al. (2008). Thus, at first glance, these new observations appear to only impact the location of one of the two most extreme outliers in the original plot.

Perhaps more importantly, we have reproduced the 70/160 μm color temperature versus 12 + log(O/H) plot of Engelbracht et al. (2008) with the addition of direct abundance objects from this work in Figure 3.9. Note that the star-bursting objects from Engelbracht et al. (2008) tend to have higher dust temperatures than the low intensity objects studied in this paper. This may mean that the trend of increasing far-infrared dust temperature with decreasing metallicity was just a slice of a larger picture, where the selected samples were limited by star formation rates, which biased the view to a more narrow window. With a more complete range of intensities in star forming galaxies now plotted, no clear trend emerges.

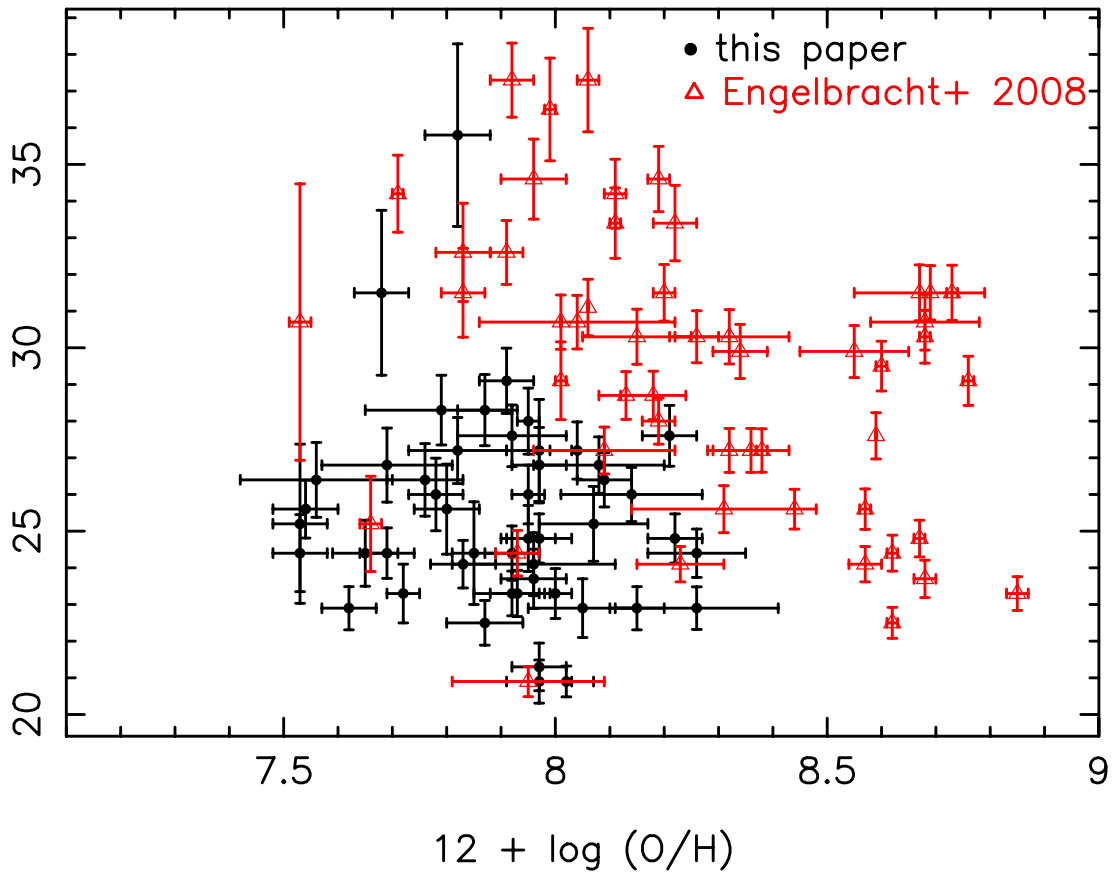

Figure 3.9: 70/160 μm color temperature versus 12 + log(O/H) is plotted for the objects presented in this paper with direct oxygen abundances. In comparison, star-bursting galaxies from Engelbracht et al. (2008) with strong-line abundances seem to have larger temperatures at a given metallicity.

Table 3.9. Strong-Line Oxygen Abundances for [O III] λ4363 Non-Detections

		12 + log(O/H)			
Galaxy	[N II]/[O II]	R_{23}	ONS	N2	O3N2
NGC 404	0.04	7.23 (L)	7.55 (3)	8.53	8.56
KKH 037	0.06	8.32 (U)	8.33 (1)	8.53	8.56
CGCG 035-007	0.05	8.00 (L)	8.10 (3)	8.57	8.37
UGC 5672	0.06	8.00 (L)	8.26 (3)	8.37	8.29
UGC 5692	0.15	8.40 (U)	8.08 (3)	8.53	8.31
UGC 6782	0.08	7.85 (L)	···	8.18	8.27
UGC 6900	0.12	8.00 (U)	7.69 (3)	8.08	8.17
UGC 7599	···	8.09 (U)	···	···	···
UGC 7639	0.05	7.77 (L)	7.99 (3)	8.50	8.42
UGC 8245	0.04	7.59 (L)	7.78 (3)	8.40	8.39
UGC 9405	0.11	7.77 (L)	8.22 (3)	8.63	8.40
UGC 10818	0.09	7.82 (L)	···	8.45	8.29
KKH 098	0.04	7.61 (L)	7.66 (3)	8.17	8.27

Note. — Strong-line abundances are calculated for HII regions with no [O III] λ4363 detections. Most objects in our sample have at least one HII region with a direct abundance determination, but 12 objects have good spectra and no [O III] λ4363 measurement. Four strong-line calibrations are given for these objects: 1) The R_{23} method of McGaugh (1991) is listed in column (3), where the appropriate branch was selected based on the [N II]/[O II] ratio given in column (2). [N II]/[O II]$\approx$ 0.1 draws the branch division. Branch selection is denoted by (L) for lower branch and (U) for upper branch. 2) The ONS calibration of Pilyugin et al. (2010) is given in column (4). Pilyugin et al. (2010) divides their calibration into 3 classes of HII regions, where we have used (1) for regions with $\log(N_2) > -0.1$, (2) for $\log(N_2) < -0.1$ and $\log(N_2/S_2) < -0.25$, and (3) for $\log(N_2/S_2) > -0.25$. 3) The N2 calibration, corrected for N/O ratio variations by PMC09, is given in column (5). 4) The O3N2 calibration, also corrected for N/O ratio variations by PMC09, is given in column (6).

Chapter 4

New Radial Abundance Gradients for NGC 628 and NGC 2403

Accepted to be published in The Astrophysical Journal by D.A. Berg, E.D. Skillman, D.R. Garnett, K.V. Croxall, A.R. Marble, J.D. Smith, K. Gordon, & R.C. Kennicutt, Jr.

Abstract

Motived by recent ISM studies, we present high quality MMT and Gemini spectroscopic observations of H II regions in the nearby spiral galaxies NGC 628 and NGC 2403 in order to measure their chemical abundance gradients. Using long-slit and multi-object mask optical spectroscopy, we obtained measurements of the temperature sensitive auroral lines [O III] λ4363 and/or [N II] λ5755 at a strength of 4σ or greater in 11 H II regions in NGC 628 and 7 regions in NGC 2403. These observations allow us, for the first time, to derive an oxygen abundance gradient in NGC 628 based solely on "direct" oxygen abundances of H II regions: 12 + log(O/H) = (8.43±0.03) + (-0.017±0.002)×R_g (dex/kpc), with a dispersion in log(O/H) of σ = 0.10 dex, from 14 regions with a radial coverage of ∼2-19 kpc. This

is a significantly shallower slope than found by previous "strong-line" abundance studies. In NGC 2403, we derive an oxygen abundance gradient of 12 + log(O/H) = (8.48±0.04) + (-0.032±0.007)×R_g (dex/kpc), with a dispersion in log(O/H) of σ = 0.07 dex, from 7 H II with a radial coverage of ∼1-10 kpc.

Additionally, we measure the N, S, Ne, and Ar abundances. We find the N/O ratio decreases with increasing radius for the inner disk, but reaches a plateau past R_{25} in NGC 628. NGC 2403 also has a negative N/O gradient with radius, but we do not sample the outer disk of the galaxy past R_{25} and so do not see evidence for a plateau. This bi-modal pattern measured for NGC 628 indicates dominant contributions from secondary nitrogen inside of the R_{25} transition and dominantly primary nitrogen farther out. As expected for α-process elements, S/O, Ne/O, and Ar/O are consistent with constant values over a range in oxygen abundance.

4.1 Introduction

H II regions can be used to study absolute and relative abundances in the interstellar medium (ISM) of galaxies. Aller (1942) and Searle (1971) were the first to infer radial gradients in excitation across the disks of spiral galaxies. Since then, numerous studies have shown that, typically, spiral galaxies have radial abundance gradients in the sense of decreasing absolute abundances with increasing galactocentric radius. This trend was first measured in our own galaxy by Shaver et al. (1983) and was confirmed by observations of other nearby spiral galaxies (e.g., Pagel & Edmunds, 1981; Shields, 1990). Thus, spiral galaxies in the nearby universe with low inclinations offer the opportunity to measure chemical abundances and subsequently compare these abundances with variations in physical conditions.

The dust properties of the ISM in spiral galaxies (such as the dust-to-gas ratio and the abundance of polycyclic aromatic hydrocarbons (PAHs)) are known to show systematic radial variations. Previous studies have investigated the correlation between PAH emission and metallicity, and found that PAH emission drops below a critical metallicity of 12+log(O/H)≈8.0 in nearby dwarf galaxies (e.g., Engelbracht et al., 2005,

2008; Marble et al., 2010). These works suggest that metallicity may play a role in PAH processing, and thus PAH abundance relative to total dust content, but other factors such as star formation and/or the local radiation field density affect the excitation of those molecules. Other studies have supported the hypothesis that grain formation and modification is affected by local metallicity (e.g., Smith et al., 2007; Sandstrom et al., 2012).

Whether or not this result is universal is key to understanding PAH behavior in the ISM and requires a greater pool of reliable data. Smith et al. (2005) carried out a successful *Spitzer* observing campaign with deep, spatially resolved, low-resolution spectral maps from 5 to 38 microns in three nearby galaxies (M 101, NGC 628, and NGC 2403) to address these questions. Since the physical conditions in the ISM are likely important to the star formation process and play a role in the composition, conditions, and size distribution of dust grains, understanding the connection between chemical abundances and the physical conditions in the ISM is fundamental to understanding star formation and galaxy evolution. Thus we are motivated to measure reliable direct abundance gradients for NGC 628 and NGC 2403; these results are being incorporated into the PAH studies of Sandstrom et al. (2013) and Smith et al. (2013).

Detailed direct abundance studies exist for only a handful of spiral galaxies. For example, direct H II region abundances have been successfully measured for 20 high signal-to-noise H II region spectra in M 101 by Kennicutt et al. (2003a). However, only two H II region auroral line detections exist in the literature for NGC 628 (Castellanos et al., 2002), and so no direct oxygen abundance gradient has ever been reported. The H II regions of NGC 2403 have been studied by Garnett et al. (1997b), but there were concerns about the linearity of the detector used.

In order to place gradients on the same scale for comparison amongst galaxies, reliable and consistent derivations of abundances are needed (see, e.g., Moustakas et al., 2010). However, the vast majority of nebular abundance measurements for H II regions in spiral galaxies are based upon strong-line observations which lack a direct measurement of the electron temperature in the ionized gas. The conversion of these strong-line observations into chemical abundances can be very uncertain and biased (Kennicutt et al., 2003a; Bresolin, 2007; Yin et al., 2007; Pérez-Montero & Contini, 2009; Berg et al.,

2011), limiting their ability to provide meaningful comparisons between different galaxies. Therefore, a direct measurement of the electron temperature - typically derived from the ratio of auroral to collisionally excited lines - is needed for each H II region. Throughout the remainder of the paper, abundances determined in this fashion will be referred to as direct abundances. Since the auroral lines become exponentially weaker with decreasing temperature (increasing abundance), observations become increasingly challenging at higher metallicities (small radii in spiral galaxies). Nonetheless, with large telescope apertures and efficient spectrographs, it is possible to determine accurate chemical abundance gradients for spiral galaxies (e.g., Kennicutt et al., 2003a; Garnett et al., 2004; Bresolin, Kennicutt, & Garnett, 2004; Bresolin, 2007; Bresolin et al., 2009a,b; Bresolin , 2011; Zurita & Bresolin, 2012). Note that direct chemical abundances are not without problems (they assume a uniform temperature distribution, ignoring temperature fluctuations) and great progress is being made to overcome their limitations (e.g., Esteban et al., 2009; Peña-Guerrero et al., 2012; Nicholls et al., 2012). Even so, direct abundances do provide a stable and well understood scale by which to make comparisons between galaxies.

A major unresolved issue in H II region abundance studies is the importance of primary versus secondary production of nitrogen. Oxygen production is generally understood to be dominated by primary nucleosynthesis from massive stars and delivered early after a star formation event. Like oxygen, nitrogen can be produced by massive stars (and delivered early with the primary oxygen), as well as by intermediate mass stars (and delivered relatively later). Nitrogen can have both primary and secondary origins. Garnett (1990) found a relatively constant relationship in the N/O ratio versus O/H for low metallicity star-forming galaxies. At higher metallicities (i.e., $12+\log(\mathrm{O/H}) \geq 8.0$), secondary nitrogen production becomes increasingly significant, causing the average N/O to increase with O/H (Pagel, 1985). We can, therefore, use the radial relationship of N/O in spiral galaxies to determine which nucleosynthetic mechanisms are dominant.

A further goal of H II region spectroscopic studies it to measure α-element abundances as an observational constraint of the IMF and stellar nucleosynthesis models. Sulfur, neon, and argon are all α-process elements which are produced through hydrostatic burning and explosive nucleosynthesis: neon is a product of carbon burning,

while sulfur and argon are produced during oxygen burning. In a comprehensive study of M33, Kwitter & Aller (1981) found that Ne, N, S, and Ar gradients followed that which they derived for oxygen. The stellar nucleosynthesis calculations of Woosley & Weaver (1995) modeled these trends, indicating the α-elements and oxygen are produced mainly in massive stars in a small mass range, and thus are expected to trace each other closely. In contrast to this viewpoint, Willner & Nelson-Patel (2002) derived a neon gradient that is significantly shallower than the oxygen gradient observed in M33. While sulfur is also traditionally assumed to have a constant S/O ratio (Garnett, 1989), some specific cases, such as the work of Vilchez et al. (1988) on M33, find a slower decline of sulfur than oxygen with radius. Thus additional α-element observations are needed to properly constrain stellar nucleosynthesis models.

Here we present new MMT and Gemini observations of H II regions in NGC 628 and NGC 2403, which allow improved measurements of their chemical abundance gradients. These allow us to estimate the abundance gradient of NGC 628 for the first time solely from direct abundances, and to improve the abundance gradient of NGC 2403 by increasing the number of H II regions with direct abundance measurements. In Section 5.2 we describe the MMT and Gemini observations and how we processed the spectra. Emission line measurements and abundance determinations are detailed in § 5.3, which allows the discussion of the oxygen abundance gradient in § 4.4.1, the nitrogen abundance gradient in § 4.4.2, and of the sulfur, neon, and argon abundances in § 4.4.3. Finally, we summarize our findings in § 5.5.

4.2 New Spectroscopic Observations

4.2.1 NGC 628 Spectra

NGC 628 (M 74) is a late-type giant spiral ScI galaxy with a systematic velocity of 656 km s^{-1}. We adopt a distance of 7.2 Mpc (Van Dyk et al., 2006) and an inclination of $i \approx 5^{\circ}$ (Shostak & van der Kruit, 1984), with a resulting scale of 35 pc arcsec^{-1}. The optical parameters of NGC 628 are listed in Table 4.1. NGC 628 is an excellent target due to its small inclination, extended structure, and undisturbed optical profile. The gas-phase oxygen abundance of NGC 628 has been previously studied using long-slit spectroscopy (e.g., Talent, 1983; McCall et al., 1985; Zaritsky et al., 1994; Ferguson et

Table 4.1. Properties of NGC 628 and NGC 2403

Property	NGC 628	NGC 2403
R.A.	01:36:41.747	07:36:51.400
Dec.	15:47:01.18	65:36:09.20
Type	ScI	SABcd
Adopted D (Mpc)	7.2 ± 1.0[1]	3.16 ± 0.07[6]
m_B (mag)	9.95[2]	8.93[2]
Redshift	0.002192	0.000445
Inclination (degrees)	5[3]	60[7]
P.A. (degrees)	12[4]	126[8]
R_{25} (arcmin)	5.25[5]	10.95[5]
R_{25} (kpc)	10.95	10.07

Note. — Optical properties for NGC 628 and NGC 2403. Row 1 and 2 give the R.A. and Dec. of the optical center in units of hours, minutes, and seconds, and decrees, arcminutes, and arcseconds respectively. Row 5 lists redshifts taken from the NASA/IPAC Extragalactic Database. Row 8 gives the optical radius at the B_{25} mag arcsec^{-2} of the system. Row 9 gives the optical radius of the galaxy given the adopted distance.

References. — (1) Van Dyk et al. (2006); (2) Lee et al. (2011); (3) Shostak & van der Kruit (1984); (4) Egusa et al. (2009); (5) Kendall et al. (2011); (6) Jacobs et al. (2009); (7) Garnett et al. (1997b); (8) Fraternali et al. (2002)

al., 1998; van Zee et al., 1998; Bresolin, Kennicutt, & Garnett, 1999; Castellanos et al., 2002; Moustakas et al., 2010; Gusev et al., 2012; Cedrés et al., 2012), and integral field spectroscopy (e.g., Rosales-Ortega et al., 2011). Using strong-line abundances, these studies mostly found a constant gradient out to $R_g \sim 1.7 \cdot R_{25}$. In contrast, Rosales-Ortega et al. (2011) found a trimodal oxygen abundance gradient, where the innermost distribution is nearly flat, followed by a steep negative gradient out to R_{25}, and another nearly constant gradient beyond the optical edge of the galaxy. Additionally, they found that the slope of the gradient depends strongly on the abundance calibrator used, concluding that this may be due to the potential for [N II]-based empirical indices to overestimate oxygen abundance at high N/O ratios and vice versa (see e.g., Pérez-Montero & Contini, 2009).

New MMT and Gemini observations were acquired in order to achieve high signal-to-noise (S/N) spectra with the goal of detecting the faint [O III] λ4363 or [N II] λ5755 auroral lines at a strength of 4σ or higher. The Gemini observations were obtained from two multi-slit fields covering the inner parts of NGC 628 and these were supplemented by MMT observations of individual H II regions in the outer parts of NGC 628.

Intermediate-resolution spectra of H II regions in NGC 628 were obtained with the Gemini Multi-Object Spectrographs (GMOS) (Hook et al., 2004) on the UT dates of 2006 September 21 and November 17. The multi-object mode of GMOS, which uses custom-designed, laser-milled masks, offers the possibility of obtaining spectra of many H II regions simultaneously. Pre-imaging in an Hα filter was used to identify H II regions and determine accurate astrometry for the masks. H II regions were selected based on high Hα surface brightness and a large radial coverage of the disk.

Two masks were observed in queue mode, one of the North-West corner of NGC 628, and one placed on the South-East corner. The NW and SE masks contained slits 1.5″ wide covering 7 and 8 different H II regions respectively. Slit lengths varied between 15-50″ depending on the the size of the targeted H II region and the proximity of other slits on the mask. Both blue and red spectra were obtained using a 600 line grating, giving a resolution of 0.45 Å per pixel and a full width half maximum resolution of $\approx$ 6 Å. The red side additionally used the GG455_G0305 order blocking filter. Typical exposure times were 3×1675 seconds with the mask fixed to a position angle of zero, and the observations were obtained near transit. Observations were centered at 4600 Å,

4625 Å, and 4650 Å in the blue, and 6100 Å, 6125 Å, and 6150 Å in the red, to ensure full spectral coverage across the detector gaps.

The NGC 628 MMT observations were obtained with the Blue Channel spectrograph (Schmidt et al., 1989) on the UT dates of 2008 October 30-November 1, 2009 June 15-22, and 2010 January 11-12. Sky conditions varied, but data were only acquired during minimal cloud coverage and approximately arcsecond seeing. A 500 line grating, $1''$ slit, and UV-36 blocking filter were used, yielding an approximate dispersion of 1.2 Å per pixel, a full width at half maximum resolution of $\lesssim 3$ Å, and a wavelength coverage of 3690–6790 Å. The MMT and Blue Channel spectrograph combination provided the balance between sensitivity, resolution, and wavelength coverage conditions necessary to measure all emission lines relevant to oxygen abundance determinations. Bias frames, flat-field lamp images, and sky flats were taken each night. Multiple standard stars from Oke (1990) with spectral energy distributions peaking in the blue and containing minimal absorption were observed throughout the night using a $5''$ slit over a range of airmasses.

In each H II region, the slit center was aligned with Hα emission such that the surface brightness over the area of the slit was maximized. Typically, three 1200 or 1800 second exposures were made for the MMT observations, with the slit at a fixed position angle which approximated the parallactic angle at the midpoint of the observation. This, in addition to observing the galaxies at airmasses less than 1.5, served to minimize the wavelength-dependent light loss due to differential refraction (Filippenko, 1982).

Finally, combined helium, argon, and neon arc lamps were observed at each pointing at the MMT, while copper-argon arc lamps were obtained at GEMINI for accurate wavelength calibration. Tables 5.1 and 5.2 list the log information for both the GMOS and MMT observations. Figure 5.1 shows the R-band continuum and Hα continuum-subtracted images for NGC 628, with slit positions from Tables 5.1 and 5.2 shown with black lines centered on red circles. The slit centers are marked in the Hα image by red circles.

Table 4.2. Logs for NGC 628 Gemini Observations

NGC 628 GMOS Slits								
(1) H II Region	(2) Alternate IDs	(3) R.A. (2000)	(4) Dec. (2000)	(5) Slit Size	(6) Slit PA (deg)	(7) T_{int} (sec)	(8) Offset (R.A., Dec.) (arcsec)	(9) R_g (kpc)
NGC628+041-029		01:36:44.50	15:46:32.3	1.5"×15"	0.0	3 × 1675	41.3, -28.9	1.77±0.25
NGC628-034+044		01:36:39.46	15:47:45.0	1.5"×20"	0.0	3 × 1675	-34.3, 43.8	1.95±0.27
NGC628+009+076		01:36:42.34	15:48:17.0	1.5"×20"	0.0	3 × 1675	8.9, 75.8	2.66±0.37
NGC628-076-029		01:36:36.71	15:46:32.7	1.5"×40"	0.0	3 × 1675	-75.6, -28.5	2.83±0.39
NGC628-059+084		01:36:37.84	15:48:24.7	1.5"×20"	0.0	3 × 1675	-58.6, 83.5	3.57±0.50
NGC628+082-074		01:36:47.19	15:45:47.0	1.5"×40"	0.0	3 × 1675	81.6, -74.2	3.86±0.54
NGC628+057-106		01:36:45.53	15:45:15.6	1.5"×20"	0.0	3 × 1675	56.7, -105.6	4.19±0.58
NGC628-134+069		01:36:32.82	15:48:09.8	1.5"×15"	0.0	3 × 1675	-133.9, 68.6	5.27±0.73
NGC628+083-140		01:36:47.31	15:44:41.6	1.5"×20"	0.0	3 × 1675	83.4, -139.6	5.69±0.79
NGC628-044-159		01:36:38.79	15:44:22.4	1.5"×30"	0.0	3 × 1675	-44.4, -158.8	5.76±0.80
NGC628-002+182		01:36:41.61	15:50:03.3	1.5"×30"	0.0	3 × 1675	-2.1, 182.1	6.36±0.89
NGC628+185-052		01:36:54.11	15:46:09.2	1.5"×15"	0.0	3 × 1675	185.4, -52.0	6.75±0.94
NGC628-190+080		01:36:29.08	15:48:21.4	1.5"×15"	0.0	3 × 1675	-190.0, 80.2	7.23±1.00
NGC628-090+186		01:36:35.76	15:50:07.2	1.5"×40"	0.0	3 × 1675	-89.8, 186.0	7.22±1.00
NGC628+240+368		01:36:57.73	15:47:08.9	1.5"×50"	0.0	3 × 1675	239.7, 367.7	15.33±2.13

Note. — Observing logs for H II regions observed in NGC 628 using GMOS on the UT dates of 21 September 2006 and 17 November 2006. H II region ID is listed in Column (1). Column (2) is present for listing literature IDs, but none are available. The right ascension and declination of the individual H II regions are given in units of hours, minutes, and seconds, and decrees, arcminutes, and arcseconds respectively. The position angle (PA) gives the rotation of the slit counter clockwise from North. The H II region distances from the center of the galaxy are listed in Column (9), where the uncertainty in the distance has been propagated to the galactocentric radii.

Table 4.3. Logs for NGC 628 MMT Observations

NGC 628 MMT Slits								
(1) H II Region	(2) Alternate IDs	(3) R.A. (2000)	(4) Dec. (2000)	(5) Slit Size	(6) Slit PA (deg)	(7) T_{int} (sec)	(8) Offset (R.A., Dec.) (arcsec)	(9) R_g (kpc)
NGC628+253+011	F B	01:37:12.49	15:47:12.2	1"×180"	68.0	3 × 1200	253.5, 11.0	8.89±1.24
NGC628+267+017		01:37:26.40	15:47:17.8	1"×180"	68.0	3 × 1200	267.4, 16.6	9.38±1.31
NGC628+277+020		01:37:35.67	15:47:21.6	1"×180"	68.0	3 × 1200	276.7, 20.4	9.72±1.35
NGC628+295-016	vZ 6	01:37:01.39	15:46:45.5	1"×180"	30.0	3 × 1800	294.6, -15.7	10.34±1.44
NGC628-277+241	F C	01:31:45.97	15:55:01.8	1"×180"	72.0	3 × 1800	-277.3, 240.7	12.85±1.79
NGC628-288+240		01:31:35.31	15:55:01.0	1"×180"	72.0	3 × 1800	-288.0, 239.9	13.12±1.82
NGC628+185+356	F E	01:39:59.43	15:58:53.1	1"×180"	-26.0	3 × 1800	185.3, 355.8	14.01±1.95
NGC628+186+425		01:39:59.88	16:00:02.1	1"×180"	-26.0	3 × 1800	185.7, 424.8	16.19±2.25
NGC628+503+208	F F	01:37:15.26	15:50:29.1	1"×180"	-35.0	3 × 1800	502.7, 207.9	19.04±2.65

Note. — Observing logs for H II regions observed in NGC 628 at the MMT on the UT dates of 31 October 2008. H II region IDs are listed in Column (1). Other literature IDs are given in Column (2): Ferguson et al. (1998, F) and van Zee et al. (1998, vZ). The right ascension and declination of the individual H II regions are given in units of hours, minutes, and seconds, and decrees, arcminutes, and arcseconds respectively. The position angle (PA) gives the rotation of the slit counter clockwise from North. The H II region distances from the center of the galaxy are listed in Column (9), where the uncertainty in the distance has been propagated to the galactocentric radii.

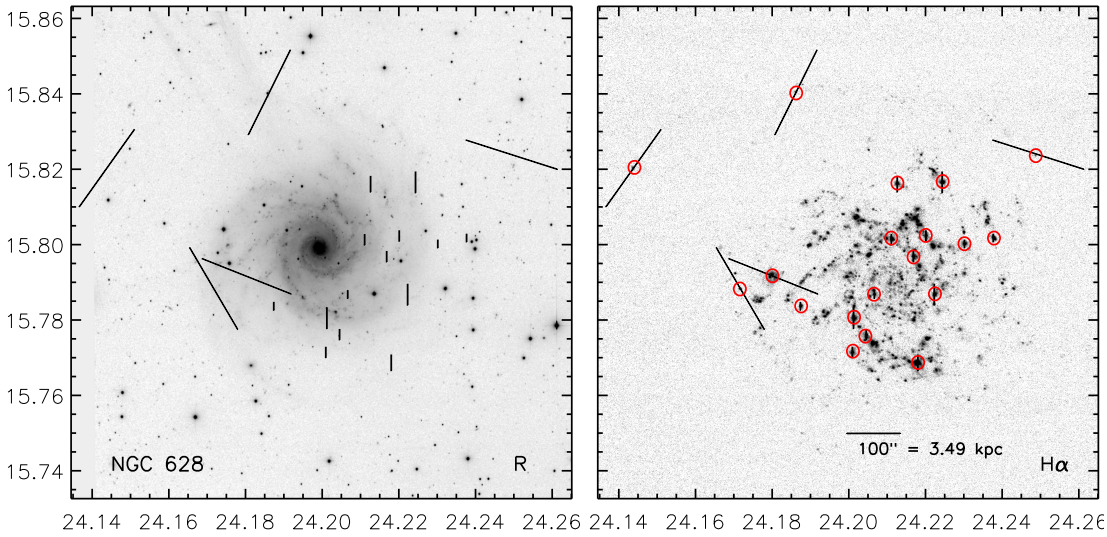

Figure 4.1: R-band and continuum-subtracted Hα images of NGC 628 (van Zee et al., in prep.). The lines represent the various slit positions observed at Gemini and the MMT. The central slit positions targeted H II regions and are indicated with red circles. See Tables 5.1 and 5.2 for more details.

4.2.2 NGC 2403 Spectra

As a bright, nearby galaxy with a favorable inclination, NGC 2403 allows observations of the chemical composition throughout its disk. NGC 2403 is an intermediate luminosity, isolated spiral SABcd galaxy in the M81 Group. We adopt a distance of 3.16 Mpc (Jacobs et al., 2009) and an inclination of $\approx 60^{\circ}$ with a resulting scale of 15.3 pc arcsec^{-1}. The optical parameters of NGC 2403 are listed in Table 4.1. Several strong-line spectroscopic studies relevant to our work exist for NGC 2403 (e.g., McCall et al., 1985; Fierro et al., 1986; van Zee et al., 1998). In contrast, Garnett et al. (1997b) measured direct abundances using the [O III] λ4363, [S III] λ6312, and [O II] λ7320-7330 emission lines to determine the electron temperatures for 9 H II regions. Although the [O III] λ4363 line was detected at high confidence in these regions, there were some lingering concerns about the effects of the non-linearity of the IPCS detector that appear at moderately high count rates (Jenkins, 1987). Thus, checking on the reliability of the previous observations and increasing the number of measurements and radial coverage is desirable.

New MMT observations were acquired in order to achieve high signal-to-noise (S/N) spectra with the goal of measuring direct abundances. Observations for NGC 2403 were acquired using the Blue Channel Spectrograph at the MMT on the UT dates of 2006 February 1-4. A setup similar to the NGC 628 observations was used, but the exposure time was varied corresponding to the surface brightness of the region. A 500 mm^{-1} grating was used providing a 3650-6790 Å coverage. The H II regions of NGC 2403 have been identified and cataloged by Véron & Sauvayre (1965), Hodge & Kennicutt (1983), and Sivan et al. (1990). Targets were chosen to overlap with the sample from Garnett et al. (1997b, here after referred to as G97) and also to improve the radial coverage. For five of the targets, a 832 mm^{-1} grating was also used, providing additional wavelength coverage from 5495 to 7405 Å.

The log information for the NGC 2403 MMT observations are tabulated in Table 5.3. Figure 5.2 shows the R-band continuum and Hα continuum-subtracted images for NGC 2403, with central slit positions from Table 5.3 indicated by red circles for targets overlapping with the G97 sample and by red squares for new targets.

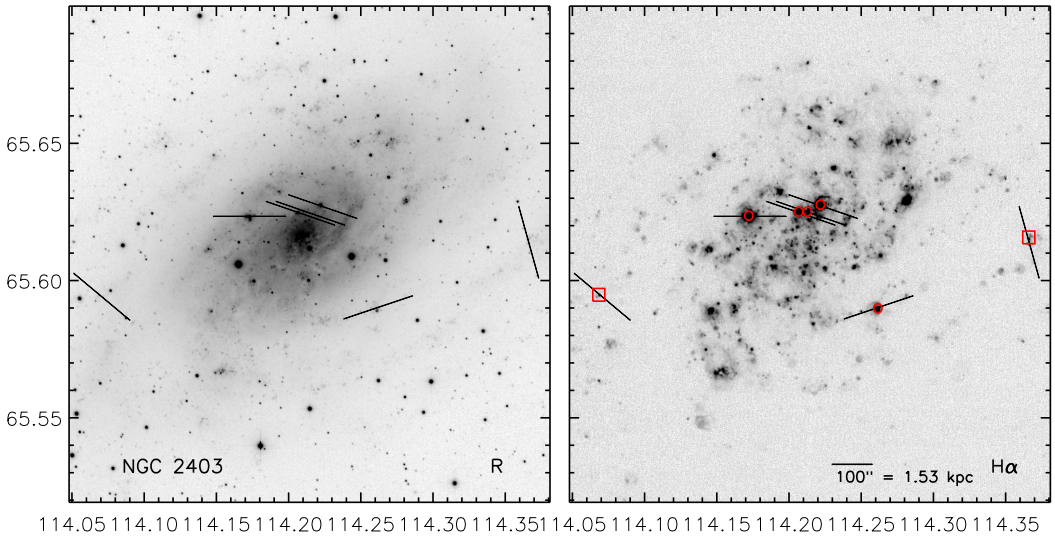

Figure 4.2: R-band and continuum-subtracted Hα images of NGC 2403 (van Zee et al., in prep.). The lines represent the various slit positions observed at the MMT, where the central slit positions from Table 5.3 are indicated by red circles for targets overlapping with the G97 sample and by red squares for new targets. See Table 5.3 for more details.

Table 4.4. Logs for NGC 2403 MMT Observations

NGC 2403 MMT Slits								
(1) H II Region	(2) Alternate IDs	(3) R.A. (2000)	(4) Dec. (2000)	(5) Slit Size	(6) Slit PA (deg)	(7) T_{int} (sec)	(8) Offset (R.A., Dec.) (arcsec)	(9) R_g (kpc)
NGC2403-007+036	VS 35, HK 313	07:36:50.3	65:36:45	1"×180"	-71.5	6 × 900	-7, 36	0.87±0.02
NGC2403-030+045	VS 24, HK 361	07:36:46.6	65:36:54	1"×180"	-71.5	6 × 900	-30, 45	0.97±0.02
NGC2403+013+031	VS 38, HK 270	07:36:53.5	65:36:40	1"×180"	-71.5	6 × 900	13, 31	1.01±0.02
NGC2403+104+024	VS 44, HK 128	07:37:08.2	65:36:33	1"×180"	-90.0	11 × 300	104, 24	2.69±0.06
NGC2403-133-146	VS 9	07:36:29.9	65:33:43	1"×180"	-108.0	6 × 300	-133, -146	6.02±0.13
NGC2403+376-106	HK 376	07:37:52.1	65:34:23	1"×180"	-231.0	3 × 900	376, -106	6.98±0.16
NGC2403-423-010	HK 423	07:35:43.1	65:35:59	1"×180"	-231.0	5 × 1800	-423, -10	9.40±0.21

Note. — Observing logs for H II regions observed in NGC 2403 at the MMT on the UT dates of 31 October 2008 and 1-2 November 2008 and using GMOS on the UT dates of 21 September 2006 and 17 November 2006, and observing log for H II regions observed in NGC 2403 at the MMT on the UT dates of 2006 February 1-4. H II region IDs are listed in Column (1). Other literature IDs are given in Column (2): Véron & Sauvayre (1965, VS) and Hodge & Kennicutt (1983, HK). The right ascension and declination of the individual H II regions are given in units of hours, minutes, and seconds, and decrees, arcminutes, and arcseconds respectively. The position angle (PA) gives the rotation of the slit counter clockwise from North. The H II region distances from the center of the galaxy are listed in Column (9), where the uncertainty in the distance has been propagated to the galactocentric radii.

4.2.3 Spectra Reduction

See discussion in Appendix A for details of the spectral reduction.

4.3 Nebular Abundance Analsysis

4.3.1 Emission Line Measurements

The emission line measurements described in Appendix B were applied here. Additional constraints were placed on the faint lines, including the [O III] λ4363 and [N II] λ5755 auroral lines, such that their FWHMs match the neighboring strong-line fits.

11 H II regions in our NGC 628 sample were measured to have [O III] λ4363 and/or [N II] λ5755 line strengths $> 4\sigma$; three additional objects had auroral line strengths $> 3\sigma$. In NGC 2403, 7 of the H II regions auroral line detections had strengths of 4σ or greater. Note that the [O III] λ4363 line is often difficult to detect due to strong mercury line contamination (λ4358) at some observatories, however, NGC 628 has a large enough redshift (z$\sim$ 0.0022) to clearly distinguish the lines. The redshift for NGC 2403 is lower (z$\sim$ 0.0004), but this concern is negated by the fact that six of the seven H II regions in our sample also have a temperature measurement from [N II] λ5755. For all of the objects in the present samples, flux line strengths and corresponding errors are listed in Tables 4.5-4.7. We concentrate the rest of our analysis on the objects for which direct electron temperature and chemical abundance determinations can be made.

Table 4.5. Emission-Line Intensities for Gemini Observations of NGC 628

	$I(\lambda)/I(\mathrm{H}\beta)$				
Ion	+9+76	-76-29	-59+84	+82-74	-134+69
[O II] λ3727	1.78±0.07	1.66±0.06	2.34±0.05	1.83±0.07	2.48±0.09
H9 λ3835	0.061±0.005	0.03±0.01	···	···	···
He I+H8 λ3889	0.23±0.01	0.22±0.01	0.32±0.01	0.12±0.01	0.17±0.01
[Ne III]+H7 λ3968	0.16±0.01	0.13±0.01	0.15±0.01	0.11±0.01	0.14±0.01
Hδ λ4101	0.28±0.01	0.27±0.01	0.26±0.01	0.27±0.01	0.27±0.01
Hγ λ4340	0.50±0.02	0.53±0.01	0.47±0.01	0.49±0.01	0.46±0.01
[O III] λ4363	···	···	···	···	···
He I λ4471	0.023±0.003	0.023±0.002	0.035±0.03	···	0.022±0.002
Hβ λ4861	1.00±0.02	1.00±0.02	1.00±0.02	1.00±0.02	1.00±0.02
[O III] λ4959	0.069±0.001	0.086±0.002	0.23±0.01	0.083±0.002	0.231±0.005
[O III] λ5007	0.183±0.004	0.26±0.01	0.67±0.01	0.239±0.004	0.68±0.01
N I λ5199	0.013±0.001	0.020±0.001	0.013±0.001	···	8.2±0.8E-4
[N II] λ5755	6.7±0.5E-3	7.7±0.5E-3	0.007±0.001	4.8±1.6E-3	0.005±0.001
He I λ5876	0.086±0.001	0.083±0.002	0.136±0.003	0.084±0.002	0.09±0.002
[O I] λ6300	0.017±0.001	0.027±0.001	0.024±0.001	0.018±0.001	0.016±0.001
[S III] λ6312	3.5±0.4E-3	0.003±0.001	0.006±0.001	0.001±0.001	0.008±0.001
[O I] λ6363	6.0±0.4E-3	0.007±0.001	0.007±0.001	0.007±0.001	0.006±0.001
[N II] λ6548	0.34±0.01	0.30±0.01	0.31±0.01	0.30±0.01	0.21±0.01
Hα λ6563	2.98±0.10	2.99±0.10	2.97±0.06	2.94±0.11	2.85±0.10
[N II] λ6584	1.02±0.04	0.93±0.03	0.92±0.02	0.88±0.03	0.64±0.02
He I λ6678	0.026±0.001	0.024±0.001	0.030±0.001	0.025±0.001	0.027±0.001
[S II] λ6717	0.31±0.01	0.37±0.01	0.31±0.01	0.33±0.01	0.25±0.01
[S II] λ6731	0.22±0.01	0.27±0.01	0.24±0.01	0.25±0.01	0.18±0.01
He I λ7065	0.012±0.001	0.011±0.001	0.020±0.001	0.012±0.001	0.015±0.001
[Ar III] λ7136	0.040±0.002	0.033±0.001	0.066±0.001	0.033±0.001	0.060±0.003
[C II] λ7236	4.5±0.3E-3	···	···	···	···
He I λ7281	4.4±0.3E-3	···	···	0.005±0.001	3.3±0.4E-3
[O II] λ7320	10.0±0.5E-3	···	0.018±0.001	0.013±0.001	0.018±0.001
[O II] λ7330	6.9±0.4E-3	···	0.016±0.001	0.009±0.001	0.011±0.001
C(Hβ)	0.71±0.04	0.55±0.04	0.72±0.01	0.58±0.04	0.30±0.04
F(Hβ)	73.9±0.5	88.9±0.8	52.1±0.0	57.7±0.2	75.9±0.5
EW(Hβ)	226	90.9	143	44.5	67.1
EW(Hα)	1340	622	420	361	550.

Table 4.5—Continued

	$I(\lambda)/I(\mathrm{H}\beta)$				
Ion	-44-159	-2+182	+185-52	-190+80	-90+186
[O II] λ3727	···	2.32±0.09	1.67±0.06	2.73±0.10	2.82±0.06
H10 λ3798	···	···	···	···	0.029±0.003
H9 λ3835	···	0.08±0.01	0.11±0.004	0.062±0.003	···
[Ne III] λ3868	0.16±0.01	0.06±0.01	···	0.050±0.003	0.073±0.003
He I+H8 λ3889	0.19±0.01	0.21±0.01	0.31±0.01	0.21±0.01	0.188±0.003
[Ne III]+H7 λ3968	0.15±0.01	0.022±0.005	0.19±0.01	0.19±0.01	0.173±0.001
[S II] λ4068	···	···	···	0.017±0.002	0.009±0.001
Hδ λ4101	0.26±0.01	0.26±0.01	0.27±0.01	0.267±0.007	0.26±0.01
Hγ λ4340	0.51±0.01	0.51±0.01	0.49±0.01	0.48±0.01	0.48±0.01
[O III] λ4363	0.015±0.003	···	···	7.4±0.8E-3	0.010±0.001
He I λ4471	0.034±0.002	0.032±0.002	0.026±0.004	0.028±0.002	0.035±0.001
[Fe III] λ4658	···	···	···	···	0.011±0.001
He II λ4686	···	···	···	···	0.049±0.001
Hβ λ4861	1.00±0.02	1.00±0.02	1.00±0.02	1.00±0.02	1.00±0.02
He I λ4921	···	0.009±0.001	···	···	8.8±0.0E-3
[O III] λ4959	0.72±0.01	0.46±0.01	0.30±0.01	0.39±0.01	0.53±0.01
[O III] λ5007	2.17±0.04	1.33±0.03	0.88±0.02	1.20±0.02	1.56±0.03
N I λ5199	···	0.007±0.001	0.012±0.001	0.01±0.01	8.4±0.3E-3
[Fe III] λ5271	···	···	···	···	2.2±0.4E-3
[Cl III] λ5518	0.005±0.001	3.9±0.6E-3	···	···	···
[Cl III] λ5538	···	2.4±0.6E-3	···	2.7±0.4E-3	···
[N II] λ5755	0.004±0.001	0.005±0.001	0.007±0.001	5.3±0.3E-3	5.5±0.4E-3
He I λ5876	0.126±0.003	0.111±0.002	0.106±0.003	0.103±0.003	0.131±0.003
[O I] λ6300	0.021±0.001	0.016±0.001	0.022±0.001	0.032±0.001	19.5±0.4E-3
[S III] λ6312	0.009±0.001	0.009±0.001	···	9.0±0.3E-3	11.5±0.4E-3
[O I] λ6363	0.007±0.001	0.005±0.001	0.006±0.001	0.011±0.001	6.2±0.4E-3
[N II] λ6548	0.14±0.01	0.139±0.005	0.20±0.01	0.19±0.01	0.175±0.004
Hα λ6563	2.97±0.10	2.91±0.10	2.89±0.10	2.93±0.10	2.89±0.06
[N II] λ6584	0.39±0.01	0.41±0.01	0.60±0.02	0.59±0.02	0.52±0.01
He I λ6678	0.038±0.001	0.033±0.001	0.032±0.001	0.031±0.001	0.031±0.001
[S II] λ6717	0.22±0.01	0.19±0.01	0.29±0.011	0.34±0.01	0.235±0.005
[S II] λ6731	0.16±0.01	0.135±0.005	0.20±0.007	0.25±0.01	0.171±0.003
He I λ7065	0.021±0.001	0.017±0.001	0.014±0.001	···	19.7±0.4E-3
[Ar III] λ7136	0.092±0.004	0.075±0.003	0.060±0.003	···	0.081±0.002
He I λ7281	0.005±0.001	4.6±0.4E-3	···	···	···
[O II] λ7320	0.017±0.001	0.018±0.001	···	···	···
[O II] λ7330	0.014±0.001	0.014±0.001	···	···	···
C(Hβ)	0.36±0.04	0.22±0.04	0.33±0.04	0.32±0.04	0.34±0.01
F(Hβ)	212±0	57.9±0.2	47.3±0.9	75.7±0.5	220.±0
EW(Hβ)	71	111	155	174	153
EW(Hα)	516	897	1137	1350	1120

Note. — Optical line fluxes for H II regions measured from Gemini NGC 628 spectra using deblended Gaussian fits and multiple component fits when necessary. Fluxes are relative to Hβ = 1.00 and are corrected for reddening. The Hβ flux is given for reference, with units of 10^{-16} erg s^{-1} cm^{-2}. EWs are given in units of Å. Note that uncertainties listed in this table reflect the statistical uncertainties in the flux through the slit only, and do not account for slit losses.

4.3.2 Reddening Corrections

Standard reddening corrections were applied (see discussion in Appendix B), but the parameters depend on the physical environment of the H II region. For our NGC 628 sample, the electron temperature covers a range of 6,300 K to 14,100 K in the high ionization zone and from 7,400 K to 13,300 K in the low ionization zone. NGC 2403 exhibits a smaller electron temperature range from 7,700 K to 11,300 K in the high ionization zone and from 8,300 K to 10,900 K in the low ionization zone (see discussion of electron temperatures in Section 3.3). These values guide our chose of parameters to use from Hummer & Storey (1987). The reddening results are tabulated in Tables 4.5-4.7. For NGC 628 we find a range in A_V of 0.13 to 1.56 and a slightly smaller range for NGC 2403 of 0.04 to 1.26.

Table 4.6. Emission-Line Intensities for MMT Observations of NGC 628

	$I(\lambda)/I(\mathrm{H}\beta)$			
ion	+295-16	-277+240	+186+355	+503+208
[O II] λ3727	1.59±0.12	3.10±0.06	2.61±0.08	2.81±0.10
H12 λ3750	0.026±0.004	···	0.036±0.001	0.026±0.008
H11 λ3771	0.035±0.004	···	0.041±0.001	0.035±0.008
H10 λ3798	0.046±0.005	···	0.05±0.01	0.05±0.01
He I λ3820	0.009±0.004	···	···	···
H9 λ3835	0.068±0.006	···	0.09±0.01	0.06±0.01
[Ne III] λ3868	0.35±0.02	0.14±0.02	0.31±0.01	0.27±0.01
He I+H8 λ3889	0.19±0.01	0.24±0.02	0.20±0.01	0.19±0.01
[Ne III]+H7 λ3968	0.26±0.02	0.25±0.02	0.26±0.01	0.25±0.01
He I λ4026	0.016±0.002	···	···	0.022±0.006
[S II] λ4068	0.009±0.002	···	···	0.013±0.006
Hδ λ4101	0.25±0.01	0.26±0.02	0.28±0.01	0.27±0.01
Hγ λ4340	0.47±0.02	0.47±0.02	0.47±0.01	0.45±0.01
[O III] λ4363	0.031±0.002	0.035±0.011	0.029±0.008	0.036±0.002
He I λ4471	0.038±0.002	···	0.041±0.007	0.040±0.005
Hβ λ4861	1.00±0.02	1.00±0.02	1.00±0.01	1.00±0.02
He I λ4921	0.010±0.001	···	···	0.010±0.003
[O III] λ4959	1.52±0.03	0.65±0.01	1.21±0.02	1.14±0.02
[O III] λ5007	4.53±0.10	1.94±0.03	3.64±0.07	3.43±0.07
He I λ5015	0.018±0.001	···	···	0.019±0.003
[Cl III] λ5518	0.004±0.001	···	···	···
He I λ5876	0.12±0.01	0.05±0.02	0.095±0.005	0.10±0.01
[O I] λ6300	0.016±0.001	···	0.019±0.004	0.027±0.005
[S III] λ6312	0.015±0.001	···	0.016±0.004	0.012±0.005
[O I] λ6363	0.005±0.001	···	0.010±0.004	0.010±0.005
[N II] λ6548	0.038±0.003	0.07±0.01	0.058±0.005	0.054±0.006
Hα λ6563	2.91±0.10	2.86±0.06	2.91±0.08	2.84±0.010
[N II] λ6584	0.12±0.01	0.24±0.01	0.175±0.006	0.16±0.03
He I λ6678	0.034±0.009	0.029±0.010	0.029±0.004	0.032±0.004
[S II] λ6717	0.099±0.008	0.25±0.01	0.16±0.02	0.18±0.01
[S II] λ6731	0.070±0.005	0.16±0.01	0.10±0.01	0.12±0.01
C(Hβ)	0.27±0.10	0.06±0.01	0.39±0.03	0.18±0.04
F(Hβ)	33.4±0.7	4.62±0.08	7.29±0.04	10.7±0.2
EW(Hβ)	228	68.8	161	369
EW(Hα)	1220	412	944	2020

Note. — Optical line fluxes for H II regions measured from MMT NGC 628 spectra using deblended Gaussian fits and multiple component fits when necessary. Fluxes are relative to Hβ = 1.00 and are corrected for reddening. The Hβ flux is given for reference, with units of 10^{-16} erg s^{-1} cm^{-2}. EWs are given in units of Å. Note that uncertainties listed in this table reflect the statistical uncertainties in the flux through the slit only, and do not account for slit losses.

Table 4.7: Emission-Line Intensities for MMT Observations of NGC 2403

	$I(\lambda)/I(\mathrm{H}\beta)$						
ion	-7+36	-30+45	+13+31	+104+24	-133-146	+376-106	-423-10
[O II] λ3727	2.82±0.12	1.90±0.08	2.34±0.10	2.47±0.10	2.44±0.11	2.44±0.11	2.31±0.10
H12 λ3750	0.018±0.002	···	0.020±0.002	0.027±0.001	0.020±0.001	···	0.021±0.001
H11 λ3771	0.030±0.002	···	0.025±0.002	0.032±0.002	0.030±0.002	0.050±0.005	0.030±0.002
H10 λ3798	0.047±0.002	···	0.036±0.002	0.042±0.002	0.041±0.002	0.050±0.004	0.040±0.002
He I λ3820	···	···	···	···	0.008±0.001	···	···
H9 λ3835	0.075±0.004	···	0.061±0.003	0.065±0.002	0.062±0.003	0.063±0.004	0.065±0.003
[Ne III] λ3868	0.046±0.002	0.038±0.002	0.062±0.003	0.090±0.004	0.25±0.01	0.18±0.01	0.29±0.01
He I+H8 λ3889	0.20±0.01	0.26±0.01	0.18±0.01	0.18±0.01	0.18±0.01	0.19±0.01	0.18±0.01
[Ne III]+H7 λ3968	0.18±0.01	0.17±0.01	0.14±0.01	0.18±0.01	0.21±0.01	0.21±0.01	0.21±0.01
He I λ4026	0.015±0.001	···	0.008±0.002	0.013±0.001	0.015±0.001	···	0.012±0.001
[S II] λ4068	0.021±0.002	···	0.012±0.002	0.014±0.002	0.019±0.001	···	0.020±0.002
Hδ λ4101	0.29±0.01	0.26±0.01	0.26±0.01	0.26±0.01	0.26±0.01	0.26±0.01	0.27±0.01
Hγ λ4340	0.52±0.02	0.47±0.01	0.48±0.01	0.48±0.01	0.47±0.01	0.48±0.01	0.48±0.01
[O III] λ4363	5.5±1.2E-3	···	0.007±0.002	7.7±0.5E-3	0.034±0.001	0.019±0.002	0.038±0.001
He I λ4387	···	···	···	···	3.5±0.9E-3	···	0.003±0.001
He I λ4471	0.040±0.001	0.018±0.002	0.031±0.002	2.7±0.5E-3	0.040±0.001	0.035±0.003	0.035±0.001
[Fe III] λ4658	···	···	···	8.0±0.4E-3	6.0±0.7E-3	···	5.8±0.7E-3
[Ar IV] + HeI λ4713	···	···	···	···	5.0±0.7E-3	···	4.5±0.7E-3
Hβ λ4861	1.00±0.02	1.00±0.02	1.00±0.02	1.00±0.02	1.00±0.02	1.00±0.02	1.00±0.02
He I λ4921	···	···	6.8±1.0E-3	10.9±0.4E-3	0.010±0.001	0.010±0.002	8.5±0.8E-3
[O III] λ4959	0.43±0.01	0.333±0.008	0.43±0.01	0.65±0.01	1.27±0.03	1.09±0.03	1.33±0.03
[O III] λ5007	1.26±0.03	1.00±0.01	1.28±0.03	1.96±0.05	3.78±0.09	3.25±0.07	4.00±0.09
He I λ5015	0.023±0.001	0.014±0.002	0.020±0.001	0.024±0.001	0.023±0.001	···	0.028±0.001
N I λ5199	0.009±0.001	0.006±0.002	6.2±1.0E-3	9.2±0.4E-3	0.004±0.001	0.005±0.002	5.9±0.7E-3
[Fe III] λ5271	···	···	···	3.8±0.3E-3	2.8±0.7E-3	···	···
[Cl III] λ5518	3.5±0.7E-3	5.3±0.9E-3	3.4±1.0E-3	3.9±0.3E-3	4.1±0.8E-3	···	3.7±0.7E-3
[Cl III] λ5538	2.2±0.7E-3	···	2.4±1.0E-3	2.7±0.3E-3	2.7±0.7E-3	···	2.9±0.7E-3
[N II] λ5755	5.2±0.6E-3	3.7±0.9E-3	3.5±0.4E-3	4.2±0.5E-3	2.4±0.3E-3	···	2.2±0.7E-3
He I λ5876	0.117±0.004	0.107±0.004	0.106±0.003	0.116±0.004	0.116±0.004	0.129±0.005	0.109±0.004
[O I] λ6300	0.013±0.001	8.8±0.9E-3	9.0±0.5E-3	0.020±0.001	0.028±0.001	0.006±0.002	0.023±0.001
[S III] λ6312	0.008±0.001	6.0±0.9E-3	6.0±0.4E-3	11.6±0.4E-3	0.015±0.001	0.014±0.002	0.013±0.001
[O I] λ6363	4.2±0.5E-3	2.56±0.9E-3	3.5±0.4E-3	6.6±0.3E-3	9.3±0.5E-3	0.005±0.002	7.4±0.8E-3
[N II] λ6548	0.18±0.01	0.15±0.01	0.15±0.01	0.124±0.005	0.039±0.002	0.060±0.003	0.044±0.002
Hα λ6563	2.87±0.12	2.93±0.12	2.88±0.12	2.91±0.12	2.83±0.12	2.88±0.12	2.83±0.12
[N II] λ6584	0.52±0.02	0.45±0.02	0.46±0.02	0.37±0.02	0.18±0.01	0.17±0.01	0.13±0.01
He I λ6678	0.032±0.001	0.027±0.001	0.026±0.001	0.032±0.001	0.029±0.001	0.030±0.002	0.025±0.001
[S II] λ6717	0.24±0.01	0.22±0.01	0.23±0.01	0.21±0.01	0.18±0.01	0.15±0.01	0.131±0.006
[S II] λ6731	0.17±0.01	0.16±0.01	0.16±0.01	0.16±0.01	0.14±0.01	0.111±0.005	0.096±0.004
He I λ7065	0.020±0.004	0.017±0.003	0.014±0.001	0.026±0.001	···	···	···
[Ar III] λ7136	0.089±0.008	0.073±0.005	0.061±0.004	0.093±0.005	···	···	···
[O II] λ7325	0.029±0.005	0.027±0.005	0.020±0.004	0.048±0.003	···	···	···
C(Hβ)	0.58±0.05	0.10±0.05	0.02±0.05	0.17±0.05	0.06±0.05	0.36±0.05	0.15±0.05
EW(Hβ)	248	25.4	60.9	164	165	103	172
EW(Hα)	1394	186	284	1050	953	941	883

Note. — Optical line fluxes for H II regions measured from the MMT NGC 2403 spectra using deblended Gaussian fits and multiple component fits when necessary. Fluxes are relative to Hβ = 1.00 and are corrected for reddening. The Hβ flux is given for reference, with units of 10^{-16} erg s^{-1} cm^{-2}. EWs are given in units of Å. Note that uncertainties listed in this table reflect the statistical uncertainties in the flux through the slit only, and do not account for slit losses.

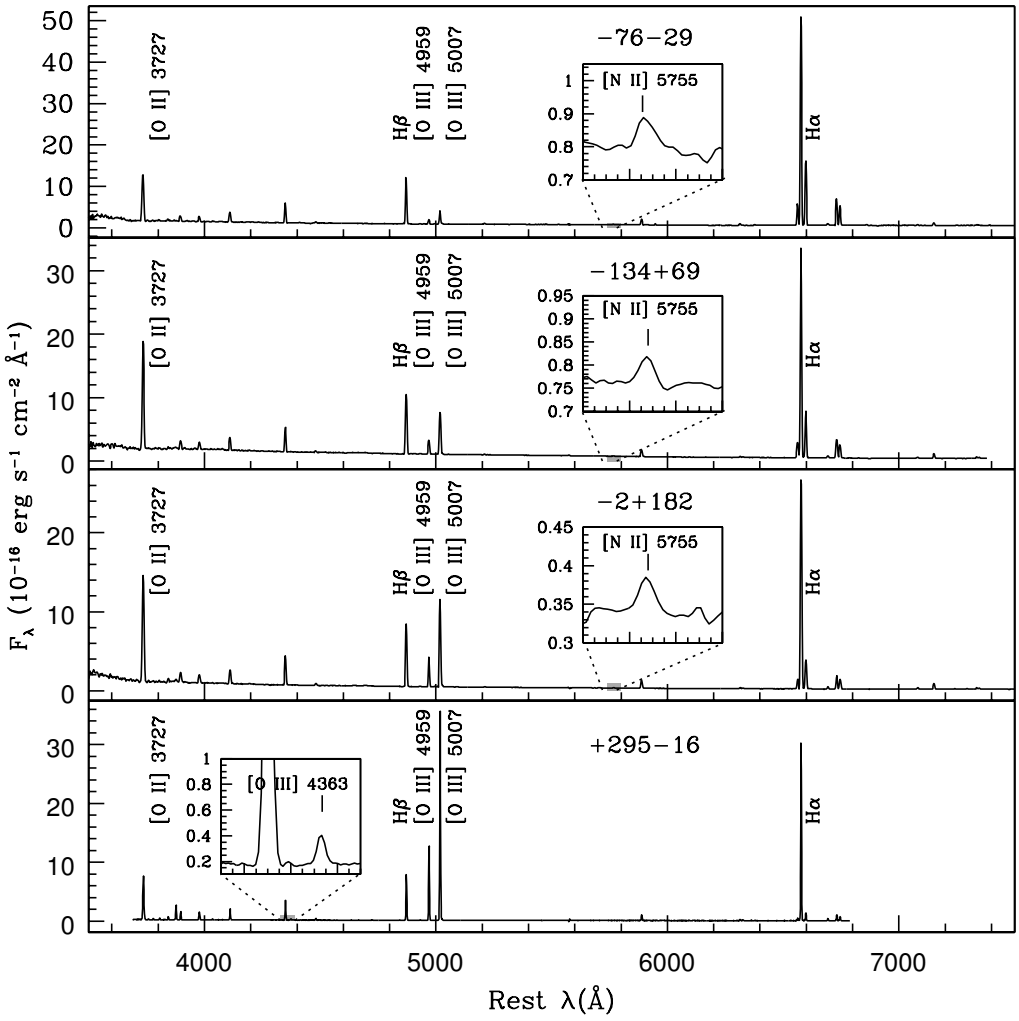

Figure 4.3: Sample MMT and GMOS spectra of the H II regions observed across the face of NGC 628 with auroral line detections at a strength of 4σ or greater. The top panel is at a galactocentric radius of 2.83 kpc and has the smallest [O III]/[O II] ratio, indicative of low excitation. Each subsequent spectra is at larger radii and has higher excitation. The [O III] λ4363 and [N II] λ5755 auroral lines are expanded to highlight the quality of these spectra.

4.3.3 Electron Temperature and Density Determinations

A more thorough discussion of electron temperatures and densities is given in Appendix C. In NGC 628, we measured [O III] λ4363 at a strength of 4σ or greater in five H II regions and measured [N II] λ5755 at a strength of 4σ or greater in ten H II regions. Three of these H II regions had both strong [O III] λ4363 and [N II] λ5755 such that we were able to measure 11 total H II regions with direct abundances from at least one strong auroral line. We extend our NGC 628 sample to 14 by including 3 more H II regions that have a 3σ detections of the auroral line.

In NGC 2403, we measured [O III] λ4363 at a strength of 4σ or greater in five H II regions and measured [N II] λ5755 at a strength of 4σ or greater in six H II regions such that all seven H II regions have strong auroral line measurements. For the H II regions in NGC 628 and NGC 2403 with strong auroral lines, we then determined electron temperatures from the associated temperature sensitive "auroral" to "nebular" ratio of collisionally excited lines.

For six of our spectra in NGC 628 and one spectrum in NGC 2403 where a strong [O III]λ4363 was not measured, we were able to determine a temperature using the [N II] I($\lambda\lambda$6548,6584)/I(λ5755) ratio. Both the [O III] and [N II] auroral lines were measured in four H II regions in NGC 628 and five H II regions in NGC 2403, allowing us to compare electron temperature estimates for the high ionization zone from two different diagnostics. On average, [O III] predicts a higher electron temperature by 1,100 K in NGC 628 and by 700 K in NGC 2403. In the five H II regions in NGC 628 and four H II regions in NGC 2403 with temperature estimates from both [O II] and [N II], we find that the T_e(O II) estimates are 900 K and 600 K larger on average than those from [N II]. This may be due in large part to the fact that the [O II] $\lambda\lambda 7320, 7330$ doublet is located in a spectral region containing strong OH airglow emission lines. Additionally, differences in the electron temperature determinations may originate from errors in the standard H II region physics assumed. Peimbert (1967) introduced the temperature inhomogeneity parameter, t^2, to be used as a statistical correction to chemical abundances. In order to account for temperature and ionization structures which differ from standard assumptions, Peña-Guerrero et al. (2012) used t^2 corrections to re-calibrate the strong-line method of Pagel (1985). In a different attempt, Nicholls et al. (2012) suggest that the electrons in a H II region may depart from a Maxwell-Boltzmann equilibrium

energy distribution, and instead suggest the adoption of a "κ-distribution". However, further work is needed to ascertain the most effective solution. The above temperatures are tabulated in Tables 4.8-4.10.

4.3.4 Ionic and Total Abundances

Ionic and total abundances are listed in Tables 4.8-4.10. We report direct oxygen abundances for 14 H II regions in NGC 628 (11 of which meet our 4σ criterion) and new direct oxygen abundances for seven NGC 2403 H II regions. Details of the abundance calculations can be found in Appendix C.

4.4 The Abundance Gradients in NGC 628 and NGC 2403

4.4.1 Oxygen

To analyze the oxygen abundance gradients for NGC 628 and NGC 2403 we have plotted the 3σ (open circles) and 4σ (filled symbols) direct abundance detections versus galactocentric radius in Figures 4.4 and 4.5 respectively. We determine the most likely linear fits to the data using the FITEXY routine in IDL. This routine uses a least-squares minimization in one-dimension where both independent and dependent variables have associated errors. For the present abundance gradients, the uncertainties in oxygen abundance and galactocentric radius, propagated from the uncertainty of the distance to the galaxy, have been used as weights.

NGC 628

In Figure 4.4 we plot direct oxygen abundance versus galactocentric radius for NGC 628. The filled points represent all of the targets with direct abundances measured at a strength of 4σ or greater and the open points are three additional H II regions with auroral line detections at a strength of 3σ. Our sample is fairly well dispersed over the range of $R_g \sim 2 - 23$ kpc, containing 10 H II regions within the isophotal radius ($R_{25} \sim 10.25$ kpc) and four extending beyond R_{25}. As expected from studies of spiral galaxies, the innermost H II regions tend to have higher oxygen abundances and the outermost H II regions have comparatively low oxygen abundances.

Table 4.8: Ionic and Total Abundances for Gemini Observations of NGC 628

Hα Region	+9+76	-76-29	-59+84	+82-74	-134+69
$t(O_2)_{measured}$ (K)	8400±200	···	9500±100	9000±200	8800±200
$t(O_3)_{measured}$ (K)	···	···	···	···	···
$t(N_2)_{measured}$ (K)	7900±200	8500±200	8300±200	7400±800	8300±500
$t(S_3)_{measured}$ (K)	···	···	···	···	···
$t(O_2)_{used}$ (K)	7900±200	8500±200	8300±200	7400±800	8300±200
$t(O_3)_{used}$ (K)	7000±500	7800±500	7600±500	6300±700	7600±400
$t(N_2)_{used}$ (K)	7900±200	8500±200	8300±200	7400±800	8300±500
$t(S_3)_{used}$ (K)	7500±500	8200±500	8000±500	6900±700	8000±500
O^+/H^+ ($\times10^5$)	23.0±3.1	14.4±1.7	22.3±3.2	33.0±19.4	23.3±7.2
O^{++}/H^+ ($\times10^5$)	3.19±1.04	2.60±0.68	7.59±2.09	6.51±0.23	7.61±0.22
O/H ($\times10^5$)	26.2±3.3	17.0±1.8	29.8±3.8	39.5±19.4	30.9±7.2
12 + log(O/H)$_D$ (dex)	8.42±0.05	8.23±0.04	8.47±0.05	8.60±0.17†	8.49±0.09
12 + log(O/H)$_P$ (dex)	8.37±0.05	8.12±0.04	8.06±0.03	8.27±0.04	8.11±0.04
N^+/H^+ ($\times10^6$)	40.6±3.7	29.0±2.4	30.5±0.28	42.8±15.0	21.0±4.0
N ICF	1.139±0.172	1.180±0.143	1.341±0.168	1.197±0.695	1.326±0.331
log(N/O) (dex)	-0.75±0.02	-0.69±0.02	-0.86±0.02	-0.88±0.05	-1.04±0.03
N/H ($\times10^6$)	46.6±6.4	34.5±4.1	41.3±0.6	51.5±25.9	27.9±6.8
12 + log(N/H) (dex)	7.67±0.06	7.54±0.05	7.62±0.05	7.71±0.18	7.45±0.10
S^+/H^+ ($\times10^7$)	24.8±2.3	23.8±2.0	21.5±0.2	32.9±11.3	16.9±3.2
S^{++}/H^+ ($\times10^7$)	36.5±15.0	18.3±7.7	44.9±16.1	22.6±20.9	53.4±18.5
S ICF	0.995±0.044	1.005±0.052	1.058±0.088	1.010±0.276	1.054±0.176
S/O	0.023±0.007	0.025±0.006	0.024±0.007	0.014±0.010	0.024±0.009
log(S/O) (dex)	-1.63±0.11	-1.60±0.09	-1.63±0.12	-1.85±0.23	-1.62±0.14
S/H ($\times10^6$)	6.10±1.55	4.23±0.83	7.02±1.73	5.60±2.83	7.41±2.25
12 + log(S/H) (dex)	6.78±0.10	6.63±0.08	6.85±0.10	6.75±0.18	6.87±0.12
Ne^{++}/H^+ ($\times10^6$)	···	···	···	···	···
Ne ICF	···	···	···	···	···
Ne/O	···	···	···	···	···
log(Ne/O) (dex)	···	···	···	···	···
Ne/H ($\times10^5$)	···	···	···	···	···
12 + log(Ne/H) (dex)	···	···	···	···	···
Ar^{++}/H^+ ($\times10^7$)	8.34±1.87	5.21±0.97	11.3±2.2	8.87±2.13	10.2±1.9
Ar ICF	4.683±0.368	3.578±0.258	2.155±0.116	3.282±0.228	2.216±0.122
log(Ar/O) (dex)	-1.83±0.12	-1.96±0.10	-2.09±0.10	-2.13±0.21	-2.14±0.13
Ar/H ($\times10^6$)	3.90±1.05	1.87±0.42	2.43±0.56	2.91±0.84	2.25±0.50
12 + log(Ar/H) (dex)	6.59±0.10	6.27±0.09	6.39±0.09	6.46±0.11	6.35±0.09

Table 4.8—Continued

Hα Region	-44-159	-2+182	+185-52	-190+80	-90+186
$t(O_2)_{measured}$ (K)	···	9300±200	···	···	···
$t(O_3)_{measured}$ (K)	10100±800	···	···	9900±800	10000±400
$t(N_2)_{measured}$ (K)	8800±900	9700±500	9300±700	8700±200	9200±200
$t(S_3)_{measured}$ (K)	···	···	···	···	···
$t(O_2)_{used}$ (K)	8800±900	9700±500	9300±700	8700±200	9200±200
$t(O_3)_{used}$ (K)	10100±800	9600±500	9000±400	9900±800	10000±400
$t(N_2)_{used}$ (K)	8800±900	9700±500	9300±700	8700±200	9200±200
$t(S_3)_{used}$ (K)	10100±800	9700±500	9200±500	9900±800	10000±400
O^+/H^+ ($\times10^5$)	15.0±7.6	10.0±2.2	8.80±2.88	20.7±2.4	16.3±2.0
O^{++}/H^+ ($\times10^5$)	7.72±1.94	5.74±0.16	4.76±1.36	4.56±1.21	5.81±0.80
O/H ($\times10^5$)	22.7±7.8	15.8±2.2	13.6±2.9	25.2±2.7	22.1±2.2
12 + $\log(O/H)_D$ (dex)	8.36±0.13	8.20±0.06	8.13±0.08	8.40±0.04	8.34±0.04
12 + $\log(O/H)_P$ (dex)	7.02±0.03	7.87±0.03	7.67±0.03	8.03±0.03	8.00±0.02
N^+/H^+ ($\times10^6$)	10.9±3.3	8.39±1.19	13.7±2.8	16.9±0.1	12.7±0.99
N ICF	1.514±0.479	1.572±0.201	1.541±0.301	1.221±0.145	1.357±0.128
log(N/O) (dex)	-1.14±0.04	-1.08±0.03	-0.80±0.03	-1.08±0.02	-1.11±0.02
N/H ($\times10^6$)	16.4±5.8	13.2±0.2	2.14±0.48	20.8±2.5	17.2±1.7
12 + log(N/H) (dex)	7.21±0.13	7.12±0.06	7.33±0.09	7.32±0.05	7.24±0.04
S^+/H^+ ($\times10^7$)	12.7±3.8	8.23±1.15	13.5±2.7	20.4±1.7	11.9±0.9
S^{++}/H^+ ($\times10^7$)	20.1±6.8	25.3±0.6	···	21.7±7.5	26.9±5.8
S ICF	1.112±0.252	1.127±0.103	···	1.018±0.063	1.064±0.070
S/O	0.016±0.007	0.024±0.006	···	0.017±0.004	0.019±0.003
log(S/O) (dex)	-1.80±0.17	-1.62±0.09	···	-1.77±0.09	-1.73±0.07
S/H ($\times10^6$)	3.64±1.13	3.78±0.70	···	4.28±0.81	4.13±0.64
12 + log(S/H) (dex)	6.56±0.12	6.58±0.07	···	6.63±0.08	6.62±0.06
Ne^{++}/H^+ ($\times10^6$)	17.4±5.5	7.31±1.20	···	5.80±1.97	8.24±0.35
Ne ICF	2.947±0.479	2.750±0.201	···	5.533±0.145	3.798±0.128
Ne/O	0.23±0.02	0.13±0.02	···	0.13±0.01	0.14±0.01
log(Ne/O) (dex)	-0.65±0.03	-0.90±0.07	···	-0.90±0.04	-0.85±0.02
Ne/H ($\times10^5$)	5.12±1.81	2.01±0.44	···	3.21±0.47	3.13±0.32
12 + log(Ne/H) (dex)	7.71±0.13	7.30±0.09	···	7.51±0.06	7.50±0.04
Ar^{++}/H^+ ($\times10^7$)	8.33±1.58	7.55±1.01	6.88±1.00	···	7.53±0.92
Ar ICF	1.734±0.073	1.661±0.066	1.697±0.757	···	2.093±0.109
log(Ar/O) (dex)	-2.20±0.16	-2.10±0.09	-2.07±0.11	···	-2.15±0.07
Ar/H ($\times10^6$)	1.44±0.33	1.25±0.20	1.17±0.20	···	1.58±0.23
12 + log(Ar/H) (dex)	6.16±0.09	6.10±0.06	6.07±0.07	···	6.20±0.06

Note. — Electron temperatures and ionic and total abundances for objects with an [O III] $\lambda4363$ or [N II] $\lambda5755$ line signal to noise ratio of 3σ or greater. Electron temperatures were calculated using either the [O III] $(\lambda4959 + \lambda5007)/\lambda4363$ or the [N II] $(\lambda6548 + \lambda6584)/\lambda5755$ diagnostic line ratio.

Table 4.9: Ionic and Total Abundances for MMT Observations of NGC 628

Hα Region	+295-16	-277+240	+186+355	+503+208
$t(O_2)_{measured}$ (K)	···	···	···	···
$t(O_3)_{measured}$ (K)	10200±200	···	10700±1000	11800±200
$t(N_2)_{measured}$ (K)	···	···	···	···
$t(S_3)_{measured}$ (K)	···	···	···	···
$t(O_2)_{used}$ (K)	11200±500	11800±2300	11500±1100	12100±500
$t(O_3)_{used}$ (K)	10200±200	12500±2500	10700±1000	11800±200
$t(N_2)_{used}$ (K)	11200±500	11800±2300	11500±1100	12100±500
$t(S_3)_{used}$ (K)	10100±500	12100±2400	10600±1000	11500±500
O^+/H^+ ($\times10^5$)	3.63±0.68	5.86±4.30	5.35±1.87	4.70±0.71
O^{++}/H^+ ($\times10^5$)	15.7±1.1	3.37±1.81	10.6±3.0	7.23±0.43
O/H ($\times10^5$)	19.4±1.3	9.24±4.66	15.9±3.6	11.9±0.9
12 + log(O/H)$_D$ (dex)	8.29±0.03	7.97±0.18†	8.20±0.09†	8.08±0.03
12 + log(O/H)$_P$ (dex)	7.82±0.02	8.04±0.02	7.94±0.02	7.97±0.03
N^+/H^+ ($\times10^6$)	1.66±0.24	2.86±1.33	2.27±0.52	1.86±0.44
N ICF	5.329±0.076	1.575±0.686	2.976±0.253	2.537±0.092
log(N/O) (dex)	-1.33±0.04	-1.30±0.05	-1.37±0.03	-1.40±0.08
N/H ($\times10^6$)	9.07±1.15	4.61±2.39	6.80±1.60	4.75±0.99
12 + log(N/H) (dex)	6.96±0.05	6.66±0.18	6.83±0.09	6.68±0.08
S^+/H^+ ($\times10^7$)	2.93±0.43	6.30±0.28	4.19±0.90	4.37±0.46
S^{++}/H^+ ($\times10^7$)	31.5±6.8	···	28.8±1.34	15.9±6.4
S ICF	1.639±0.170	···	1.305±0.139	1.258±0.043
S/O	0.029±0.005	···	0.027±0.011	0.021±0.006
log(S/O) (dex)	-1.54±0.07	···	-1.57±0.15	-1.67±0.10
S/H ($\times10^6$)	5.64±0.90	···	4.31±1.42	2.55±0.65
12 + log(S/H) (dex)	6.75±0.06	···	6.63±0.12	6.41±0.10
Ne^{++}/H^+ ($\times10^6$)	36.3±3.8	6.46±4.44	25.8±9.35	15.6±1.2
Ne ICF	1.231±0.076	2.738±0.686	1.506±0.253	1.650±0.092
Ne/O	0.23±0.02	0.19±0.04	0.24±0.02	0.22±0.01
log(Ne/O) (dex)	-0.64±0.04	-0.72±0.08	-0.61±0.04	-0.67±0.02
Ne/H ($\times10^5$)	4.47±0.54	1.77±0.96	3.88±0.94	2.57±0.23
12 + log(Ne/H) (dex)	7.65±0.053	7.25±0.19	7.59±0.09	7.41±0.04
Ar^{++}/H^+ ($\times10^7$)	···	···	···	···
Ar ICF	···	···	···	···
log(Ar/O) (dex)	···	···	···	···
Ar/H ($\times10^6$)	···	···	···	···
12 + log(Ar/H) (dex)	···	···	···	···

Note. — Electron temperatures and ionic and total abundances for objects with an [O III] λ4363 or [N II] λ5755 line signal to noise ratio of 3σ or greater. Electron temperatures were calculated using either the [O III] (λ4959 + λ5007)/λ4363 or the [N II] (λ6548 + λ6584)/λ5755 diagnostic line ratio. †Abundance based on a 3σ detection of [O III] λ4363.

Table 4.10: Ionic and Total Abundances for MMT Observations of NGC 2403

Hα Region	-7+36	-30+45	+13+31	+104+24	-133-146	+376-106	-423-10
$t(O_2)_{measured}$ (K)	8500±500	9400±400	8100±500	10100±200	···	···	···
$t(O_3)_{measured}$ (K)	8900±600	···	9600±800	8700±200	11100±200	9700±300	11300±100
$t(N_2)_{measured}$ (K)	8900±400	8400±700	8300±300	9300±400	10000±500	···	10800±1500
$t(S_3)_{measured}$ (K)	···	···	···	···	···	···	···
$t(O_2)_{used}$ (K)	8900±400	8400±400	8300±300	9300±400	10000±500	10900±500	10800±1500
$t(O_3)_{used}$ (K)	8900±600	7700±700	9600±800	8700±200	11100±200	9700±300	11300±100
$t(N_2)_{used}$ (K)	8900±400	8400±700	8300±300	9300±400	10000±500	10900±500	10800±1500
$t(S_3)_{used}$ (K)	9100±600	8100±700	9700±800	8900±500	10900±500	9800±500	11100±500
O^+/H^+ ($\times10^5$)	18.6±3.5	17.5±7.5	23.0±4.6	13.0±2.5	9.36±1.97	6.26±1.2	6.10±3.32
O^{++}/H^+ ($\times10^5$)	7.17±1.64	10.8±2.9	5.39±1.55	12.3±1.0	9.66±0.49	13.4±1.7	9.48±0.47
O/H ($\times10^5$)	25.8±3.9	28.3±8.0	28.4±4.9	25.3±2.7	19.0±2.0	19.7±2.0	15.6±3.4
12 + log(O/H)$_D$ (dex)	8.41±0.06	8.45±0.11†*	8.45±0.07*	8.40±0.04†*	8.28±0.04	8.29±0.04	8.19±0.08
12 + log(O/H)$_P$ (dex)	8.04±0.04	7.76±0.04	7.88±0.04	7.88±0.03	7.92±0.03	7.89±0.03	7.90±0.03
N^+/H^+ ($\times10^6$)	13.9±1.7	14.8±3.9	15.4±2.1	8.59±1.10	3.15±0.43	2.61±0.33	1.97±0.66
N ICF	1.386±0.204	1.615±0.387	1.235±0.237	1.950±0.147	2.032±0.149	3.144±0.118	2.554±0.303
log(N/O) (dex)	-1.12±0.03	-1.07±0.04	-1.17±0.03	-1.18±0.03	-1.43±0.03	-1.38±0.03	-1.49±0.04
N/H ($\times10^6$)	19.4±3.2	24.0±7.1	19.1±3.6	16.8±2.1	7.05±0.89	8.17±1.01	5.04±1.21
12 + log(N/H) (dex)	7.29±0.07	7.38±0.11	7.28±0.07	7.23±0.05	6.85±0.05	6.91±0.05	6.70±0.09
S^+/H^+ ($\times10^7$)	13.1±1.6	14.3±3.7	15.4±2.0	10.5±1.3	7.40±1.00	4.90±0.61	4.29±1.41
S^{++}/H^+ ($\times10^7$)	27.9±8.5	41.3±15.2	15.9±6.0	46.8±1.2	24.1±4.4	36.9±9.2	18.4±3.4
S ICF	1.070±0.110	1.137±0.188	1.022±0.108	1.195±0.057	1.205±0.057	1.325±0.079	1.260±0.152
S/O	0.018±0.005	0.022±0.009	0.011±0.003	0.027±0.006	0.020±0.003	0.028±0.006	0.018±0.005
log(S/O) (dex)	-1.77±0.10	-1.65±0.15	-1.95±0.11	-1.57±0.09	-1.70±0.07	-1.55±0.08	-1.74±0.11
S/H ($\times10^6$)	4.39±0.97	6.32±1.89	3.20±0.72	6.84±1.29	3.97±0.49	5.54±0.98	2.86±0.51
12 + log(S/H) (dex)	6.64±0.09	6.80±0.11	6.50±0.09	6.84±0.08	6.58±0.05	6.74±0.07	6.46±0.07
Ne^{++}/H^+ ($\times10^6$)	8.59±2.49	15.6±5.4	8.14±2.97	19.1±1.9	17.6±1.1	23.5±3.7	18.8±1.2
Ne ICF	3.591±0.204	2.625±0.387	5.260±0.237	2.052±0.147	1.969±0.149	1.466±0.118	1.643±0.303
Ne/O	0.12±0.01	0.15±0.01	0.15±0.01	0.15±0.01	0.18±0.01	0.18±0.01	0.20±0.01
log(Ne/O) (dex)	-0.92±0.04	-0.84±0.04	-0.82±0.04	-0.81±0.03	-0.74±0.02	-0.76±0.03	-0.70±0.02
Ne/H ($\times10^5$)	3.09±0.53	4.10±1.24	4.28±0.84	3.92±0.48	3.46±0.42	34.5±4.3	3.09±0.69
12 + log(Ne/H) (dex)	7.49±0.07	7.61±0.11	7.63±0.08	7.59±0.05	7.54±0.05	7.54±0.05	7.50±0.09
Ar^{++}/H^+ ($\times10^7$)	10.5±2.0	12.2±2.5	6.02±1.32	11.5±1.8	···	···	···
Ar ICF	2.000±0.993	1.619±0.730	2.825±0.183	1.468±0.078	···	···	···
log(Ar/O) (dex)	-2.09±0.11	-2.16±0.14	-2.22±0.12	-2.17±0.09	···	···	···
Ar/H ($\times10^6$)	2.10±0.47	1.98±0.48	1.70±0.45	1.69±0.32	···	···	···
12 + log(Ar/H) (dex)	6.32±0.09	6.30±0.09	6.23±0.10	6.23±0.07	···	···	···

Note. — Electron temperatures and ionic and total abundances for objects with an [O III] λ4363 or [N II] λ5755 line signal to noise ratio of 4σ or greater. Electron temperatures were calculated using either the [O III] (λ4959 + λ5007)/λ4363 or the [N II] (λ6548 + λ6584)/λ5755 diagnostic line ratio.

†Abundance based on a 3σ detection of [O III] λ4363.

*H II region overlaps with the G97 sample.

The best fit to characterize the gradient of the 11 objects in the current 4σ sample with direct oxygen abundance measurements is given by:

$$12 + \log(\mathrm{O/H}) = (8.43 \pm 0.03) + (-0.017 \pm 0.002) \times R_g \text{ (dex/kpc)}, \tag{4.1}$$

with a dispersion in log(O/H) of $\sigma = 0.10$ dex. Additionally, we fit the 3σ sample and found no difference in the resulting fit within the significant digits that we quote here. While the addition of the 3σ does not alter the fit, we choose to fit only the 4σ data in order to protect against false detections of the weak auroral lines.

The gas-phase oxygen abundance of NGC 628 has been previously studied using empirical calibrations (e.g., Talent, 1983; McCall et al., 1985; Zaritsky et al., 1994; Ferguson et al., 1998; van Zee et al., 1998; Bresolin, Kennicutt, & Garnett, 1999; Castellanos et al., 2002; Pilyugin et al., 2004; Moustakas et al., 2010; Gusev et al., 2012; Cedrés et al., 2012), and integral field spectroscopy (e.g., Rosales-Ortega et al., 2011). For comparison, we have plotted the strong-line relationships of Kobulnicky & Kewley (2004) and Pilyugin & Thuan (2005) for NGC 628 as compiled by Moustakas et al. (2010) from literature values. Both methods are based on the metallicity-sensitive R_{23} parameter (Pagel et al., 1979), with an additional excitation parameter that corrects for ionization (referred to as the "P-method"). Using optical spectroscopy of 34 H II regions, Moustakas et al. (2010) found

$$12 + \log(\mathrm{O/H}) = 9.19 - 0.052 \times R_g(\mathrm{dex/kpc}). \tag{4.2}$$

for the Kobulnicky & Kewley (2004) relationship and

$$12 + \log(\mathrm{O/H}) = 8.43 - 0.024 \times R_g(\mathrm{dex/kpc}). \tag{4.3}$$

for the Pilyugin & Thuan (2005) relationship, based on 33 H II regions.

Pilyugin et al. (2004) found a significantly steeper gradient in NGC 628 using an earlier version of the P-method (Pilyugin, 2001):

$$12 + \log(\mathrm{O/H}) = 8.68 - 0.040 \times R_g(\mathrm{dex/kpc}). \tag{4.4}$$

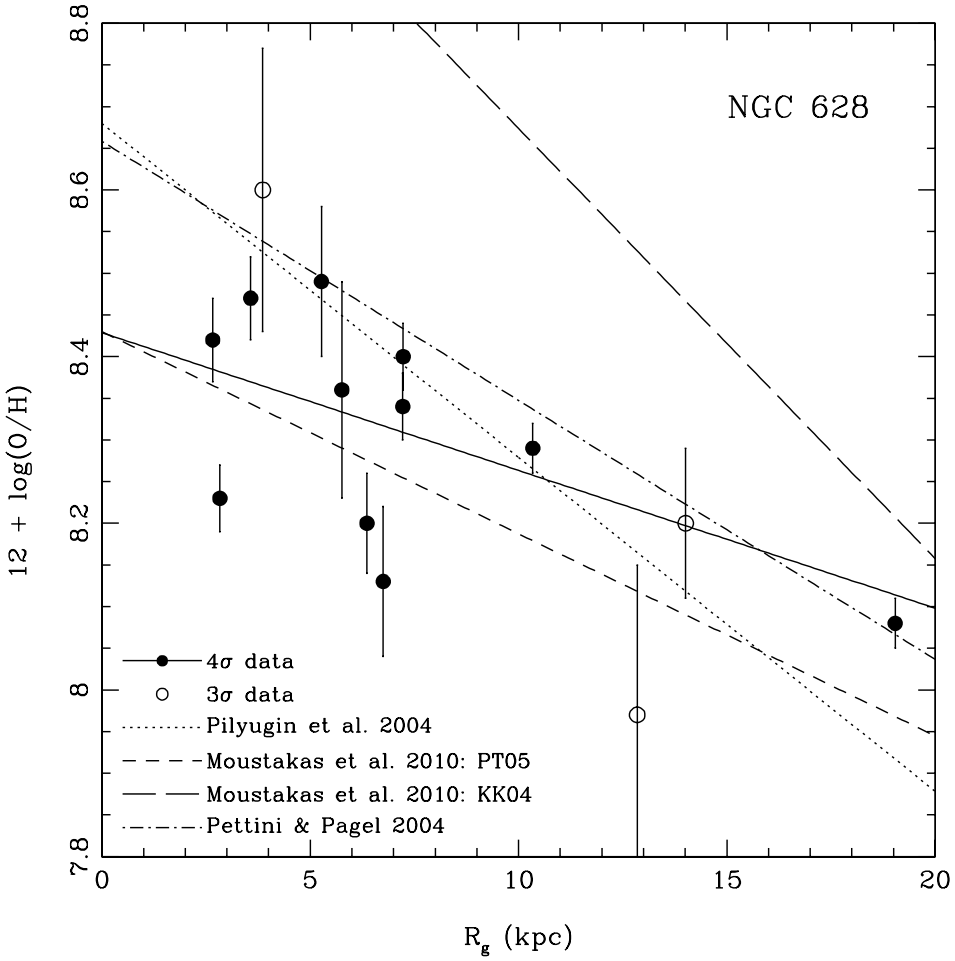

Figure 4.4: Direct oxygen abundances from Gemini and the MMT are plotted versus galactocentric radius for NGC 628. Solid points have auroral line detections at a strength at 4σ or greater and the open points have detections at strengths of 3σ. The solid line depicts the least-squares best fit to the 4σ data. For comparison, the strong-line oxygen abundance gradient determined by Pilyugin et al. (2004) using the P-method (Pilyugin, 2001) is plotted as a dotted line and the gradients from Moustakas et al. (2010) using the Pilyugin & Thuan (2005) and Kobulnicky & Kewley (2004) P-methods are plotted as short-dashed and long-dashed lines respectively. Additionally, we used the N2 calibration of Pettini & Pagel (2004) to determined the strong-line abundance gradient for the present observations and plotted the fit as a dotted-dashed line. Note the difference between the direct and strong-line relationships, which is especially significant considering no other solely direct abundance studies have been published for NGC 628.

However, Bresolin et al. (2012) used observations of NGC 1512 and NGC 3621 to show that, of the strong-line methods in wide use, the N2 calibration of Pettini & Pagel (2004) best matches the auroral line abundances. We have applied this method to our observations and plotted the least- squares fit to the results as a dotted-dashed line in Figure 4.4. Interestingly, this fit lies close to auroral line abundances, but has a steeper slope and an approximately 0.2 dex high intercept at the center. Rosales-Ortega et al. (2011) used a variety of methods with integral field spectroscopy to determine the radial oxygen abundance gradient for NGC 628. Using their ff-T_e method, they calculated a linear fit of

$$12 + \log(\mathrm{O/H}) = (8.70 \pm 0.01) + (-0.026 \pm 0.001) \times R_g(\mathrm{dex/kpc}). \qquad (4.5)$$

Rosales-Ortega et al. (2011) also examined the gradient using three other strong-line calibrators, finding that the slope of the gradient varies significantly among different calibrators. They conclude that this may be due to the potential for empirical indices based on the [N II] emission lines to overestimate oxygen abundance at high N/O ratios and vice versa (see e.g., Pérez-Montero & Contini, 2009). This is easily seen in our Figure 4.6 as the Pilyugin & Thuan (2005) and Moustakas et al. (2010) relationships extend to much higher oxygen abundances with increasing N/O .

NGC 2403

The present sample includes three H II regions with reported T(O III) in common with G97: VS 24, VS 44, and VS 9. A comparison of the derived electron temperatures and oxygen abundances shows general, but not perfect agreement. Specifically, for VS 24, G97 derived an O III temperature of 7,600 ± 400 K and an oxygen abundance of 8.41 ± 0.09 compared with a temperature of 7,700 ± 700 K and an oxygen abundance of 8.45 ± 0.11derived here. For VS 44, G97 derived an O III temperature of 8,300 ± 400 and an oxygen abundance of 8.49 ± 0.09 compared with a temperature of 8,700 ± 200 and an oxygen abundance of 8.40 ± 0.04 derived here. For VS 9, G97 derived an O III temperature of 11,700 ± 400 and an oxygen abundance of 8.10 ± 0.03 compared with a temperature of 11,100 ± 200 and an oxygen abundance of 8.28 ± 0.04 derived here. Thus, all of the above measurements agree within 1σ, except for the oxygen

abundance of VS 9. As it turns out, G97 did not measure a blue spectrum for VS 9, but, instead, combined the blue spectrum from McCall et al. (1985) with a red spectrum from the MMT. Thus, from the two spectra in common, it appears that the potential non-linearities in the detector are not a concern and that the G97 observations can be compared directly. Given the above, we derive the oxygen abundance gradient both with (1) only the newly obtained observations and (2) from combining the new observations with the previous observations obtained by G97.

In Figure 4.5 we plot direct oxygen abundance versus galactocentric radius for NGC 2403. Our observations are depicted by solid symbols, the data in common with G97 are given by filled circles and new regions by filled squares. Additional direct observations made by G97 are plotted as open circles. Combining these data, there are 11 points displayed for the inner galaxy extending out to ~ 10 kpc. Again we see decreasing oxygen abundance with increasing radius, but with a slightly steeper gradient than that of NGC 628.

The weighted least-squares fit (dotted dahsed line) to the seven new observations (filled symbols) presented here can be expressed as:

$$12 + \log(\mathrm{O/H}) = (8.46 \pm 0.04) + (-0.027 \pm 0.008) \times R_g \text{ (dex/kpc)}, \qquad (4.6)$$

with a dispersion in log(O/H) of $\sigma = 0.02$ dex.

In comparison, the best weighted fit (solid line) to characterize the gradient of the 11 points, both new and old, in NGC 2403 with direct oxygen abundance measurements results in:

$$12 + \log(\mathrm{O/H}) = (8.48 \pm 0.04) + (-0.032 \pm 0.007) \times R_g \text{ (dex/kpc)}, \qquad (4.7)$$

with a dispersion in log(O/H) of $\sigma = 0.07$ dex. This result is equivalent to the relationship derived for just the new observations, so we carry forward with the addition of the G97 observations to increment our sample.

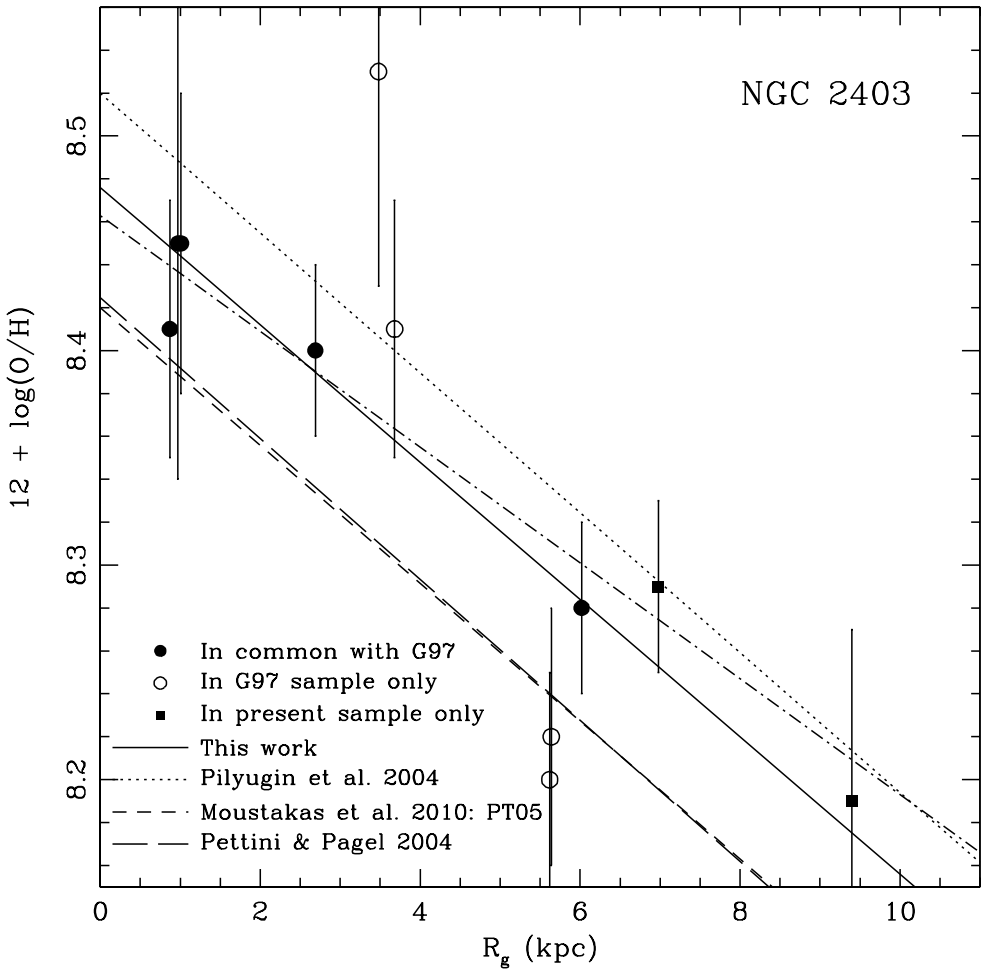

Figure 4.5: Direct oxygen abundances from the MMT are plotted versus galactocentric radius for NGC 2403. The solid circles are observations that overlap with G97 and the solid squares are observations of new regions. Additional direct observations made by G97 are plotted as open circles. The solid line is a least-squares fit to these data, with little visual or statistical dispersion among our data, but some discrepancy with the G97 data. The dotted dashed line is the fit given for just our data by Equation 4.6. The strong-line oxygen abundance gradient determined by Pilyugin et al. (2004) using the P-method (Pilyugin, 2001) is plotted as a dotted line and the gradient determined by Moustakas et al. (2010) using the Pilyugin & Thuan (2005) P-method as a short dashed line for comparison. Additionally, we used the N2 calibration of Pettini & Pagel (2004) to determined the strong-line abundance gradient for the present observations and plotted the fit as a long dashed line.

For NGC 2403, several spectroscopic studies exist where abundances were determined using empirical calibrations (e.g., McCall et al., 1985; Fierro et al., 1986; van Zee et al., 1998; Garnett et al., 1999; Bresolin, Kennicutt, & Garnett, 1999), as well as a single study using direct abundances (Garnett et al., 1997b). The dotted line in Figure 4.5 is the fit of Pilyugin et al. (2004) using the strong-line P-method (Pilyugin, 2001):

$$12 + \log(\mathrm{O/H}) = 8.52 - 0.033 \times R_g \text{ (dex/kpc)}. \tag{4.8}$$

The dashed line is the fit of Moustakas et al. (2010) using the strong line method from Pilyugin & Thuan (2005):

$$12 + \log(\mathrm{O/H}) = 8.42 - 0.032 \times R_g \text{ (dex/kpc)}. \tag{4.9}$$

Further, we apply the strong-line N2 calibration (Pettini & Pagel, 2004) recommended by Bresolin et al. (2012) to our data and plot the least-squares fit as a dotted-dashed line in Figure 4.5. Here the N2 calibration is nearly identical to the P-method of Pilyugin & Thuan (2005). The radial oxygen abundance slope of NGC 2403 is robust, where the fit to direct and strong-line abundance determinations have congruent slopes, but are vertically offset from one another.

Oxygen Abundance in Context

The direct abundance measurements of NGC 628 and NGC 2403 presented here allow comparisons against other spiral galaxies with consistent and reliable derivations. Few previous detailed studies of direct abundances for spiral galaxies exist in the literature, and those that do demonstrate a wide range in abundance gradient slope: $\sim -0.01 - 0.04$ dex/kpc. For example, Bresolin (2011) found a slope of -0.042 dex/kpc for the oxygen abundance gradient in M33, in contrast to the measurement of -0.012 dex/kpc by Crockett et al., (2006). Other examples include a slope of -0.023 dex/kpc measured for M31 (Bresolin et al., 2012), -0.011 dex/kpc for NGC 4258 (Bresolin , 2011), and -0.020 dex/kpc for M51 (Bresolin, Kennicutt, & Garnett, 2004). Thus, in comparison, the gradients measured using the direct method for NGC 628 (-0.014±0.002 dex/kpc) and NGC 2403 (-0.028±0.007 dex/kpc) are consistent with studies of other non-barred spiral galaxies (e.g., M33, M31, NGC 4258, and M51).

The new direct radial abundance gradients presented here also highlight discrepancies amongst abundance methods when compared to strong-line oxygen abundance calibrations. For NGC 2403, the abundance gradient slope is relatively robust for all abundance calibrations shown in Figure 4.5. However, the strong-line abundance calibrations from the literature are shifted above and below the direct abundance relationship. For NGC 628, we measure a much shallower direct radial abundance gradient slope relative to a variety of other methods from the literature. In particular, previous studies find higher y-intercepts and thus a significantly higher oxygen abundance predicted for the nucleus of the disk. Among the observations presented in Figure 4.4, the three direct abundances measured for galactocentric radii less than 5 kpc lie within the vertical scatter of the data, but break from the decreasing abundance trend established at larger radii. These measurements agree with chemical evolution models which predict flatter gradients in the dense inner regions of spirals due to the breakdown of the instantaneous recycling approximation (e.g., Prantsoz et al., 2000; Chiappini et al., 2003). The systematically lower direct oxygen abundances measured for NGC 2403 relative to the strong-line P-method gradient of Pilyugin et al. (2004) and the low direct oxygen abundances measured for the inner 5 kpcs of NGC 628 could also be due to temperature fluctuations or gradients. Such temperature inhomogeneities in metal rich H II regions have been shown to cause oxygen abundances to be systematically underestimated by as much as ~ 0.4 dex (e.g., Stasińska, 2005; Bresolin, 2007). As discussed in Section 4.3.3, several methods have recently emerged to correct for these temperature fluctuations (e.g., Peña-Guerrero et al., 2012; Nicholls et al., 2012), but further work is needed to determine if any are universal solutions to the problem.

4.4.2 Nitrogen

Garnett (1990) found a relatively constant relationship in the N/O ratio versus O/H for low metallicity star-forming galaxies, but with a scatter larger than could be understood in terms of observational uncertainties. He suggested that different delivery times of N and O could explain the relatively large scatter seen in N/O at low metallicities. For example, when a low metallicity galaxy has a burst of star formation, contributions from massive stars will drive O to higher values, while driving N/O values lower. Later,

contributions from intermediate mass stars will raise the N/O while keeping O/H constant. Then, if many star-forming galaxies at this oxygen abundance are measured, but are at various times since their burst initiated, a spread in N/O will be seen. At higher metallicities (i.e., 12+log(O/H) $\geq$ 8.0), secondary nitrogen production becomes increasingly significant, causing the average N/O to increase with O/H (Pagel, 1985). We can, therefore, use the radial relationship of N/O in spiral galaxies to determine which nucleosynthetic mechanisms are dominant. We present the absolute and relative nitrogen abundances for NGC 628 and NGC 2403 in Tables 4.8-4.10.

NGC 628

The upper panel of Figure 4.6 displays the trend of log(N/O) with galactocentric radius in NGC 628. For N/O, the range of values extend from log(N/O) = -0.69 at small radii, decreasing outward to -1.40 at larger radii. Pilyugin et al. (2004) used a single linear fit to characterize the N/O relationship with galactocentric radii and found a fairly shallow radial gradient (dotted line). Following this approach, we find a much shallower relationship for the 4σ data:

$$\log(\mathrm{N/O}) = (-0.49 \pm 0.08) + (-0.089 \pm 0.011) \times R_g \quad (\mathrm{dex/kpc}), \tag{4.10}$$

with a dispersion in log(N/O) of $\sigma = 0.11$ dex. This weighted least squares fit to all 11 4σ data points is plotted as a dashed line in Figure 4.6.

By visual inspection, the data appear to lie in two separate regions. The range from the inner part of the galaxy out to a galactocentric radius of $\approx$ 10 kpc, near the luminosity radius (R_{25} = 10.95 kpc), is fit reasonably well by a steeply declining fit (solid line):

$$\log(\mathrm{N/O}) = (-0.45 \pm 0.08) + (-0.100 \pm 0.013) \times R_g \quad (\mathrm{dex/kpc}), \tag{4.11}$$

with a dispersion in log(N/O) of $\sigma = 0.12$ dex. This relationship agrees well with the fit found by (Pilyugin et al., 2004), which only sampled the inner galaxy. Beyond R_g = 10 kpc, the outer galaxy appears to flatten out in N/O ratio, and so can be fit with a constant value of log(N/O) = -1.35 (solid line), with a dispersion of $\sigma = 0.04$ dex. The H II regions of NGC 628 measured at distances beyond R_{25}, which have

relatively low oxygen abundances (12+log(O/H) $<$ 8.3), have an average N/O ratio that is high relative to the plateau seen for low metallicity dwarf galaxies (e.g., Garnett 1990: log(N/O) = -1.46; van Zee & Haynes 2006: log(N/O) = -1.41; Nava et al. 2006: log(N/O) = -1.43; Berg et al. 2012: log(N/O) = -1.56). However, the average value of log(N/O) = -1.35 measured here for $8.0 \lesssim 12 + \log(\mathrm{O/H}) \lesssim 8.3$ is in agreement with the N/O ratios seen for dwarf galaxies of similar oxygen abundances in Figure 6 of Berg et al. (2012). An additional point worth noting is the scatter in log(N/O) highlighted in the upper panel of Figure 4.6 for $5 \lesssim R_g \lesssim 7$. NGC628+185-52 is especially discrepant, deviating by more than 0.2 dex from the linear fit. If this spread is real and not just due to observational uncertainties, it could be indicative of local nitrogen pollution by intermediate mass stars.

The lower panel of Figure 4.6 allows us to further examine this bi-modal relationship by fitting the N/O ratio over the range in oxygen abundance. The clear trend observed versus radius in the upper panel is not obvious in the plot versus oxygen abundance. If we assume the bi-modal relationship is correct, there are three points with 12+log(O/H) $<$ 8.25 that have N/O values that are located more than 5σ above the average value of the outer disk in the upper panel. It is interesting that the three largest outliers from this plot correspond to the three measurements of oxygen abundance (at the 4σ detection level) below the best fit in Figure 4, including NGC+185-52, which is the highly discrepant point in the upper panel of Figure 4.6. This could indicate that these regions have oxygen abundances that are underestimated, possibly due to temperature inhomogeneities within the H II region (Peimbert , 1967) or a non Maxwell-Boltzmann electron distribution (Nicholls et al., 2012). If we combine the oxygen abundance radial gradient calculated in Equation 7 with the inner N/O abundance gradient from the upper panel of Figure 4.6 (Equation 16), the result is the steep dashed line in the lower panel. Based on this relationship, there is a large scatter in N/O abundance for a given oxygen abundance. Instead, the data in the bottom panel of Figure 4.6 is best fit by a standard linear least-squares fit to the entire data range (solid line):

$$\log(\mathrm{N/O}) = -4.25 + 0.388 \times 12{+}\log(\mathrm{O/H}), \tag{4.12}$$

with a dispersion in log(N/O) of $\sigma = 0.21$ dex.

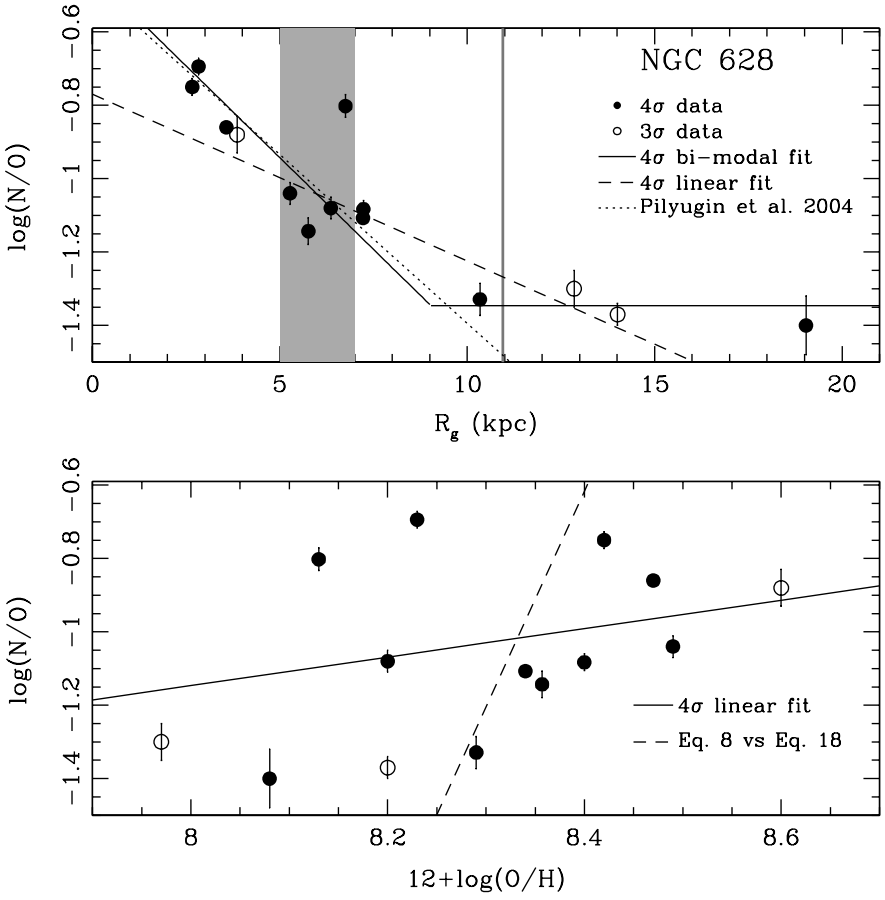

Figure 4.6: Top: The N/O ratio relationship is plotted with galactocentric radius for NGC 628. The dashed line represents our least-squares fit over the entire 4σ dataset. This linear fit is significantly shallower than the relationship determined by Pilyugin et al. (2004) (dotted line). However, these data are better fit by a bi-modal relationship (solid lines), where a steeper gradient exists in the inner part of the galaxy and flattens out past 10 kpc. A vertical line has been added to mark the luminosity radius at $R_{25} = 10.95$ kpc. We also highlight the data in the $5 \lesssim R_g \lesssim 7$ range, as it displays significant scatter relative to the rest of the fit. Bottom: N/O is plotted over the range in O/H, as is commonly done to look for regions dominated by different nitrogen production mechanisms. The solid fit is a simple least-squares linear fit to the data. The dashed line is derived from the inner galaxy fits in Figure 4.4 and the upper panel here. The scatter in this plot suggests large variations in nitrogen or temperature structure for a given oxygen abundance/region.

These nitrogen variations offer a different explanation for the divergence of the direct abundance gradient and the strong-line N2 gradient seen for NGC 628 in Figure 4.4.

Following the method laid out in Zahid et al. (2011), we use a likelihood ratio F-test in order to quantify the significance of the bi-modal model versus the linear model fit. In the case where ${\chi_1}^2 > {\chi_2}^2$, the F-statistic is given by

$$F = \frac{\frac{{\chi_1}^2 - {\chi_2}^2}{P_2 - P_1}}{\frac{{\chi_2}^2}{N - P_2}}, \tag{4.13}$$

where ${\chi_1}^2$ corresponds to model 1, which is always the simpler model of the two, P is the number of parameters of the fit and N is the number of data points. Under the null hypothesis that model 2 does not give a significantly better fit than model 1, F has an F-distribution characterized by $(P_2 - P_1, N - P_2)$ degrees of freedom. However, if ${\chi_1}^2 < {\chi_2}^2$ an alternative F-statistic must be used:

$$F = \frac{{\chi_1}^2/dof_1}{{\chi_2}^2/dof_2}, \tag{4.14}$$

where the degrees of freedom are given by $dof_i = N - P_i$ such that F has an F-distribution with (dof_1, dof_2). In the present case, model 1 is a 2-parameter linear fit, with a ${\chi_1}^2 \approx 13.3$ and model 2 is a 5-parameter bi-modal fit (each of the two lines has a parameter for slope and intercept, plus an additional parameter for the location of the break), with a ${\chi_2}^2 \approx 4.7$. This gives an $F = 3.68$ with (3,6) degrees of freedom. We then used the IDL routine MPFTEST (Markwardt, 2009) to determine that the null-hypothesis only has a significance level of 8.2%. This result suggests that model 2 is a significant improvement over model 1 at the 91.8% confidence level, where the break occurs near 12+log(O/H) = 8.3, which roughly corresponds with $R_g = R_{25}$. Thus, we find that while the N/O abundance follows a bi-modal relationship with galactocentric distance, significant variations in either temperature or nitrogen abundance result in a large scatter for a given oxygen abundance.

NGC 2403

The top panel of Figure 4.7 displays the trend of log(N/O) with galactocentric radius in NGC 2403. The gradient in N/O for NGC 2403 is much shallower at small radii than

in NGC 628. Near the center, the measured log(N/O) values only reach −1.07, and then level off at a value of log(N/O) = −1.42 past R_g = 6 kpc. If we characterize the combined 11 point data set with a single least squares weighted fit (solid line), we find a fit of

$$\log(\mathrm{N/O}) = (-1.08 \pm 0.02) + (-0.043 \pm 0.003) \times R_g \text{ (dex/kpc)}, \tag{4.15}$$

with a dispersion in log(N/O) of σ = 0.05 dex. Pilyugin et al. (2004) also used a single linear fit to characterize the N/O relationship with galactocentric radii, finding a slightly steeper radial gradient (dotted line):

$$\log(\mathrm{N/O}) = -1.040 - 0.064 \times R_g \text{ (dex/kpc)}. \tag{4.16}$$

Unlike the trend seen for N/O in NGC 628, visually the NGC 2403 data do no follow a bi-modal relationship, and an F-test confirms this. However, the luminosity radius for NGC 2403 is R_{25} = 10.1 kpc, and so the outer optical disk is not sampled by our data set. If the R_{25} of a galaxy is typically where the break in the N/O ratio occurs, then we would not expect to see it in our analysis of NGC 2403, and a declining gradient makes sense with respect to our results for NGC 628. While a general declining trend is observed, note that the vertical spread in the data is relatively small compared to the gradient seen in Figure 4.6 for NGC 628. At the radial extent of our data, the N/O decline reaches log(N/O)$\sim$ −1.5. Perhaps a plateau in N/O exists near this level farther out in the galaxy (past R_{25}), similar to the plateau seen for dwarf galaxies (see, e.g., Garnett, 1990; Berg et al., 2012). In the lower panel of Figure 4.7 we have plotted 12+log(O/H) vs. log(N/O) for a second look at the N/O relationship. The 4σ data are fit best by a simple least-squares fit (solid line):

$$\log(\mathrm{N/O}) = -7.56 + 0.755 \times 12{+}\log(\mathrm{O/H}), \tag{4.17}$$

with a dispersion in log(N/O) of σ = 0.10 dex. Again, it is likely that our data did not sample large enough galactocentric radii or low enough metallicities to see the plateau related to primary nitrogen production.

Nitrogen Abundance in Context

If the trends of increasing N/O ratios towards the center of both galaxies are real, it would be indicative of the effects of secondary N production in those regions. Note that Garnett (1990) proposed that much of the scatter in the 12+log(O/H) vs. log(N/O) relationship could be explained by the time delay between producing oxygen in massive stars and secondary nitrogen from intermediate mass stars. Then local nitrogen pollution from intermediate mass stars could provide an explanation for the scatter we see in our data in the inner disks.

In the outer disk, many previous studies note no correlation between 12+log(O/H) and the relative N/O abundance, but do not sample data at radii greater than R_{25} (e.g., Bresolin, Kennicutt, & Garnett, 2004; Bresolin et al., 2005; Bresolin , 2011; Zurita & Bresolin, 2012). Barred spiral galaxies are known to show a flattening in their gradient correlated with the strength of their bar (Martin & Roy, 1994). For example, Zahid et al. (2011) measured a break in the strongly barred spiral, NGC 3359, near 12+log(O/H)$\approx$ 8.3, corresponding to radii between $1 \cdot R_{25}$ and $1.5 \cdot R_{25}$. Similarly, Kennicutt et al. (2003a) found a break near 12+log(O/H)$\approx$ 8.0 and $R_g = 1 \cdot R_{25}$ in M101 and Bresolin et al. (2009b) showed M83 exhibits a break near $R_g = 1 \cdot R_{25}$ and 12+log(O/H)$\geq$ 8.3. However, a few examples of observed breaks in non-barred spiral galaxies also exist in the literature. Goddard et al. (2011) used a variety of strong-line methods in the mixed spiral galaxy, NGC 4625, to show a break near 12+log(O/H) $>$ 8.3 at $R_g = R_{25}$ and Bresolin et al. (2012) measured a break in the non-barred spiral NGC 3621 near $R_g = 1 \cdot R_{25}$ for oxygen abundances in the range of 8.3 $<$ 12+log(O/H) $<$ 8.7 (depending on the abundance method used).

In the present data of NGC 628, and the examples listed above, a pattern is emerging in which N production is transitioning from secondary to primary past R_{25}. Breaks have typically been explained as the result of gas being mixed by radial flows associated with a bar (e.g., Vila-Costas & Edmunds, 1992; Zaritsky et al., 1994; Dutil & Roy, 1999). However, if breaks are observed to be common to all spiral galaxies, then a more general theory will be needed to include non-barred spiral galaxies (for instance, see Bresolin, Kennicutt, & Garnett (1999) for discussion of other theories).

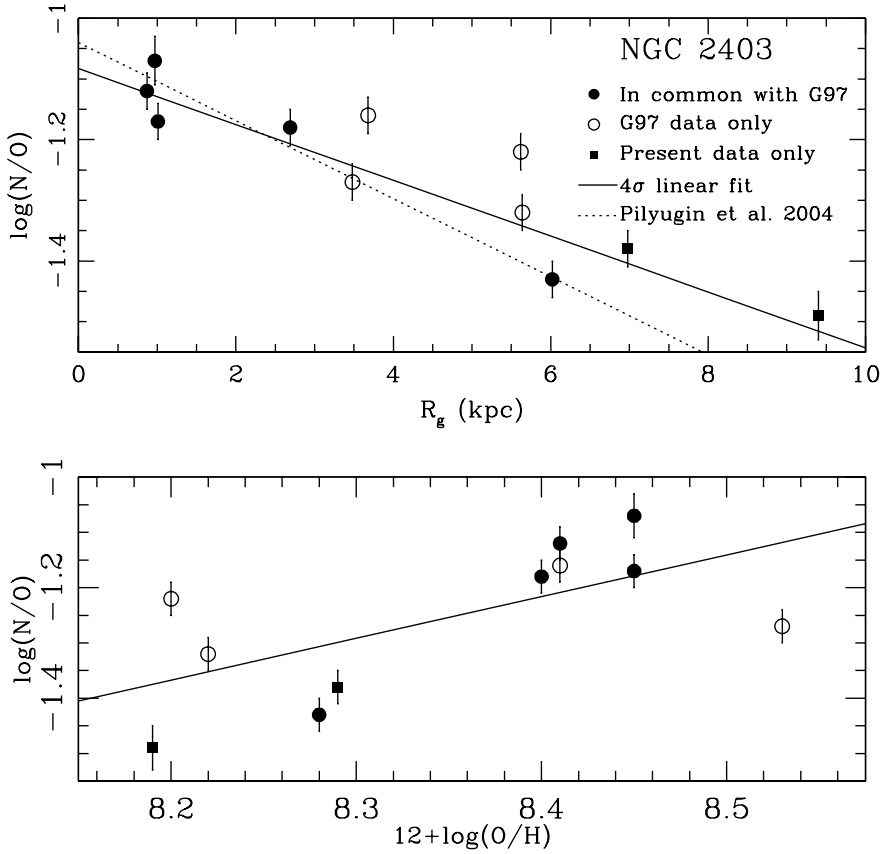

Figure 4.7: Top: The N/O ratio relationship is plotted with galactocentric radius for NGC 2403. The solid line represents the least-squares fit to the present data plus G97 data over the full radial extent of the observations. This linear fit demonstrates a somewhat shallower slope than the relationship determined by Pilyugin et al. (2004) (dotted line). Note that these data only sample the inner disk of NGC 2403 ($R < R_{25}$). Bottom: The solid line represents the best fit to the data: a simple least-squares linear relationship.

Furthermore, the break in log(N/O) (near 12+log(O/H) $>$ 8.3) is observed at a much higher oxygen abundance than has been widely observed in dwarf galaxies (see e.g., Garnett, 1990; Izotov & Thuan, 1999; van Zee & Haynes, 2006; Nava et al., 2006; Berg et al., 2012). If further studies confirm this elevated level for turnover, it would have the potential to provide new insights into the production of nitrogen and possible

metallicity-dependent yields. Note that Pilyugin (2003) challenged the existence of breaks, showing that artificial breaks can be observed when the strong-line R_{23} method is used to determine abundances. This result further motivates the need for a more significant sample of spiral galaxies with direct abundance gradients and spanning a wide range of Hubble types.

For isolated galaxies there is still no strong consensus on how metals and gas are transported. Possible mechanisms of gas mixing include magnetorotational instabilities (Sellwood & Balbus, 1999), gas outflows and infall (Santillán, Sánchez-Salcedo, & Franco, 2007; Dalcanton, 2007; Zahid et al., 2012), differential rotation (Wada & Norman, 1999), and spiral-bar resonance over-lap (Minchev & Famaey, 2010). Cold mode flows have been measured in several spiral galaxies from H I studies (see e.g., Ryan-Weber et al., 2003; Elson, de Blok, & Kraan-Korteweg, 2010), and are consistent with driving central material outward and mixing into the extended disk, causing higher-than-expected oxygen abundances in the plateau. Salim & Rich (2010) and Lemonias et al. (2011), among others, have argued that cold-mode accretion feeds the ongoing star formation in extended disks, but the low metallicity expected for pristine infalling gas contrasts with the moderately high oxygen abundances measured in the disk. Alternatively, Werk et al. (2011) argue for the hot gas phase mixing scenario proposed by Tassis, Kravtsov, & Gnedin (2008), an argument nearly identical to those in Kobulnicky & Skillman (1996) and Kobulnicky & Skillman (1997a). However, this model assumes that mergers are the dominant source of turbulence, and thus doesn't answer the question of isolated spiral galaxies. Further, Tumlinson et al. (2011) suggest a different process of "recycled winds", where material is driven into the halo by star formation and later reacquired by the galaxy. As discussed in Bresolin (2011), many questions concerning the mechanisms of galactic disk assembly and evolution remain and will need to be answered using ongoing and future work involving optical spectroscopy of faint H II regions out to large galactocentric radii in spiral galaxies.

4.4.3 Sulfur, Neon, and Argon

Stellar nucleosynthesis calculations (e.g., Woosley & Weaver, 1995) indicate that α-element and oxygen production occur mainly in massive stars of a small mass range, and thus are expected to trace each other closely. To test this idea in NGC 628 and

NGC 2403, we measured the absolute and relative sulfur, neon, and argon abundances, which are tabulated in Tables 4.8-4.10.

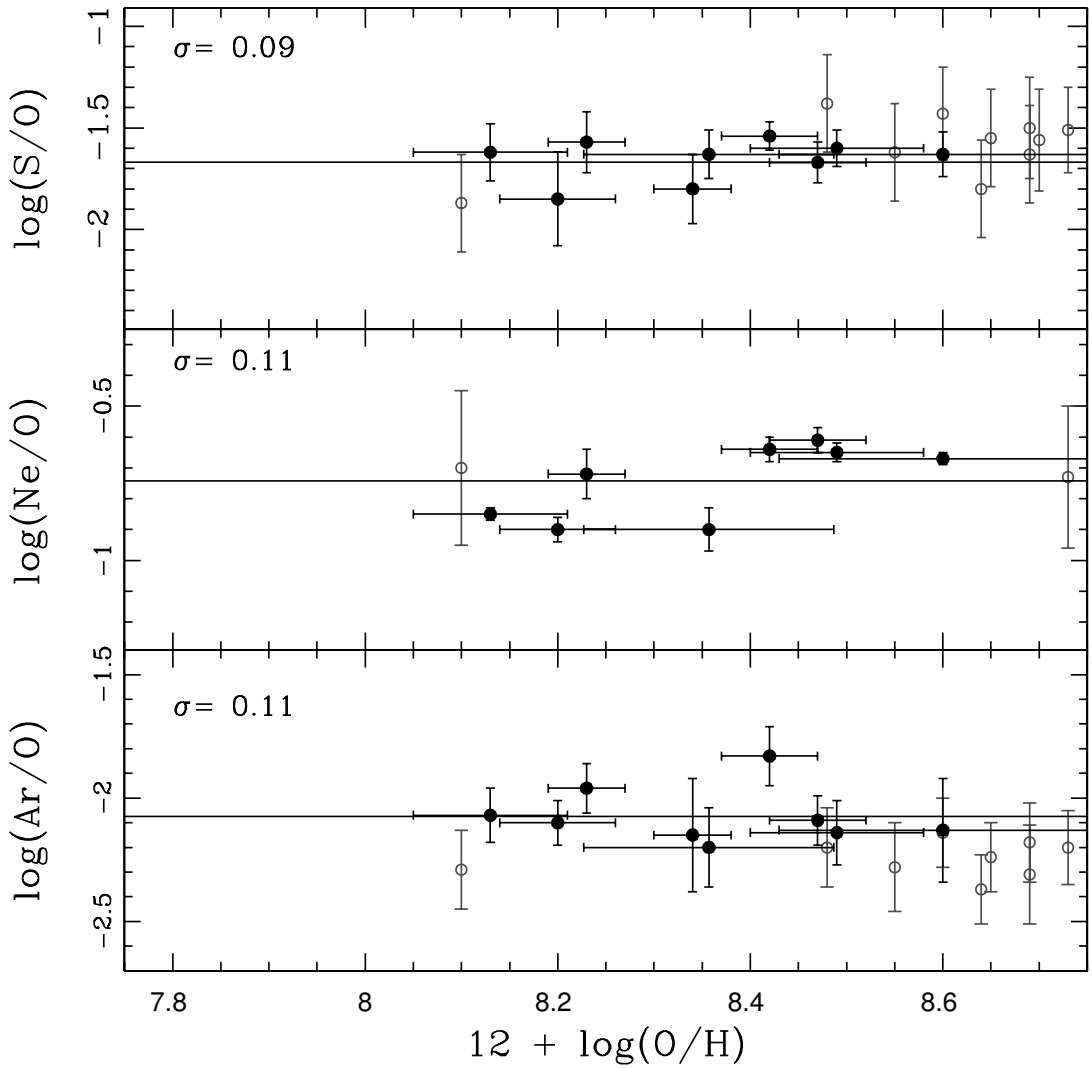

Figure 4.8: α-elements are plotted versus oxygen abundance for NGC 628. The present data are plotted as solid points and fit with α-element averages (solid lines). Data from van Zee et al. (1998, open circles) are plotted in comparison, helping to extend the coverage over oxygen abundance. This larger data set generally follows the constant α/O abundance vs. O for each element.

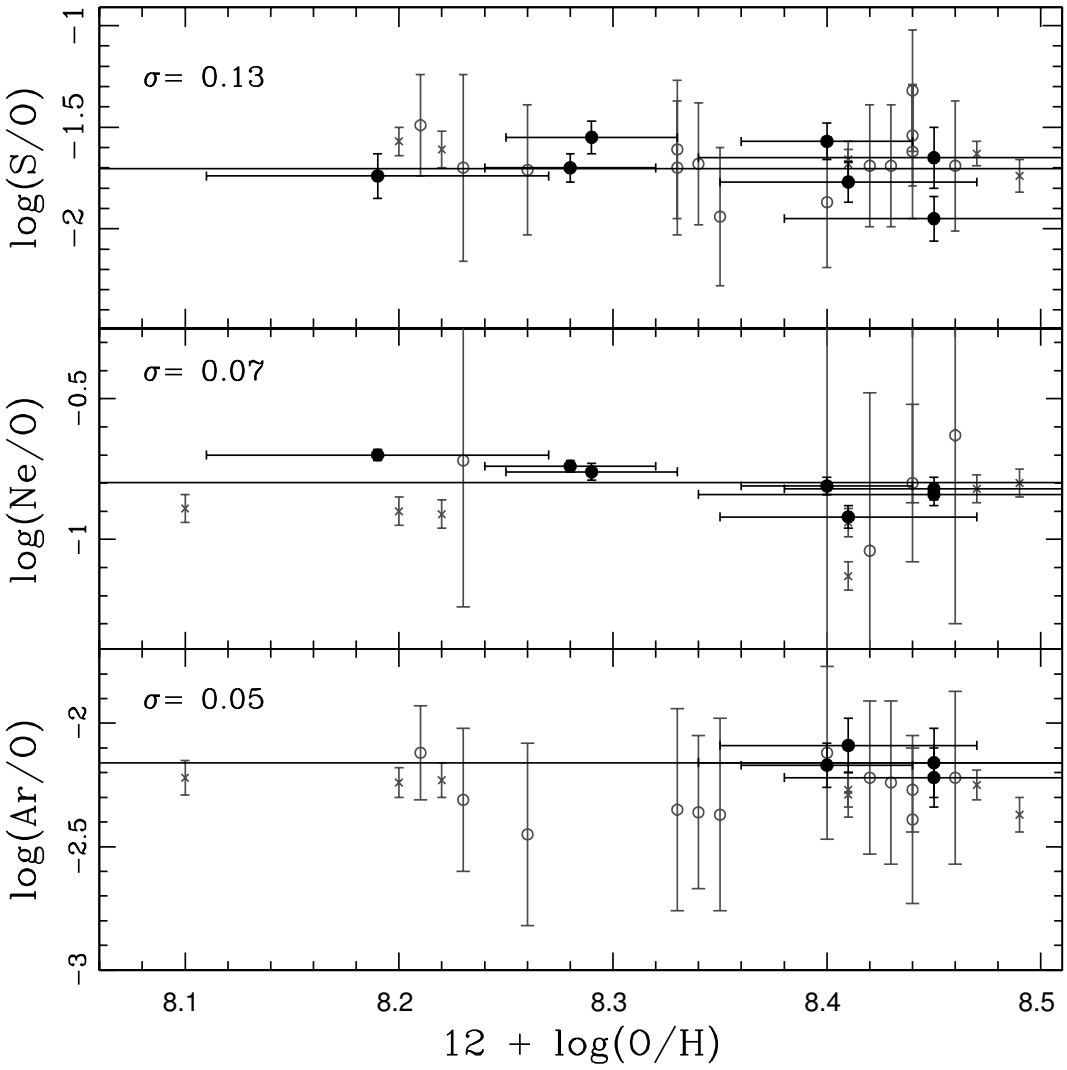

Figure 4.9: α-elements are plotted versus oxygen abundance for NGC 2403. The present data are plotted as solid points and fit with α-element averages (solid lines). Data from G97 (crosses) and from van Zee et al. (1998, open circles) are plotted in comparison, helping to extend the coverage over oxygen abundance. This larger data set generally follows the constant α/O abundance vs. O for each element.

NGC 628

Sulfur, neon, and argon abundances measured for NGC 628 are plotted versus oxygen abundance in Figure 4.8(a). For each element we have fit the average alpha abundance for the present sample with a solid line and the standard deviation displayed. For comparison, we also determined the error weighted least-squares fit using FITEXY, but found the fits to be no better than the flat relationships. In addition, we plot strong-line abundances from van Zee et al. (1998) as open circles in Figure4.8(a). We fit the combined data set with a simple least-squares linear relationship, which was found to be nearly constant in all three cases. Even with the addition of the van Zee et al. (1998) data, the scatter around a constant value is small compared to the large range in oxygen abundance sampled. Thus, the α-elements in NGC 628 investigated here can all be described by a constant relationship over oxygen abundance such that the α-elements behave as expected for the nucleosynthetic products of massive stars.

α-Elements in Context

In a comprehensive study of M33, Kwitter & Aller (1981) found that Ne, N, S, and Ar gradients followed that which they derived for oxygen. From stellar nucleosynthesis calculations (e.g., Woosley & Weaver, 1995), oxygen and neon both seem to be produced mainly in stars larger than 10 solar masses, and thus are expected to trace each other closely. Similarly, Henry (1990) finds that Ne/O is constant over a wide range of O/H for planetary nebulae. Thus, the present gradient analysis for NGC 628 and NGC 2403 agree with previous findings that α/O remains constant over the range in oxygen abundance.

In contrast to this viewpoint, Willner & Nelson-Patel (2002) derived a neon gradient that is significantly shallower than the oxygen gradient observed in M33. While sulfur is also traditionally assumed to have a constant S/O ratio (Garnett, 1989), some specific cases, such as the work of Vilchez et al. (1988) on M33, find a slower decline of sulfur than oxygen with radius. Thus, a larger sample of galaxies are needed to determine whether constant α-element abundance gradients are a universal trend amongst spiral galaxies.

The conclusions drawn from Tables 4.9-4.10 and Figure 4.8 support the convention

Table 4.5. Adopted Abundance Gradients for NGC 628 and NGC 2403

Ratio (log)	Equation of Correlation	σ	Portion of Disk
	NGC 628		
12+log(O/H) vs. R_g	y = (8.43±0.03) + (-0.017±0.002)×x	0.10	Total
log(N/O) vs. R_g	y = (-0.45±0.08) + (-0.100±0.013)×x	0.11	Inner
	y = -1.35	0.04	Outer
log(N/O) vs. 12+log(O/H)	y = -4.25 + 0.388×x	0.21	Total
log(S/O) vs. 12+log(O/H)	y = -1.67	0.09	Total
log(Ne/O) vs. 12+log(O/H)	y = -0.74	0.11	Total
log(Ar/O) vs. 12+log(O/H)	y = -2.07	0.11	Total
	NGC 2403		
12+log(O/H) vs. R_g	y = (8.48±0.04) + (-0.032±0.007)×x	0.07	Total
log(N/O) vs. R_g	y = (-1.08±0.02) + (-0.043±0.004)×x	0.05	Total
log(N/O) vs. 12+log(O/H)	y = -7.56 + 0.755×x	0.10	Total
log(S/O) vs. 12+log(O/H)	y = -1.67	0.09	Total
log(Ne/O) vs. 12+log(O/H)	y = -0.74	0.11	Total
log(Ar/O) vs. 12+log(O/H)	y = -2.07	0.11	Total

Note. — The adopted best fits to the abundance gradients measured for the 4σ NGC 628 data and the combined sample of present observations plus G97 for NGC 2403.

that α-element abundances (S, Ar, and Ne) and O evolve in lockstep for both NGC 628 and NGC 2403. The final adopted fits to the abundance gradients for NGC 628 and NGC 2403 are given in Table 4.5.

4.5 Conclusions

Spiral galaxies pose a challenge to abundance work, as a single abundance measurement is not sufficient to characterize the entire galaxy. Thus, high quality spectra of many H II regions that enable direct abundances are required to securely measure the oxygen abundance gradient.

We have uniformly determined oxygen abundance metallicities for 14 H II regions in the local spiral galaxy NGC 628 and seven H II regions in NGC 2403. With high-quality spectroscopic observations, we measured the intrinsically faint [O III] λ4363

and/or [N II] λ5755 auroral lines at a strength of 3σ or greater, and explicitly determine electron temperatures in all 14 H II regions in NGC 628. The seven H II regions in NGC 2403 were chosen to have strong auroral emission lines and, therefore, all have electron temperatures determined at a significance above 4σ. From these high quality data sets, we come to the following conclusions:

(1) Oxygen abundance gradient:

- From the 4σ data of NGC 628, we derive an oxygen abundance gradient of 12 + log(O/H) = (8.43±0.03) + (-0.017±0.002)×R_g (dex/kpc), with a dispersion in log(O/H) of σ = 0.10. This result is the first ever direct oxygen abundance gradient for H II regions in NGC 628, and has a significantly shallower slope than found by previous empirical abundance studies.

- From the 4σ data of NGC 2403, we derive an oxygen abundance gradient of 12 + log(O/H) = $(8.48 \pm 0.04) + (-0.032 \pm 0.007) \times R_g$ (dex/kpc), with a modest dispersion of $\sigma = 0.07$. As all previous studies of NGC 2403 have relied primarily on strong-line abundances, with only a small number of direct abundances, this result is an improved metallicity gradient analysis.

- These new oxygen abundance gradients for NGC 628 and NGC 2403 will improve the relationship amongst spiral galaxies for $L_{\sum PAH}/L_{TIR}$ vs. oxygen abundance.

(2) Nitrogen abundance gradient:

- The N/O ratio in NGC 628 demonstrates a negative gradient with increasing galactocentric radius in the inner disk. Further out in the outer disk, this relationship flattens out, where we find a plateau past $R_g = R_{25}$ near an oxygen abundance of 12+log(O/H) = 8.3. Similar trends are seen in other spiral galaxies, where the R_{25} radius and oxygen abundances of 12+log(O/H) = 8.3 and greater mark points of transition in nitrogen production.

- The N/O ratio in NGC 2403 also demonstrates a negative gradient with increasing galactocentric radius throughout the disk. In contrast to the trend seen in

NGC 628, NGC 2403 is best fit with a single linear relationship between N/O ratio and radius.

- In NGC 2403, and in previous studies, cases where a galaxy's N/O ratio is observed to follow a single linear trend do not include observations in their extended disks beyond R_{25}. Thus, the mechanism of nitrogen production in these galaxies are not readily comparable to galaxies with observations of greater radial coverage.

(3) α-process elements:

- As expected for α-process elements, S/O, Ne/O, and Ar/O appear to be constant over a range in oxygen abundance in both NGC 628 and NGC 2403 such that the α-elements and O are produced in lock-step.

Since there is a general paucity of abundance data from individual spiral galaxies, more of these accurate H II region datasets are necessary to understand individual galaxy processes and relative trends among galaxies.

4.6 Acknowledgements

We are grateful to the referee for a quick and insightful report which substantially improved the organization and scientific impact of the paper. We are also grateful to Liese van Zee for helpful discussion and the use of her Hα and R-band imaging. Special thanks to Henry Lee for his role helping to prepare the Gemini observations. DAB is grateful for support from a Penrose Fellowship, a NASA Space Grant Fellowship, and a Dissertation Fellowship from the University of Minnesota. EDS is grateful for partial support from the University of Minnesota and NSF Grant AST-1109066.

Observations reported here were obtained at the MMT Observatory, a joint facility of the Smithsonian Institution and the University of Arizona. MMT observations were obtained as part of the University of Minnesota's guaranteed time on Steward Observatory facilities through membership in the Research Corporation and its support for the Large Binocular Telescope. This work is based, in part, on observations obtained

at the Gemini Observatory, which is operated by the Association of Universities for Research in Astronomy, Inc., under a cooperative agreement with the NSF on behalf of the Gemini partnership: the National Science Foundation (United States), the National Research Council (Canada), CONICYT (Chile), the Australian Research Council (Australia), Ministrio da Cincia, Tecnologia e Inovao (Brazil) and Ministerio de Ciencia, Tecnologa e Innovacin Productiva (Argentina). The authors wish to recognize and acknowledge the very significant cultural role and reverence that the summit of Mauna Kea has always had within the indigenous Hawaiian community. We are most fortunate to have the opportunity to conduct observations from this mountain.

This research has made use of NASA's Astrophysics Data System Bibliographic Services and the NASA/IPAC Extragalactic Database (NED), which is operated by the Jet Propulsion Laboratory, California Institute of Technology, under contract with the National Aeronautics and Space Administration. This work was initiated as part of the Spitzer Space Telescope Legacy Science Program and was supported by National Aeronautics and Space Administration (NASA) through contract 1336000 issued by the Jet Propulsion Laboratory (JPL), California Institute of Technology (Caltech) under NASA contract 1407.

Chapter 5

An Updated Direct Radial Abundance Gradient for M31

Danielle A. Berg, Evan D. Skillman, Kevin V. Croxall, and PHAT Team,
in preparation for submission to ApJ

Abstract

We present high quality spectroscopic observations of H II regions in the Local Group spiral galaxy M31, in order to measure the true chemical abundance gradient. To properly characterize the abundance trends in M31, we target our observations to H II regions in the Panchromatic Hubble Andromeda Treasury (PHAT) field, for which no previous abundance gradient exists. Using long-slit optical spectroscopy of the highest surface brightness H II regions in the PHAT quadrant, we obtain strong-line abundance estimates of 22 regions, but only measure a temperature sensitive auroral line (needed for direct abundance calculations) in 4 regions. Despite being the nearest large spiral galaxy outside of the Milky Way, direct abundances have have rarely been measured in M31. Recently, Zurita & Bresolin (2012) measured the largest set of high quality direct abundances for M31 yet, detecting significant auroral lines in 9 H II regions. However, these points lie in clumps at essentially two radial points. Adding our detections to the Zurita & Bresolin (2012) sample creates a sample of 13 detections at 6 different

radii spanning the inner $\sim 4 - 16$ kpc of the disk. With this sample we will measure the most complete direct radial gradient for M31 to date, and compare to previous strong-line studies.

5.1 Introduction

H II regions can be used to study relative and absolute abundances in nearby galaxies. Spiral galaxies in the Local Volume with low inclinations offer a laboratory in which we can measure abundances across the surface to analyze the chemical processes occurring there. Aller (1942) and Searle (1971) were the first to utilize this fact to infer radial gradients in excitation across the disks of spiral galaxies. Radial abundance gradients have since been observed in the sense that galaxy centers harbor the most metals, which tend to decrease with increasing galactocentric radius. This trend was first measured in our own galaxy by Shaver et al. (1983), and was confirmed by observations of other nearby spiral galaxies (e.g., Pagel & Edmunds, 1981; Shields, 1990).

The abundance gradient across the face of a galaxy is the manifestation of the physical processes present over the lifetime of that galaxy. Gas infall and outflow from the galaxy, the initial mass function, the star formation efficiency over time, radial migration, and dynamical processes, such as bar formation, can all have large radial impacts. Thus, studies of chemical abundance gradients across the surface of nearby spirals can be used to place observational-based constraints on theories of galactic chemical evolution (e.g., Maciel et al., 2005; Mollá & Díaz, 2005; Magrini et al., 2009; Carigi & Peimbert, 2011).

In order to place gradients on the same scale for comparison amongst galaxies, reliable and consistent derivations of abundances are needed. Zaritsky et al. (1994) used strong-line calibrations to measure radial oxygen abundance trends for 39 spiral galaxies, finding a wide range in gradients spanning 0 to -0.23 dex kpc^{-1}. While strong-line methods are easier to measure and have enabled extensive abundance studies, they are biased by the emission lines they depend upon, limiting their ability to provide meaningful comparisons between different galaxies (e.g., Kewley & Ellison, 2008; Berg et al., 2011). In fact, the nebular lines used by these methods depend on the emissivities of each line, which in turn are highly dependent on electron temperature. Therefore,

Table 5.1. Properties of M31

Property	Value	Reference
R.A. (J2000)	00:42:44.33	Skrutskie et al. (2006)
Dec. (J2000)	41:16:07.50	Skrutskie et al. (2006)
Type	SA(s)b	
Adopted D (Mpc)	744±33	Vilardell et al. (2010)
m_B (mag)	4.16±0.19	de Vaucouleurs et al. (1991)
Redshift	-0.001001	
Inclination	77°	Corbelli et al. (2010)
P.A. (degrees)	38°	Corbelli et al. (2010)
R_{25} (arcmin)	95±2	de Vaucouleurs et al. (1991)
R_{25} (kpc)	21±1	

Note. — Optical properties for M31. Row 1 and 2 give the RA and Dec of the optical center in units of hours, minutes, and seconds, and decrees, arcminutes, and arcseconds respectively. Row 5 gives the redshift, taken from the NASA/IPAC Extragalactic Database. Row 8 gives the optical radius at the B_{25} mag arcsec^{-2} of the system. Row 9 gives the optical radius of the galaxy given the adopted distance.

a direct measurement of the electron temperature - typically derived from the ratio of auroral to collisionally excited lines - is needed at each point across the galaxy. Note that this is difficult if the metallicity is very large in the galaxy's center, since this can push $T_e < 8000$ K where the auroral lines become too weak to measure and the abundances must then be derived indirectly via empirical calibrations.

M31, the Andromeda galaxy, is a SA(s)b spiral galaxy, similar to our own. It is our nearest neighbor and the largest galaxy of the Local Group. M31 has a large inclination of $i \approx 77°$, making the identification of features across the surface more difficult, but at a proximity of d= 744 kpc (Vilardell et al., 2010) spatially detailed studies are possible. Because M31 is a spiral galaxy that appears to closely mimic our own and our understanding of the universe begins with the need for detailed knowledge of physical processes that can only be calibrated nearby, it is arguably the most well-studied galaxy in the universe. Being large and complex, one can find a large range of environments and events within M31, making it the best proxy for properties of galaxies near and far. We have chosen to elect the physical properties of M31 as detailed by Zurita & Bresolin

(2012) for ease of comparison. Table 5.1 lists the optical properties of M31.

Recognizing that M31provides a huge laboratory of data nearly at our fingertips, the Panchromatic Hubble Andromeda Treasury (PHAT) was created. PHAT is an ongoing *Hubble Space Telescope* Multi-Cycle Treasury program designed to image roughly 1/3 of M31's star-forming disk in six filters, spanning from the ultraviolet (UV) to the near-infrared (NIR). The full survey of 828 orbits will provide high-quality, resolved photometry of millions of individual stars, which provide strong constraints on stellar temperatures, bolometric luminosities, and extinction. The PHAT project seeks to provide the tightest constraints to date on the stellar initial mass function, observation-based calibrations for models of clusters and stellar evolution, and characterize the dust and gas physical properties throughout the disk. However, one crucial parameter, the abundance gradient, acts as the achilles heal of Andromeda.

There is a lack of secure H II region abundances in the literature for M31, preventing the detailed understanding of stellar nucleosynthesis in spirals, the ability to derive, among others, accurate star formation histories, comparisons to chemical histories measured from stellar and PNe abundances, and the understanding of chemical mixing processes. Baade & Arp (1964) were the first to create a catalog of H II regions in M31. A more complete imaging study of M31, at a spatial resolution of $4''$ ($\sim$ 15 pc), was produced by Pellet et al. (1978), cataloging the positions, dimensions, and fluxes of 967 H II regions. Azimlu et al. (2011) produced the most recent catalog of emission nebulae in M31, using the high resolution ($1''$,$\sim$ 3.8 pc) Hα imaging of Massey et al. (2006) to identify 3961 distinct H II regions. Despite this large number of emission regions and the proximity of M31, abundance estimates are only available for $\lesssim 7\%$ of them (Sanders et al., 2012). Several strong-line abundance studies have been performed (Dennefeld & Kunth, 1981; Blair et al., 1982; Galarza et al., 1999; Bresolin, Kennicutt, & Garnett, 1999; Sanders et al., 2012), measuring gradients with slopes ranging from -0.020 to -0.037 dex/kpc. Additionally, abundances have been calculated for super novae (e.g., Sanders et al., 2012), massive stars (e.g., Venn et al., 2000; Smartt et al., 2001; Trundle et al., 2002), red giant stars (Worthey et al., 2005), planetary nebulae (e.g., Jacoby & Ford, 1986; Jacoby & Ciardullo, 1999; Richer et al., 1999; Kwitter et al., 2012), and globular clusters (e.g., Huchra et al., 1991; Colucci et al., 2009). However, oxygen abundances via the direct method have only been calculated for H II regions in

two studies to date: Esteban et al. (2009) measured a direct oxygen abundance in a single H II region and Zurita & Bresolin (2012) detected auroral line emission in 9 H II regions. Furthermore, these 10 measurements overlap in galactocentric radius, sampling only 2 different regions, and spanning a range of $\sim 8 - 16$ kpc from the nuclear center. The summary of previous abundance observations for M31 is given in Table 5.2.

In order to better establish the direct oxygen abundance gradient in M31 we obtained new MMT and Palomar long-slit optical spectra with the goal of measuring previously undetected direct abundances in H II regions. In Section 5.2, a description of the observations and reductions are given. Plans for emission line measurements and abundance determinations are outlined in § 5.3. This will allow an analysis of the abundance gradients in M31 and comparisons to previous strong-line determinations and gradients measured in other nearby spiral galaxies (e.g., Berg et al., 2013).

5.2 Data

5.2.1 Spectra

Observations

New MMT and Palomar 5m observations were acquired in order to achieve high signal-to-noise (S/N) spectra with the goal of detecting the faint [N II] λ5755 auroral lines at a strength of 4σ or higher.[1] The MMT observations were obtained with the Blue Channel spectrograph (Schmidt et al., 1989) on the UT dates of 27-28 September 2011. Sky conditions varied, but data were only acquired during minimal cloud coverage and approximately arcsecond seeing. A 500 line grating, $1''$ slit, and UV-36 blocking filter were used, yielding an approximate dispersion of 1.2 Å per pixel, a full width at half maximum resolution of $\lesssim 3$ Å, and a wavelength coverage of 3690–6790 Å. The MMT and Blue Channel spectrograph combination provided the balance between sensitivity, resolution, and wavelength coverage conditions necessary to measure all emission lines relevant to oxygen abundance determinations.

Additional spectra of H II regions in M31 were obtained with the double-spectrograph on the 5m at Palomar on the UT dates of 25-26 August 2011 and 31 November 2011. A

[1] [O III] λ4363 is not detected in our spectra as both observatory sites have Hg λ4358 contamination that overlaps O III] λ4363 at the negative redshift of M31.

Table 5.2. Previous Abundance Studies of M31

Reference	Type	of Observations	Gradient (dex/kpc)
Rubin et al. (1972)	SL H II	53	Variable
Dennefeld & Kunth (1981)	SL H II	8	-0.037, -0.024[1]
Blair et al. (1982)	SL H II	11	-0.029
Galarza et al. (1999)	SL H II	46	-0.06
Bresolin, Kennicutt, & Garnett (1999)	SL H II	6	···
Sanders et al. (2012)	SL H II	192	-0.020
Esteban et al. (2009)	D H II	1	···
Zurita & Bresolin (2012)	D H II	9	-0.028[2]
Sanders et al. (2012)	D SN	51	Flat
Venn et al. (2000)	Stars	4	-0.029
Smartt et al. (2001)	Stars	2	···
Trundle et al. (2002)	Stars	7	-0.006
Worthey et al. (2005)	CMD	11[3]	···
Jacoby & Ford (1986)	PNe	3	···
Jacoby & Ciardullo (1999)	PNe	15	···
Richer et al. (1999)	PNe	30	···
Kwitter et al. (2012)	PNe	16	-0.011
Huchra et al. (1991)	GC	150	···
Colucci et al. (2009)	GC	5	···

Note. — Previous measurements of abundances in M31 are listed. While this list is not comprehensive, it includes most studies with new observations and a variety of techniques: SL H II = strong-line H II region abundances, D H II = direct H II region abundances, D SN = direct super novae abundances, CMD = abundances of red giant stars implied from CMD photometry, PNe = planetary nebulae abundances, globular cluster abundances.

[1]Values for the O3N2 method of (Alloin et al., 1979) and O_{32} of (Pagel et al., 1979) respectively.

[2]Slope is from the fit to the 9 data points measured by citetzurita12 plus additional observation from Esteban et al. (2009).

[3]Worthey et al. (2005) observed many stars in 11 fields throughout M31.

600 line/mm grating and $1''$ slit were used, with a wavelength coverage of $\lesssim 3000-7000$ Å in the blue and $4700-11000$ Å in the red. The large wavelength coverage of the double spectrograph combined with its high throughput over this range made it an ideal instrument for our abundance work.

For all observations, bias frames, flat-field lamp images, and sky flats were taken each night. Multiple standard stars from Oke (1990) with spectral energy distributions peaking in the blue and containing minimal line absorption were observed throughout the night using a $5''$ slit over a range of airmasses.

In each H II region, the slit center was aligned with Hα emission such that the surface brightness over the area of the slit was maximized. Three 1200 second exposures were made for both the MMT and Palomar observations, with the slit at a fixed position angle which approximated the parallactic angle at the midpoint of the observation. This, in addition to observing the galaxies at airmasses less than 1.5, served to minimize the wavelength-dependent light loss due to differential refraction (Filippenko, 1982). Finally, combined helium, argon, and neon arc lamps were observed at each pointing for accurate wavelength calibration. Table 5.3 lists the log information for both the MMT and Palomar observations. Figure 5.1 shows an Hα image for M31 created from combining fields 2, 3, 4, and 5 from Massey et al. (2006), with central slit positions from Table 5.2 marked by red circles. The PHAT region is outlined in blue.

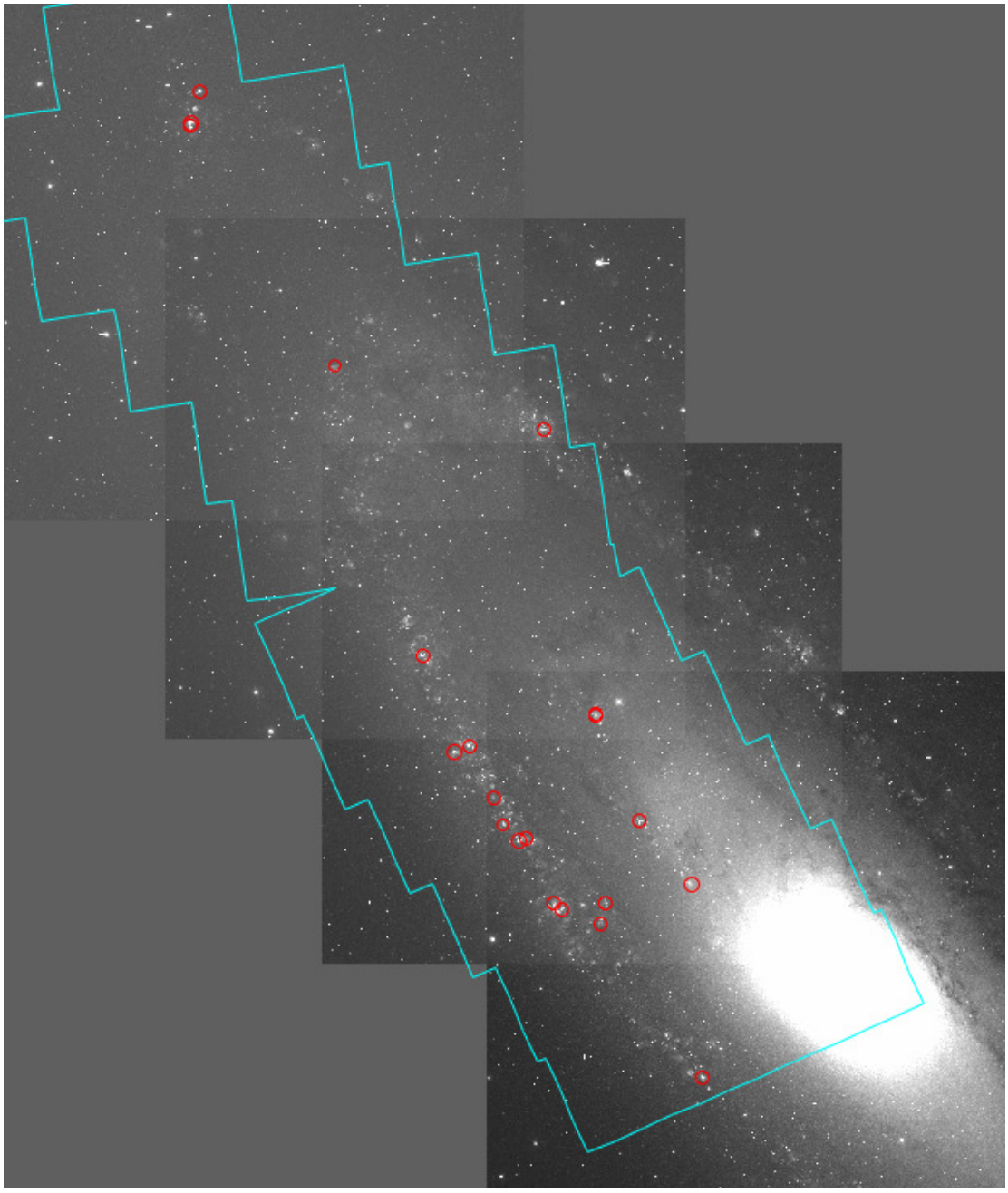

Figure 5.1: Hα image of M31, created by combining Hα images of fields 2, 3, 4, and 5 from Massey et al. (2006). The H II regions observed are circled in red, and are all located in the PHAT region which is outlined in blue. See Table 5.3 for observation details.

Table 5.3. Observing Logs for M31 MMT and Palomar Observations

Slit Position	RA (2000)	Dec (2000)	Slit PA (deg)	Offset (RA, Dec) (arcsec)	R_g (kpc)	Observatory
M31+15.0+6.0	00:43:38.92	41:22:23.24	2.132	14.978, 6.004	2.015	MMT
M31+15.1+10.0	00:43:56.32	41:26:31.50	2.516	15.050, 10.006	2.385	Palomar
M31+29.9+17.004	00:44:12.04	41:33:24.3	2.525	29.866, 17.004	2.413	Palomar
M31+29.9+17.005	00:44:12.11	41:33:25.60	2.526	29.866, 17.005	2.414	Palomar
M31+29.9+35.0	00:44:30.69	41:51:55.10	2.760	29.943, 35.013	2.694	Palomar
M31+15.0-7.0	00:43:34.93	41:09:52.90	3.939	14.961, -6.988	3.701	Palomar
M31+29.85+5.0	00:44:08.38	41:21:12.79	3.965	29.850, 5.001	3.735	Palomar
M31+29.9+3.0	00:44:10.10	41:19:50.95	4.277	29.857, 3.012	4.027	MMT
M31+45.0+39.0	00:45:43.46	41:55:54.96	4.756	44.996, 39.013	4.571	Palomar
M31+29.96+9.0	00:44:35.77	41:25:18.31	4.880	29.964, 9.003	4.601	MMT
M31+29.9+4.0	00:44:23:56	41:20:48.75	4.887	29.914, 4.011	4.602	MMT
M31+29.92+5.0	00:44:26.13	41:21:12.82	4.969	29.924, 5.001	4.679	MMT
M31+29.98+9.0	00:44:38.31	41:25:11.50	5.040	29.975, 9.001	4.752	Palomar
M31+30.0+15.0	00:44:55.94	41:31:21.53	5.115	30.048, 15.003	4.834	MMT
M31+30.0+12.0	00:44:47.34	41:28:01.87	5.120	30.013, 11.998	4.832	Palomar
M31+30.0+10.0	00:44:43.69	41:26:16.00	5.179	29.997, 10.002	4.885	Palomar
M31+44.9+21.0	00:45:11.97	41:37:13.90	5.184	44.865, 21.001	4.913	Palomar
M31+44.8+14.0	00:45:00.43	41:30:52.55	5.433	44.817, 14.012	5.132	Palomar
M31+59.9-2.0	00:46:31.47	42:13:42.65	5.611	59.947, -1.991	5.432	Palomar
M31+60.0-3.99	00:46:34.62	42:11:43.99	5.820	59.960, -3.990	5.620	Palomar
M31+60.0 -4.00	00:46:34.60	42:11:25.94	5.836	59.960, -3.995	5.633	Palomar
M31+60.0-5.0	00:46:34.31	41:11:42.90	13.807	59.960, -4.991	12.981	Palomar

Note. — Observing logs for H II regions observed in M31 at the MMT on the UT dates of 27-28 September 2011 and using the Palomar 5m on the UT dates of 25-26 August 2011 and 31 November 2011. All observations were taken through a 1"×180" slit at the MMT and a 1″×128″ slit at Palomar, with 3×120 second exposures. H II region ID is listed in Column 1. The M31 IDs are assigned by their offsets, and ordered by distance. The right ascension and declination of the individual H II regions are given in units of hours, minutes, and seconds, and decrees, arcminutes, and arcseconds respectively. The position angle (PA) gives the rotation of the slit counter clockwise from North. The distance from the center of the galaxy is listed in Column 7.

Spectra Reduction

MMT and Palomar spectra were reduced and extracted using standard packages in IRAF.[2] Reduction of spectra included bias subtraction and flat fielding based on observations of the quartz halogen lamps. A spectral trace of a bright continuum source was used to define the trace for all slits in each field. As the slits were long compared to the spatial extent of the individual H II regions, the sky background was removed from the two-dimensional spectra via the subtraction of local measurements adjacent to the H II region. Note that this local sky subtraction does have the potential to over-subtract strong lines relative to weaker emission lines, as the temperature of the diffuse ISM is different from the temperature within the H II regions. In the case of the Palomar observations, the red and blue spectra were observed simultaneously, and the continuum is well matched where spectra overlap, indicating matched extraction apertures.

Figure 5.2 shows the resulting one-dimensional Palomar spectra for M31+60.0-5.0 as an example of what is extracted for each H II region in M31. The inset window displays a narrower spectral range to emphasize the auroral line detection at [N II] λ5755. Even the highest-quality spectra observed of the brightest H II regions in M31 only weakly detect the temperature-sensitive [N II] λ5755 auroral line, making direct oxygen abundances extremely difficult to measure and explaining the paucity of previous measurements. Note that the overlapping Hg λ4358 line obscures any measurement of [O III] λ4363.

[2] IRAF is distributed by the National Optical Astronomical Observatories.

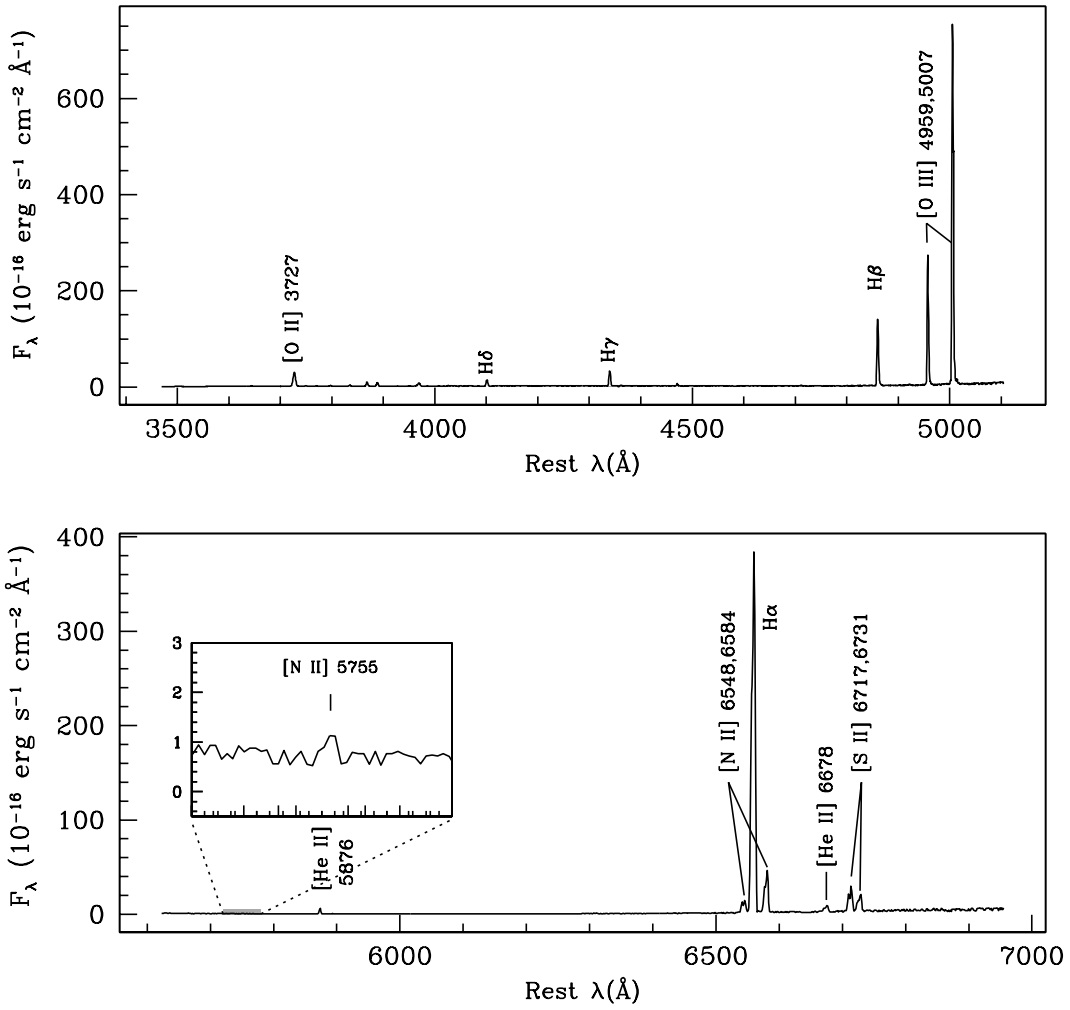

Figure 5.2: An example of the H II region Palomar spectra for M31+60.0-5.0. The top panel displays the blue spectrum and the bottom the red spectrum. Note the strong emission seen for [O III] $\lambda\lambda 4959, 5007$, [N II] $\lambda\lambda 6548, 6584$, and [S II] $\lambda\lambda 6717, 6731$, but very weak detection of [N II] $\lambda 5755$. We emphasize the fact that even though these spectra are of very high quality, fidelity, and signal-to-noise, the temperature-sensitive auroral line is only weakly detected.

5.3 Nebular Abundance Analsysis

5.3.1 Emission Line Measurements

We have extracted emission line spectra for 22 H II regions in M31, 4 of which have strong visible detections of the [N II] λ5755 auroral line. The next step will be to measure the emission line strengths using the standard methods available within IRAF and discussed in the previous chapters of this thesis. In particular, experience has shown us that emission lines are not always fit well by Gaussians, and so we will integrate under the emission line curve using the average local continuum as the base. As usual, special attention will be paid to the Balmer lines to account for the troughs of significant underlying stellar absorption which are observed when an older stellar population is present. Standard reddening corrections will be applied as discussed in Appendix B. Finally, flux line strengths, reddening, and equivalent widths for the Balmer lines will be tabulated for each spectrum.

5.4 Direct Abundance Determinations

5.4.1 Electron Temperature and Density Determinations

For H II regions, accurate direct oxygen abundance determinations require a reliable electron temperature measurement. This is typically done by observing a temperature sensitive auroral line. We will take advantage of the [N II] λ5755 auroral line to accomplish this. To establish a low-uncertainty electron temperature estimate, we define a strong auroral line measurement using a 4σ criterion, but may include detections at the 3σ level due to the difficulty of observing the auroral lines in M31.

Electron temperatures will be determined for these H II regions with strong auroral lines using the [N II] temperature-sensitive auroral to nebular ratio of collisionally excited lines: [N II] I($\lambda\lambda$6548,6584)/I(λ5755). This will be done using the IRAF task TEMDEN, which computes the electron temperature of the ionized nebular gas within the 5-level atom approximation. At a simple level, an H II region can be modeled by two separate volumes, one of low ionization and one of high ionization. For the low ionization zone, we assume T_e(N II) = T_e(O II). The O^+ (low ionization) zone electron temperature can be related to the O^{++} (high ionization) zone electron temperature

(e.g., Campbell et al., 1986; Pagel et al., 1992). We will apply the relation between t_2 (T_e(O II)) and t_3 (T_e(O III)) proposed by Pagel et al. (1992), based on the photoionization modeling of Stasińska (1990), in reverse in order to determine the high ionization zone temperature:

$$t_e(\text{O III}) = \frac{t_e(\text{N II}) - 0.3}{0.7} \tag{5.1}$$

where $t_e = T_e/10^4$ K. Additionally, we calculate a separate T_e(S III) because the S^{++} ionization zone lies partially in both the O^+ and the O^{++} zones:

$$t_e(\text{S III}) = 0.83 \times t_e(\text{O III}) + 0.17. \tag{5.2}$$

To model the physical conditions in the star-forming region, we will determine the electron densities using the [S II] $\lambda\lambda$6717,6731 ratio. In previous chapters we were able to test and assume the low density limit in dwarf galaxies, but a wide range of environments exist across the disk of a spiral galaxy, and so electron density should be calculated for each region when possible.

5.4.2 Ionic Abundances

Ionic abundances will be calculated in a manner consistent with Chapter 4, using:

$$\frac{N(X^i)}{N(H^+)} = \frac{I_{\lambda(i)}}{I_{H\beta}} \frac{j_{H\beta}}{j_{\lambda(i)}}, \tag{5.3}$$

where emissivity coefficients are taken from the IONIC routine in IRAF. Ionization correction factors will be calculated to correct for unobserved ionic states. Further work and analysis will follow the example set by Chapter 4.

5.5 Conclusions

M31, our neighboring sister galaxy, provides a seemingly endless laboratory of data nearly at our fingertips, yet direct abundance observations, of H II regions remain fairly elusive. Recognizing the need for a more detailed study of M31, the Panchromatic Hubble Andromeda Treasury (PHAT) has used the *Hubble Space Telescope* to image roughly 1/3 of M31's star-forming disk in six filters, spanning from the ultraviolet (UV)

to the near-infrared (NIR). The PHAT project seeks to provide the tightest constraints to date on the stellar initial mass function, observation-based calibrations for models of clusters and stellar evolution, and characterize the dust and gas physical properties throughout the disk, all of which would benefit from a more secure measurement of the abundance gradient across the disk of M31.

We present high quality spectroscopic observations of H II regions in the Local Group spiral galaxy M31, in order to measure the true chemical abundance gradient. Using long-slit optical spectroscopy of the highest surface brightness H II regions in the PHAT quadrant, we obtain strong-line abundance estimates of 22 regions, but only measure a temperature sensitive auroral line (needed for direct abundance calculations) in 4 regions. Despite being the nearest large spiral galaxy outside of the Milky Way, direct abundances have have rarely been measured in M31. Combining our observations with the Zurita & Bresolin (2012) sample of 9 H II region direct detections, we created a sample of 13 detections at 6 different radii spanning the inner $\sim 4-16$ kpc of the disk. With this sample we will measure the most complete direct radial gradient for M31 to date, and compare to previous strong-line studies.

5.6 Acknowledgements

Special thanks to Evan Kirby for his role in obtaining observations from Palomar and many helpful discussions. DAB is grateful for support from a Penrose Fellowship, a NASA Space Grant Fellowship, and a Dissertation Fellowship from the University of Minnesota. EDS is grateful for partial support from the University of Minnesota and NSF Grant AST-1109066.

Observations reported here were obtained at the MMT Observatory, a joint facility of the Smithsonian Institution and the University of Arizona. MMT observations were obtained as part of the University of Minnesota's guaranteed time on Steward Observatory facilities through membership in the Research Corporation and its support for the Large Binocular Telescope. This work is based, in part, on observations obtained at the Gemini Observatory, which is operated by the Association of Universities for Research in Astronomy, Inc., under a cooperative agreement with the NSF on behalf

of the Gemini partnership: the National Science Foundation (United States), the National Research Council (Canada), CONICYT (Chile), the Australian Research Council (Australia), Ministrio da Cincia, Tecnologia e Inovao (Brazil) and Ministerio de Ciencia, Tecnologa e Innovacin Productiva (Argentina). The authors wish to recognize and acknowledge the very significant cultural role and reverence that the summit of Mauna Kea has always had within the indigenous Hawaiian community. We are most fortunate to have the opportunity to conduct observations from this mountain.

This research has made use of NASA's Astrophysics Data System Bibliographic Services and the NASA/IPAC Extragalactic Database (NED), which is operated by the Jet Propulsion Laboratory, California Institute of Technology, under contract with the National Aeronautics and Space Administration. This work was initiated as part of the Spitzer Space Telescope Legacy Science Program and was supported by National Aeronautics and Space Administration (NASA) through contract 1336000 issued by the Jet Propulsion Laboratory (JPL), California Institute of Technology (Caltech) under NASA contract 1407.

Chapter 6

Summary of Conclusions: Primary Results

6.1 Re-examining SDSS Mass-Metallicity Outliers

In Chapter 2 we examine outliers from the low-mass, high oxygen abundance galaxy sample reported by Peeples et al. (2008). Optical spectra for four of 41 of these luminosity-metallicity outliers were re-observed using the blue channel spectrograph at the MMT and analyzed. As an improvement over the SDSS spectra, extended blue wavelength coverage allowed all ionic species of oxygen to be evaluated simultaneously, while also considering the implications of additional spectral features, such as nitrogen abundance, excitation, and underlying stellar absorption. With this analysis we found:

- Three of four galaxies have relatively low excitation ($\log(O_{32}) < -0.4$).
- All four galaxies exhibited high N/O values.

  Most strong-line abundance methods are calibrated against young star forming regions, which have high excitation ratios and minimal nitrogen enrichment since delayed secondary nitrogen production has not yet occurred. The characteristics listed in the first two bullets suggest the galaxies studied here are not readily comparable using strong-line abundance calibrations, and likely predict the significant oxygen abundance deviations seen in the Peeples et al. (2008).

- In comparison to the photoionization models of Stasińska & Leitherer (1996) (which include the effects of aging of the exciting stars), and the empirical calibrations of PMC09 (which correct for variations in the N/O ratio), we found that significantly lower oxygen abundances are favored. The Stasińska & Leitherer (1996) oxygen abundances are in line with those expected from the luminosities and stellar masses of the galaxies, while the PMC09 estimates shift oxygen abundances in the right direction. While the "very low mass" sample displays low star formation rates, the normal star formation within the "main" sample rules out exhaustive star formation as the variable responsible for the unusual sample spectra.

We propose that the four low-mass, high oxygen abundance SDSS galaxies examined in Chapter 2 are best described as nitrogen enriched. A dwarf galaxy may experience an episode of nitrogen enrichment if it has recently passed through the "Wolf-Rayet galaxy" phase.

6.2 Direct Oxygen Abundances for Low Luminosity LVL Galaxies

in Chapter 3, we have determined uniform oxygen abundance metallicities for 31 low-luminosity galaxies from the *Spitzer* LVL survey in order to fill in the sparsely populated low-luminosity end of the M-Z relationship. With high-resolution spectral observations taken at the MMT, we were able to measure the intrinsically faint [O III] λ4363 fluxes at strengths of 4σ or greater and explicitly determine electron temperatures. Metallicity measurements are important for characterizing many other properties, especially when the more reliable direct method is used. However, metallicity relationships tend to suffer from small number statistics in the low-luminosity regime. In particular, these measurements allowed us to better characterize the luminosity-metallicity and mass-metallicity relationships by doubling the number of reliable low-luminosity measurements. We created a "Combined Select" sample of objects that have both reliable direct oxygen abundance determinations and distances estimated from the tip of the red giant branch or Cepheid variables. With this sample, we find:

- Both the luminosity-metallicity and the mass-metallicity relationships agree well with previous relationships defined for low-luminosities.

- From the 38 objects making up the "Combined Select" sample, we found an optical L-Z relationship of $12 + \log(\mathrm{O/H}) = (6.27 \pm 0.21) + (-0.11 \pm 0.01)M_B$, with a dispersion of $\sigma = 0.15$. In comparison, the near-IR L-Z relationship for this data is $12 + \log(\mathrm{O/H}) = (6.10 \pm 0.21) + (-0.10 \pm 0.01)M_{[4.5]}$, with a dispersion of $\sigma = 0.14$. While the slopes of the two L-Z relationships agree, our findings confirm the work of L06 in that the near-IR relationship has lower scatter.

- By converting NIR luminosity to a stellar mass estimate, we determined the M-Z relationship for our data to be $12 + \log(\mathrm{O/H}) = (5.61 \pm 0.24) + (0.29 \pm 0.03)M_\star$, with a dispersion of $\sigma = 0.15$. In agreement with the idea that mass is more fundamentally related to metallicity than luminosity, we find that the intrinsic scatter of the optical L-Z, NIR L-Z, and M-Z relationships decreases from 0.13 to 0.12 to 0.08.

- However, the total dispersion of the M-Z relationship was measured to be no smaller than the L-Z relationships. This suggests, given a reliable distance measurement and appropriate photometry, luminosity is just as strong of a metallicity indicator as stellar mass.

- Furthermore, with the dispersions in luminosity and mass roughly equal, either may be used in combination with a reliable distance determination to estimate metallicity of a low-luminosity dwarf with more confidence than when using strong-line calibrations.

- Our observations of N/O abundances are in agreement with previous studies. We find a positive correlation between N/O ratio and B-V color for $0.05 \lesssim B - V \lesssim 0.75$; $\log(\mathrm{N/O}) = (-1.92 \pm 0.08) + (1.18 \pm 0.19) \times (B - V)$, with a dispersion of $\sigma = 0.14$.

- In agreement with observations of blue compact galaxies, there are no objects with high N/O ratio ($\log(\mathrm{N/O}) > -1.4$) below $12+\log(\mathrm{O/H})=7.7$. Since the typical low-luminosity galaxy in the Local Volume displays roughly constant star formation

over the age of the universe, the small dispersion in N/O at low values of O/H cannot be due to the very recent birth of the galaxy.

The data presented in this chapter agree with previous studies, but come from a larger, tighter parent sample and thus offer a M-Z relationship for dwarf galaxies with reduced uncertainties. Due to the small dispersions measured for both the L-Z and M-Z relationships, we suggest that either may be used in combination with a reliable distance determination to estimate metallicity of a low luminosity dwarf galaxy with more confidence than when using strong-line calibrations.

6.3 New Radial Abundance Gradients for NGC 628 and NGC 2403

Spiral galaxies pose a challenge to abundance work, as a single abundance measurement is not sufficient to characterize the entire galaxy. Thus, high quality spectra of many H II regions that enable direct abundances are required to securely measure the oxygen abundance gradient.

We have uniformly determined oxygen abundance metallicities for 14 H II regions in the local spiral galaxy NGC 628 and seven H II regions in NGC 2403. With high-quality spectroscopic observations, we measured the intrinsically faint [O III] λ4363 and/or [N II] λ5755 auroral lines at a strength of 3σ or greater, and explicitly determine electron temperatures in all 14 H II regions in NGC 628. The seven H II regions in NGC 2403 were chosen to have strong auroral emission lines and, therefore, all have electron temperatures determined at a significance above 4σ. From these high quality data sets, we come to the following conclusions:

(1) Oxygen abundance gradient:

- From the 4σ data of NGC 628, we derive an oxygen abundance gradient of 12 + log(O/H) = (8.43±0.02) + (-0.017±0.002)$\times R_g$ (dex/kpc), with a dispersion in log(O/H) of σ = 0.11. This result is the first ever direct oxygen abundance gradient for H II regions in NGC 628, and has a significantly shallower slope than found by previous empirical abundance studies.

- From the 4σ data of NGC 2403, we derive an oxygen abundance gradient of 12 + log(O/H) = $(8.47 \pm 0.02) + (-0.028 \pm 0.007) \times R_g$ (dex/kpc), with a modest dispersion of $\sigma = 0.07$. As all previous studies of NGC 2403 have relied primarily on strong-line abundances, with only a small number of direct abundances, this result is an improved metallicity gradient analysis.

- By applying the new oxygen abundance gradients for NGC 628 and NGC 2403 and comparing to detailed studies of M 101, we find a tighter relationship amongst spiral galaxies for increasing $L_{\sum PAH}/L_{TIR}$ with oxygen abundance for metal-rich regions. At lower oxygen abundances, we see a dropped plateau in PAH emission that is similar to previous studies, however, we find a higher transition. Further detailed auroral abundance gradients for spiral galaxies are needed to complete this picture.

(2) Nitrogen abundance gradient:

- The N/O ratio in NGC 628 demonstrates a negative gradient with increasing galactocentric radius in the inner disk. Further out in the outer disk, this relationship flattens out, where we find a plateau past $R_g = R_{25}$ near an oxygen abundance of 12+log(O/H) = 8.3. Similar trends are seen in other spiral galaxies, where the R_{25} radius and oxygen abundances of 12+log(O/H) = 8.3 and greater mark points of transition in nitrogen production.

- The N/O ratio in NGC 2403 also demonstrates a negative gradient with increasing galactocentric radius throughout the disk. In contrast to the trend seen in NGC 628, NGC 2403 is best fit with a single linear relationship between N/O ratio and radius.

- In NGC 2403, and in previous studies, cases where a galaxy's N/O ratio is observed to follow a single linear trend do not include observations in their extended disks beyond R_{25}. Thus, the mechanism of nitrogen production in these galaxies are not readily comparable to galaxies with observations of greater radial coverage.

(3) α-process elements:

- As expected for α-process elements, S/O, Ne/O, and Ar/O appear to be constant over a range in oxygen abundance in both NGC 628 and NGC 2403 such that the

α-elements and O are produced in lock-step. However, these results are based on few data points, and thus should be weighted tenuously.

Since there is a general paucity of abundance data from individual spiral galaxies, more of these accurate H II region datasets are necessary to understand individual galaxy processes and relative trends among galaxies.

6.4 An Updated Direct Radial Abundance Gradient for M31

The Panchromatic Hubble Andromeda Treasury (PHAT) has used the *Hubble Space Telescope* to image roughly 1/3 of M31's star-forming disk in six filters, spanning from the ultraviolet (UV) to the near-infrared (NIR). The PHAT project seeks to provide the tightest constraints to date on the stellar initial mass function, observation-based calibrations for models of clusters and stellar evolution, and characterize the dust and gas physical properties throughout the disk, all of which would benefit from a more secure measurement of the abundance gradient across the disk of M31.

We present high quality spectroscopic observations of H II regions in the local spiral galaxy M31, in order to measure the true chemical abundance gradient. We observed long-slit optical spectroscopy on the 6.5-m MMT and 5-m Palomar telescopes of the highest surface brightness H II regions in the PHAT quadrant. We obtain emission-line spectra of 22 regions, but only measure a temperature sensitive auroral line (needed for direct abundance calculations) in 4 regions. Despite being the nearest large spiral galaxy outside of the Milky Way, direct abundances have have rarely been measured in M31. We will combine our observations with the work of Zurita & Bresolin (2012) to create a sample of 13 detections at 6 different radii spanning the inner $\sim 4 - 16$ kpc of the disk. With this sample we will measure the most complete direct radial gradient for M31 to date, and compare to previous strong-line studies.

Chapter 7

Future Work

The work presented in this thesis has addressed several questions regarding ISM studies and extragalactic chemical evolution, while stimulating several new areas of investigation and laying the foundation for more in depth analysis. In particular, two studies are in the initial phases to access the evolution of carbon and oxygen in dwarf galaxies and to compare trends amongst spiral galaxies by building a database of galaxies with reliable and consistent direct abundance observations.

7.1 The Evolution of C/O in Dwarf Galaxies

Motivation for the Investigation of C and O in Dwarf Galaxies

Because C and O are an important source of interior opacity in stars, knowledge of the time evolution of CNO abundances is necessary to properly model stellar isochrones. Furthermore, because these lines originate principally in star forming regions, they trace the physical conditions in the gas from which the current generation of massive stars (MS) are forming. Equally significant, this interstellar gas carries the signature of the interplay between star formation, gas accretion, and supernova-driven feedback across cosmic time. Figure 1, from Kobulnicky & Skillman (1998), displays some of the highest-quality C/O measurements taken to date, many taken with the now retired Faint Object Spectrograph (FOS) on the *Hubble Space Telescope* (HST). Included are the observations from Kobulnicky & Skillman (1998) as well as 11 metal-poor systems

from Garnett et al. (1997a), Garnett et al. (1995b), and Dufour (1984). The considerable scatter and uncertainties displayed by these data challenge our ability to differentiate between hypotheses describing carbon (and nitrogen) production in low metallicity H II regions.

A review of the state of CNO measurements at the time is given in Garnett et al. (1995a, ; hereafter G95). Similar reviews have also been discussed in Izotov & Thuan (1999), Garnett et al. (1999), and Gustafsson et al. (1999). The G95 review found: (1) G95 HST FOS observations show a monotonic increase in C/O from log(C/O)~ -0.9 at 12+log(O/H)$\approx$7.4 to log(C/O)~ -0.5 at 12+log(O/H)$\approx$8.3. This trend contrasts that seen in Galactic stars, where the C/O ratio is roughly constant over this range in O abundance (e.g., Gustafsson et al., 1999). With a better assessment of this trend in H II regions, we will compare to stellar evolutionary models and nucleosynthetic time scales. (2) There are too few measurements available to address the intrinsic dispersion in C/O at a fixed O/H. Garnett (1990) discusses the likelihood of large fluctuations in C/O at a fixed O/H as a result of delayed C ejection from intermediate-mass stars (IMS) of various starburst episodes. HST measurements of C/O for our larger sample of dwarf galaxies will permit us to perform a statistical analysis of the dispersion in C/O.

More recently, Guseva et al. (2011) compared the relationship between C/O and O/H for new observations and literature values. Assuming the C^{++}/O^{++} RL ratio as a measure of C/O, they conclude the C/O ratio increases with O/H. In contrast, Izotov & Thuan (1999) find a remarkably small dispersion in the C/O and N/O ratios at very low O abundances and claim this as strong evidence against time-delayed production of C and primary N in the lowest metallicity blue compact galaxies (BCGs). Further, the absence of time-delayed C and N is consistent with the scenario that galaxies with 12+logO/H$\leq$7.6 are now undergoing their first burst of SF, and that they are therefore young, with ages $\leq$ 40 Myr. If very low metallicity BCGs are indeed young, this would argue against the commonly held belief that C and N are produced by IMSs ($3M_{\odot} \leq M \leq 9M_{\odot}$) in low metallicity galaxies, as these stars would not have yet completed their evolution. In our own Milky Way, Mattsson (2010) used chemical evolution models to show that the major source of C is from low- and IMSs, providing as much as 80% of the C in the ISM. However, Mattsson also suggests an evolving, top-heavy initial mass

function is needed during the early stages of Galactic evolution to explain the observed declining trend in C/O with increasing O/H in the solar neighborhood (Fabbian et al., 2009). Although low- and IMSs may provide the simplest explanation of observed C trends, the stellar origin of C remains a highly debated question. With a 3-fold increase in the sample of reliable C/O measurements in metal deficient dwarfs, we can determine the underlying trend of C with O, and thus the dominant source of C production, but also assess the nature of the C/O scatter at a given value of O/H.

It is also interesting to compare C/O abundances in H II regions with other systems to decipher nucleosynthesis and chemical enrichment in the early Universe. Tsujimoto & Bekki (2011) find that the most metal-poor damped Lyα (DLA) absorbers exhibit relatively high C/O ratios for 12+log(O/H)7.0, which contradict low-redshift extragalactic H II region measurements. Rather, Tsujimoto & Bekki (2011) suggest an upper truncation of the initial mass function producing fewer MSs in metal-poor DLA systems as a possible explanation. Given this recent interest in the possibility of non-universal initial mass functions in low-mass (low- metallicity) galaxies, a better characterization of the behavior of C/O is vital.

Some secondary objectives which can be addressed with our observations are: (1) Our observational setup allows us to observe Si III] λ1883,1896 at no extra cost in observing time. We can use these measurements to derive Si/O ratios, derive Si depletions relative to O in H II regions, and study the evolution of Si/O as a function of metallicity and dust-to-gas ratio. Garnett et al. (1995b) found that, on average, only half of the total silicon abundance is incorporated into dust grains in H II regions. Confirming this result would imply grain modification is occurring within these H II environments. We note that in many IUE spectra of extragalactic H II regions the Si III] lines are the next strongest after C III], but in some they are unexpectedly absent. (2) G95 found that N III] proved difficult to measure, but we can measure a N/O abundance from the optical spectra available for our sample. This will allow us to test C/O variations as a function of N/O variations. In particular, Kobulnicky et al. (1997b) measured H II region abundances in NGC 5232 using FOS on HST and found regions with enhanced in N abundance, but no corresponding increase in C, suggesting that N production is decoupled from C and O production. We will test this conclusion with our HST COS observations. (3) We can use the stellar UV continuum to study the stellar population

content as a function of metallicity (Fanelli et al., 1988, e.g.,).

7.1.1 Spectroscopic UV Observing Plan

Carbon has been historically difficult to observe in extragalactic H II regions. Carbon has no strong transitions of its important ionization states in the optical, and there are no IR transitions for C^{+2}, the main ionization state of C, in H II regions. Other methods have been explored as means to measure C abundances, such as optical recombination lines (RLs) of C II (Esteban et al., 2009). However, there are significant discrepancies between abundances from RLs vs. CELs, and the C II tend to vanish at low metallicities. Stars are another way to determine abundances, but this is done with the most luminous stars, which in extragalactic H II regions tend to be evolved giants and super giants, whose surfaces are complicated by the effects of internal mixing (Venn, 1995). The UV conveniently contains transitions for O III], N III], C III], Si III, and Ne III] all within the 1600-2000 Å range. These transitions have high excitation energies (6-8 eV), and so are best observed in low metallicity environments where T_e is high such as in the star forming regions of our sample. Observations of C lines in about a dozen H II regions have been obtained with IUE, but for most of these the C line detections are marginal. UV FOS observations have proven successful in obtaining secure measurements of O III] and C III], but only for 6 dwarf galaxies in the same O abundance range as our sample (12+log(O/H)$\leq$8.2). In nearly all cases, improved measurements of the C lines are desirable.

With many new low-metallicity nearby dwarf galaxies found with the completion of the Sloan Digital Sky Survey (SDSS) and the addition of the Cosmic Origin Spectrograph (COS) on the HST, previous studies can be improved upon by creating a statistically significant sample of low-metallicity dwarfs with high-quality carbon and oxygen abundances. COS on the HST is scheduled to perform spectroscopic measurements of the UV O and C emission lines (O III] λ1660-1666 and C III] λ1906-1909) for a sample of extragalactic H II regions in 12 metal-poor dwarf galaxies. COS achieves improved sensitivity over previous UV spectrographs and has a UV coverage from $1150 - 3200$ Å allowing simultaneous measurement of O III] $\lambda 1661 - 1666$ and C III] $\lambda 1907 - 1909$ for C/O ratio determinations, and reducing uncertainty due to reddening effects. Further, by focusing on a low-metallicity sample, uncertainties due to metallicity dependent

yields and other factors are avoided.

In order to establish the C/O relationship with O/H in the sparsely measured metal poor regime, we have chosen objects with high emission line surface brightnesses and low metallicity which span a large range in O abundance. Figure 7.1 shows the bright, compact targets of our proposed sample, which allow maximum flux through the 2.5″ COS aperture. Further selection criteria was implemented to ensure high-quality emission line observations based on the properties of the successful targets in G95. In every case we have excellent ground based optical spectra, and have chosen our targets to have strong [O III] λ4363 emission lines, providing a direct measurement of the T_e in the nebulae. Further, we selected objects with high ionizations ([O III] λ5007/[O II] λ3727) to increase the observability of the UV O III] line.

7.1.2 Science Objectives

We will use these data to study the relative variation of C with respect to O, which yields information on the time evolution of these elements and their nucleosynthetic origins. C and O are thought to originate primarily from stars of different mass ranges, where O is synthesized mostly in MSs (M $10M_{\odot}$), while C is produced in both MSs and intermediate-mass stars (IMS). Following this assumption, a simple chemical evolution model with instantaneous recycling predicts C/O$\propto$O/H if IMSs dominate C production. On the other hand, if C/O were constant, it would imply primary production of both C and O. Garnett et al. (1995b) used HST FOS observations to show that C/O continuously increases with increasing O/H in metal-poor systems, implying C is largely produced by IMSs . However, this result is based upon only 5 observations below a metallicity of 12+log(O/H)=8.0. Using analytical models of stellar yields compared to C/O abundances of disk F and G stars , B stars, and halo stars, and a limited number of H II regions, Henry et al. (2000) found that 97% of the total C was produced by MSs. While the Garnett et al. (1995b) sample provided a good foundation from which secure C/O observational trends can be built, the sample size was small enough that it is susceptible to skew from a single data point. Building upon the work of Garnett et al. (1995b), our COS observations would allow us to evaluate the above trends with the first statistically robust relationship of secure C/O abundances, drawn from a combined sample 19 low-metallicity dwarf galaxies.

7.1.3 Summary of Future C/O Work

Our knowledge of the relative C and O abundances in other galaxies has not advanced significantly since the work of Garnett et al. (1995a, 1997a, 1999), as this work was relatively expensive in terms of HST observing time. With the optimal wavelength coverage offered by COS and its improved sensitivity over other UV spectrographs and a significantly larger database of optical spectra thanks to all sky-surveys such as the Sloan Digital Sky Survey (SDSS), we will obtain spectroscopy of 12 dwarf galaxies, increasing the number of metal-poor galaxies with reliable C and O abundances by a factor of 3. Given the recent interest in possibilities of non-universal initial mass functions in low-mass (low-metallicity) galaxies, a secure characterization of the behavior of C/O is vital.

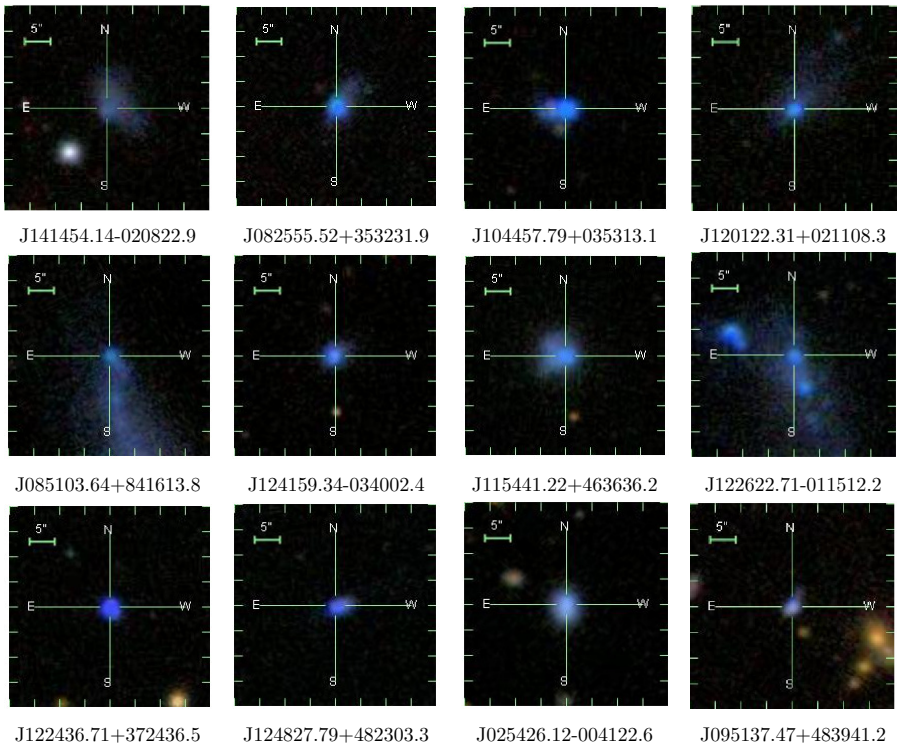

Figure 7.1: SDSS images of the targets in our sample. Notice the bright blue appearance and compact morphologies signifying ongoing star formation and high surface brightnesses which allow for maximum flux through the 2.5″ COS aperture.

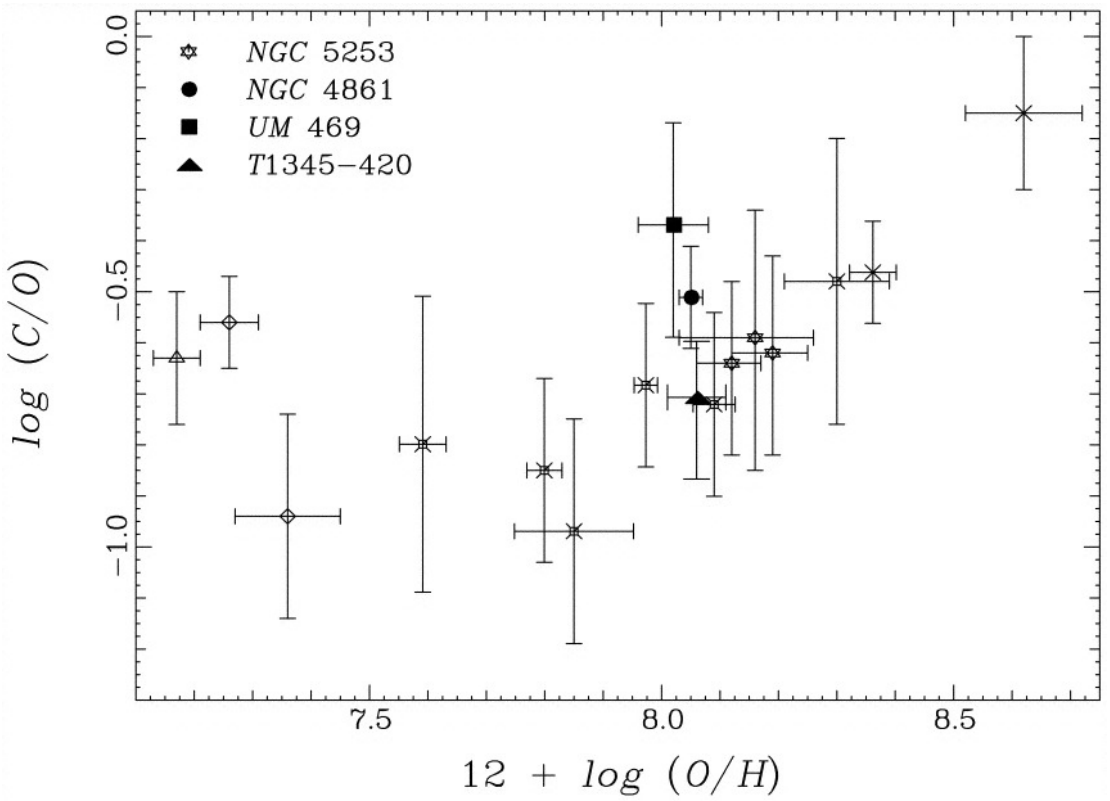

Figure 7.2: Plot of 12 + log (O/H) vs. log (C/O) from Kobulnicky & Skillman (1998). Included for comparison are 11 other metal-poor systems from Garnett et al. (1997a, diamonds), Garnett et al. (1995b, crossed circles), and Dufour (1984, crosses). Three independent locations within NGC 5253 (Kobulnicky et al., 1997b) are also plotted as stars.

7.2 CHAOS: CHemical Abundances Of Spirals

7.2.1 Motivation for the Investigation of Abundance Gradients

Unlike the uniform physical conditions observed for dwarf galaxies, properties of the ISM of spiral galaxies are known to show radial variations, such as in their dust-to-gas ratio and abundance ratios. Motivated by the need to place gradients on the same scale for comparisons amongst galaxies, we presented direct abundance gradients of the nearby spiral galaxies NGC 628 and NGC 2403 in Chapter 4. By using only high signal-to-noise direct oxygen abundance measurements, we set a reliable and consistent

basis for comparing to previous direct abundance studies and the derivation of future abundance gradients in spirals. However, a large enough database to compare relative trends amongst galaxies does not yet exist. Our lack of secure abundances in nearby spiral galaxies limits our ability to understand (1) chemical abundance gradients, (2) dispersion in abundances at a given radius, (3) stellar nucleosynthetic yields, which place constraints on the stellar IMF, (4) the chemical evolution of galaxies at high redshift, and thus, (5) the chemical enrichment history of the universe.

CHemical Abundances Of Spirals (CHAOS) is a NSF program which uses the University of Minnesota's (co-PI: Evan D. Skillman) and The Ohio State University's (co-PI: Richard W. Pogge) guaranteed time on the Large Binocular Telescope (LBT) to definitively establish, for the first time, chemical abundances of a statistically significant sample of H II regions in nearby spiral galaxies. In order to achieve our goal of absolute chemical abundance gradients in spiral galaxies, we have begun to obtain, reduce, and analyze a sample of approximately 1,000 high quality H II region spectra from 13 spiral galaxies drawn from the Spitzer Infrared Nearby Galaxies Survey (SINGS).

7.2.2 Sample and Observing Description

Target selection began with the sample of nearby galaxies from the Spitzer Infrared Nearby Galaxies Survey (SINGS; PI: Kennicutt, see Kennicutt et al., 2003b). The SINGS galaxies compose a well defined sample of spiral galaxies with numerous H II regions, and have been studied in depth, with Spitzer observations and large ancillary data sets. These galaxies have resolved 3.6160 μm imaging, 540 μm IRS spectroscopy of the central regions plus select extra-nuclear H II regions, high-quality H I and CO gas maps with detailed 2-D rotation curves. Additionally, Herschel PACS and SPIRE imaging as well as far-IR spectroscopy of selected H II regions have been observed under the KINGFISH program (PI: Kennicutt, see Kennicutt et al., 2011). Incorporating this already large composite database with new spectroscopic abundances will allow us to model the chemical evolution of these galaxies.

The Multi-Object Double Spectrograph (MODS, Pogge et al., 2010) on the LBT has been designed for high photometric fidelity over more than one octave in wavelength. Because MODS is a double spectrograph, all lines are observed simultaneously, which leads to both a higher efficiency and higher fidelity. Although the faint auroral

lines ([O III] λ4363, [N II] λ5755, [S III] λ6312, [O II] λ7325, and [S II] λ4076) are at very different wavelengths from their stronger nebular lines counterparts ([O III] λ5007, [N II] λ6584, [S III] λ9069, [O II] λ3727, and [S II] λ6731, respectively), MODS offers high fidelity over more than an octave in wavelength and high throughput at short wavelengths ($\lambda < 3600$Å), providing the wavelength coverage needed for multiple temperature and density diagnostics. Further, we observe the large $5' \times 5'$ MODS field of views with multi-slit masks. We design each mask to overlay slits on $\sim$20 of the highest surface brightness H II regions (based on continuum-subtracted Hα imaging) and include individual slits designated for sky subtraction.

7.2.3 Scientific Objectives

The primary goal of the CHAOS project is to accurately determine, for the first time, the absolute chemical abundances of a statistically significant sample of H II regions in nearby spiral galaxies. To date we have observed 19 mask fields in 9 spiral galaxies. With a rough average of $\sim$ 20 H II regions observed per mask, $\sim$ 400 H II region spectra have been collected. The CHAOS team has developed a MODS reduction pipeline and all observed spectra have subsequently been reduced, extracted, and calibrated. In practice, the function of MODS has matched of exceeded expectations. Figure 7.3 displays an example of a set of the high caliber spectra that can be obtained with the MODS/LBT combo. Some key highlights of the data include detections of the very weak Balmer emission lines down to H12 at λ3750, the high significance of the temperature sensitive [O III] λ4363 emission line, detections of He I λ5015, the auroral lines [N II] λ5755 and [S III] λ6312, He I λ6678, [S III] $\lambda\lambda$9060,9532, and the Paschen sequence.

The unique capabilities of LBT/MODS has allowed us to use multiple emission line diagnostics to determine the physical conditions in the H II regions. We are currently in the process of modifying available line fitting pipelines to meet the specifications of MODS spectra. Special care is being taken to ensure the pipeline consistently measures emission lines as expected by comparing all $\sim$ 60 H II region spectra fits to measurements by hand in IRAF. Once we have converged on the desired level of accuracy, absolute and relative chemical abundances can be determined with uncertainties less than 0.2 dex.

One observations of all 13 spiral galaxies are complete, we will posses a survey of

$\sim$1000 high signal-to-noise H II region spectra from which we will analyze the chemical abundance gradients and dispersions in abundances at a given radius. By comparing these observations with disk-galaxy formation models we will place fundamental constraints on the gas accretion and star formation histories of disk galaxies. Further, by accurately establishing H II region chemical abundances across the disks of spiral galaxies and the range of physical conditions present within them, we reliably calibrate strong-line abundance methods without sample selection effects for the first time. We can then apply such a universal strong-line calibration to distant galaxies, improving our understanding of chemical evolution at high redshift. Most importantly, this work will definitively resolve the systematic discrepancy in the nebular abundance scale.

The ongoing dwarf C/O and CHAOS projects described here will provide a wealth of unprecedented data about radial abundance gradients, chemical mixing time scales, dust abundances, and the sources of elemental production, all of which will help shape our future understanding of chemical evolution.

(a) Blue Spectrum

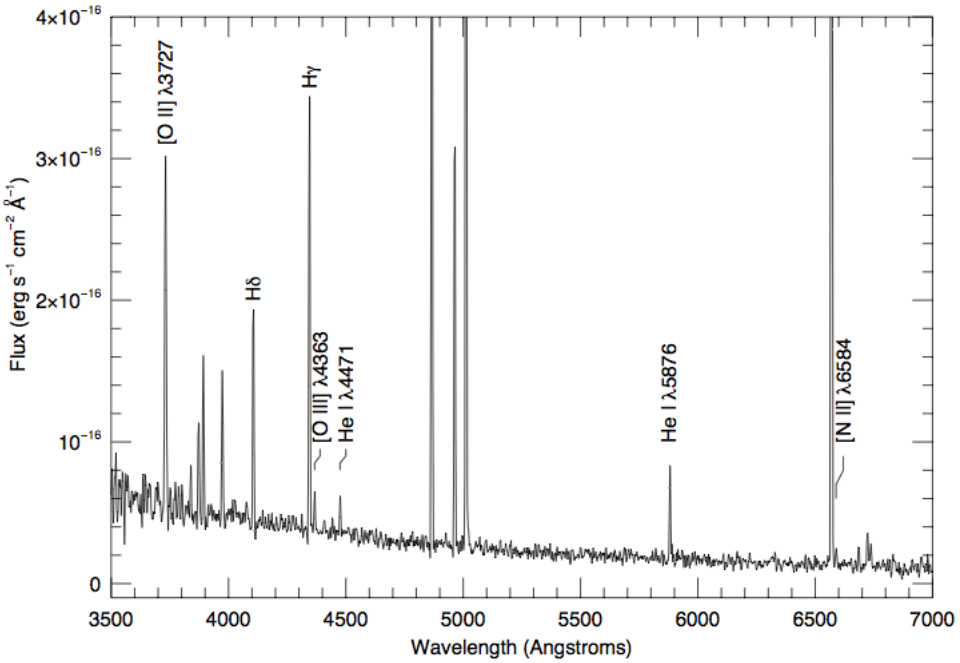

(b) Red Spectrum

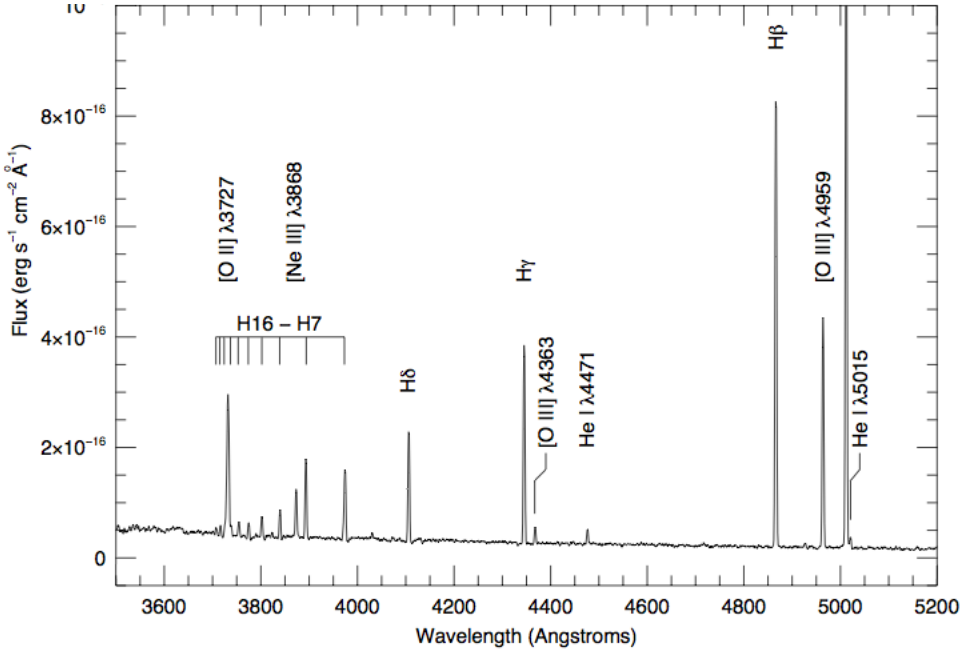

Figure 7.3: Example of high caliber MODS/LBT spectra of Leo P (Skillman et al., 2013).

References

Adelman-McCarthy, J. K., et al. 2006, ApJS, 162, 38

Aller, L. H. 1942, ApJ, 95, 52

Alloin, D., Collin-Souffrin, S., Joly, M., & Vigroux, L. 1979, A&A, 78, 200

Amorín, R. O., Mu noz-Tu nón, C., Aguerri, J. A. L., Cairós, L. M., & Caon, N. 2007, A&A, 467, 541

Amorín, R. O., Pérez-Montero, E., & Vílchez, J. M. 2010, ApJ, 715, L128

Annibali, F., Aloisi, A., Mack, J., Tosi, M., van der Marel, R. P., Angeretti, L., Leitherer, C., & Sirianni, M. 2008, AJ, 135, 1900

Azimlu, M., Marciniak, R., & Barmby, P. 2011, AJ, 142, 139

Baade, W., & Arp, H. 1964, ApJ, 139, 1027

Barazza, F. D. and Binggeli, B., & Prugniel, P. 2001, A&A, 373, 12

Bell, E. F., & de Jong, R. S. 2001, ApJ, 550, 212

Berg, D. A., Skillman, E. D., & Marble, A. R. 2011, ApJ, 738, 2

Berg, D. A. et al. 2012, ApJ, 754, 98

Berg, D. A. et al. 2013, ApJ, *accepted*

Blair, W. P., Kirshner, R. P., & Chevalier, R. A. 1982, ApJ, 254, 50

Blanton, M. R., & Moustakas, J. 2009, ARA&A, 47, 159

Bresolin, F., Kennicutt, R. C., Jr., & Garnett, D. R. 1999, ApJ, 510, 104

Bresolin, F., Garnett, D. R., & Kennicutt, Jr., R. C. 2004, ApJ, 615, 228

Bresolin, F., Schaerer, D., González Delgado, R. M., & Stasińska, G. 2005, A&A, 441, 981

Bresolin, F. 2007, ApJ, 656, 186

Bresolin, F., Gieren, W., Kudritzki, R.-P., et al. 2009a, ApJ, 700, 309

Bresolin, F., Ryan-Weber, E., Kennicutt, R. C., & Goddard, Q. 2009, ApJ, 695, 580

Bresolin, F. 2011, ApJ, 730, 129

Bresolin, F., Kennicutt, R. C., & Ryan-Weber, E. 2012, ApJ, 750, 122

Brinchmann, J., Charlot, S., White, S. D. M., Tremonti, C., Kauffmann, G., Heckman, T. & Brinkmann, J. 2004, MNRAS, 351, 1151

Brinchmann, J., & Ellis, R. S. 2000, ApJ, 536, 77

Brooks, A. M., Governato, F., Booth, C. M., Willman, B., Gardner, J. P., Wadsley, J., Stinson, G., & Quinn, T. 2007, ApJ, 655, L17

Bruzual, G. & Charlot, S. 2003, MNRAS, 344, 1000

Campbell, A., Terlevich, R., & Melnick, J. 1986, MNRAS, 223, 811

Cannon, J. M., Dohm-Palmer, R. C., Skillman, E. D., Bomans, D. J., Côté, S., & Miller, B. W. 2003, AJ, 126, 2806

Cardelli, J. A., Clayton, G. C., & Mathis, J. S. 1989, ApJ, 345, 245

Carigi, L., & Peimbert, M. 2011, , 47, 139

Castellanos, M., Díaz, A. I., & Terlevich, E. 2002, MNRAS, 329, 315

Cedrés, B., Cepa, J., Bongiovanni, Á., Castañeda, H., Sánchez-Portal, M., & Tomita, A. 2012, A&A, 545, A43

Charlot, S., & Longhetti, M. 2001, MNRAS, 323, 887

Chiappini, C., Romano, D., & Matteucci, F. 2003, MNRAS, 339, 63

Cole, A. A., Skillman, E. D., Tolstoy, E., et al. 2007, ApJ, 659, L17

Colucci, J. E., Bernstein, R. A., Cameron, S., McWilliam, A., & Cohen, J. G. 2009, ApJ, 704, 385

Cook, D. O., Seth, A. C., Dale, D. A., et al. 2012, ApJ, 751, 100

Cooper, M. C., Tremonti, C. A., Newman, J. A., & Zabludoff, A. I. 2008, MNRAS, 390, 245

Conroy, C., & Gunn, J. E. 2010, ApJ, 712, 833

Contini, T., Treyer, M. A., Sullican, M., & Ellison, R. S. 2002, MNRAS, 330, 75

Corbelli, E., Lorenzoni, S., Walterbos, R., Braun, R., & Thilker, D. 2010, A&A, 511, A89

Crawford, D. L., & Barnes, J. V. 1970, AJ, 75, 978

Crockett, N. R., Garnett, D. R., Massey, P., & Jacoby, G. 2006, ApJ, 637, 741

Croxall, K. V., van Zee, L., Lee, H., Skillman, E. D., Lee, J. C., Ct, S., Kennicutt, R. C., & Miller, B. W. 2009, ApJ, 705, 723

Dalcanton, J. J. 2007, ApJ, 658, 941

Dalcanton, J. J., et al. 2009, ApJS, 183, 67

Dale, D. A., et al. 2009, ApJ, 703, 517

Dekel, A., & Silk, J. 1986, ApJ, 303, 39

Denicoló, G., Terlevich, R., & Terlevich, E. 2002, MNRAS, 330, 69

Dennefeld, M., & Kunth, D. 1981, AJ, 86, 989

de Vaucouleurs, G., de Vaucouleurs, A., Corwin, H. G., Jr., Buta, R. J., Paturel, G., & Fouque, P. 1991, Third Reference Catalogue of Bright Galaxies Volume 1-3, XII, 2069 pp. 7 figs.. Springer-Verlag Berlin Heidelberg New York

Dohm-Palmer, R. C., Skillman, E. D., Gallagher, J., et al. 1998, AJ, 116, 1227

Dolphin, A. E., et al. 2003, AJ, 125, 1261

Dufour, R. J. 1984, PASP, 96, 787

Dutil, Y. & Roy, J.-R. 1999, ApJ, 516, 62

Draine, B. T., et al. 2007, ApJ, 663, 866

Egusa, F., Kohno, K., Sofue, Y., Nakanishi, H., & Komugi, S. 2009, ApJ, 697, 1870

Ekta, Chengalur, J. N., & Pustilnik, S. A. 2008, MNRAS, 391, 881

Ekta, B., & Chengalur, J. N. 2010, MNRAS, 406, 1238

Ellison, S. L., Patton, D. R., Simard, L., & McConnachie, A. W. 2008b, AJ, 135, 1877

Elson, E. C., de Blok, W. J. G., & Kraan-Korteweg, R. C. 2010, 404, 2061

Engelbracht, C. W., Gordon, K. D., Rieke, G. H., Werner, M. W., Dale, D. A., & Latter, W. B. 2005, ApJ, 628, L29

Engelbracht, C. W., Rieke, G. H., Gordon, K. D., Smith, J.-D. T., Werner, M. W., Moustakas, J., Willmer, C. N. A., & Vanzi, L. 2008, ApJ, 678, 804

Esteban, C., Bresolin, F., Peimbert, M., et al. 2009, ApJ, 700, 654

Fabbian, D., Nissen, P. E., Asplund, M., Pettini, M., & Akerman, C. 2009, AA, 500, 1143

Fanelli, M.N., O'Connell, R.W., & Thuan, T.X., 1988, ApJ, 334, 665

Fazio, G. G., et al. 2004, ApJS, 154, 10

Ferguson, A. M. N., Gallagher, J. S., & Wyse, R. F. G. 1998, AJ, 116, 673

Ferland, G. J., Korista, K. T., Verner, D. A., Ferguson, J. W., Kingdon, J. B., & Verner, E. M. 1998, PASP, 110, 761

Fierro, J., Torres-Peimbert, S., & Peimbert, M. 1986, PASP, 98, 1032

Filippenko, A. V. 1982, PASP, 94, 715

Fouesneau, M., & Lançon, A. 2010, A&A, 521, A22

Fraternali, F., van Moorsel, G., Sancisi, R., & Oosterloo, T. 2002, AJ, 123, 3124

Galarza, V. C., Walterbos, R. A. M., & Braun, R. 1999, AJ, 118, 2775

Gallagher, III, J. S., & Hunter, D. A. 1989, AJ, 98, 806

Garnett, D. R., & Shields, G. A. 1987, ApJ, 317, 82

Garnett, D. R. 1989, ApJ, 345, 282

Garnett, D. R. 1990, ApJ, 363, 142

Garnett, D. R., Dufour, R. J., Peimbert, M., et al. 1995, ApJ, 449, L77

Garnett, D. R., Skillman, E. D., Dufour, R. J., et al. 1995b, ApJ, 443, 64

Garnett, D. R., Skillman, E. D., Dufour, R. J., & Shields, G. A. 1997a, ApJ, 481, 174

Garnett, D. R., Shields, G. A., Skillman, E. D., Sagan, S. P., & Dufour, R. J. 1997b, ApJ, 498, 63

Garnett, D. R., Shields, G. A., Peimbert, M., Torres-Peimbert, S., Skillman, E. D., Dufour, R. J., Terlevich, E., & Terlevich, R. J. 1999, ApJ, 513, 168

Garnett, D. R. 2002, ApJ, 581, 1019

Garnett, D. R., Edmunds, M. G., Henry, R. B. C., Pagel, B. E. J., & Skillman, E. D. 2004, AJ, 128, 2772

Gil de Paz, A., Zamorano, J., & Gallego, J. 2000a, A&A, 361, 465

Gil de Paz, A., Zamorano, J., Gallego, J., & Domínguez, F. d. B. 2000b, A&AS, 145, 377

Gil de Paz, A., Boissier, S., Madore, B. F., et al. 2007, ApJS, 173, 185

González Delgado, R. M., Leitherer, C., & Heckman, T. M. 1999, ApJS, 125, 489

Gordon, K. D., Engelbracht, C. W., Rieke, G. H., Misselt, K. A., Smith, J.-D. T., & Kennicutt, Jr., R. C. 2008, ApJ, 682, 336

Goddard, Q. E., Bresolin, F., Kennicutt, R. C., Ryan-Weber, E. V., & Rosales-Ortega, F. F. 2011, MNRAS, 412, 1246

Gusev, A. S., Pilyugin, L. S., Sakhibov, F., et al. 2012, MNRAS, 424, 1930

Guseva, N. G., Papaderos, P., Meyer, H. T., Izotov, Y. I., & Fricke, K. J. 2009, å, 505, 63

Guseva, N. G., Izotov, Y. I., Stasińska, G., et al. 2011, A&A, 529, A149

Gustafsson B., Karlson T., Olsson E., Edvardsson B., & Ryde N. 1999, å342, 426

Esteban, C., & Vilchez, J. M. 1992, ApJ, 390, 536

Hendry, M. A., Smartt, S. J., Maund, J. R., et al. 2012, MNRAS, 359, 906

Henry, R. B. C. 1990, ApJ, 356, 229

Henry, R. B. C., Edmunds, M. G., & Köppen, J. 2000, ApJ, 541, 660

Henry, R. B. C., Nava, A., & Prochaska, J. X. 2006, ApJ, 647, 984

Heraudeau, P., & Simien, F. 1996, A&AS, 118, 111

Hodge, P. W., & Kennicutt, R. C., Jr. 1983, AJ, 88, 296

Hook, I. M., Jørgensen, I., Allington-Smith, J. R., et al. 2004, PASP, 116, 425

Hopp, U., & Schulte-Ladbeck, R. E. 1991, A&A, 248, 1

Huchra, J. P., Brodie, J. P., & Kent, S. M. 1991, ApJ, 370, 495

Hummer, D. G., & Storey, P. J. 1987, MNRAS, 224, 801

Hunter, D. A., Gallagher, J. S., & Rautenkranz, D. 1982, ApJS, 49, 53

Hunter, D. A., & Gallagher, III, J. S. 1985, ApJS, 58, 533

Hunter, D. A., & Hoffman, L. 1999, AJ, 117, 2789

Izotov, Y. I., Stasińska, G., Meynet, G., Guseva, N. G., & Thuan, T. X. 2006, A&A, 448, 955

Izotov, Y. I., & Thuan, T. X. 1999, ApJ, 511, 639

Izotov, Y. I., & Thuan, T. X. 2007a, ApJ, 665, 1115

Izotov, Y. I., Thuan, T. X., & Stasińska, G. 2007b, ApJ, 662, 15

Izotov, Y. I., Thuan, T. X., & Guseva, N. G. 2012, å, 546, A122

Jacoby, G. H., & Ford, H. C. 1986, ApJ, 304, 490

Jacoby, G. H., & Ciardullo, R. 1999, ApJ, 515, 169

Jacobs, B. A., Rizzi, L., Tully, R. B., et al. 2009, AJ, 138, 332

James, B. L., Tsamis, Y. G., Barlow, M. J., et al. 2009, MNRAS, 398, 2

Jenkins, C. R. 1987, MNRAS, 226, 341

Jester, S., et al. 2005, AJ, 130, 873

Johnson, B. D., Weisz, D. R., Dalcanton, J. J., et al. 2013, ApJ, 772, 8

Kamphuis, J., & Briggs, F. 1992, A&A, 253, 335

Karachentsev, I. D., Kopylov, A. I., & Kopylova, F. G. 1994, Bull. Special Astrophys. Obs., 38, 5

Karachentsev, I. D., et al. 2003, A&A, 398, 479

Karachentsev, I. D., et al. 2006, AJ, 131, 1361

Kauffmann, G., et al. 2003, MNRAS, 341, 33

Kehrig, C., Vílchez, J. M., Sánchez, S. F., et al. 2008, A&A, 477, 813

Kendall, S., Kennicutt, R. C., Clarke, C. 2011, MNRAS, 414, 538

Kennicutt, R. C., Jr., Bresolin, F., & Garnett, D. R. 2003a, ApJ, 591, 801

Kennicutt, R. C., Jr., Armus, L., Bendo, G., et al. 2003b, PASP, 115, 928

Kennicutt, R. C., Jr., Lee, J. C., Funes, S. J., José G., Sakai, S., & Akiyama, S. 2008, ApJS, 178, 247

Kewley, L. J., Jansen, R. A., & Geller, M. J. 2005, PASP, 117, 227

Kewley, L. J. & Ellison, S. L. 2008, ApJ, 681, 1183

Kennicutt, R. C., Calzetti, D., Aniano, G., et al. 2011, PASP, 123, 1347

Kinman, T. D., & Hintzen, P. 1981, PASP, 93, 405

Kniazev, A. Y., Grebel, E. K., Hao, L., Strauss, M. A., Brinkmann, J., & Fukugita, M. 2003, ApJ, 593, L73

Kniazev, A. Y., Pustilnik, S. A., Grebel, E. K., Lee, H., & Pramskij, A. G. 2004, ApJS, 153, 429

Kniazev, A. Y., Grebel, E. K., Pustilnik, S. A., Pramskij, A. G., & Zucker, D. B. 2005, AJ, 130, 1558

Kobulnicky, H. A., & Skillman, E. D. 1996, ApJ, 471, 211

Kobulnicky, H. A., & Skillman, E. D. 1997a, ApJ, 489, 636

Kobulnicky, H. A., Skillman, E. D., Roy, J.-R., Walsh, J. R., & Rosa, M. R. 1997b, ApJ, 477, 679

Kobulnicky, H. A., Skillman, E. D., Roy, J.-R., Walsh, J. R., & Rosa, M. R. 1997, ApJ, 477, 679

Kobulnicky, H.A. & Skillman, E.D. 1998, ApJ, 497, 601

Kobulnicky, H. A., Kennicutt, Jr., R. C., & Pizagno, J. L. 1999, ApJ, 514, 544

Kobulnicky, H. A., Willmer, C. N. A., Phillips, A. C., et al. 2003, ApJ, 599, 1006

Kobulnicky, H. A., & Kewley, L. J. 2004, ApJ, 617, 240

Köppen, J., Weidner, C., & Kroupa, P. 2007, MNRAS, 375, 673

Kunth, D., & Sargent, W. L. W. 1981, A&A, 101, L5

Kwitter, K. B. & Aller, L. H. 1981, MNRAS, 195, 939

Kwitter, K. B., Lehman, E. M. M., Balick, B., & Henry, R. B. C. 2012, ApJ, 753, 12

Lee, J. C., Gil de Paz, A., Kennicutt, R. C., Jr., et al. 2011, ApJS, 192, 6

Lee, J. C., Salzer, J. J., & Melbourne, J. 2004, ApJ, 616, 752

Lee, H., Grebel, E. K., & Hodge, P. W. 2003a, A&A, 401, 141

Lee, H., McCall, M. L., Kingsburgh, R. L., Ross, R., & Stevenson, C. C. 2003b, AJ, 125, 146

Lee, H., & Skillman, E. D. 2004, ApJ, 614, 698

Lee, H., Skillman, E. D., & Venn, K. A. 2005, ApJ, 620, 223

Lee, H., Skillman, E. D., & Venn, K. A. 2006b, ApJ, 642, 813

Lee, H., Skillman, E. D., Cannon, J. M., Jackson, D. C., Gehrz, R. D., Polomski, E. F., & Woodward, C. E. 2006a, ApJ, 647, 970

Leitherer, C., & Heckman, T. M. 1995, ApJS, 96, 9

Leitherer, C., & Ekstrom, S. 2011, arXiv:1111.5204

Leitner, S. N., & Kravtsov, A. V. 2011, ApJ, 734, 48

Lemonias, J. J., Schiminovich, D., Thilker, D., et al. 2011, ApJ, 733, 74

Lequeux, J., Peimbert, M., Rayo, J. F., Serrano, A., & Torres-Peimbert, S. 1979, A&A, 80, 155

Liang, Y. C., Yin, S. Y., Hammer, F., Deng, L. C., Flores, H., & Zhang, B. 2006, ApJ, 652, 257

Liang, Y. C., Hu, J. Y., Liu, F. S., & Liu, Z. T. 2007, AJ, 134, 759

López-Sánchez, Á. R., & Esteban, C. 2010, A&A, 517, A85

López-Sánchez, Á. R., Koribalski, B. S., van Eymeren, J., et al. 2012, MNRAS, 419, 1051

Maciel, W. J., Lago, L. G., & Costa, R. D. D. 2005, A&A, 433, 127

Magrini, L., Sestito, P., Randich, S., & Galli, D. 2009, A&A, 494, 95

Maiolino, R., et al. 2008, A&A, 488, 463

Makarova, L. N., & Karachentsev, I. D. 1998, A&AS, 133, 181

Makarova, L., Karachentsev, I., Takalo, L. O., Heinaemaeki, P., & Valtonen, M. 1998, A&AS, 128, 459

Mannucci, F., Cresci, G., Maiolino, R., Marconi, A., & Gnerucci, A. 2010, MNRAS, 408, 2115

Marble, A. R., et al. 2010, ApJ, 715, 506

Markwardt, C. B. 2009, in ASP Conf. Ser. 411, Astronomical Data Analysis Software and Systems XVIII, ed. D. A. Bohlender, D. Durand, & P. Dowler (San Francisco, CA: ASP), 251

Martin, P. & Roy, J.-R. 1994, ApJ, 424, 599

Martin, C. L. 1997, ApJ, 491, 561

Massey, P., Olsen, K. A. G., Hodge, P. W., et al. 2006, AJ, 131, 2478

Matteucci, F., & Tosi, M. 1985, MNRAS, 217, 391

Mattsson, L. 2010, Å, 515, A68

McCall, M. L., Rybski, P. M., & Shields, G. A. 1985, ApJS, 57, 1

McCall, M. L. 2004, AJ, 128, 2144

McGaugh, S. S. 1991, ApJ, 380, 140

McGaugh, S. S. 1994, ApJ, 426, 135

Meidt, S. E., Schinnerer, E., Knapen, J. H., et al. 2012, ApJ, 744, 17

Melbourne, J., Williams, B. F., Dalcanton, J. J., et al. 2012, ApJ, 748, 47

Miller, B. W., & Hodge, P. 1996, ApJ, 458, 467

Minchev, I. & Famaey, B. 2010, ApJ, 722, 112

Mollá, M., & Díaz, A. I. 2005, MNRAS, 358, 521

Mollá, M., Vílchez, J. M., Gavilán, M., & Díaz, A. I. 2006, MNRAS, 372, 1069

Moustakas, J., & Kennicutt, Jr., R. C. 2006, ApJS, 164, 81

Moustakas, J., Kennicutt, R. C., Jr., Tremonti, C. A., Dale, D. A., Smith, J.-D. T., & Calzetti, D. 2010, ApJS, 190, 233

Moustakas, J., Zaritsky, D., Brown, M., Cool, R., Dey, A., Eisenstein, D. J., Gonzalez, A. H., Jannuzi, B., Jones, C., Kochanek, C. S., Murray, S. S., Wild, V 2012, ApJ, *accepted*

Natali, G., Pedichini, F., & Righini, M. 1992, A&A, 256, 79

Nava, A., Casebeer, D., Henry, R. B. C., & Jevremovic, D. 2006, ApJ, 645, 1076

Nicholls, D. C., Dopita, M. A., & Sutherland, R. S. 2012, ApJ, 752, 148

Noeske, K. G., Guseva, N. G., Fricke, K. J., et al. 2000, A&A, 361, 33

Oke, J. B. 1990, AJ, 99, 1621

Oey, M. S., & Shields, J. C. 2000, ApJ, 539, 687

Olive, K. A., & Skillman, E. D. 2001, , 6, 119

Pagel, B. E. J., Edmunds, M. G., Blackwell, D. E., Chun, M. S., & Smith, G. 1979, MNRAS, 189, 95

Pagel, B. E. J., & Edmunds, M. G. 1981, ARA&A, 19, 77

Pagel, B. E. J. 1985, European Southern Observatory Conference and Workshop Proceedings, 21, 155

Pagel, B. E. J., Simonson, E. A., Terlevich, R. J., & Edmunds, M. G. 1992, MNRAS, 255, 325

Peeples, M. S., Pogge, R. W., & Stanek, K. Z. 2008, ApJ, 685, 904

Peeples, M. S., Pogge, R. W., & Stanek, K. Z. 2009, ApJ, 695, 259

Peimbert, M. 1967, ApJ, 150, 825

Peimbert, M., & Costero, R. 1969, Boletin de los Observatorios Tonantzintla y Tacubaya, 5, 3

Pellet, A., Astier, N., Viale, A., et al. 1978, A&AS, 31, 439

Peña-Guerrero, M. A., Peimbert, A., & Peimbert, M. 2012, ApJ, 756, L14

Pettini, M. & Pagel, B. E. J. 2004, MNRAS, 348, L59

Pérez-Montero, E., & Contini, T. 2009, MNRAS, 398, 949

Pérez-Montero, E., Vílchez, J. M., Cedrés, B., et al. 2011, A&A, 532, A141

Pilyugin, L. S. 2001, A&A, 369, 594

Pilyugin, L. S. 2001a, A&A, 369, 594

Pilyugin, L. S. 2001b, A&A, 373, 56

Pilyugin, L. S. 2003, A&A, 397, 109

Pilyugin, L. S., Vílchez, J. M., & Contini, T. 2004, A&A, 425, 849

Pilyugin, L. S., & Thuan, T. X. 2005, ApJ, 631, 231

Pilyugin, L. S., Vílchez, J. M., & Thuan, T. X. 2010, ApJ, 720, 1738

Pogge, R. W., Atwood, B., Brewer, D. F., et al. 2010, The multi-object double spectrographs for the Large Binocular Telescope, Society of Photo-Optical Instrumentation Engineers (SPIE) Conference Series, 7735

Prantzos, N. & Boissier, S. 2000, MNRAS, 313, 338

Press, W. H., Teukolsky, S. A., Vetterling, W. T., & Flannery, B. P. 1992, Numerical recipes in C: The art of scientific computing, Second Edition, Cambridge: University Press

Prugniel, P., Bica, E., Klotz, A., & Alloin, D. 1993, A&AS, 98, 229

Pustilnik, S. A., Kniazev, A. Y., & Pramskij, A. G. 2005, A&A, 443, 91

Pustilnik, S. A., Tepliakova, A. L., & Kniazev, A. Y. 2008a, Astronomy Letters, 34, 457

Pustilnik, S. A., Tepliakova, A. L., Kniazev, A. Y., & Burenkov, A. N. 2008b, MNRAS, 388, L24

Reach, W. T., et al. 2005, PASP, 117, 978

Rekola, R., Jerjen, H., & Flynn, C. 2005, A&A, 437, 823

Richer, M. G., Stasińska, G., & McCall, M. L. 1999, A&AS, 135, 203

Rizzi, L., Tully, R. B., Makarov, D., Makarova, L., Dolphin, A. E., Sakai, S., & Shaya, E. J. 2007, ApJ, 661, 815

Rosales-Ortega, F. F., Díaz, A. I., Kennicutt, R. C., & Sánchez, S. F. 2011, MNRAS, 415, 2439

Rosenberg, J. L., Ashby, M. L. N., Salzer, J. J., & Huang, J.-S. 2006, ApJ, 636, 742

Roy, J.-R., & Kunth, D. 1995, A&A, 294, 432

Rubin, V. C., Krishna Kumar, C., & Ford, W. K., Jr. 1972, ApJ, 177, 31

Russell, S. C. & Dopita, M. A. 1990, ApJS, 74, 93

Ryan-Weber, E., Webster, R., & Bekki, K. 2003, The IGM/Galaxy Connection. The Distribution of Baryons at z=0, 281, 223

Sabbadin, F., Ortolani, S., & Bianchini, A. 1984, A&A, 131, 1

Sakai, S., Ferrarese, L., Kennicutt, R. C., Jr., & Saha, A. 2004, ApJ, 608, 42

Salim, S., et al. 2007, ApJS, 173, 267

Salim, S. and Rich, R. M. 2010, ApJ, 714, L290

Salzer, J. J., Lee, J. C., Melbourne, J., et al. 2005, ApJ, 624, 661

Sanders, N. E., Caldwell, N., McDowell, J., & Harding, P. 2012, ApJ, 758, 133

Sandstrom, K. M., Bolatto, A. D., Bot, C., et al. 2012, ApJ, 744, 20

Sandstrom, K. M., et al. 2013, in preparation

Sanna, N., et al. 2008, ApJ, 688, L69

Santillán, A., Sánchez-Salcedo, F. J., & Franco, J. 2007, ApJ, 662, L19

Savaglio, S., et al. 2005, ApJ, 635, 260

Saviane, I., Ivanov, V. D., Held, E. V., Alloin, D., Rich, R. M., Bresolin, F., & Rizzi, L. 2008, A&A, 487, 901

Schmidt, G. D., Weymann, R. J., & Foltz, C. B. 1989, PASP, 101, 713

Schlegel, D. J., Finkbeiner, D. P., & Davis, M. 1998, ApJ, 500, 525

Sellwood, J. A. & Balbus, S. A. 1999, ApJ, 511, 660

Searle, L. 1971, ApJ, 168, 327

Shapley, A. E., Erb, D. K., Pettini, M., Steidel, C. C., & Adelberger, K. L. 2004, ApJ, 612, 108

Sharina, M. E., Karachentsev, I. D., & Tikhonov, N. A. 1996, A&AS, 119, 499

Sharina, M. E., Karachentsev, I. D., & Tikhonov, N. A. 1999, Astronomy Letters, 25, 322

Shaver, P. A., McGee, R. X., Newton, L. M., Danks, A. C., & Pottasch, S. R. 1983, MNRAS, 204, 53

Shields, G. A. 1990, ARA&A, 28, 525

Shostak, G. S., & van der Kruit, P. C. 1984, A&A, 132, 20

Sivan, J.-P., Maucherat, A. J., Petit, H., & Comte, G. 1990, A&A, 237, 23

Skillman, E. D., Terlevich, R., Teuben, P. J., & van Woerden, H. 1988, A&A, 198, 33

Skillman, E. D., Kennicutt, R. C., & Hodge, P. W. 1989, ApJ, 347, 875

Skillman, E. D. 1985, ApJ, 290, 449

Skillman, E. D., Televich, R. J., Kennicutt, Jr., R. C., Garnett, D. R., & Terlevich, E. 1994, ApJ, 431, 172

Skillman, E. D., Kennicutt, R. C., Jr., Shields, G. A., & Zaritsky, D. 1996, ApJ, 462, 147

Skillman, E. D., Côté, S., & Miller, B. W. 2003, AJ, 125, 610

Skillman, E. D., Salzer, J. J., Berg, D. A., et al. 2013, AJ, 146, 3

Skrutskie, M. F., Cutri, R. M., Stiening, R., et al. 2006, AJ, 131, 1163

Smartt, S. J., Crowther, P. A., Dufton, P. L., et al. 2001, MNRAS, 325, 257

Smith, J., Armus, L., Dale, D., et al. 2005, Spitzer Proposal, 20518

Smith, J. D. T., Draine, B. T., Dale, D. A., et al. 2007, ApJ, 656, 770

Smith, J.D., et al. 2013, in preparation

Springob, C. M., Masters, K. L., Haynes, M. P., Giovanelli, R., & Marinoni, C. 2009, ApJS, 182, 474

Stasińska, G. 1990, A&AS, 83, 501

Stasińska, G., & Leitherer, C. 1996, ApJS, 107, 661

Stasińska, G. 2005, A&A, 434, 507

Stasińska, G. 2010, in IAU Symp. 262, Stellar Populations–Planning for the Next Decade, ed. G. Bruzual & S. Charlot (Cambridge: Cambridge Univ. Press), 93

Tassis, K., Kravtsov, A. V., & Gnedin, N. Y. 2008, ApJ, 672, 888

Taylor, V. A., Jansen, R. A., Windhorst, R. A., Odewahn, S. C., & Hibbard, J. E. 2005, ApJ, 630, 784

Talent, D. L. 1983, PASP, 95, 986

Thuan, T. X., Izotov, Y. I., & Lipovetsky, V. A. 1995, ApJ, 445, 108

Thuan, T. X., & Izotov, Y. I. 2005, ApJS, 161, 240

Tolstoy, E., Gallagher, J. S., Cole, A. A., et al. 1998, AJ, 116, 1244

Tonry, J. L., Dressler, A., Blakeslee, J. P., et al. 2001, ApJ, 546, 681

Tosi, M., Sabbi, E., Bellazzini, M., Aloisi, A., Greggio, L., Leitherer, C., & Montegriffo, P. 2001, AJ, 122, 1271

Tremonti, C. A., Heckman, T. M., Kauffmann, G., Brinchmann, J., Charlot, S., White, S. D. M., Seibert, M., Peng, E. W., Schlegel, D. J., Uomoto, A., Fukugita, M., & Brinkmann, J. 2004, ApJ, 613, 898

Trundle, C., Dufton, P. L., Lennon, D. J., Smartt, S. J., & Urbaneja, M. A. 2002, A&A, 395, 519

Tsujimoto, T. & Bekki, K. 2011, Å, 530, A78

Tüllmann, R., Rosa, M. R., Elwert, T., Bomans, D. J., Ferguson, A. M. N., & Dettmar, R.-J. 2003, A&A, 412, 69

Tully, R. B., et al. 2006, AJ, 132, 729

Tumlinson, J., Thom, C., Werk, J. K., et al. 2011, , 334, 948

Vaduvescu, O., McCall, M. L., & Richer, M. G. 2007, AJ, 134, 604

Van Dyk, S. D., Li, W., & Filippenko, A. V. 2006, PASP, 118, 351

van Zee, L. 2000, ApJ, 543, L31

van Zee, L., Haynes, M. P., & Salzer, J. J. 1997a, AJ, 114, 2497

van Zee, L., Haynes, M. P., & Salzer, J. J. 1997b, AJ, 114, 2479

van Zee, L., Salzer, J. J., Haynes, M. P., O'Donoghue, A. A., & Balonek, T. J. 1998b, AJ, 116, 2805

van Zee, L., Salzer, J. J., Haynes, M. P., O'Donoghue, A. A., & Balonek, T. J. 1998b, AJ, 116, 2805

van Zee, L., & Haynes, M. P. 2006a, ApJ, 636, 214

van Zee, L., Skillman, E. D., & Haynes, M. P. 2006b, ApJ, 637, 269

van Zee, L., et al. 2013, in preparation

Vázquez, G. A., & Leitherer, C. 2005, ApJ, 621, 695

Venn, K., 1995, ApJ, 449, 839

Venn, K. A., McCarthy, J. K., Lennon, D. J., et al. 2000, ApJ, 541, 610

Véron, P., & Sauvayre, A. 1965, Annales d'Astrophysique, 28, 698

Vila-Costas, M. B., & Edmunds, M. G. 1992, MNRAS, 259, 121

Vila-Costas, M. B., & Edmunds, M. G. 1993, MNRAS, 265, 199

Vilardell, F., Ribas, I., Jordi, C., Fitzpatrick, E. L., & Guinan, E. F. 2010, A&A, 509, A70

Vilchez, J. M., Pagel, B. E. J., Diaz, A. I., Terlevich, E., & Edmunds, M. G. 1988, MNRAS, 235, 633

Vollmann, K., & Eversberg, T. 2006, Astronomische Nachrichten, 327, 862

Wada, K. & Norman, C. A. 1999, ApJ, 516, L13

Weisz, D. R., Dalcanton, J. J., Williams, B. F., et al. 2011, ApJ, 739, 5

Werk, J. K., Putman, M. E., Meurer, G. R., & Santiago-Figueroa, N. 2011, ApJ, 735, 71

Wheeler, J. C., Sneden, C., & Truran, J. W. 1989, ARA&A, 27, 279

Williams, M. J., Bureau, M., & Cappellari, M. 2010, MNRAS, 409, 1330

Willner, S. P. & Nelson-Patel, K. 2002, ApJ, 568, 679

Woosley, S. E. & Weaver, T. A. 1995, ApJS, 101, 181

Worthey, G., España, A., MacArthur, L. A., & Courteau, S. 2005, ApJ, 631, 820

Yin, S. Y., Liang, Y. C., Hammer, F., Brinchmann, J., Zhang, B., Deng, L. C., & Flores, H. 2007, A&A, 462, 535

York, D. G., et al. 2000, AJ, 120, 1579

Zahid, H. J. & Bresolin, F. 2011, AJ, 141, 192

Zahid, H. J., Dima, G. I., Kewley, L. J., Erb, D. K., & Davé, R. 2012, ApJ, 757, 54

Zaritsky, D., Kennicutt, Jr., R. C., & Huchra, J. P. 1994, ApJ, 420, 87

Zurita, A., & Bresolin, F. 2012, MNRAS, 427, 1463

Appendix A

Data Reduction of Optical Spectroscopy

A.1 MMT Data Reduction

All MMT observations used in this thesis were processed using ISPEC2D (Moustakas & Kennicutt, 2006), a long-slit spectroscopy data reduction package written in IDL. A master bias frame was created from $\gtrsim 20$ zero second exposures by discarding the highest and lowest value at each pixel and taking the median. Master sky and dome flats were similarly constructed after normalizing the counts in the individual images. Those calibration files were then used to bias-subtract, flat-field, and illumination-correct the raw data frames. Dark current was measured to be an insignificant ~ 1 e^- per pixel per hour and was not corrected for.

Misalignment between the trace of the light in the dispersion direction and the orientation of the CCD detector was rectified via the mean trace of the standard stars for each night, providing alignment to within a pixel across the detector. A two-dimensional sky subtraction was performed using individually selected sky apertures, followed by a wavelength calibration applied from the HeArNe comparison lamps taken at the same telescope pointing. Airmass dependent atmospheric extinction and reddening were corrected for using the standard Kitt Peak extinction curve (Crawford & Barnes, 1970).

For each target, the multiple sub-exposures were combined, eliminating cosmic rays in the process. The resulting images were then flux-calibrated using the sensitivity curve

derived from the standard star observations taken throughout a given night. Finally, the trace fit to the strongest continuum source in the slit was used to extract the galaxy light within the apertures that encompassed $\gtrsim 99\%$ of the spatially smooth and centrally peaked emission.

A.2 GMOS Data Reduction

GMOS spectra were reduced and extracted using the `GMOS` package of IRAF. Reduction of spectra included bias subtraction and flat fielding based on observations of the quartz halogen lamp on the GCAL unit. A spectral trace of a bright continuum source was used to define the trace for all slits in each field. The shape of this trace was consistent in all exposures of a given field. As the slits were long compared to the spatial extent of the individual H II regions, the sky background was removed from the two-dimensional spectra via the subtraction of local measurements adjacent to the H II region. This local sky subtraction does have the potential to over-subtract strong lines relative to weaker emission lines, as the temperature of the diffuse ISM may be different from the temperature within the H II regions. However, the contributions to measured emission lines from the diffuse ISM is deemed to be negligible as all slits showed comparable backgrounds to the two slits that were both long and situated at the edge of NGC 628's disk. While red and blue spectra were not observed simultaneously, we note that the continuum is well matched where spectra overlap, indicating stable sky conditions and matched extraction apertures.

Appendix B

Emission Line Measurements

B.1 Technique

Emission line strengths were measured using standard methods available within IRAF.[1]

In particular, the SPLOT routine was used to analyze the extracted one-dimensional spectra and to fit Gaussian profiles to emission lines to determine their integrated fluxes. The Hα and the adjacent [N II] lines were fitted simultaneously for an accurate deblending. Special attention was paid to the Balmer lines, which are sometimes located in troughs of significant underlying stellar absorption. All Balmer lines were fit simultaneously with multiple components where the absorption was fit by a broad, negative Lorentzian profile and the emission was fit by a narrow, positive Gaussian profile. Additional constraints were placed on the faint lines, including the [O III] λ4363 and [N II] λ5755 auroral lines, such that their FWHMs match the neighboring strong-line fits.

Skillman et al. (1994) give a strict accounting of the standard errors (δL) associated with a given line strength (L):

$$\frac{\delta L}{L} = \frac{\{C_1 + C_2 + (n_o/\sqrt{n_s})S + nAN^2 + [2.3f(\lambda)\delta C(\mathrm{H}\beta)L]^2 + [0.01L]^2 + [\delta F L]^2\}^{1/2}}{L}. \tag{B.1}$$

[1] IRAF is distributed by the National Optical Astronomy Observatories, which are operated by the Association of Universities for Research in Astronomy, Inc., under cooperative agreement with the National Science Foundation.

Due to the quality of the detectors used the read out noise term (nAN^2) is negligible compared to the other dominating terms. For weak lines, the uncertainty is dominated by error from the continuum subtraction, meaning that the C_2 (counts in the continuum) term is the dominating fraction of the C_1 (total counts in line, continuum, and sky) term. For the lines with flux measurements much stronger than the rms noise of the continuum, (usually the Hα lines and often the [O III] $\lambda\lambda$4959,5007 doublet) the error is dominated by flux calibration error term ($[\delta FL]^2$) and the reddening error term ($[2.3f(\lambda)\delta C(H\beta)L]^2$). Thus, in the case of our spectra, the errors of the flux measurements were approximated using

$$\delta F_\lambda \approx \sqrt{(2 \times \sqrt{n_p} \times rms)^2 + (0.02 \times F_\lambda)^2}, \tag{B.2}$$

where n_p is the number of pixels spanning the Gaussian profile fit to the narrow emission lines. The root mean squared (rms) noise in the continuum was taken to be the average of the rms on each side of an emission line. Then, the first (rms) term determines the approximate uncertainty for the weak lines, and the second (F_λ) term dominates the uncertainty for the strong lines. In the latter case, a minimum uncertainty of 2% was assumed, which is the typical error in fitting flux calibrated points to standard Oke (1990) stars.

In the cases where we were not able to detect [O III] λ4363 and He II λ4686 at the level of more than 3 σ in any of the spectra, a flux upper limit was estimated using Equation B.2. We calculated upper limits on the electron temperatures based on these λ4363 fluxes, but none provided significant constraints for abundance calculations.

B.2 Reddening Corrections

The wide range of observed wavelengths require fluxes to be corrected for extinction and reddening. The relative intensities of the Balmer lines are nearly independent of both density and temperature, so they can be used to solve for the reddening. The spectra were de-reddened using the reddening law of Cardelli et al. (1989), parametrized by $A_V = 3.1\ E(B-V)$, where the extinction, $A_1(\lambda)$ was calculated using the York

Extinction Solver (McCall, 2004).[2] With these values, the reddening, $E(B-V)$, can be derived using

$$\log \frac{I(H\alpha)}{I(H\beta)} = \log \frac{F(H\alpha)}{F(H\beta)} + 0.4\ E(B-V)\ [A_1(H\alpha) - A_1(H\beta)], \tag{B.3}$$

where $F(\mathrm{H}\alpha)/F(\mathrm{H}\beta)$ is the observed flux ratio and $I(\mathrm{H}\alpha)/I(\mathrm{H}\beta)$ is the de-reddened line intensity ratio using case B from Hummer & Storey (1987), assuming an electron temperature calculated from the [O III] line ratio and $\mathrm{n}_e = 10^2$ cm^{-3}. When we cannot estimate the electron temperature from the faint lines, we assume standard H II region characteristics. In Chapter 2, we assumed $\mathrm{T}_e = 1.25 \times 10^4$ K and $\mathrm{n}_e = 10^2$ cm^{-3}, which is typical for objects of average metallicity. At the extreme ends of the metallicity scale, $\mathrm{T}_e = 0.75 \times 10^4$ K can be used for cool, metal rich regions and $\mathrm{T}_e = 1.75 \times 10^4$ K for hot, metal cool regions. Following Lee & Skillman (2004) the reddening value can be converted to the logarithmic extinction at $H\beta$ as

$$c(H\beta) = 1.43\ E(B-V). \tag{B.4}$$

In the case of Chapter 2, a first order reddening correction was performed, using only the Hα/Hβ ratio, but was compared to the blue Balmer lines for consistency. For the other Chapters in this book, when all the necessary Balmer lines are present, we evaluate our reddening corrections by using a chi-squared minimization technique in comparing calculated to theoretical values to ensure the best combined solution for the Hδ/Hβ, Hγ/Hβ, and Hα/Hβ ratios (see discussion in Olive & Skillman, 2001). For those cases where underlying absorption was accounted for in measuring the individual emission lines, we fix underlying absorption to be zero in the minimization; otherwise reddening and underlying absorption were solved for simultaneously.

[2] http://www1.cadc-ccda.hia-iha.nrc-cnrc.gc.ca/community/YorkExtinctionSolver/

Appendix C

Abundance Determinations

C.1 Electron Temperature and Density Determinations

For H II regions, accurate direct oxygen abundance determinations require reliable electron temperature measurements. This is typically done by observing a temperature sensitive auroral line. I have taken advantage of two such lines: the [O III] λ4363 and [N II] λ5755 auroral lines. To establish a low-uncertainty electron temperature estimate, we define a strong auroral line measurement using a 4σ criterion. We then can determine electron temperatures from the associated temperature sensitive "auroral" to "nebular" ratio of collisionally excited lines.

An H II region can be modeled by two separate volumes, one of low ionization and one of high ionization. For the high ionization zone, we used the [O III] I($\lambda\lambda$4959,5007)/I(λ4363) ratio to derive a temperature using the IRAF task `TEMDEN`. This task computes the electron temperature of the ionized nebular gas within the 5-level atom approximation. The O^+ (low ionization) zone electron temperature can be related to the O^{++} (high ionization) zone electron temperature (e.g., Campbell et al., 1986; Pagel et al., 1992). We used the relation between t_2 ($T_e(O^+)$) and t_3 ($T_e(O^{++})$) proposed by Pagel et al. (1992), based on the photoionization modeling of Stasińska (1990) to determine the low ionization zone temperature:

$$t_e(\text{O II})^{-1} = 0.5 \times [t_e(\text{O III})^{-1} + 0.8], \tag{C.1}$$

where $t_e = T_e/10^4$ K.

For spectra in which a strong [O III]λ4363 was not measured, we can next try to determine a temperature using the [N II] I($\lambda\lambda$6548,6584)/I(λ5755) ratio, where we assume T_e(N II) = T_e(O II). The high ionization zone temperature can then be determined using Equation C.1 in reverse. While I prioritize the [O III] temperature estimate in this work, further studies are needed to determine for what cases the [N II] temperature diagnostic is more reliable, and where the differences originate. Note that [O II] $\lambda\lambda 7320, 7330$ was measured in multiple H II regions in Chapter 4, however, Zurita & Bresolin (2012) have shown that the error in using [O II] is much larger than in using [N II] to derive a temperature for the low ionization zone.

Additionally, we calculate a separate T_e(S III) because the S^{++} ionization zone lies partially in both the O^+ and the O^{++} zones:

$$t_e(\text{S III}) = 0.83 \times t_e(\text{O III}) + 0.17. \tag{C.2}$$

[S II] $\lambda\lambda$6717,6731 was used to determine the electron densities, which are consistent with the low density limit for all objects discussed here. For all abundance calculations we assume $n_e = 10^2$ cm^{-3} (which is consistent with the 1σ upper bounds and produces identical results for all lower values of n_e).

C.2 Ionic and Total Abundances

Ionic abundances were calculated with:

$$\frac{N(X^i)}{N(H^+)} = \frac{I_{\lambda(i)}}{I_{H\beta}} \frac{j_{H\beta}}{j_{\lambda(i)}} . \tag{C.3}$$

The emissivity coefficients, which are functions of both temperature and density, were determined using the `IONIC` routine in IRAF with atomic data updated as reported in Bresolin et al. (2009a). This routine applies the 5-level atom approximation, assuming an electron density of $n_e = 10^2$ cm^{-3} and the appropriate ionization zone electron temperature.

Total oxygen abundances (O/H) are calculated from the simple sum of O^+/H^+ and O^{++}/H^+. The other abundance determinations require ionization correction factors

(ICF) to account for unobserved ionic species. For nitrogen, we employ the common assumption that $N/O = N^+/O^+$ (Peimbert , 1967). This allows us to directly compare our results with other studies in the literature. Nava et al. (2006) have investigated the validity of this assumption. They concluded that it could be improved upon with modern photoionization models, but was valid at the precision of about 10%.

Collisionally excited emission lines of sulfur, neon, and argon were also observed in many of our spectra. For Ne we use a fairly straightforward ICF: $ICF(Ne) = (O^+ + O^{++})/O^{++}$ (Crockett et al.,, 2006). S and Ar present more complicated situations as S^{++} and Ar^{++} span both the O^+ and the O^{++} zones. Thuan et al. (1995) have determined the analytic ICF approximations for both S and Ar using the model calculations of photoionized H II regions by Stasińska (1990). We employ these ICFs from Thuan et al. (1995) to correct for the unobserved S^{+3}, Ar^{+2}, and Ar^{+4} states.